Microscopic description of magnetic model compounds
- from one-dimensional magnetic insulators to three-dimensional itinerant metals

DISSERTATION

zur Erlangung des akademischen Grades

Doktor rerum naturalium
(Dr. rer. nat.)

vorgelegt

der Fakultät Mathematik und Naturwissenschaften
der Technischen Universität Dresden

von

DIPL. PHYS. MIRIAM SCHMITT

geboren am 18.01.1980 in Bamberg

Eingereicht am 08.07.2011

Die Dissertation wurde in der Zeit von Juli 2007 bis Juni 2011 im
Max-Planck-Insitut für chemische Physik fester Stoffe angefertigt.

Tag der Verteidigung: 22.11.2012

Gutachter: Prof. Dr. Jeroen van den Brink
Prof. Yuri Grin

Die eine Generation baut die Straße auf der die nächste fährt.
Chinesisches Sprichwort

Für meinen Doktorvater Helmut Eschrig, der ein großer "Straßenbauer" war, und meiner Tochter Nola, die erst mit dem Laufen beginnt.

Contents

Contents

List of abbreviations

AFM	antiferromagnetic
AMF	around mean field
AL	atomic limit
ASA	atomic sphere approximation
a.u.	atomic units
BEB	Blackman-Esterling-Berk
CPA	coherent potential approximation
(c)T-phase	(collapsed) tetragonal phase
DAC	diamond anvil cell
DCC	double counting correction
DFT	density functional theory
DMFT	dynamical mean field theory
DOS	density of states
ED	exact diagonalization
EFG	electric field gradient
ELI	electron localizability indicator
ESRF	European Synchrotron Radiation Facility
ESR	electron spin resonance
EoS	equation of states
FLL	fully localized limit
FM	ferromagnetic
FPLO	full-potential local-orbital (minimum-basis)
f.u.	formula unit
GGA	generalized gradient approximation
GKA	Goodenough-Kanamori-Anderson
HTSE	high temperature series expansion
(L)APW	(linearised) augmented plane wave
LMTO	linear muffin tin orbital
L(S)DA	local (spin) density approximation
MT	muffin tin
ND	neutron diffraction
NMR	nuclear magnetic resonance
NN	nearest neighbors
NNN	next nearest neighbors
RE	rare earth
QCP	quantum critical point
QMC	quantum Monte Carlo
SC	super cell
SDW	spin density wave (columnar/stripe-type AFM order)
TB	tight binding

VCA	virtual crystal approximation
WF	Wannier function
WP	Wyckoff position
XANES	x-ray absorption near edge spectroscopy
XAS	x-ray absorption spectroscopy
xc	exchange and correlation
XMCD	x-ray magnetic circular dichroism
XRD	x-ray diffraction

1. Introduction

Solid state physics comprises many interesting physical phenomena driven by the complex interplay of the crystal structure, magnetic and orbital degrees of freedom, quantum fluctuations and correlation. The discovery of materials, which exhibit exotic phenomena like low dimensional magnetism, superconductivity, thermoelectricity or multiferroic behavior, leads to various applications that even found their way into our daily live. For such technical applications and the purposive modification of materials, the understanding of the underlaying mechanisms in solids is a precondition. In this context, the close interplay of theory and experimental techniques is a powerful approach to gain deep insights into basic concepts to describe complex materials.

For a long time, a common purpose of theoretical physicist and chemists working in the field of condensed matter, was to develop microscopically based methods, which allow a reliable description of the electronic and magnetic properties for real materials, solely based on their crystal structure. While in the early 80's the calculation of small systems including few atoms were a sever challenge, such a sophisticated theoretical approach was a mere dream. However, nowadays DFT based band structure programs become broadly available with the possibility to calculate systems with several hundreds of atoms in reasonable time scales and high accuracy, using standard computers due to the rapid technical and conceptional development in the last decades. These improvements allow to study the intimate interplay of the crystal structure and the physical properties of solids and support the search for underlying mechanisms of different phenomena from microscopic grounds. The controlled modification of individual parameters and the systematic computational search even within large parameter spaces help to identify and separate the influence of crucial parameters in often complex relations. The combination of detailed electronic structure calculations with subsequent model calculations succeeds in most cases to describe macroscopic properties by simplified relations based on few main parameters, only, and allows to develop an intuitive picture. However, such studies always have to balance between the necessary accuracy and the maximum simplicity of the derived model description. Such combined approaches do not only provide microscopic insights, but also more and more predictive power.

Nevertheless, several examples appeared in the last years, where DFT based investigations result in essentially different or even controversial models. Examples are the descriptions of the magnetic model compounds $Sr_2Cu(PO_4)_2$,[1, 2, 3] $Na_3Cu_2SbO_6$ [4, 5] or CuNCN.[6, 7] In the simplest case, such discrepancies originate from too crude computational approximations which can bias the calculated electronic structure in an uncontrolled way. But also the reliable modeling of real material effects like disorder, vacancies or partial site occupation, which can become crucial for the physical properties of a system, is far from trivial and often restricted by the numerical feasibility. Also considering strong correlations with an important influence on transition metal or rare earth compounds, containing $3d$ and $4f$ states, are still challenging for present day theory and depend on several parameters that are not precisely known like the Coulomb correlation strength U.

Therefore, in many cases it is important for the development of reliable models for new and complex materials to combine electronic structure calculations with model simulations

of experimental data.

The importance of such a combined approach is underlined by several examples in recent years, where the intuitively guided derivation of magnetic models based on a limited number of experimental data entirely failed. Prominent examples are the controversially discussed magnetic models of volborthite ($Cu_3V_2O_7(OH)_2 \cdot 2H_2O$), $LiVCuO_4$, $LiCu_2O_2$, dioptase ($Cu_6Si_6O_{18} \cdot 6H_2O$) and CuNCN.[8, 9, 10]

In volborthite, the difficulty raises already from the lack of unambiguous criteria to chose a specific model, since a kagome model results in a nearly identical fit compared to a coupled Heisenberg chain model. In contrast, the appropriate model for $LiVCuO_4$ or $LiCu_2O_2$ are rather clear, but the evaluation of the experimental data lead to multiple solutions due to an internal symmetry of the fitted model itself. In these cases, different parameter sets belonging to different regions of the phase diagram, e.g., the AFM-AFM or FM-AFM regime, can describe the experimental data with similar accuracy. Finally, the development of models from structural considerations only are far from trivial and can be at least misleading. The modification or scaling of known models for related systems to derive the magnetic model for dioptase or CuNCN failed in the past.

In all these cases, the evaluation of proper magnetic models largely profited from the combination of experimental methods with detailed electronic structure calculations. In this way, the ambiguity in the interpretation of the experimental data can be resolved, using a magnetic model derived from a microscopic basis.

Furthermore, recent studies demonstrated the impact of structural details, like side groups of the magnetically active building blocks, on the magnetic interactions by their strong influence on the ligand field. Since the refinement of the position of light elements is experimentally challenging, reliable solutions could be achieved successfully by the combination with DFT based structure relaxations for several examples.

However, not only theoretical methods were largely improved over the last years, but also experimental techniques allowing measurements upon extreme conditions like high pressures and high magnetic fields, besides very low temperatures. Since pressure and magnetic fields are rather simple to simulate theoretically, the close interaction between theory and experiment not only probes the derived model descriptions, but also refines and improves existing models and techniques. The simulation of the influence of systematic variations and modifications of measurable properties by magnetic fields, temperature or chemical and hydrostatic pressure, narrows the interesting parameter region for promising experiments. Especially high pressure experiments are a powerful tool since they allow a continuos change of the crystal structure on a rather large energy scale without the drawbacks of an increased chemical complexity.

In this work, we focus on the theoretical description of low dimensional magnets and magnetic, intermetallic compounds. We combined DFT based electronic structure and model calculations to develop the magnetic properties of the compounds from microscopic grounds. The developed, intuitive pictures were challenged by model simulations with various experiments, probing microscopic and macroscopic properties. This combined approach allows to investigate the close interplay of the crystal structure and the magnetic properties of real materials even with complex relations between structural, magnetic and orbital degrees of freedom. Our theoretical results not only provide reliable descriptions of real materials, containing disorder, partial site occupation and strong correlations, but also predict fascinating phenomena upon extreme conditions. In part, these theoretical predictions are already confirmed by own experimental data collected on large scale facilities.

In particular, we introduce in the first part of this work the basic concepts of density functional theory as the underlying theory of the full potential local orbital scheme FPLO used for the electronic structure calculation within this theses. Especially the possibilities and limitations to consider real material effects like disorder, vacancies or correlations are briefly discussed. Furthermore, we introduce our subsequent mapping approach to represent the results of electronic structure calculation by simple physical models. The method section closes with a short overview of the applied experimental techniques and characteristic set-ups for high pressure experiments performed at the European Synchrotron Radiation Facility in Grenoble.

In the second part of the work we focus on the development of magnetic models of low dimensional transition metal compounds with respect to their structural peculiarities by combining theoretical calculations, simulations and experimental measurements. The family of low dimensional spin 1/2 systems attracts always huge interest due to their fascinating phase diagrams including many exotic ground states. The Cu^{2+} cuprates and halides investigated in this work illustrate the great variety of different phenomena fueling the large interest in this class of systems. We studied these strongly correlated systems on a model level with respect to their intimate interplay between structural and magnetic degrees of freedom, as well as the crucial influence of quantum fluctuations on their magnetic ground states. Quantum fluctuations become especially important if the compounds under consideration exhibit strong frustrations, which can originate from both, pure geometry or competing exchange interactions. In this work, we restricted our investigations to compounds in which the magnetically active building blocks are arranged to edge shared chains or related variants. In such systems, usually a strong competition between NN and NNN interactions appears. Whereas the studied edge shared chain and square lattice compounds can be described in most cases by quasi 1D (2D) $J_1 - J_2$ models, the structural dimer compounds can be best modeled by alternating Heisenberg chains $J_{1a} - J_{1b}$. The systematic variations of structural peculiarities, the exchange of ligands, shift of side groups or exchange of interconnecting ions elucidate the complex interplay of different parameter on the magnetic ground state and allows to reduce the variety of interactions to few crucial parameters only. In one of the compounds even orbital degrees of freedom become relevant for the ground state.

Based on the experience regarding a reliable description of different low dimensional magnets, we try to derive general trends and relations for this class of compounds. Thus, we investigated in a comparative study the influence of the particular treatment of correlation by the choice of the unknown Coulomb repulsion U, or the double counting correction, on the leading exchange integrals as well as the effects originating from structural distortion or a changed Cu-O-Cu bond angle.

In the third part of this work, we demonstrate that our approach can be applied successfully not only to insulating materials with localized moments and strong correlation, but also to metals with correlation effects of different strength, reaching from itinerant systems to metallic compounds containing well localized moments, with even predictive power. All intermetallic compounds under consideration exhibit a structural phase transition under pressure, but with completely different underlying mechanisms. Based on a joint theoretical and experimental study we probed the role of magnetism for the appearance of phase transitions and unravel stepwise the driving forces in the systems. The computational predictions for the behavior of the compounds under extreme conditions are partially challenged by own state of the art experiments using XRD, XAS and XMCD measurements

1. Introduction

upon high pressure at modern synchrotron facilities.

Although several theoretical predictions could be already confirmed, there remain several open problems and new questions. A collection of these questions and promising ongoing projects is given at the end of the summary.

2. Methods

To study the dependence of the electronic and magnetic properties of real compounds on their structural details we combine electronic structure and model calculations with experimental measurements.

Our computational approach is based on density functional theory (DFT) band structure calculations using the full potential local orbital scheme FPLO. Beside the analysis of the electronic structure and the selective modification of single parameters, we perform model calculation on top of these results. The subsequent mapping of the low energy states onto appropriate models provides a deep insight into the underlaying mechanisms and allows to develop comprehensive pictures from microscopic grounds.

Thermodynamic measurements (like magnetic susceptibility and heat capacity), nuclear magnetic resonance (NMR) and electron spin resonance (ESR) experiments allow to connect theoretically developed models with the physical properties of compounds by simulations. The systematic modification of systems by substitution or by the variation of external conditions, performing experiments in high magnetic fields, at low temperatures or under high pressure, probe and refine the existing theoretical description. Especially experiments under high pressure allow a systematic, continuos variation of the crystal structure without the drawbacks of disorder or a local change of the crystal fields. Since high pressure experiments are limited to small sample volumes, such experiments usually need the high brilliance of synchrotron light facilities.

While part of the combined theoretical and experimental studies are done in close collaboration with experimentalists (synthesis, thermodynamic measurements, NMR, ESR), probing physical properties in a concerted way, we performed own experiments at the European Synchrotron Radiation Facility (ESRF) in Grenoble motivated and proposed by our theoretical predictions.

In the following section, the underlaying concepts of DFT and the implementation in modern band structure codes, as basis for our theoretical investigation, are described shortly. Especially the limitations and difficulties to consider real compound effects like disorder, vacancies and correlation are discussed. Furthermore, our mapping approach of the electronic structure onto simple physical models is introduced.

In the second paragraph the high pressure technique and the experimental setup for x-ray diffraction (XRD), x-ray absorption spectroscopy (XAS) and x-ray magnetic circular dichroism (XMCD) under high pressure at the two beam lines ID09 and ID24 at the ESRF are shortly described.

2.1. Electronic structure and magnetic models for real compounds

Although during the last decades technical improvements lead to increased computational speed and parallelization of codes and theoreticians succeeded in the development of new functionals and refined implementation concepts (improved algorithms), it remains challenging for computational solid state physics to describe relevant physical properties of

real compounds from their crystal structure, only. The intrinsic problem is related to the enormous number of degrees of freedom (10^{23}) for a solid.

The many particle problem of interacting atoms in a solid can be described by the Schrödinger equation with a many-particle wave function. This leads to a differential equation which turns out to be rather complex, even for small systems, and usually fails to be solved analytically or numerically. Furthermore the many-particle wave function of the Schrödinger equation contains information not needed for the calculation of macroscopic properties as ground state energy or the magnetic moments. The density functional theory, based on the theorems of Hohenberg, Kohn and Sham, simplifies the problem by using the electron density to transform the many-particle Schrödinger equation of N particles for the ground state into N coupled single-particle equations. This way, the computational effort can be reduced enormoudly and even large systems become treatable with good accuracy. In principle, this theory is exact, but asks for an unknown exchange and correlation functional while calculating real compounds. Thus, approximations are needed ultimately.

2.1.1. Describing a solid

In a simple picture, a solid contains a lattice of interacting atoms. While the inner electrons are strongly bound to the nuclei, their influence on the physical and chemical properties is usually small. Physical properties like the binding situation, conductivity, susceptibility or heat capacity are mainly ruled by the quasi free valence electrons. The short overview about the basic ideas to describe a solid theoretically starts from the simple picture of a lattice of interacting nuclei and electrons.

Theoretically, a solid with N_e electrons and N_n nuclei can be described as a many particle problem of interacting electrons and nuclei by the stationary Schrödinger equation

$$\hat{H}\left|\psi\right\rangle = E\left|\psi\right\rangle$$

where $\langle \vec{r}_1, \vec{r}_2, ...\vec{r}_{N_e}, \vec{R}_1, \vec{R}_2, ...\vec{R}_{N_n}|\psi\rangle = \psi(\vec{r}_1, \vec{r}_2, ..., \vec{r_{N_e}}, \vec{R}_1, \vec{R}_2, ..., \vec{R_{N_n}})$ is the many particle wave function and $\hat{H} = \hat{H}_e + \hat{H}_n + \hat{H}_{en}$ the Hamilton operator. For the electronic and nuclear part of the system the kinetic energy and a Coulomb term is considered

$$\hat{H}_e = \sum_{\alpha=1}^{N_e} \frac{\vec{p}_\alpha^2}{2m_e} + \frac{1}{2}\sum_{\alpha\neq\beta}^{N_e} \frac{e^2}{|\vec{r}_\alpha - \vec{r}_\beta|} \tag{2.1}$$

$$\hat{H}_n = \sum_{i=1}^{N_n} \frac{\vec{p}_i^2}{2M_i} + \frac{1}{2}\sum_{i\neq j}^{N_n} \frac{Z_i Z_j}{\left|\vec{R}_i - \vec{R}_j\right|}, \tag{2.2}$$

while the interaction of the two subsystems is described by

$$\hat{H}_{en} = - \sum_{\alpha,i}^{N_e,N_n} \frac{Z_i}{\left|\vec{r}_\alpha - \vec{R}_i\right|}. \tag{2.3}$$

This many-particle Schrödinger equation, constructed from the simple consideration above, is far to complex for an exact solution due to the large number of degrees of freedom.

A first simplification of the problem can be achieved by the large mass difference between protons and electrons. The three orders of magnitude larger mass of protons results in

an about 10^3 to 10^5 larger mass of the nuclei compared to the electrons and allows to separate the motion of the light, fast electrons from the heavy, slow nuclei. The adiabatic or Born-Oppenheimer approximation [11] is based on the idea, that the light electrons follow the nuclei instantaneously and thus, being always in equilibrium with an effective external potential formed by the nuclei of the system. This approximation is valid for low temperatures and limited in the case of strong electron-phonon coupling or high phonon energies, especially for light atoms. Following the adiabatic approximation the kinetic energy of the nuclei can be neglected (due to their large mass) and the second term of $\hat{H}_n$ is reduced to a constant C.

Thus, the Hamiltonian writes now

$$\hat{H} = \hat{T} + \hat{W} + \hat{V}_{ext} \tag{2.4}$$

with the kinetic energy of the electrons $\hat{T}$, an electron-electron interaction term $\hat{W}$ (Coulomb term) and $\hat{V}_{ext}$, an interaction term of the electrons with an external potential caused by the nuclei:

$$\hat{T} = \sum_{\alpha=1}^{N_e} \frac{\vec{p}_\alpha^2}{2m_e}, \qquad \hat{W} = \frac{1}{2} \sum_{\alpha\neq\beta}^{N_e} \frac{e^2}{|\vec{r}_\alpha - \vec{r}_\beta|}$$

and

$$\hat{V}_{ext} = \sum_\alpha v_{ext}(\vec{r}_\alpha) + C = \sum_{\alpha,i}^{N_e,N_n} \frac{Z_j}{\left|\vec{r}_\alpha - \vec{R}_i\right|} + C$$

However, the difficulty to solve the many-particle wave function for this Schrödinger equation still remains.

The two theorems of Hohenberg and Kohn [12] overcome this problems and allow to transform the many-particle Schrödinger equation for the ground state into the Kohn-Sham equation based on single-particle wave functions. The exact mathematical expansion of this theory was developed later by Levy[13] and Lieb[14].

The first theorem proves, that for a ground state with the ground state energy $E_G = \langle\psi_G|\hat{H}|\psi_G\rangle$, the external potential v_{ext} is a unique functional of the ground state density $n_G = \langle\psi_G|\,\psi\psi^*\,|\psi_G\rangle$. Thus, the unique transformation of $v_{ext}(\vec{r})$ into the functional dependance $v_{ext}[n_G(\vec{r})]$, permits to describe the full many-particle ground state $|\psi_G\rangle$ by the ground state density n_G acting on a single particle in a unique way.

The second theorem is the Hohenberg-Kohn variational principle, which states that the ground state energy for a given potential $E_G[v_{ext}]$ is determined by minimizing the functional of the energy under the constraint of a fixed particle number.

$$E_G[v_{ext}] = \min_n \left\{ F_{HK}[n] + \int v_{ext}(\vec{r})n(\vec{r})d\vec{r}; \int n(\vec{r})d\vec{r} = N_e \right\} \tag{2.5}$$

To map the many particle problem of the solid to a density functional based description, the universal Hohenberg-Kohn functional $F_{HK}[n] = \min_n \left\{ \langle\psi_n|\hat{T} + \hat{W}|\psi_n\rangle \right\}$ is decomposed accordingly to

$$F_{HK}[n] = T_0[n] + E_H[n] + E_{xc}[n].$$

While the relation for the external potential is already known $V_{ext}[n] = \int v_{ext}(\vec{r})n(\vec{r})d\vec{r}$, the remaining terms can be formulated by the electron density $n(\vec{r})$ as a sum over the still unknown single-particle wave functions $\phi(\vec{r})$ within the Kohn-Sham representation,

2. Methods

in particular $n(\vec{r}) = \sum_\alpha \phi_\alpha^*(\vec{r}) n_\alpha(\vec{r}) \phi_\alpha(\vec{r})$. Thus, $F_{HK}[n]$ contains the kinetic energy of a non-interacting electron gas $T_0[n]$

$$T_0[n] = \min_\phi \left\{ \sum_\alpha \langle \phi_\alpha^*(\vec{r})| - \frac{\hbar^2}{2m_e} \nabla^2 |\phi_\alpha(\vec{r})\rangle ; \phi_\alpha \to n(\vec{r}) \right\},$$

the Hartree term including self-interaction

$$E_H[n] = \frac{e^2}{2} \int d^3r \int d^3r' \frac{n(\vec{r}) n(\vec{r'})}{|\vec{r} - \vec{r'}|}$$

and an exchange and correlation term

$$E_{xc}[n] = F_{HK}[n] - (T_0[n] + E_H[n])$$

considering all exchange and correlation effects beyond the mean-field description of the Hartree term as well as the correction of the self-interaction included (unfortunately) in $E_H[n]$.

To evaluate the ground state energy, the functional

$$E_G[v_{ext}] = \min_n \left\{ T_0[n] + E_H[n] + E_{xc}[n] + V_{ext}[n]; \int n(\vec{r}) d\vec{r} = N_e \right\} \tag{2.6}$$

is varied by the still unknown single-particle wave functions $\phi(\vec{r})$ under the constraint of the orthonormality $(n(\vec{r}) = \sum_\alpha^{N_e} \phi_\alpha^* \cdot \phi_\alpha$ with $\langle \phi_\alpha | \phi_\beta \rangle = \delta_{\alpha\beta})$ and finally results in the so called Kohn-Sham equation with the Lagrange multipliers ε_α:

$$\left\{ -\frac{\hbar^2}{2m} \nabla^2 + V_{eff}(\vec{r}) \right\} \phi_\alpha(\vec{r}) = \varepsilon_\alpha \phi_\alpha(\vec{r}) \tag{2.7}$$

where

$$V_{eff}(\vec{r}) = v_{ext}(\vec{r}) + v_H + v_{xc} \tag{2.8}$$

The effective potential V_{eff} contains the external potential originating from the nuclei v_{ext}, the Hartree potential from the electron-electron interaction v_H and an exchange and correlation potential $v_{xc} = \delta E_{xc}[n(\vec{r})]/\delta n(\vec{r})$. If the exchange and correlation term is known the description of the solid within the Born-Oppenheimer approximation is exact.

The Lagrange parameter ε_α and $\phi_\alpha(\vec{r})$ are in first place the parameters of a mathematical construction and have no direct physical meaning. However, for weakly correlated systems they can be related/assigned to quasiparticle energies and wave functions. In this cases the band energies close to the Fermi energy can be interpreted as quasi particle excitations allowing a comparison with experimental band structures.

Thus, the theorems of Hohenberg and Kohn allow to transform the many particle wave function description of a solid into the Kohn-Sham equation. Its a crucial achievement as the Kohn-Sham equations are formulating a self-consistent problem, which can be solved in an iterative way. The starting density is usually build up from a superposition of atomic densities.

2.1.2. Basic exchange and correlation functionals

The difficulty to calculate the physical ground state properties of a solid from its crystal structure with relevant accuracy is transferred to the problem of constructing reliable exchange and correlation functionals. Since these functionals are unknown, various different approaches are under development. Moreover, it is often hard to estimate which functional works best for a certain problem or class of compounds.

In the case of weakly correlated systems, where the electron density varies slowly, the locale density approximation (LDA) is one of the commonly used functionals.[15] It is based on the theory of the homogeneous electron gas. To estimate the exchange and correlation functional, needed in the Kohn-Sham equation, the solid is divided into small cells. For each individual cell an averaged homogenous electron density is assumed.

$$E_{xc}[n] = \int \varepsilon_{xc}^{homo}[n] n(\vec{r}) d\vec{r}$$

Based on Monte Carlo simulations the exchange and correlation energies can be determined cell by cell with high accuracy by comparing the total energy of the well known model system, the homogeneous electron gas, with the individual contributions of its kinetic or Coulomb energy.[16, 17] Different parametrization for $\varepsilon_{xc}^{homo}[n]$ have resulted in different LDA functionals, for example by Barth and Hedin[18], Perdew and Zunger[19] or Perdew and Wang[20]. Throuout this work the parametrization of Perdew and Wang is used. The LDA works surprisingly well also for inhomogeneous systems as molecules or simple metals. However, it is well known that LDA overestimates binding energies resulting usually in 1 to 2 % too short atom-atom distances (overbinding). The strait-forward generalization of the LDA method including the spin degree of freedom of the electrons results in the local spin density approximation LSDA without changing the underlaying theoretical concepts.[18]

The generalized gradient approximation (GGA) is of similar popularity as LDA and implemented in most of the present day DFT programs. Here, the exchange and correlation functional is calculated not only considering a locally homogeneous electron density, but also its gradient. Several different GGA functionals exist differing by their construction like Perdew-Burke-Ernzerhof [21]. In contrast to LDA, GGA achieves more realistic inter atomic distances, but often overestimates magnetism.

An other approach to treat the exchange and correlation potential of real compounds are hybrid functionals which combine mean-field like LDA or GGA functionals with contributions of exact exchanges from Hartree-Fock calculations[22]. This approach suits especially for molecules. Usually hybrid functionals are constructed by linear combinations of the individual contributions where their weights are parametrized. These parameters are refined by fitting the theoretical calculated properties to experimental data, like atomization energies, ionization potentials, proton affinities, and total atomic energies. Popular examples are the B3LYP [23, 24] functional, HSE06[25] or B971[26].

Unfortunately, the above described LDA and GGA methods fail when describing strongly correlated systems like transition metal oxides or rare earth systems. For the huge compound family of undoped cuprates with localized $3d$ states, investigated in Section 3, LDA or GGA find a metallic ground state in contradiction to their experimentally observed insulating behavior. Thus, an improved treatment of these states is required, presented in the next paragraph.

2.1.3. Strong correlations

For strongly correlated system with $3d$ or $4f$ states like transition metal oxides, the assumption of a slowly varying electron density does not hold and the LDA or GGA is not sufficient anymore to describe the solid. Therefore the functional is expanded by an additional, orbital depending term satisfying the character of the correlated orbital by including explicitly the Coulomb repulsion between two electrons with opposite spin occupying the same orbital. This is the LSDA+U approximation. The correction leads to an energy difference of the correlated orbital between single or double occupation. The energy split correspond to the value of U. This mean field like treatment of the correlation influences properties like hybridization or localization being known to influence various physical properties. Since adding the Coulomb repulsion in the LSDA+U approach considers the correlation for selected orbitals in a mean field treatment, its contribution already included in the exchange and correlation functional of the LSDA has to be subtracted. This is achieved by a double counting correction. There are two commonly used double counting correction (DCC) schemes: the around mean field (AMF) and the fully localized limit (FLL)[1].[27] These two DCCs differ mainly for half filled shells. The AMF DCC assumes a correct description by LSDA for systems with half filled shells. Thus, the energy shift of the corresponding bands is correlated to the occupation of the specific state and consequently minimal for half filling. In contrast, the FLL DCC is based on a symmetric energy split $(U-J)$ between single and double occupied orbitals and therefore independent of the explicit occupation of the state (or shell). This construction allows to reproduce excitation spectra by quasi particle excitations. In many cases it is ambiguous which DCC yields the appropriate description for a certain compound since a theoretical justification is missing.

As input parameters, the unknown screened Coulomb repulsion U and the intra-atomic exchange integral J have to be estimated. By construction, the parameters determining the orbital correction depend strongly on the basis of the calculation scheme and the specific compound. In principle, these values can be calculated by constrained LSDA calculations [28]. Alternatively, the parameters can be adjusted by the comparison of calculated physical properties to experimental data, e.g., the gap size, magnetic moment, exchange integrals or the electric field gradient.[29, 30] The two parameters U and J are connected by the Slater integrals, determining the functional. For d or f systems the following relations are derived from atomic calculations, which can be applied to many systems relatively independent from the material: $U = F_0$ and $J = (F_2 + F_4)/14$ for d orbitals and $J = (286F_2 + 195F_4 + 250F_6)/6435$ for f orbitals.[31] The parameter J is mostly a atomic property and in first place determined by the kind of atom rather than the composition of the system, whereas the atomic U is screened in the solid according its atomic surrounding. This asks for a careful evaluation of U.

The dynamic character of the correlation is treated imperfectly in LSDA+U. This becomes crucial for systems, where the correlated states are placed close to the Fermi energy being sensitive to fluctuations. Such systems ask for an improved treatment like provided by the dynamic mean field theory (DMFT). [32, 33]

---

[1]The FLL is also called atomic limit (AL)

2.1.4. Band structure codes

To solve the self consistent problem of the Kohn-Sham equations for real materials a variety of DFT codes exists.The main challenge of these DFT programs is to find the optimal balance between accuracy and efficiency. High accuracy for a large number of atoms and a dens k-mesh should match with a short processing time and small file size (requested memory space).

The different schemes depend on the specific description of the potential, the chosen basis and the treatment of electrons and can be distinguished regarding their strategies to reduce the computational effort.

One possibility to reduce significantly the computational effort is the approximation of the potential realized in Muffin-Tin (MT) programs. In MT codes, the potential is divided into non-overlapping spheres and an interstitial region where the potential is simplified by a constant. There exist also Atomic Sphere Approximation (ASA) based programs, where the spheres are allowed to overlap, which treat the interstitial region approximately only (e.g. TB-LMTO-ASA, Stuttgart).

Alternatively, computational effort can be reduced by using pseudo potentials, which reduce the number of (valence) electrons treated explicitly. Therefore, the strongly bonded core electrons and nuclei are combined to an effective ionic potential. This effective potential, which differs from the real potential of the compound, is called pseudo potential. However, within the effective ionic potential the reduced number of valence electrons is treated (e.g. SIESTA, VASP, ABINIT). This assumption provides powerful schemes which allow to calculate systems with a large number of atoms or to relax many sites at the same time (e.g. important for the calculation of phonon spectra). In exchange, pseudo potentials have problems in the appropriate description of heavy elements and high pressure, since the semi-core or core electrons are not considered explicitly. Especially for strongly anisotropic compounds it can become crucial to check the faster MT or pseudo potential calculations against the results of full potential codes, since the adjustment of parameters like the size of spheres in ASA programs can affect the quality of the calculations. An example of the insufficient description of the potential, led to inaccurate results for $Sr_2Cu(PO_4)_2$ recently.[2, 3] On the other hand, the discrepancy of optimized H sites based on different approaches could originate from inadequate pseudo potentials (compare Section 3.1.3).

Examples for full potential, all electron codes are the programs WIEN2K[34], FPLO[35] or FP-LMTO[36]. These schemes differ in the treatment of their basis. While the FP-LMTO is based on linearized muffin-tin orbitals and FPLO uses a local orbital basis, the basis of WIEN2K is constructed by the combination of (linearized augmented) plane waves with local orbitals. A local basis has the advantage of a reduced basis set and an easier chemical interpretation compared to plane waves. On the other hand, plane waves can be converged in a controlled way. Since the computational time of a DFT program is usually determined by the time to diagonalize the matrix of the basis, the choice of the basis set directly influences the computational effort, since the computational time scales with N^3 for a matrix of the order of N. On the other hand a larger basis set improves the accuracy of the description.

The FPLO scheme

In this work the electronic structure calculations were performed applying the full potential local orbital program FPLO, using a basis of adjusted, overlapping, non orthogonal atom

centered orbitals.[35, 37, 38] Up to version FPLO5 a minimum basis set of overlapping orbitals keeps the matrix sizes small, allowing to calculate large cells with good accuracy in reasonable time scales. The self-adjusting minimum basis can be completed by a few semi-core and polarization states. In addition, the separation of all electrons into orthogonal core states and overlapping valence electrons allows to reduce the eigenvalue problem of the Kohn-Sham equation into an effective valence eigenvalue problem reducing the effective matrix size further, and thus reducing considerably the computational effort.

In order to solve the Kohn-Sham equation (compare Eq. 2.7) the single particle wave functions ϕ_α are expanded in a specific basis $\phi_\alpha = \sum_n c_n^i \phi_n^B$. Thus, the problem to solve the Kohn-Sham equation $H_{KS}\phi_\alpha - \varepsilon_i\phi_\alpha = 0$ turns (technically) into the problem to diagonalize

$$\sum_n (\langle \phi_m^B | H_{KS} | \phi_n^B \rangle - \varepsilon_i \langle \phi_m^B | \phi_n^B \rangle) c_n^i = 0$$

in order to determine the unknown coefficients c_n^i of the basis.

In the FPLO scheme ϕ_α are expressed as Bloch states in accordance with the periodicity of the lattice, which are expanded in terms of localized atomic like orbitals.

$$\phi_\alpha(\vec{r}) = \sum_n^N c_n^i \phi_n(\vec{r} - \vec{R} - \vec{s}) e^{i\vec{k}(\vec{R}+\vec{s})}$$

Where $\phi_n(\vec{r} - \vec{R} - \vec{s})$ consist of radial functions and spherical harmonics.

These orbitals are not orthogonal. Due to their atomic like character which is more efficient to describe an atom based system compared to a set of plane waves, a small number of these states is sufficient to describe the solid in good accuracy. The basis states are divided into core and valence states. While the core states are strongly localized and orthogonal (no overlap between the core states of neighboring sites), the orbitals of the valence states are non-orthogonal and overlap with the valence- and core states of neighboring sites. A confining potential $v^{conf} = (r/r_0)^N$ compresses the valence states, depending on the nearest neighbor distance r_{NN} by $r_0 = (x_0 r_{NN}/2)^{3/2}$ while x_0 is optimized with respect to the total energy during every iteration step.[2] The compression of the valence states not only reduces the overlap of the valence states, but also influences the curvature of this wave functions adjusting the orbital energies to the typical band energies. The separation of the basis into orthogonal core and overlapping valence states resolves the (overlap) matrix of the basis into a representation containing a core-core block, a valence-valence block and two core-valence blocks. Since the core states are orthogonal, the core-core block of the matrix is already diagonalized. The remaining parts of the matrix can be diagonalized independently. By an algebraic transformation, including the orthogonalization of valence states and the introduction of an overlap matrix, this eigenvalue problem can be reduced into an effective eigenvalue problem containing only the valence states. Since the computational time for the diagonalization of a matrix scales with N^3, where N is its size, the described decomposition reduces the calculational effort.

The starting basis and density of the electronic structure calculation are constructed by the superposition of atomic wave functions and densities obtained from atomic Kohn-Sham equations. This way the density contains local (netto) and overlap parts. The deconvolution of the two-center overlap parts by shape functions allows to describe the density

---

[2]So FPLO5 has a self-adjusting, not fixed basis set.

by local, atom-centered overlapping non-spherical contributions (expanded by spherical harmonics).

$$n(\vec{r}) = \sum_{\vec{R}\vec{r},lm} n_{\vec{s},lm}(|\vec{r} - \vec{R} - \vec{s}|)Y_{lm}(\vec{r} - \vec{R} - \vec{s})$$

Since the Hartree part of the potential v_H is calculated from the electron density (compare Eq. 2.8), it is also formed by local, overlapping contributions. Following the Kohn-Sham equation the coefficients c_n^i of the basis are evaluated. After the optimization of the basis the new density and the respective potential is constructed. As convergency criteria the differences in the densities between two iteration steps is considered.

$$n^{\text{start}}(\vec{r}) \longrightarrow V_{eff}[n(\vec{r})] \Rightarrow^{\text{Eq. 2.7}} c_n^i, \phi_\alpha(\vec{r}) \longrightarrow n^{\text{new}}(\vec{r})$$

FPLO allows to calculate total energies within the chemical accuracy of 1 to 50 mHa per atom, while relative energies are reliable even on a μHa scale. The scheme has the same accuracy as the well established WIEN2K program, but exhibits a considerable shorter computational time for large systems. Energy differences, density of states and band structures are usually in excellent agreement.

Since the FPLO scheme was further developed and expanded during the period of this work and the different versions show complementary advantages (mainly between FPLO5 and FPLO6), the main differences of this versions are discussed shortly. The main change between the versions FPLO5 and FPLO6 is the construction of the basis set. While in FPLO5 a minimum self-adjusting basis is used, which is optimized during every iteration step, from FPLO6 onwards the basis is fixed, since it is already completed by polarization states and a second set of valence orbitals (double numerical basis). The reduction of computational time from the fixed basis overcomes the expansion of the basis compared to the default basis in FPLO5. Thus FPLO6 combines a better accuracy together with a shorter computational time without the users engagement. This comes with several changes:
The fixed basis in FPLO6 prevents the user from the effort to adjust the basis for a special problem, but on the other side it impedes the individual modification of the basis, which can not be changed anymore in an easy way.
Besides the differences in the basis also the construction of the potential changed from FPLO5 to FPLO6. While in FPLO5 the potential was decomposed into site-centered contributions, in FPLO6 the potential is calculated on a fixed real space grid (3D Becke) [3]. This improves the description of open structures (like layered compounds or compounds with short O-H bonds) without the workaround of empty spheres. However, therefore the implementation of the CPA approach is impeded since the scattering processes are determined by the total potential per site. Thus the CPA is missing in the scheme from version FPLO6.
Further versions (up to FPLO9) up to now have no conceptional changes, but were improved by additional features like the implementation of a GGA functional (e.g. used in Sec. 3.1.2), Wannier functions (e.g. used in Sec. 3), forces to relax crystal structures (e.g. used in Sec. 3.1.3) or a molecule module (e.g. compare Sec. 3.2). In addition, in some cases the band structure calculations were performed by publicly unreleased versions allowing to

---

[3]Only the Hartree potential is stored site-centered, while the Ewald and exchange- and correlation potential are parametrized on a 3D grit causing a point-wise construction of the total potential on the grit of the real space.

evaluate bonding and anti-bonding states by inter-site band characters (see Sec. 4.1.2) or to evaluate the full relativistic orbital resolved density of states (see Sec. 4.1.1). These features will be most likely available in future versions.

2.1.5. Disorder and vacancies

Real materials often differ from their ideal crystal structure and a stoichiometric occupation of all sites, resulting in effects like vacancies, substitutional disorder, impurities or split positions. Often these deviation from ideal compounds determine and influence significantly the physical properties like e.g. charge doping in the new Fe-pnictides influences the onset of the superconducting phase [39] or small Al deficiency suppresses the electron-phonon coupling and in consequence the onset of superconductivity in AlB_2.[40]

The proper description of such effects is therefore of special importance. There exist different approaches to model such substitutional disorder with sizable difference in their computational effort and accuracy.

(i) A rough and simple approximation is the rigid band method which considers just the changed number of electron in the system caused by a substitutional occupation or vacancies by a simple shift of the Fermi energy. Therefore, the compound is calculated with fully occupied sites, while the Fermi energy in the DOS is shifted by hand accordingly. Any influence of the changed electron number onto the potential or wave function is neglected. Nevertheless, this simplified picture allows to estimate trends or principle tendencies in many cases.

(ii) In contrast to the rigid band method, the virtual crystal approximation (VCA) considers not only the shifted Fermi energy but also changes in the potential caused by the variation of the number of electrons in the system. In this approximation substitution is modeled by virtual atoms. Therefore, each site of the atom under consideration is replaced by a modified atom with an adjusted number of electrons regarding the averaged electron number at the special site which is often a non-integer number. To ensure charge balance the number of protons is modified as well. As a consequence, the atomic energy is influenced, impeding a direct comparison of total energies with regular, ordered configurations of the same compound. The improved approach of the VCA describes the disorder by an averaged changed potential, which works especially well, if the partial occupation and the modified number of electrons is related to a subsystem of the compound that provides charge to the physically active part of the system. In turn, if the partial occupation essentially influences the electron reservoir of the compound, physical properties are well described by VCA calculations and can be used for comparison.

(iii) The coherent potential approximation (CPA) is a further improvement of describing substitutional disorder, but on the other hand the computational effort is strongly increased with respect to an unstable convergency behavior (many local minima) and an increase of required computational resources. While the VCA is based on a modified, averaged crystal potential created from virtual atoms, in CPA the compound is described by the averaged ensemble of all possible occupation configurations. Technically in the CPA the wave functions are replaced by Greens functions which allow to consider a scattering of the electrons at the inhomogeneity of the lattice. Due to a changed representation of the basis and a related change of the representation of the potential in the new FPLO version which influences the decomposition into single-site quantities used for technical reasons in the numerical treatment, the CPA is not implemented in FPLO versions newer than FPLO6.

(iv) Local effects originating from substitution or vacancies and short-range effects can be best simulated by the super cell (SC) method. Thus the large number of configuration concerning the disorder is modeled by the construction of selected SCs with long range order. As no further approximations are done, the results of different configurations can be compared easily. Effects like local distortion can be simulated by substitution or creating a single vacancy and the subsequent relaxation of the surrounding atoms. Although this method is technical easy, it is strongly restricted by the size of SCs and the related computational time. Especially the modeling of small changes in the electron concentration or small site substitutions ask for unmanageable large cells or a strongly reduced symmetry. Whereas a partial occupation of a site by 50% can easily be modeled by a doubling of the unit cell, 25% needs already a four times enlarged unit cell.

The combination of these approaches allow in many cases to develop an appropriate picture including local and global effects.

2.1.6. Models on top of DFT

The complete and accurate description of a compound on computational grounds requires a reliable basic theory, but at the same time an intuitive picture of real compounds, is often impeded by the complexity of such a description.

The reduction of the complete information to few main parameters determining a specific macroscopic property of a compound can largely support the understanding of the relevant physical mechanisms. A common approach is the mapping of the relevant states (subspace) of the electronic structure onto simple models.

For low temperatures and small excitation energies it is often possible to simplify the description by considering only the interaction between a restricted number of orbitals that are most relevant for a physical property. These orbitals can be identified by LDA calculations and further mapped by a model description. This way, few parameters are often sufficient to understand the general behavior of a system.

For the investigation of the magnetic properties of low dimensional magnets (see Sec. 3), we use a combination of two independent model approaches, which allows to unravel the underlying interactions responsible for a certain magnetic ground state and to evaluate quantitatively these parameters. Therefore, we combine (i) an effective tight-binding (TB) model with (ii) super cell (SC) calculations using LSDA+U.

Although LDA results in a metallic ground state for all investigated $3d$ transition metal compounds, in contradiction to their insulating behavior[4], it delivers important details of the electronic structure and provides the relevant bands for the development of a microscopically based picture of the magnetic ground state. The metallic solution for undoped cuprates is a well known shortcoming of LDA as it underestimates the strong correlation of the Cu $3d$ states. The related strong Coulomb repulsion on the Cu site can be considered explicitly by a model approach as e.g. a single band Hubbard model using the TB parametrization derived from the LDA. This leads to an insulating ground state in agreement with the experiment. The described method was successfully used by many groups in the last years [41, 42, 43].

The TB model approach on top of DFT calculations allows to develop the magnetic ground state of a system based on a microscopic basis. Within the TB model, which is developed

---

[4]The insulating character can usually already concluded from the color of the crystals.

for strongly bounded electrons (or holes) with limited interaction to the surrounding atoms (sites) of the solid, the electronic band structure is determined by the hopping of electrons between a restricted number of sites, only. Thus, the hopping regime of a system determines its magnetic ground state. For real materials, the leading interactions in the system, their range and hierarchy can be evaluated by mapping the relevant states of the full potential electronic structure onto a TB model. In turn, already the mere evaluation of the band width and dispersion of these bands, relevant for the magnetic exchange, along different directions of the Brillouin zone, enables a first estimation of the dimensionality or/and coupling strength of the main interactions.

By the subsequent mapping of this model via a Hubbard onto a Heisenberg model, the magnetic exchange integrals can be calculated. In an one-band TB model, with one "active" orbital per site, this so-called super exchange has AFM nature due to the Pauli principle. Within our study, we use an effective one-band TB model, where the localized electrons carrying the spin hop between effective CuO plaquette orbitals, formed by the anti bonding CuO $dp\sigma$ states. Thus, our approach supplies only AFM parts of exchange interactions, which is sufficient if FM contributions to the exchange can be neglected. For long range interactions this often an appropriate approximation. However, within the family of edge-shared compounds, FM contribution to the NN interaction are crucial and determine in many cases the magnetism of the system.[5] Therefore, we combine the TB model approach providing the interaction regime with SC calculations evaluating both, FM and AFM contributions to the exchange.

The TB model is described by the following Hamiltonian

$$H^{TB} = \sum_i \varepsilon_i - \sum_{<ij>,\sigma} t_{ij}(c^+_{i,\sigma}c_{j,\sigma} + c_{i,\sigma}c^+_{j,\sigma})$$

which contains the on-site energy ε_i of the orbital i and the hopping of an electron between site i and j represented by the transfer integral t_{ij} (corresponding to a hopping between the different plaquettes) and described by the fermion creation and annihilation operators. The transfer processes are summarized over all bonds $<ij>$.

A mapping of the relevant LDA bands onto an effective one-band TB model, yields a microscopic picture of interactions in the system and allows to estimate the cutoff for negligible long-range exchanges in further SC calculations.

Technically, two different approaches for the evaluation of fitting parameters were applied: (i) a fitting along selected paths in the Brillouin zone between high symmetry points by a least square fitting routine (The results were checked carefully by the variation of different parameter sets and different paths in the k-space to ensure convergency); and (ii) a fitting based on Wannier functions (WF) implemented in the FPLO scheme (versions newer than FPLO8)[44]. Especially in cases of a sizable hybridization or mixing into lower lying bands, the Wannier function based fitting routine gain advantage considering the whole Brillouin zone and allows to expand the model easily by additional orbital contributions.

Based on the obtained hopping terms t_{ij}, the AFM parts of exchange integrals can be evaluated by a stepwise mapping approach. Taking into account the strong correlation explicitly, the TB model is mapped onto a Hubbard model [45] with the Coulomb repulsion

---

[5]This is due to the close to 90° bond angles along the chains in accordance with the GKA rules. Compare Sec. 3.

U of two electrons with opposite spin placed at the same site i and $\hat{n}_{i\sigma} = c_{i,\sigma}c_{i,\sigma}^+$,

$$H^{Hubb} = \sum_i \varepsilon_i - \sum_{<ij>,\sigma} t_{ij}(c_{i,\sigma}^+ c_{j,\sigma} + c_{i,\sigma}c_{j,\sigma}^+) + \sum_i U_{eff}\hat{n}_{i\uparrow}\hat{n}_{i\downarrow}$$

For half filling and strong correlation $U_{eff} \gg t_{ij}$ (fulfilled for many cuprates with typical $U_{eff} \sim 3.5 - 4.5$ eV and $t_{ij} \sim 100$ meV) the Hubbard model can be subsequently mapped onto the Heisenberg model[46]

$$H^{Heis} = \sum_{<ij>} J_{ij}\vec{S}_i\vec{S}_j$$

with the exchange integrals J_{ij}. This yields the AFM parts of exchange integrals in a mean field approximation by the relation

$$J_{ij}^{AFM} = \frac{4t_{ij}^2}{U_{eff}}.$$

As described above, this approach disregards FM contributions, expected for the systems under consideration. Thus, for a complete picture we have to combine our results with an additional method, such as the the expansion of the model to a multi band model (extended Hubbard model) or alternatively by a SC approach.

To evaluate the total exchange parameters for a compound on a quantitative level, a series of SC calculations with different collinear spin arrangements are performed within the LSDA+U approximation. The LSDA+U not only considers the strong correlation of Cu $3d$ orbitals in a mean field way, but the derived exchange integrals naturally contain both, FM and AFM contributions.
Combining SCs, with different spin patterns, and a subsequent mapping of their total energy differences onto corresponding states of Heisenberg models yields the individual exchange parameters (within a Ising model).

$$H^{Heis} = \sum_{<ij>} J_{ij}\vec{S}_i\vec{S}_j$$

with the convention of $J_{ij} \leq 0$ for a FM coupling and $J_{ij} \geq 0$ for AFM couplings.
Thus, the total energy difference between two SC with different spin arrangements is determined by the values of their exchange integrals.
Since the typical energy differences (0.1 to 10 meV) are very small compared to the total energy of such SC, which are of the order of 10^5 Hartree, high numerical accuracy is of special importance. Thus, we compare only total energies calculated in the same crystal structure (within the same space group) and within the same numerical parameter setting, e.g., with the same k-points, at the same time taking advantage of the compensation of further, unknown errors.
To generate different spin patterns, SC are constructed by increasing the unit cell e.g. by a doubling of one of the axes or by a reduction of the symmetry to create artificially inequivalent sites which can be occupied with magnetic atoms having different spin directions. The SC suffer often from an unstable convergency behavior due to the problem of charge shuffling between almost identical (with respect to their charge density) but crystallographical formally different atoms. Nevertheless, convergency can be forced in many

cases by breaking the symmetry locally, e.g. by a small displacement of single atoms or small additional charges. The stepwise removal of the perturbation can stabilize the convergency of the calculation, since it benefits from the converged density of the previous step. Unfortunately, such strategies can be highly time consuming.

However, the SC method provides quantitative values for the exchange integrals including both, FM and AFM contributions, but on the other side impedes a microscopic insight as all individual contributions are summarized (FM and AFM contributions as well as contributions from super-exchange and direct exchange). The development of a TB model not only supplies the underlaying picture of the individual hopping terms, but rather justifies the assumption of a certain cutoff to consider a restricted number of exchange integrals for the SC calculations and thus a restricted size of SC. Comparing the long range exchanges derived from TB model and SC calculations is a measure for the accuracy of the approach, since FM contributions are expected to be small for far distances.

Thus, the combination of the TB and SC approach results in a detailed picture of the microscopic mechanism of the system together with accurate values of the leading exchanges. In turn, a direct comparison of TB and SC results further allows to separate the total exchange integrals in contributions mainly originating from FM and AFM coupling processes.

Note: The significant difference between the parameter U_{eff} from the Hubbard model based on the effective one-band TB model and U_{3d} from the LSDA+U approximation using SCs is often disregarded. Since these parameter act on different orbitals their differentiation is fundamental and is pointed out here for clarification: While U_{3d} refers to the local "atomic" $3d$ orbitals of the Cu atom, it depends on the underlying basis of the DFT scheme. Thus, the values for U_{3d} in the FPLO scheme differ from the corresponding values using the WIEN2K program (shift of about 1-1.5 eV, [30]) or even within the different versions of FPLO (shift by about 1 eV between versions up to FPLO5 or newer than FPLO6). Physical relevant values are in the range of $U_{3d} = 5 - 8$ eV. In contrast, U_{eff} is related to an effective orbital, here the Cu-O plaquette orbital centered at the Cu site. Since in general the effective orbital is more expanded than the local Cu $3d$ orbital, correlation effects are screened, resulting in smaller U_{eff} values. The correlation in the effective orbitals is mainly linked to the hybridization of the central atom with the surrounding ligands influenced by the linking geometry or the kind of ligands. Typical values for U_{eff} are $U_{eff} \cong 3.5$ eV for corner-shared plaquettes, $U_{eff} \cong 4$ eV for edge-shared plaquettes or $U_{eff} \cong 4.5$ eV for isolated plaquettes.[47, 48]

2.2. X-ray diffraction and x-ray absorption at extreme conditions

Experiments at high pressures allow a systematic variation of the crystal structure without the drawbacks of disorder or local changes of the crystal fields. Therefore, it is an ideal tool to modify the electronic structure of a compound in a controlled way, since additional effects originating from the complex chemical interplay are avoided.

Combining x-ray diffraction (XRD) and x-ray spectroscopy experiments (like XAS or XMCD) probes both, the crystal and the electronic structure of a system, providing a deep insight into the subtle balance between structural and electronic degrees of freedom. In combination with high pressure this approach allows to follow various phenomena and reveals often fascinating physics, e.g., the magneto elastic transition in YCo_5 (see Ref. [49] and Sec. 4.1.1) or the origin of the valence instability correlated to a structural collapse in $EuPd_3B_x$ (compare Sec. 4.2.1). However, to detect such delicate effects, the experimental conditions in "standard labs" are often not sufficient. The unique combination of high brilliance, low divergence, a high level of polarization and a (quasi) freely tunable wave length of the beam of modern synchrotron facilities makes such experiments possible.

Especially, experiments at high pressure using diamonds anvil cells require high energy x-rays and low divergence for a good resolution in reasonable time scales [50, 51]. Synchrotron facilities of the third generation guarantee the required flux, stability and technical set-up for small beam spots as precondition for such experiments with a reliable resolution.[6] However, the detection of small effects or at delicate experimental conditions are still a severe challenge for present day experiments and probe cutting edge techniques.

The synchrotron radiation observed as undesired energy loss in the experimental set up of large acceleration rings for particle physics and first used in a "parasitic mode" is generated for scientific and technical purposes in synchrotron light sources since the end of 1960s by the acceleration of electrons through magnetic fields in electron storage rings and ranges over the entire electromagnetic spectrum. Therefore, electrons are accelerated to high (relativistic) speeds in several stages to achieve a final energy that is typically in the GeV range The maximal energy that can be achieved is limited by the radius of the storage ring and the magnetic field, e.g., the European Synchrotron Radiation Facility reaches an energy of $6\,\mathrm{GeV}$. Bunches of this accelerated electrons are injected into a storage ring where they circle for a long time, e.g., typically 12 hours. The electrons are guided in ultra-high vacuum and forced to travel in a closed path by strong magnetic fields. The related acceleration of the electrons leads to the tangential emittance of photons. The magnets in the ring do not only supply the strong magnetic fields perpendicular to the beam which are needed to convert the high electron energy into radiation, but are also needed to re-compress the beam to compensate for Coulomb forces tending to disperse the electron bunches. In particular, the storage ring contains bending magnets and insertion devices (as undulators or wigglers). The bending magnets (dipole magnets) create a homogeneous magnetic field in which the electron motion will be bended in a plane perpendicular to the field. In contrast, an undulator consists of a periodic structure of dipole magnets, resulting in an alternating, static magnetic field along the length of the undulator. Thus, electrons passing trough the periodic magnetic fields undergo oscillations and radiate photons with energies concentrated in narrow energy bands of the spectrum with a high flux. The

---

[6]The brilliance of 3rd generation Synchrotron beam exceeds other natural and artificial light sources by many orders of magnitude and reaches 10^{18} photons$\cdot$s^{-1}mm^{-2}mrad^{-2}.

relativistic effects of the fast electrons makes synchrotron radiation sources the brightest terrestrial continuos sources of x-ray radiation. The emitted intensity is guided to beam lines, which are arranged tangentially to the storage ring, containing the experimental end-station including optics and the experimental set-up. The optical devices, controlling bandwidth, photon flux, beam dimensions, focus, and collimation of the beam, are normally placed in separated hutches.

Figure 2.1.: The storage ring of the ESRF, Grenoble, hosting more than 40 different beam lines. The electrons, before injected into the storage ring, are accelerated by the combination of a linear accelerator and booster synchrotron.[52]

The x-ray diffraction (XRD), x-ray absorption (XAS) and x-ray magnetic circular dichroism (XMCD) experiments at high pressures and ambient pressure or low temperatures presented in this work were performed at the European Synchrotron Radiation Facility (ESRF) in Grenoble (France). In the following, a short overview concerning the operation and peculiarities of diamond anvil cells (DAC) as well as the two beam lines ID09A and ID24 of the ESRF are given.

2.2.1. Diamond anvil cells

The concept of a diamond anvil cell (DAC) is based on the basic relation $p = F/A$, where p is the pressure, F the applied force and A the area.[53] Therefore high pressure can be achieved by high forces on a sizable area or by a moderate force applied onto a small area. The latter idea is realized in a DAC allowing to compress small sample sizes up to pressures similar to the pressure found in the Earth's core.

A membrane and a screw type of a diamond anvil cell together with a schematic view are depicted in Fig. 2.2. The main part of a DAC is a pair of diamonds which are cut that their culets are perfectly parallel to produce uniform pressure and avoid strain. The diamonds have a size of a few millimeters with culets with a diameter of typical 0.2-0.5 mm. Pressure is generated by tightening screws or by a membrane that presses the diamonds together. This uniaxial force between the diamonds can be transformed into uniform hydrostatic pressure by a transmitting medium. Therefore, a gasket is placed between the diamonds forming a cavity for sample, pressure medium and a reference system to determine the applied pressure during the experiment. The sample can be viewed and measured through the diamonds, which are transparent for visible light and x-rays.
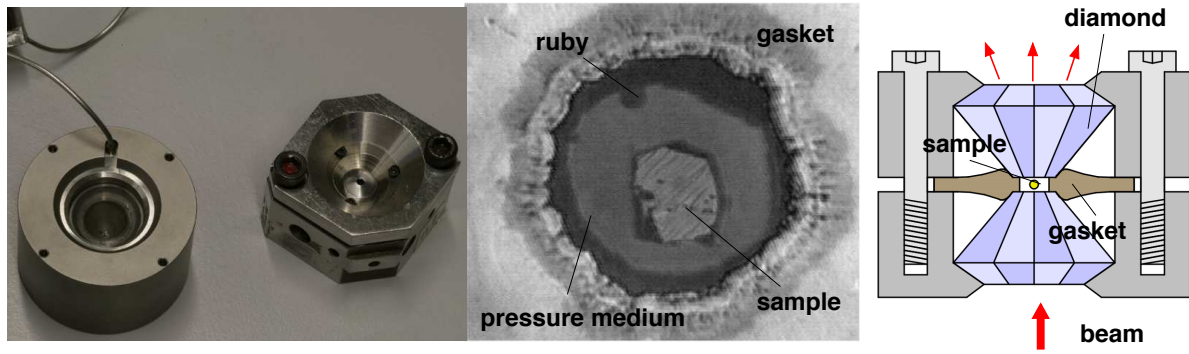
Figure 2.2.: Left: A membrane and a screw type of a DAC, Middle: View through a microscope: gasket hole filled with a single crystal and He as pressure medium at 8 GPa. Right: Schematic sketch of a DAC.

As gasket usually thin metal plates from steel, rhenium, iridium or tungsten with drilled holes of sizes between 100 - 150 μm are used.[7] Depending on the required resolution and the applied pressure range, several pressure transmitting medium are in use. While silicone oil, paraffin or a mixture of methanol/ethanol (4:1) are easy to handle and therefore rather popular, they start to freeze at about 6-10 GPa and loose their hydrostatic properties. Thus, for higher pressure ranges gases as argon, xenon, hydrogen or helium are used. Helium as the best possible available hydrostatic medium, which shows nearly perfect hydrostatic conditions even in its solid phase, allows experiments with good quality up to 30 GPa, but the loading of the DAC becomes demanding.[54] A non standard high pressure loading technic is needed (2 kbar). The applied pressure during the experiments is determined by a reference system. Most popular is the ruby fluorescence method, where the known behavior of the ruby fluorescent line under pressure is monitored.[55] But also metals as copper or platinum can be used as reference systems.

For our x-ray diffraction experiments, we used both, simple screw DACs with ethanol/methanol as pressure transmitting medium and membrane DACs loaded with helium.

For our XAS and XMCD measurements, we used nonmagnetic Cu-Be DACs with paraffin, nitrogen or silicon oil as transmitting medium. In addition special drilled diamonds where used to minimize the strong absorption effects of the diamonds at the Co K-edge (7 709 eV). In this energy (and pressure) range diamonds become opaque and reach an absorption of nearly 99%.

2.2.2. ID09-XRD under pressure

Our high pressure x-ray diffraction (XRD) experiments were performed at ID09A of the ESRF. This beam line is equipped for the determination of structural properties of solids at high pressure using angle-dispersive-diffraction in combination with the diamond anvil cell technique [50]. The beam line provides an ideal experimental environment by a stable and small beam spot together with high intensity. The whole optics for ID09 is placed in a separated hutch. The beam is focused vertically by a spherical mirror and horizontally by a bent Si monochromator. The resulting beam size on the sample is normally about 30x30

---

[7]Thus, the amount of sample needed for the measurements is mostly determined by a reasonable handling.

μm^2, but can be made as small as 10x10 μm^2 with a typical working energy of 30 keV. At ID09A, XRD can be performed for both, single crystal and powder samples. While diffraction results in few reflections in the case of single crystals, the random distribution of a polycrystalline sample leads to diffraction rings around the beam axis. Within this work all experiments were performed on powder samples. Therefore, the DAC is mounted on a goniometer and rotated during the measurements to eliminate effects of texture and to achieve a good randomness. The incoming beam is scattered according to Bragg' s law by the small crystals of the powder and detected in transmission mode. To ensure a good powder average and smooth diffraction rings, the single grains of the powder should be small compared to the beam spot (20-40 μm^2). For a precise alignment and orientation of the sample into the focus of the beam the DAC can be orientated by a computer-controlled goniometer allowing for oscillations in ϕ. The energy calibration was done using Si as a standard.
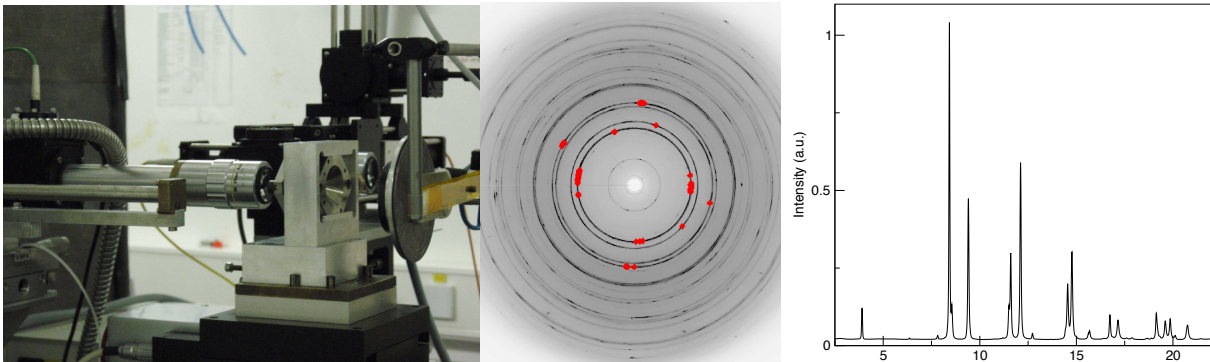
Figure 2.3.: Left: DAC mounted at ID09 with spectrometer for pressure measurement, Middle: Obtained diffraction pattern for $SrFe_{1.8}Ru_{0.2}As_2$ at 0.5 GPa with masked overexposed reflections, Right: Integrated diffraction pattern using the computer program FIT2D. The background is already subtracted.

During our measurements, the DAC was typically rotated in an angle range from 3 to 6°. The data collecting rate during the pressure experiments is determined mainly by the adjusting time of the DAC to allow the stabilization of pressure for 5 to 10 min, while the acquisition time for a single pattern is only between 2 to 10 s.

The scattered radiation is collected by an image-plate detector, an on-line Mar555 reader. The obtained data were treated by the FIT2D program [56]. After masking overexposed reflections (spots) and detector defects the collected patterns were integrated. After a background correction the lattice parameters were refined by the Rietvield method using the FULLPROF program [57]. For selected problems, we consider preferred orientation, asymmetry and sample displacement, explicitly. While the position of peaks in the integrated spectra determine the lattice spacing, the intensities contain information about the atomic sites (element and position), and the peak shapes are influenced by effects like strain, preferred orientation, absorption and displacement of the sample from the focal beam spot. Since the cross section of an element and thus its contribution to the intensity of the signal is proportional to the square of its electron number Z^2, the resolution of light elements in the vicinity to heavy elements in x-ray diffraction is at least challenging. Especially the correct determination of H positions in solids is a severe problem often yielding far too

short H bonding distances due to shift of the electron density towards the bonded atom. Therefore, the combination of XRD with results from neutron scattering supports the determination of the positions of light atoms with few electrons only (especially hydrogen) and leads to reliable structural solutions in many cases, since the uncharged neutrons are scattered by the (atomic) nuclei. On the other hand, neutron diffraction under pressure is limited by the sample size, the achieved pressures and long acquisition times.

The broadening of the diffraction rings (or peaks after integration) in the high pressure region due to non-hydrostatic effects impede the evaluation of the diffraction diagrams, especially in the case of small splittings or reflections with low intensity. However, in general a Le Bail fit using a least-squares fitting routine reaches good accuracy, where the uncertainties in the experimental data are rather determined by the evaluation of pressure than by the errors of the lattice parameters. For a full refinement the relative intensities should be taken with care, since the restricted, small volume of sample in the DAC can have a pronounced impact on the homogeneity of diffraction rings (powder rings derived from DACs are often spotty). At least for ambient pressure a comparison with an improved data set can support the analysis. Thus, we performed reference measurements at the high resolution XRD beam line ID31 at the ESRF, for selected problems.

To evaluate the measured volume-pressure dependance, an inverse Murnaghan-Birch [58, 59] equation of states (EoS) is fitted to the experimental obtained data:

$$V(p) = V_0 \cdot \left(\frac{B_0' \cdot p}{B_0} + 1 \right)^{-1/B_0'}$$

with the equilibrium volume V_0, the bulk modulus of B_0 and the compressibility B_0'.

ID09A is further equipped with a liquid-He cooled cryostat to perform high pressure experiments at low temperatures. The temperature can be stabilized within a few K. Below 100 K the stabilization time for the temperature increases significantly and the operation of DACs is impeded, making experiments more time-consuming and more difficult to handle.

2.2.3. ID24-XAS and XMCD under pressure

The energy-dispersive x-ray spectroscopy beam line ID24 allows for both, x-ray absorption spectroscopy (XAS) and x-ray magnetic circular dichroism (XMCD) experiments under pressure.[60, 61, 62] The required stability for such experiments is achieved by a non-conventional optical scheme which enables static optics conditions where no mechanical movements of the spectrometer are needed during the acquisition of the spectra. A position sensitive detector, where the beam position is correlated to energy, makes the parallel detection of the whole spectrum possible and allows a time resolution of the order of ms. Experiments can be operated in the energy range 5 - 27 KeV.

As precondition for high pressure experiments using the DAC technique, the beam line delivers a small and stable focal beam spot of about 5 x 5 μm^2 in the energy range 5 - 15 KeV and a high flux, especially important for low-energy XAS since the transmission through the diamonds decreases dramatically. For example the transmission trough a pair of 1.2 mm diamonds at the Co-K edge (7 709 eV) falls below 2%. At the Fe K-edge (7 112 eV) and Mn K-edge (6 539 eV) the transition is even suppressed to 0.4% and 0.07%, respectively. Thus, in order to reduce the absorption effects as much as possible, DACs with drilled diamonds are used. It is also possible to guide the beam in vacuum tubes to

further reduce the loss of intensity. In addition, the installation of a local feedback system to control the horizontal instabilities of the beam led to a substantial improvement in the quality of the collected data.[63]

X-ray absorption (XAS) experiments are a widely used technique to gain insight into the local geometry and the electronic structure of a solid (for an general overview see, e.g., Ref. [64, 65]). The spectra are especially sensitive to the formal oxidation state (valence), coordination chemistry (e.g., octahedral, tetrahedral coordination) of the absorbing atom, and the distances, coordination number and species of the neighboring atoms surrounding the selected element. To obtain a XAS spectrum, the absorption of a material is measured as a function of energy. In general, the relation between the incident and transmitted x-ray photons are proportional to an exponential decrease $I(E) = I_0 \cdot e^{-i\mu(E)}$, determined by the absorption coefficient μ. Roughly, increasing the energy results in an increase of the transmitted photons. When the incident x-ray energy matches the binding energy of a core electron within the sample, the number of x-rays absorbed by the sample increases dramatically, causing a drop in the transmitted x-ray intensity. This results in an absorption edge, which is named regarding the core electron which is excited following the principle quantum numbers $n = 1$, 2 and 3 corresponding to the K-, L- and M-edge, respectively. Each element of the periodic table has a set of unique absorption edges corresponding to different binding energies of its electrons. This makes XAS element selective. The fundamental process of XAS is the absorption of an x-ray photon by a core level of an atom in a solid and the consequent emission of a photoelectron. The resulting core hole is filled either via an Auger process or by capturing an electron from another shell followed by emission of a fluorescent photon. In addition, the ejected photoelectrons can interact with the electrons of the surrounding (non excited) atoms, including multiple scattering effects or inelastic scattering. This processes cause a modulation of the measured XAS near the absorption edge and leave a characteristic finger print of the electronic structure. Since a core electron is excited into an empty state, XAS probes the unoccupied part of the electronic structure. The cross sections of the process follow the quantum mechanical selection rules.

The evaluation of the XAS spectra is often done in a comparative way, fitting a spectrum by a linear combination of different (expected) contributions, observed in the spectra of related compounds. This yields often sufficient results. For the ab-initio modeling of XAS spectra several schemes are available. There are two basically different approaches to simulate the XAS signal. The DFT based evaluation of unoccupied states[8] (often considering the screening of the core hole by super cells) or the multiple scattering formalism based on a Greens functions approach.

During the XAS experiments, the absorption coefficients $\mu(E) \sim ln(I/I_0)$ of a sample is determined by measuring the incoming intensity I_0 and the transmitted intensity I of the x-ray beam as a function of energy. To yield the required signal to noise ratio we average a large number of spectra.[9] Typical acquisition times are $120\,$s (including the dead-time while moving the motors from the cell to the I_0 positions) and an averaging of 100 patterns per pressure point. As external standard for the energy calibration Co-foil was used for YCo_5. The collected data of the $EuPd_3B_x$ measurements were calibrated with respect to the

---

[8]e.g. a XANES module is implemented into the DFT scheme WIEN2K.

[9]It is rather sufficient to collect I and I_0 as close in time as possible and average several spectra, than to increase the acquisition time for one spectrum.

ambient pressure data. For our Eu containing compounds measurements were performed at the L-edge (E~6977 eV) (compare Sec. 4.2.1). The collected data were normalized to the edge and analyzed using a least squares fitting routine mapping the spectra to a combination of Lorentzian peaks and arcus sinus functions according to Ref. [66]. The valence state was determined by $\nu = 2 + I(Eu^{3+})/(I(Eu^{2+}) + I(Eu^{3+}))$ where I are the intensities of the Eu^{3+} and Eu^{2+} peaks, respectively.
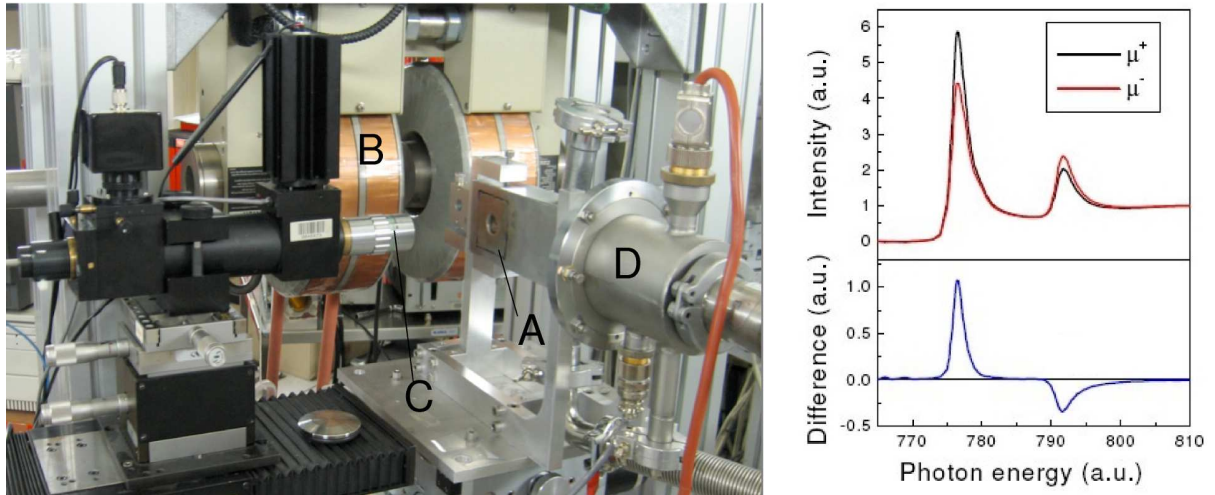
Figure 2.4.: Left: Experimental set-up for the XMCD measurements (A - DAC, B - magnet, C - spectrometer for pressure measurements, D - cryostat) Right: The XMCD signal (blue) is the difference spectrum of two XAS signals within a field measured for opposite helicity of the incoming beam.

X-ray magnetic circular dichroism (XMCD) is a difference spectrum of two x-ray absorption spectra measured with opposite circular polarization within an external magnetic field.[64] The evaluation of the obtained difference spectrum can reveal informations about the magnetic properties of the compound, in particular the spin or orbital magnetic moment. Within a magnetic field the double degenerated states for two spin directions split regarding to the Zeemann effect. Therefore, the absorption cross section differs for left and right circular polarized light, which was shown to be proportional to the difference in the spin-polarized density of states between the two spin channels.

Usually, experiments are performed at the L-edge for 3d metals (in analogy to the XAS experiments), corresponding to an excitation of the 2p electrons into the 3d states. Unfortunately, in the corresponding energy range of the Co L-edge, the transmission through the diamonds of the DAC is dramatically reduced. This changes expectations in a way, that the smaller cross section of the alternative K-edge overcomes the reduction of intensity by absorption effects. Therefore, the experiments were performed alternatively at the K-edge (excitation from 1s to 4p), which allows to observe the transition indirectly by hybridization effects with the magnetically active 3d states.

For XMCD, being a "differential XAS" technique, we measure the difference in absorption between two helicity states of the photons (left and right circular polarized) regarding $\mu^L - \mu^R = ln(I_0^L/I^L) - ln(I_0^R/I^R)$. A magnetic field of 0.7 T parallel to the X-ray beam was applied. Quarter wave plates are used to tune the helicity of the incoming beam. Since it

is equivalent to measure the difference in absorption between two helicity in a fixed magnetic field, or with fixed helicity between two opposite directions of magnetization, not the quarter wave plates are flipped during the experiment, but the direction of the magnetic field. In order to avoid systematic errors and improve the reliability of the detected small effects, we recored the XMCD signal for both polarization directions and compared the obtained signals. For each pressure point we averaged 100 data acquisitions. The XMCD data handling is fairly complex. There exists no standard modules in common DFT programs for the *ab-initio* simulation of an XMCD signal. Beside the difficulties in simulating the underlying XAS spectra like the core hole screening or multiple scattering processes, the XMCD comes with additional effects like spin-orbit coupling, which complicates the picture further. The development of sum rules was an important step for connecting the XMCD signal to physical properties of the measured compounds and often sufficient for an interpretation.[67, 68] However, for the signal of YCo_5 we used a comparative analysis of the experimental observed signal with the calculated DOS. Therefore, three Gaussians were fitted to the experimental data allowing to evaluate the development of the pre-peak region with respect to the rest of the signal. The calculated density of states in the region of unoccupied states assign the pre-peak region of the experimental signal to the Co $4p$ states.

3. Low dimensional magnets

Low dimensional magnets always attract great interest due to their fascinating phase diagrams, including many unusual ground states and giving rise to exciting physics. In this class of materials, magnetic ions with low spin states of 1/2 or 1 couple magnetically essentially along one crystallographic direction resulting in helical ordered ground states with different pitch angles (reaching from acute to obtuse pitch angles or cycloidal helices), spin Peierls states or more conventionally ordered states like ordinary FM or AFM order. At the same time, for these systems phenomena like multiferroicity, spin gap formation, spin liquid states or Bose-Einstein condensation of magnon bound states in magnetic fields give rise to lively discussions and stimulate theoreticians and experimentalists alike.

Only the simplest model of a low dimensional magnet, a 1D chain with only nearest neighbor (NN) exchanges, can be solved analytically and exhibits no long range order down to zero temperature. But already the extension of the model by an ferromagnetic (FM) NN and an anti-ferromagnetic (AFM) next nearest neighbor (NNN) exchange along the 1D chain results in FM ordering for $\alpha = J_2/J_1 \leq -0.25$ and a helical ground state for $\alpha = J_2/J_1 \geq -0.25$ with a quantum critical point in between. The details of the helical state, in particular the pitch angle, are very sensitive to additional, even small inter chain couplings, impeding the prediction of the ground state. In addition, quantum fluctuation can become crucial for the formation of the ground state, especially, if the system exhibits strong frustration.

Such frustrations can have their origin (i) in the pure geometry of the crystal structure or (ii) in competing inequivalent interactions. In Fig. 3.1 (left panel) typical frustrated geometries are illustrated. Examples for geometrical frustration in two dimensional (2D) structures with NN interactions only are triangular or Kagome lattices.[69] Prominent examples for such systems are e.g. kapellasite and haydeeite.[70] This geometries can lead to interesting phenomena like order by disorder [71] or spin liquid behavior.[72]

In contrast to the frustration by geometry, frustration can also originate from competing inequivalent interactions, such as quasi-one dimensional compounds with sizable NN and NNN exchanges. An AFM NNN interaction induces immediately frustration independent from the character of the NN exchange, which is illustrated in Fig. 3.1 (right) and provides a precondition for the formation of exotic ground states.

Realizations of such quasi 1D chain compounds with competing FM-NN and AFM-NNN couplings are Li_2CuO_2,[73] which forms ferromagnetically ordered chains, or $LiCuVO_4$,[74, 75, 76] $LiCu_2O_2$,[9] and $NaCu_2O_2$,[77, 78] all exhibiting helically ordered states but with different pitch angles. Between these phases a quantum critical point (QCP) for $\alpha = -0.25$ attracts great interest due to the subtle balance of the leading exchanges and thus a pronounced sensitivity of the system to small inter chain couplings or external parameters like high pressure or magnetic fields. Recently, the vicinity of the compound Li_2ZrCuO_4 to the classical QCP was studied.[79] Finally, the famous spin-Peierls compound $CuGeO_3$,[80] where both exchange couplings are AFM, exhibits a spin gap behavior.

Also 2D square lattices, which are unfrustrated in the presence of NN exchange only, become frustrated by the appearance of anti-ferromagnetic interactions between NNN (see
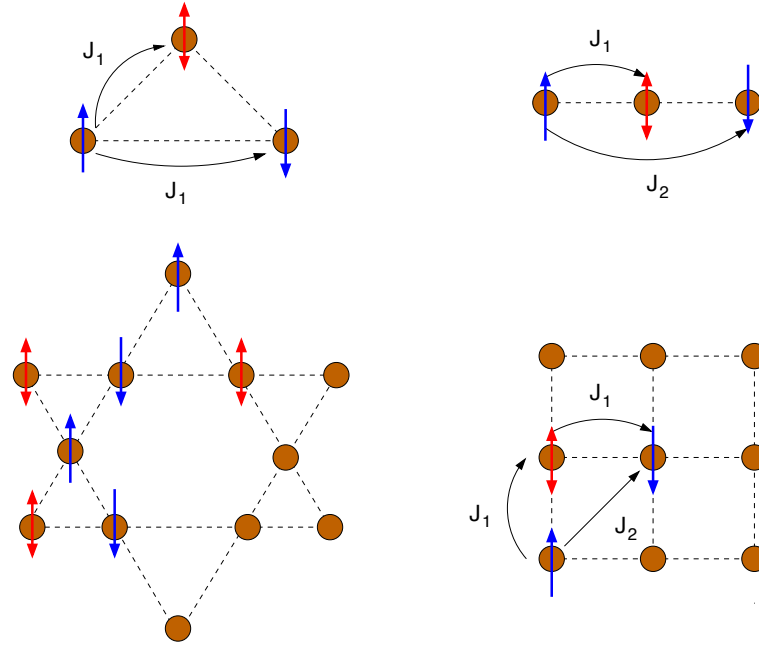
Figure 3.1.: Frustration in one- and two-dimensional systems. Left: Frustration by geometry appears in triangular or kagome lattices. Right: Also inequivalent competing interactions can result in frustration, if the NNN coupling is AFM.

Fig. 3.1). Depending on the size of this NNN interaction, AFM or a so-called columnar (C-AFM) order appears as observed for Li_2VSiO_4.[81] The critical region between this commensurate phases are discussed as possible spin-liquid states. A possible realization of this state is presently under debate for $PbVO_3$.[82, 83]

To study the rich phase diagrams of low dimensional magnets, model compounds containing magnetically active building blocks are needed. Typical examples of such building blocks are $Ti^{3+}O_6$ octahedra, $V^{4+}O_5$ square pyramids or $Cu^{2+}O_4$ plaquettes. In this work the investigations are restricted to the family of cuprates and halides with magnetically active Cu^{2+} ions. These compounds crystallize in a huge variety of crystal structures, in this way providing an ideal precondition for systematic investigations.

Since the $Cu^{2+}O_4$ plaquette with its localized, effective spin 1/2 is the fundamental building block in most of the compounds studied in this work, its main properties and typical coupling mechanisms are shortly illustrated. For the family of Cu^{2+} halides, the O ligands of the CuO_4 plaquette are exchanged by Cl or Br. However, the basic concepts remain the same.

In most cuprates, Cu^{2+} is surrounded by six O atoms. This octahedral coordination is usually distorted, resulting in two long and four short Cu-O bonds with typical distances of 1.9 - 2.0 Å and 2.5 - 2.8 Å, respectively. Within the equatorial plane of the distorted octahedron, Cu and O atoms bind covalently, forming a $[CuO_4]^{-6}$ unit (see Fig. 3.2 right). Within this coordination Cu is in a $3d^9$ and O in a $2p^6$ configuration, thus the highest Cu-O state is half filled. In Fig. 3.2 the energy scheme for the Cu-O bonding states is schematically depicted, which is determined by three main effects: (i) the crystal field or ligand field, (ii) the covalence of the Cu-O bonds and (iii) the strong correlation of the Cu
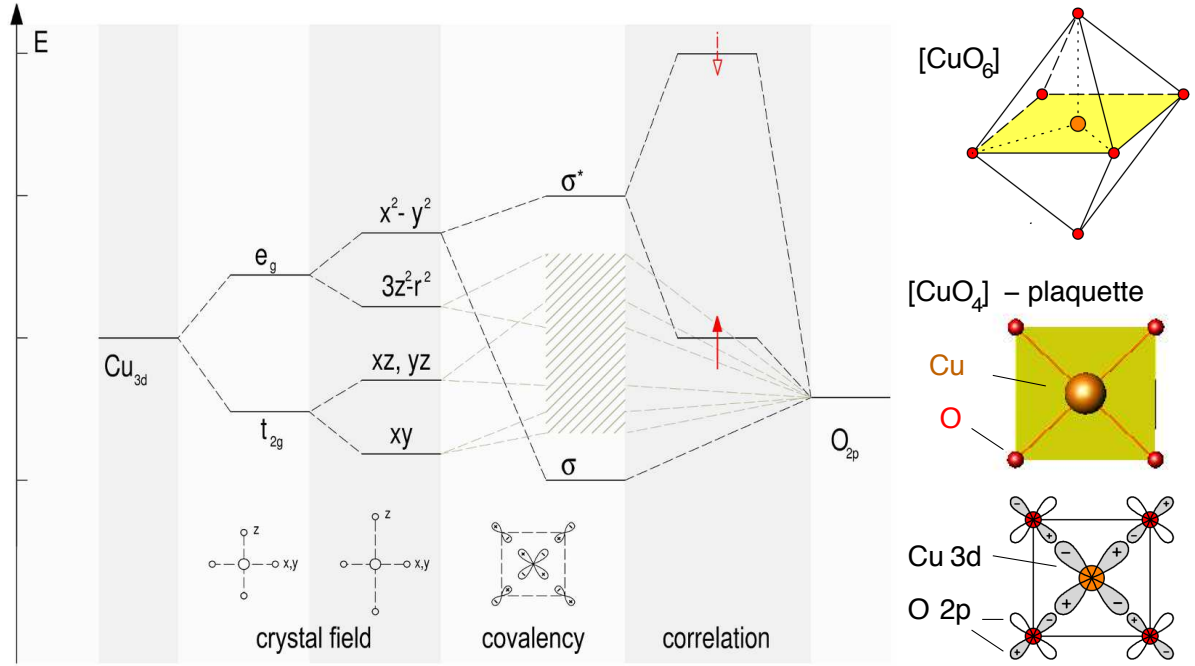
Figure 3.2.: Left: Sketch of the energy scheme of the Cu-O bond state within the CuO_4 plaquette. Crystal field effects, covalence and correlation determine the formation of a localized, effective spin $1/2$ state. The energy split by the covalence is of the same order than the energy gain by correlation. Right: Octahedral coordination of Cu^{2+} and the CuO_4 plaquette as fundamental building block of most cuprates.

$3d$ electrons. Within the octahedral coordination of six O atoms the Cu $3d$ states split into a duplet (e_g) and a triplet (t_{2g}). The ligand field of O atoms lifts the degenerated states further by the distortion of the octahedron, which is known as Jahn-Teller distortion. Thus, the energetically higher e_g states separate into the $x^2 - y^2$ and $3z^2 - r^2$ states. Usually, the $3z^2 - r^2$ orbital is lower in energy compared to the $x^2 - y^2$ state. But in rare cases, the energy balance between the two states can become very similar or even change their order as e.g. observed for Cu^{2+} coordination by CuO_5 bipyramids present in Cu_2SeO_3 or $Cu_2PO_4OH_2$ (compare Sec. 3.1.7). The next significant contribution to the energy scheme is the covalence of the Cu-O bonds, where the Cu $3dx^2 - y^2$ and O $2px, y$ form $dp\sigma$ states. Due to the large overlap of the interacting orbitals in the $dp\sigma$ state compared to the other bond types, the energy split between the bonding and anti bonding combination is rather strong and often exceeds an energy difference of about 7-8 eV. Thus, the $dp\sigma$ states often border the upper and lower edge of the valence band, while all other (anti) bonding states (e.g. $dp\pi$ or non bonding states) are placed in between. Thus, the highest energy level of the CuO_4 plaquette is the anti bonding $dp\sigma$ state and therefore only half filled.[1] Within an LDA calculation the half filled anti bonding $dp\sigma$ band crosses the Fermi energy ε_F. In contrast, due to the strong correlation of Cu $3d$ electrons undoped cuprates are usually

---

[1]The 15 electrons from O 2p and Cu 3d are distributed to 16 possible states (8 different Cu-O bonding states, where each state can be filled by two electrons with opposite spin).

insulators, which can often already be concluded from their color[2]. The strong localization of Cu $3d$ orbitals causes a large energy difference between single and double occupied orbitals, shifting the single occupied state down in energy, while the double occupied state is raised above ε_F. This energy difference due to correlation effects is of the same order than the energy difference caused by the covalence of the dpσ bond (7-8 eV). Thus, considering the strong Coulomb repulsion within the Cu $3d$ orbitals, the half filled dpσ band at ε_F vanishes, since it splits into a single occupied state placed in the middle of the valence band and an double occupied state far above ε_F.

The missing electron at the Cu site for a fully filled shell, results in an effective, localized spin $1/2$ for the CuO$_4$ plaquette. The magnetic interaction between these CuO$_4$ units is strongly determined by their linking.

In real compounds, the structural motive of CuO$_4$ plaquettes appears in many different arrangements starting from rather simple crystal structures with isolated plaquettes present in Bi$_2$CuO$_4$[84], via 1D chain arrangements observed in LiCuVO$_4$ or Sr$_2$CuO$_3$ up to complex 3D networks like in the natural mineral dioptase. This way, cuprates exhibit the structural variety to study the above mentioned phase diagrams systematically. In particular, they allow the investigation of the leading exchanges regarding linking and distortion of the magnetic building blocks or changed crystal fields.
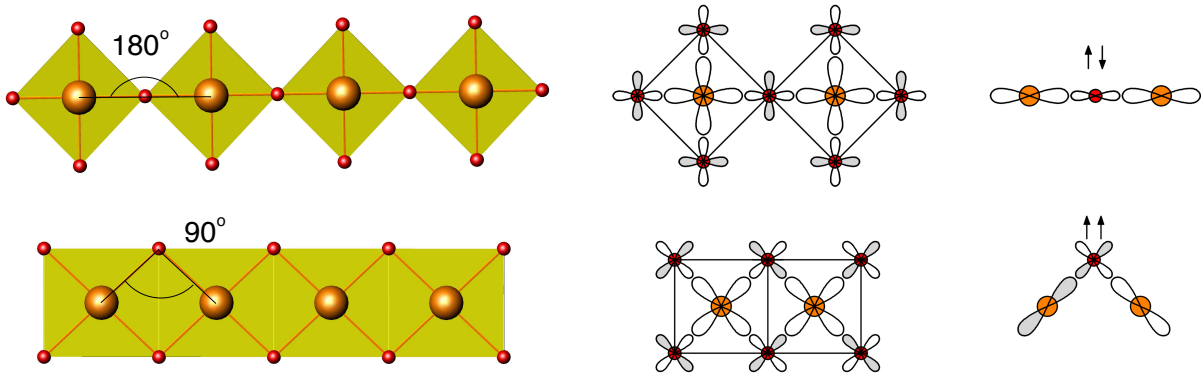
Figure 3.3.: The two archetypes of 1D chains formed by CuO$_4$ plaquettes. The corner shared chain usually results in AFM NN coupling, whereas the edge shared geometry supports FM coupling due to the perpendicular orientation of interacting orbitals.

Especially the linking of neighboring plaquettes in chain-like geometries influences directly the NN interactions as one expects from the Goodenough-Kanamori-Anderson rule.[85] Two archetypes of CuO$_4$ chains can be distinguished by their Cu-O-Cu bonding angle of neighboring plaquettes: corner-shared chains with an ideal Cu-O-Cu angle of 180° and edge-shared chains with 90°. While corner shared chains typically show AFM NN interaction, the edge shared chain type often yields FM NN exchanges. This can be directly understood by means of the orbital orientation in the materials. Since the contribution from direct exchange of neighboring Cu atoms are small in this family of compounds, the magnetic exchange is mainly transferred along the O atoms bridging the Cu sites. For corner shared chains with an Cu-O-Cu bonding angle of 180° the magnetic active Cu $3d$ orbitals of two

---

[2]The crystals are often yellow-brown, green or blue.

neighboring Cu atoms point towards each other and overlap with same O $2p$ orbital. During the exchange the electrons/holes of interacting Cu atoms hop into the same O 2p orbital. In this virtual state the spins have to be aligned anti parallel due to the Pauli principe, resulting in an AFM coupling between two Cu atoms. In the case of 90° bond angles, the interacting orbitals are perpendicular to each other. For ideal square geometry and without a crystal field there is no overlap between the O $2p_x$ and O $2p_y$ orbitals and the AFM parts of the exchange compensate. In the virtual state during the exchange the two interacting spins at O site are aligned parallel according to the Hund' s rule and result in a FM coupling of the two Cu atoms.

Although the crystal structure is often the key for the understanding of the magnetic properties of low dimensional magnets, it can be misleading to develop new magnetic models on solely structural consideration. In the recent years several examples for this problem appeared as discussed in the introduction.

Thus, the development of the proper magnetic model of new or complex systems can largely benefit from a combination of various experimental methods with a detailed microscopic analysis based on modern band structure theory. In the following such a combination of methods was used to develop the low temperature magnetic properties of several cuprates. Here we focus on systems with edge shared chain geometry. The standard planar edge shared chains are varied by different kinds of distortion or missing plaquettes. Most of the compounds can be described by $J_1 - J_2$ models in 1D or 2D or alternating $J_{1a} - J_{1b}$ chain systems.

We start our investigation with the recently synthesized compound $AgCuVO_4$, containing an unusual type of CuO_4 chains and classify the system with respect to the two archetypes of chain compounds (Sec. 3.1.1). In Sec. 3.1.2 we focus on the structural peculiarities of Li_2ZrCuO_4 and their influence on the magnetic exchange integrals trying to unravel the origin for the vicinity of the compound to the QCP between the FM and helical ordered state. Experimental measurement for the natural mineral linarite suggest a similar vicinity to the QCP compared to Li_2ZrCuO_4 (compare Sec. 3.1.3). Our investigation reveal a surprising strong influence of the H position on the magnetic ground state. Furthermore, we yield unexpected results for the two halides $CuCl_2$ and $CuBr_2$, studied in Sec. 3.1.4, which change their magnetic properties dramatically under hydration connected to the flip of magnetic active orbitals. The comparison of the different spin gap compounds $Na_3Cu_2SbO_6$, $Na_2Cu_2TeO_6$ (Sec. 3.1.5), $Cu_2(PO_3)_2CH_2$ (Sec. 3.1.6) and Cu_2PO_4OH (Sec. 3.1.7) and the evaluation of their magnetic ground states demonstrates impressively the difficulty to derive the magnetic ground state from structural grounds only. Finally, the new family of spin 1/2 square lattice compounds A_2CuEO_6, studied in Sec. 3.1.8, seems to be promising to drive the system close to the quantum critical region between the ordered phases by the substitution of different ions.

While in the first part of the paragraph several materials are investigated with respect to their magnetic ground state, we try to derive general trends and relations for the family of edge shared chain compounds in the second part.

Note: Unfortunately, there exists no standard unit for the magnetic coupling strength. In literature, meV and K are used comparably, depending on the community. Thus, for a direct comparison with literature, both units were used in this work, depending on the convention of former studies on a particular compound.

3.1. Materials

3.1.1. AgCuVO$_4$ - a model compound between two archetypes of Cu-O chains

The recently synthesized spin 1/2 compound AgCuVO$_4$ [86] crystallizes in an orthorhombic space group containing an unusual type of Cu-O chains (see Fig. 3.4). From a structural point the trans corner shared geometry[3] of AgCuVO$_4$ with a Cu-O-Cu bonding angle of about 113° can be understood as being placed in between the two archetypes of Cu-O chains, the corner- and edge-shared chain (compare Fig. 3.4, right). Whereas compounds with corner-shared chains typically exhibit AFM interactions between nearest neighbor (NN) spins, the NN interaction in edge-shared compounds can be either FM or AFM due to the vicinity of the Cu-O-Cu bonding angle to 90°. Thus, the estimation of the NN exchange for AgCuVO$_4$ by a modification of the magnetic properties of related compounds is not trivial and a classification of the compound into the systematics of already known materials is of particular interest.
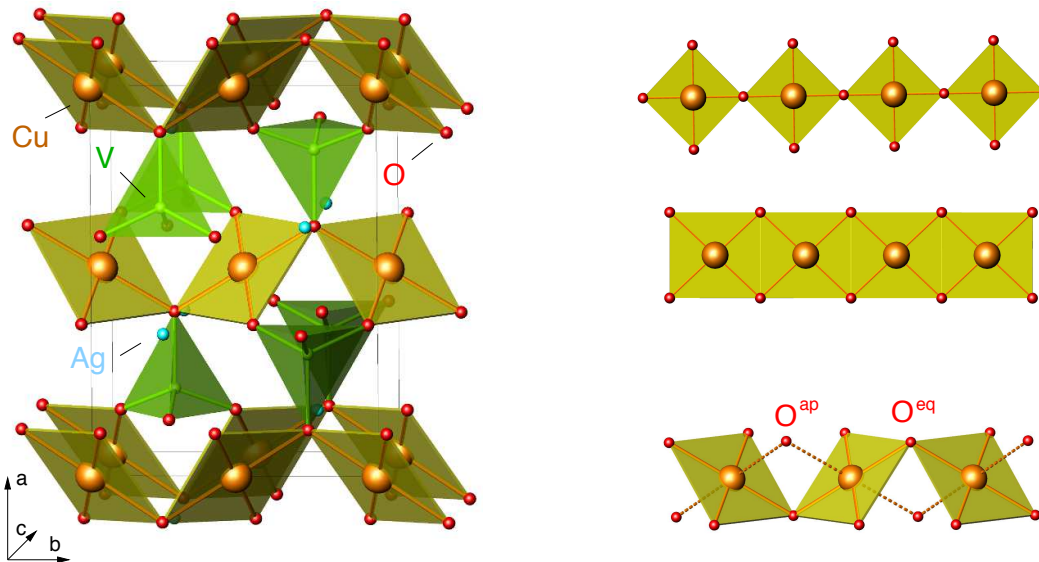
Figure 3.4.: Left: The crystal structure of AgCuVO$_4$ contains chains from trans corner shared [CuO$_4$] plaquettes. Right: Comparison of the two archetype of Cu-O chain geometries, the corner- (top panel) and edge-shared (middle panel) chain, together with the trans corner shared chain (bottom panel) geometry present in AgCuVO$_4$.

The crystal structure of AgCuVO$_4$ was determined by single crystal x-ray diffraction (XRD) at room temperature [86]. The small red crystals contain the above mentioned chains from trans corner-sharing CuO$_4$ plaquettes running along the b axis. These chains are connected by VO$_4$ tetrahedra, which contain non magnetic V^{5+}, as bridging complex ions within the chains as well as between neighboring chains. In addition, isolated Ag$^+$ ions are placed between the chains. The magnetically active Cu^{2+} ions are coordinated by six O atoms in a distorted octahedron shape, typical for many cuprates. The four short bonded O atoms

---

[3]The trans corner shared geometry corresponds to a linking of CuO$_4$ units by the O atoms along the diagonal of the plaquette.

forming a square-planar equatorial plane exhibit an averaged Cu-O^{eq} distance of 1.995 Å, while the distance to the two apical O atoms (O^{ap}) is about 2.511 Å. These rather typical distances and the standard coordination suggests that the magnetic active $3d_{x^2-y^2}$ orbital is placed in the equatorial plane of the CuO$_6$ octahedra. This way, a dominant exchange along the Cu-O-Cu angle of 113° is expected, while an exchange along the apical O^{ap} with a Cu-O-Cu bonding angle of 85° should be suppressed by the fully occupied $3d_{3z^2-r^2}$ orbital.
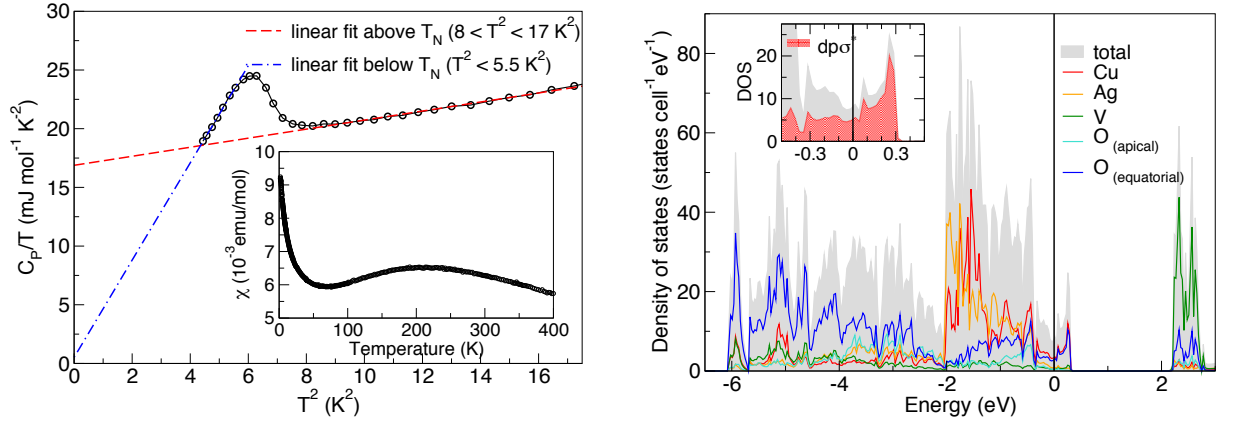
Figure 3.5.: Left: The experimental magnetic susceptibility and heat capacity of AgCuVO$_4$ exhibits a typical low dimensional behavior. Picture according to Ref. [87]. Right: Calculated atom resolved density of states for AgCuVO$_4$. The anti bonding $dp\sigma$ states close to ε_F are dominated by O and Cu states, but show no clear separation from the lower laying part of the valence band.

The experimental results from magnetic susceptibility χ, specific heat C_p and electron spin resonance (ESR) measurements describe AgCuVO$_4$ as a low dimensional compound with a magnetic ordering at low temperatures.[87] The magnetic susceptibility shows a typical low dimensional characteristic shape with a broad maximum around 200 K and a Curie-like upturn below 50 K from impurities (see Fig 3.5, left (inset)). A Bonner-Fisher fit to this data allows the estimation of the NN exchange $J_1^\chi = 335$ K. Our ESR data support the picture of a quasi 1D Heisenberg chain with dominant AFM exchange and allow to estimate $T_N = 2.5$ K, in excellent agreement with $T_N = 2.5 - 2.7$ K derived from heat capacity data (see Fig. 3.5). Furthermore, following the relation between the magnetic part of the heat capacity at low temperatures to the magnetic exchange parameter according to Ref. [88] (for an isotropic spin 1/2 chain) we obtaine $J_1^{C_p} = 330 \pm 10$ K from our C_p data. Based on the Néel temperature, the inter chain exchange $J_{ic}^{C_p}$ can be estimated to be smaller than 1 K by the relation

$$J_{ic} = T_N/(1.28\sqrt{ln(5.8J_1/T_N)}$$

from Ref. [89] (for details see Ref. [87]).

Electronic structure

Although experiments provide a consistent picture based on different independent measurements, a microscopic insight into the electronic and magnetic properties is still missing. Therefore, we carried out band structure calculation and subsequent model calculations.

In Fig. 3.5 the obtained density of states (DOS) of the valence states with a band width of about 6 eV is shown. This band width is rather typical compared with other cuprates revealing a chain-type of structural feature like $CuGeO_3$ [90] or Sr_2CuO_3 [91]. The valence band is dominated by Ag, Cu and O states. The quite narrow Ag $4d$ contribution between -2 eV and -0.5 eV indicates a Ag^+ cation. For Cu and V, the calculations yield magnetic Cu^{2+} and non-magnetic V^{5+} as could be expected from the crystal structure in terms of their coordination spheres: Cu and O form strongly distorted CuO_6 octrahedra with considerably shorter Cu-O^{eq} bonds in the equatorial plane leading to the characteristic CuO_4 plaquettes, whereas the non-magnetic V^{5+} is tetrahedrally coordinated, VO_4. In contrast magnetically active V^{4+} usually appears in square-pyramidal coordination with short apical bonds.
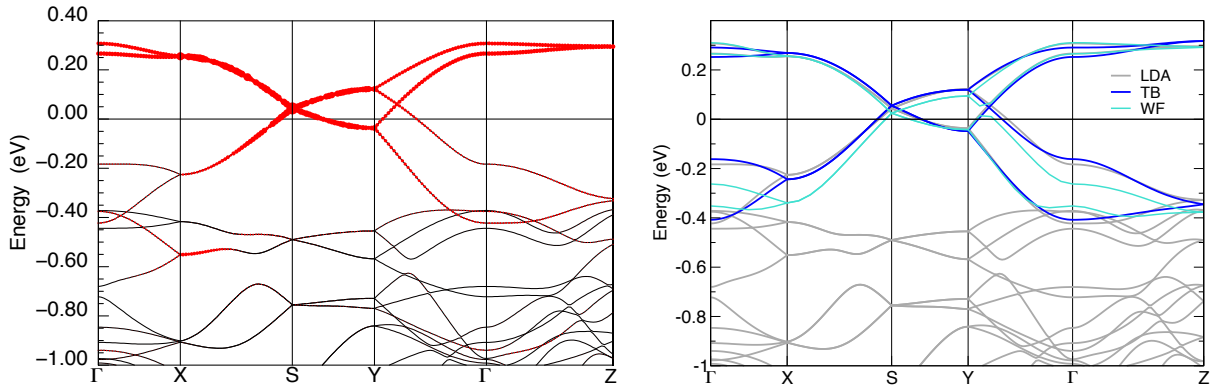
Figure 3.6.: LDA band structure together with band characters of the anti bonding CuO dpσ state (left) and the fits from TB and WF based TB model (right).

As a consequence of the Cu^{2+} state, the anti-bonding Cu-O dpσ states of the system are half filled. Corresponding to 4 Cu per unit cell, four half-filled bands cross the Fermi energy ε_F (see Fig. 3.6) in our LDA calculation, which are degenerated in large parts of the Brillouin zone (compare bands along $X-S-Y$ points). This metallic solution is in contradiction to the insulating character of the compound concluded from the red color of the crystals and a well known shortcoming of the LDA calculations. Since LDA underestimates the strong correlations of the Cu^{2+} ($3d^9$) configuration, these missing correlations can be taken into account by mapping the relevant LDA bands onto a TB model and subsequently onto a Hubbard and Heisenberg model. Alternatively, the strong Coulomb repulsion in the Cu $3d$ shell can also be considered explicitly in a mean-field like approach using the LSDA+U scheme. In this work we applied both approaches.

In many cuprates, the anti-bonding dpσ states are well separated from the lower-lying valence states (compare e.g. DOS of $PbCuSO_4(OH)_2$ in Sec. 3.1.3 or Li_2ZrCuO_4 in Sec. 3.1.2), while in $AgCuVO_4$ these states overlap with the lower lying part of the valence band due to a sizable admixture of other orbitals. The inset of Fig. 3.5 shows the orbital-resolved DOS of the Cu-O dpσ states in comparison with the total DOS. In the region between ε_F and 0.25 eV the dpσ states clearly dominate the anti bonding bands, whereas from ε_F to -0.5 eV contributions from other orbitals increase notably. Accordingly, the hybridization with lower lying parts of the valence band is also visible in Fig. 3.6 (left) where the band characters of the dpσ states spread out to lower energies (mainly around Γ and X).

Developing the magnetic model

The sizable admixture of other valence states to the anti bonding bands that are responsible for the magnetic interactions in the system impedes a straight forward mapping to an effective one-band TB model using a least square fit procedure. The ambiguousness in the selection of the relevant bands, especially between Γ and X and Γ and Z, respectively, can be removed by applying the Wannier function technique. The resulting leading transfer terms for both approaches are sketched in Fig. 3.7 (left) and the values are given in Table 3.1. The corresponding bands are highlighted in Fig. 3.6 (right panel) on top of the LDA band structure. It can be clearly seen that in the upper part the least square TB fit and the Wannier function derived bands nearly coincide, while for the lower lying region with stronger admixture both approaches show sizable deviations. This is mostly reflected in the leading nearest neighbor (NN) transfer integral t_1, whereas the much smaller coupling to further neighbors are mostly unaffected. On the other hand, the good agreement between both methods justifies the application of an effective one-band picture.
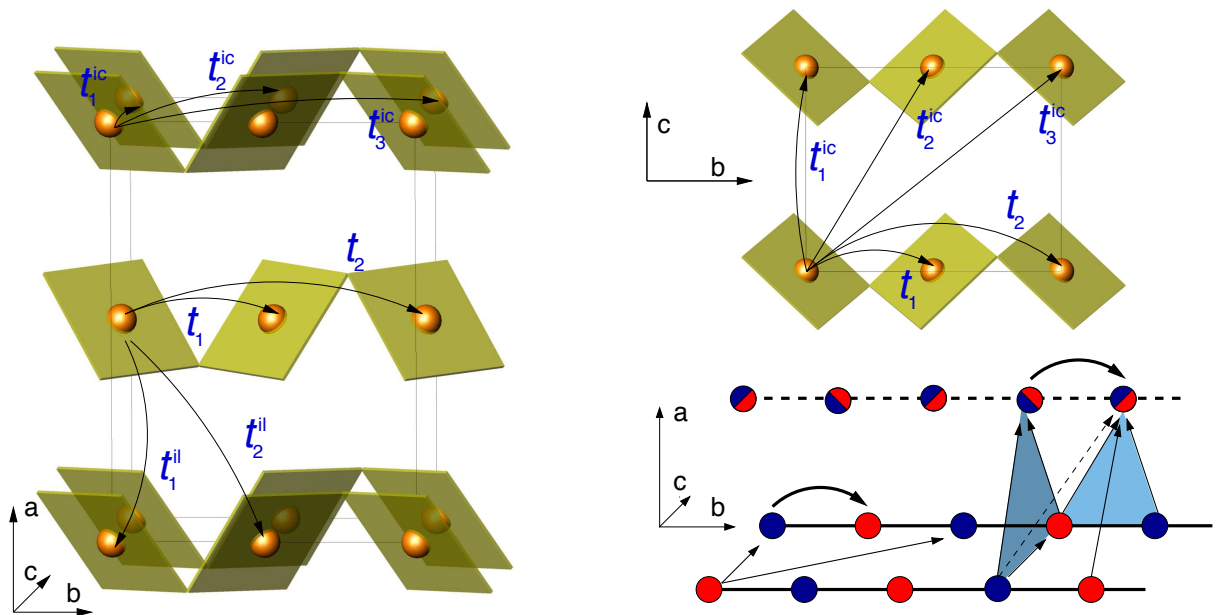
Figure 3.7.: Sketch of considered hopping paths (left) for the TB mode and obtained magnetic model for AgCuVO$_4$. The interlayer couplings have partially frustrating character influencing T_N.

t_i/meV	t_1	t_2	t_1^{ic}	t_2^{ic}	t_3^{ic}	t_1^{il}	t_2^{il}
t_i(TB)	-145	2	17	7	6/-19	-16	-11/0
t_i(WF)	-157	0	18	6	5/-20	-13	-10/3

Table 3.1.: Comparison of the leading coupling terms for AgCuVO$_4$ from TB and WF-based TB approach.

From our mapping, we obtain a clear physical picture for the relevant interactions in the system: We find weakly interacting chains along the b direction with essentially only NN coupling $t_1 \sim -157\,\text{meV}$. Consistent with the Cu-O-Cu bond angle of about 113°, this leading transfer is closer to the values for edge-shared chain geometry (e.g. $CuGeO_3$[90], Cu-O-Cu bond angle of about 99°, $t_1 \approx 175\,\text{meV}$) than for the couplings of the corner-shared chains (e.g. Sr_2CuO_3[91], Cu-O-Cu bond angle of 180°, $t_1 \approx 410\,\text{meV}$). This vicinity to the edge-shared chain compounds raises the question of the relevance of ferromagnetic contributions to the NN exchange J_1. Mapping the TB model via a Hubbard to a Heisenberg model (in the limit of strong correlations and at half filling) to describe the low lying magnetic excitations, only, yields the antiferromagnetic parts $J_i^{\text{AF}} = 4t_i^2/U_{\text{eff}}$ of the total exchanges J_i. The ferromagnetic contributions can be estimated comparing the TB derived exchange J_i^{AF} with the result of LSDA+U calculations for magnetic super cells. Using a standard one-band value $U_{\text{eff}} = 4\,\text{eV}$ [90], we obtain for the NN exchange $J_1^{\text{AF}} = 23 \pm 3\,\text{meV}$ $(265 \pm 35\,\text{K})$.[4] For the calculated range of physically relevant U_{3d} values[5] in the LSDA+U approach we obtain $J_1 = 24 \pm 3\,\text{meV}$ $(280 \pm 35\,\text{K})$ for U=6.5 eV. The good agreement between J_1^{AF} and J_1 leads us to the conclusion that ferromagnetic contributions to the NN exchange in $AgCuVO_4$ are basically negligible. The choice of U_{3d} is additionally justified by the resulting gap size of 1.5...2 eV consistent with the red color of the sample and in agreement with measurements of the absorption in the visible part of the electromagnetic spectrum at significantly lower energy for $AgCuVO_4$ in comparison with α-$AgVO_3$ (reported gap of $\approx 2.3\,\text{eV}$)[92] as a reference.
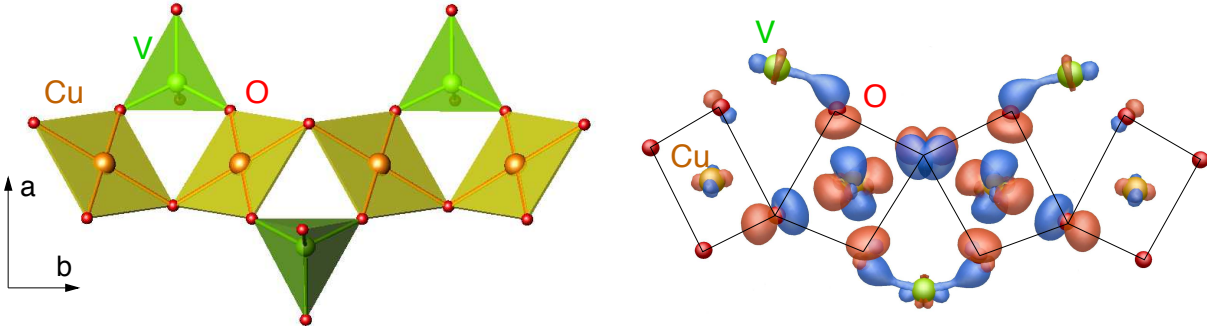

Figure 3.8.: Calculated Cu $3d(x^2 - y^2)$ related Wannier functions for a chain segment of $AgCuVO_4$. The magnetic coupling is not only mediated by the shared O^{eq}, but involves transfer paths via the VO_4 tetrahedra.

A closer inspection of the effective exchange path by the calculated Wannier functions (see Fig. 3.8, right) shows that the interaction does not appear from a coupling via the shared O^{eq} only, but also involves states of the VO_4 tetrahedra. These contributions are in line with the picture obtained from the orbital resolved DOS (see Fig. 3.5) with additional states mixing into the anti bonding $dp\sigma$ band.

Although the inter-chain couplings J^{ic} of $AgCuVO_4$ are of the order of 1/65 with respect to the NN intra-chain exchange J_1, they strongly influence the ordering temperature of the

---

[4]The error is estimated from the difference of the least square fit and the Wannier function approach for the TB model.

[5]Within the range of $U_{3d} = 6...8.5\,\text{eV}$ we obtain agreement with the experimentally reported exchange integrals for a large number of edge- and corner-shared cuprate systems.

system and allow to estimate T_N according the same relation used before to determine $J_{ic}^{C_p}$ from the Néel temperature.[89] Using $J_1 = 24\,\text{meV}$ (280 K) and an effective $J_{\text{eff}}^{ic} = 0.25\,\text{meV}$ (3 K) as an average of the inter-chain couplings J_1^{ic} and J_3^{ic} in the crystallographic bc plane and the inter-layer exchanges J_1^{il} and J_2^{il}, see Fig. 3.7, we obtain a theoretical value $T_N^{\text{theo}} = 8.6 \pm 5\,\text{K}$ for the Néel temperature.

Compared to the experimentally observed $T_N = 2.5\,\text{K}$ this is a clear overestimation by a factor of about 3.5. A closer inspection of the further magnetic interactions between chains belonging to different 'magnetic layers' separated by a diagonal component along the crystallographic a-direction (J^{il}) reveals the frustrating nature of the leading inter-layer couplings J_1^{il} and J_2^{il} (compare Fig. 3.7, right). Therefore, we can assign the deviation of the calculated and observed T_N to the latter considerable inter-chain frustration. The situation is comparable to the quasi 1D model compound Sr_2CuO_3, where a similar suppression of the ordering temperature compared to the calculation appears.[91] The strong influence of frustration on the ordering temperature is especially pronounced for the compound $Sr_2Cu(PO_4)_2$, where the leading inter-chain couplings $J_\perp$ are fully frustrated.[47] Although the main couplings are comparable to AgCuVO$_4$, the ordering temperature of $Sr_2Cu(PO_4)_2$ is smaller by a factor of about 30. The strong quantum fluctuation in quasi 1D spin 1/2 compounds not only lead to a drastic reduction of the ordering temperature, but also to a small ordered moment. Using the same exchange parameters as for the calculation for T_N we predict an ordered moment of about 0.15 μ_B (Eq. 7 in Ref. [89]).

In conclusion, our band structure calculations provide us with a picture (see Fig. 3.7) of quasi-1D NN Heisenberg chains with small inter-chain couplings where the in-plane couplings J^{ic} support AFM order, whereas sizable inter-layer frustration J^{il} impedes AFM.

Influence of pressure

Stimulated by the known intimate interplay between the crystal structure of many cuprates and their magnetic properties in combination with the unusual chain geometry of trans corner shared CuO$_4$ plaquettes, we followed the question about the stability of the crystal structure and the magnetic ground state of AgCuVO$_4$ under pressure. As the magnetic properties of the compound are dominated by the NN exchange J$_1$, which in turn is highly sensitive to the exact Cu-O-Cu bonding angle along the chains, applying pressure seems to be promising to influence or tune the system.

Thus, we performed x-ray diffraction (XRD) measurements under pressures up to 7.5 GPa using a diamond anvil cell (DAC) with ethanol/methanol as pressure transmitting medium. After an integration and background correction of the collected data, we used the FULL-PROF package[57] to refine the lattice parameters by a Le Bail fit. The crystal structure of AgCuVO$_4$ remains stable in the applied pressure range. Within the experimental accuracy, we yield a smooth decrease of the lattice parameter and a volume reduction of about 5%. The small deviation of the obtained experimental data from the theoretical fit of the Murnaghan Birch equation of states (EoS) states arise from the limitation of the pressure measurement[6] and the loss of ideal hydrostatic conditions for the pressure medium. Using the obtained lattice parameter and theoretical relaxed atomic positions as input for our electronic structure calculations, we probe the influence of pressure on

---

[6]The used screw type of DAC has to be mounted and unmounted every time to change the pressure. A slightly shifted ruby position during the Raman measurement influences the accuracy of the determined pressure.
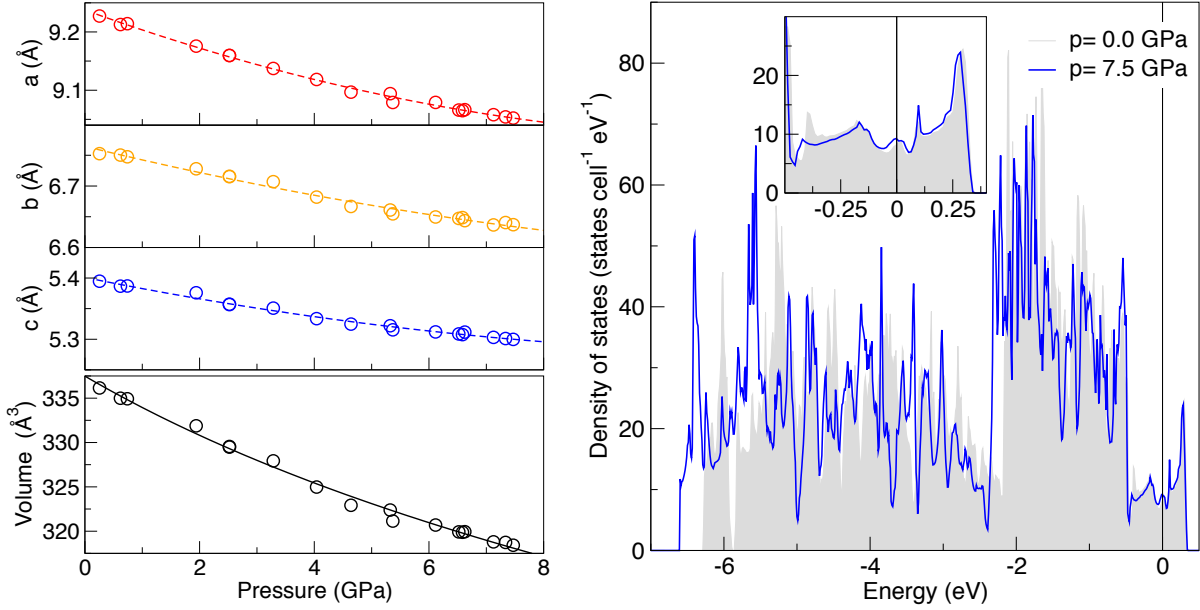
Figure 3.9.: Left: Pressure dependence of the lattice parameter and unit cell volume of AgCuVO$_4$ measured by XRD. Right: Comparison of the LDA band structure calculated for ambient pressure and the maximal applied pressure p=7.5 GPa. Beside a broadening of the band width, the valence band remains very similar.

the electronic and magnetic properties of AgCuVO$_4$. Beside a broadening of the valence band by about 0.3 eV, the comparison of the density of states for ambient pressure with the crystal structure for the maximal applied pressure (7.5 GPa) show a very similar shape (compare Fig. 3.9). Especially the anti bonding $dp\sigma$ states, relevant for the magnetic exchange, remain stable. However, the observed increased valence band width is in line with the shorter inter atomic distances in the decreased volume and thus stronger interactions. More qualitatively the maximal applied pressure changes the Cu-O-Cu bonding angle by 1° and the Cu-O distances by less than 0.06 Å resulting in a relative increase of J$_1$ by 30%. The averaged inter chain exchange J_{ic}^{HP} increases by 20-30%, resulting from an increase of in-plane interactions, whereas the inter layer couplings are weakened. However, T_N is expected to increase as well, since the strengthening of interactions within the planes should overcome the weaker inter layer couplings.

Summary

The compound AgCuVO$_4$, crystallizing in an unusual crystal structure with chains from trans-corner shared [CuO$_4$] plaquettes, was investigated in a combined theoretical and experimental study. To gain insight into the magnetic interactions of the compound, we performed electronic structure calculations revealing the quasi one dimensional character of the material. The comparison of Heisenberg models derived from effective TB model and LSDA+U calculations elucidates the coupling regime of AgCuVO$_4$ on a microscopic basis. We found the main exchange along the trans corner shared chains with $J_1^{theo} = 280 \pm 35$ K and several small inter chain couplings leading to an estimate of the AFM ordering temperature of T$_N^{theo} = 8.6$ K. Our results are in line with magnetic susceptibility

and heat capacity measurements exhibiting a pronounced one dimensional behavior. We yield $J_1^{exp} = 330\,K$ from our experimental data. Furthermore, a small inter chain coupling is evident from specific heat and ESR measurements leading to a magnetically ordered state at $T_N^{exp} = 2.5\,K$. The overestimation of T_N^{theo} from the theoretically derived magnetic model compared to the experimental observed value can be attributed to frustrated inter chain couplings along the crystallographic a direction. The compound with effective NN couplings of the order of room temperature can be classified as "in between" edge- and corner shared chains. The results of the ambient pressure study are published in Ref. [87], where also the thermodynamical data and results of ESR experiments are discussed in more detail. Applying pressure influences only slightly the chain geometry and the magnetic ground state properties of the compound. The suppressed volume results mainly in a broadening of the valence band and an increase of J_1 by 30%. However, stronger effects could appear in related chain geometries, especially in edge-shared chains. Especially for compounds close to quantum critical points, a pronounced sensitivity on pressure can be expected due to the subtle balance of the leading exchanges. An example of such a compound will be discussed in the next section.

3.1.2. Li$_2$ZrCuO$_4$ - in close vicinity to a quantum critical point

The edge shared chain compound Li$_2$ZrCuO$_4$ attracted recently large interest in solid state physics as it was found, that Li$_2$ZrCuO$_4$ is placed close to the quantum critical point (QCP) of $\alpha = -0.25$ (classical) between helical and FM order with a frustration ratio of $\alpha = -0.29$ evaluated from susceptibility and specific heat data.[79] This interest raises from a subtle balance of the main interactions of the system at the QCP. In this situation, very small additional exchange couplings can become crucial for the formation of the ground state, e.g. small inter-chain couplings. In addition, small external perturbations such as pressure or magnetic fields can have dramatic influence and drive the compound to one or the other state.

Specific heat data, measured at low temperatures in different external fields exhibit a strong field dependence, typical for the subtle balance of interactions in vicinity to a QCP. While for zero field a clear maximum at $6.4\,$K is observed, pointing to a possible phase transition, this maximum is suppressed and shifted down with increasing field (see inset of Fig. 3.10, right). In contrast, above $12\,$K the contribution to the specific heat grows for increasing fields, i.e., the entropy is shifted to higher T.

The susceptibility measured down to $2\,$K (depicted in Fig. 3.10) increases for low temperatures with a pronounced maximum at $T_{\mathrm{max}} = 7.6\,$K. As for systems at the QCP, a divergence of the susceptibility is expected, T_{max} and the results of a fitted $J_1 - J_2$ model based on exact diagonalization independently supports the placement of the compound in vicinity to the QCP.[79]
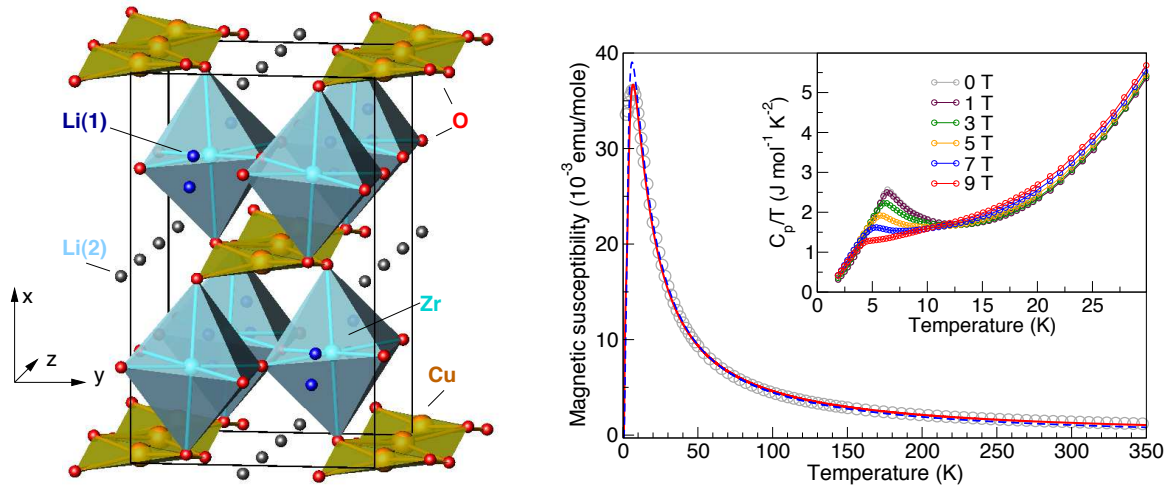
Figure 3.10.: Left: Crystal structure of γ-Li$_2$ZrCuO$_4$. The deflection of the O atoms from an ideal planar CuO$_2$ chain geometry has a crucial influence on the magnetic ground state. As second structural peculiarity the compound exhibits a Li(1) split position. Right: The measured magnetic susceptibility and field dependance of the specific heat point to a close vicinity to a QCP. Picture according to Ref. [79].

In the vicinity of a QCP, small changes in any parameter can be of crucial relevance for the realization of the ground state. This holds also for any structural detail of the compound and raises special attention to the peculiarities in the crystal structure of Li$_2$ZrCuO$_4$

compared to many cuprates, (i) a split position for one of the Li atoms and a glassy like ordering at low temperatures [93] and (ii) a distortion of the CuO_2 chains .

Here, a microscopic analysis of the magnetic exchange integrals to evaluate the influence of structural details to the magnetic properties is presented. Our study allows to elucidate the crucial importance of the structural distortion of the CuO_2 chains, which are responsible for a reduction of both the inter chain coupling and the NNN exchange, and consequently place the system close to the QCP. Furthermore, the influence of pressure, changing the distortion of chains, is studied in detail based on high pressure XRD experiments.

The γ-phase of Li_2ZrCuO_4 [93] crystallizes in an orthorhombic space group and is shown in Fig. 3.10. Since the crystal structure data in Ref. [93] and the ICSD(59618) are inconsistent, the parameters used in the calculations are provided explicitly in the Appendix B.2. The crystal structure contains distorted CuO_4 plaquettes which are arranged as edge-shared CuO_2 chains with an Cu-O-Cu bond angle of 94.13°. These edge shared CuO_2 chains form layers together with the Li(2) atoms in the yz-plane interconnected by ZrO_6 octrahedra. The alternating arrangement of the connecting ZrO_6 octrahedra lead to the deviation of the CuO_2 chains from the ideal planar geometry.

As the CuO_4 plaquettes exhibit a localized, effective spin 1/2, their linking and surrounding is of main importance for the formation of the magnetic ground state. A first structural analysis suggests sizable ferromagnetic NN exchanges caused by the close to 90° Cu-O-Cu bond angle according to the Goodenough-Kanamori-Anderson rule, if the direct Cu-Cu transfer integral can be ignored.[85]

A further structural characteristic of the γ-phase is a split position for Li(1) which is placed between the chain layers. The distance of the Li(1) atoms from the high-symmetry position is 0.37Å. While the influence of the split position of Li(1) (corresponding to 50% disorder within a classical picture, ignoring possible tunneling processes of Li(1) between the two sites of the split position) to the magnetic properties is investigated carefully, we neglect the small disorder of 3-5 % at the Li(2) and Cu site in our theoretical calculations as a good approximation.
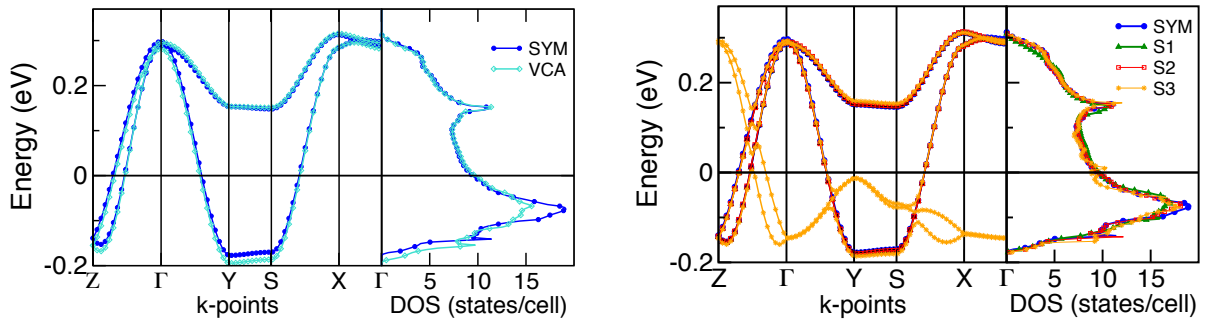

Figure 3.11.: Left: Comparison of the anti bonding $dp\sigma$ states for different model description of the Li(1) split position. The different models lead to nearly identical band structures.

Modeling the Li(1) split position

As there exists no standard procedure in band structure codes to treat split positions, several classical (i.e. within the adiabatic approximation) approaches were suggested and

discussed with respect to the influence of these model assumptions on the relevant states and related dispersion.

A careful check of the structural description of the compound as basis for the theoretical calculations is especially required, since the estimation of the importance of subtle differences in simulating the Li(1) split position is not trivial.

To start from the simplest approximation we performed electronic structure calculation for Li(1) placed at the high-symmetry position (0.25, 0.75, 0) (see also App. C.1 (SYM)).

As an alternative structural model we carried out VCA calculations (see App. C.1 (VCA)). This approach occupies both sites of the split position simultaneously by half of a Li atom. Each of this modified Li atoms is constructed by carrying the half number of valence electrons and a modified core to conserve charge. For the VCA calculations the distance between the two sites of the split position has to be enlarged to suppress the overlap of the Li valence states and ensure the convergence of the calculation.[7] Also asymmetric charge distributions between the two sites of a split position (as e.g. 0.8 and 0.2 Li) lead to nearly identical dispersion of the relevant states as long as the total charge of one Li atom per split position is conserved. However, deviations of the total charge of a split position cause sizable changes in the electronic structure.

This is also the reason why the description of the Li(1) split position by the coherent potential approximation (CPA) fails, caused by the loss of charge balance at the split position in the later approximation. In contrast to the VCA, where the total charge at each split position sums up to one Li atom, the random occupation of the Li(1) split sites in the CPA also generates cases with empty and double occupied Li(1) sites with dramatic influence on the band structure and the total energy.

As both approaches, CPA and VCA, do not change the local symmetry at the Cu site, within a further model super cells (SC) with different ordered Li(1) patterns have been calculated, breaking the local symmetry at the split position but suffer from long range order (the applied SC and Li pattern are given in App. C.2, explicitly).

The resulting bands and density of states for the different structural models show a very similar total behavior (see Fig. 3.11). Small deviations in VCA calculations can be observed in the bonding region of the valence band around -5.5 and -2.0 eV (not shown) in comparison to the high symmetry model. These differences can be understood by the influence of the two modified Li cores to the crystal potential and the corresponding shift of Li-O states.

Comparing the density of states and LDA band structure for the anti bonding $dp\sigma$ states, which are relevant for the magnetic exchanges and therefore the magnetism of the system, we found only tiny differences between the studied structural models. (i) The VCA model results in a slightly larger bandwidth compared to the other models. (ii) The high symmetry and SC models fit nearly perfectly. The additional bands of the S3 SC with an alternating Li pattern can be understood due to the doubling of the primitive cell having its origin in the symmetry breaking of the Li pattern. All SC are based on the fixed, experimental observed O positions, thus the local environment of Cu remains unchanged.

Electronic structure and magnetic model

As the different structural models for the Li(1) split position show no significant difference in behavior for the relevant low energy states (see Fig. 3.11), the electronic structure and

---

[7]Li(1) has been shifted from (0.21, 0.75, 0) to (0.18, 0.75, 0) for the VCA calculation.

the microscopic magnetic model are discussed for the SYM model as a good representative for all different structural models. To estimate more quantitatively the differences caused by the choice of the structural model, the results for the SYM and the VCA models are compared.
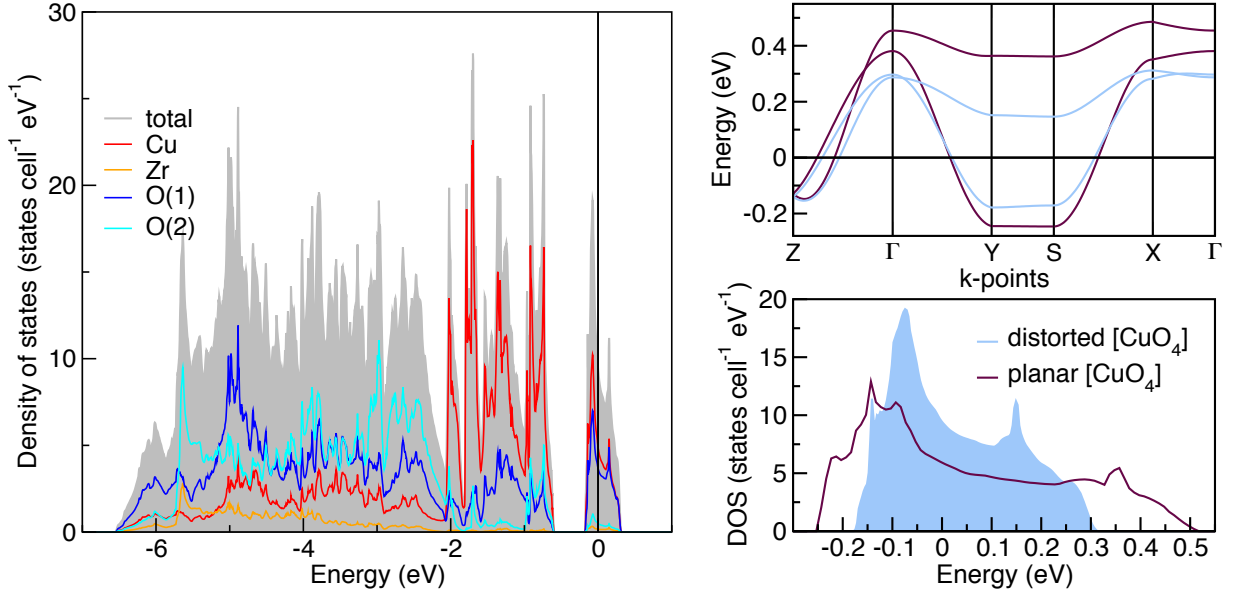

Figure 3.12.: Left: Atom resolved density of states for Li_2ZrCuO_4. The anti bonding $dp\sigma$ states are well separated from the rest of the valence band. Right: Comparison of LDA band structure and density of states close to the Fermi energy for the experimental and a fictitious, planar chain geometry. The small displacement of the O atoms from an ideal planar chain geometry results in a considerable decrease of the band width.

In Fig. 3.12 the atom resolved density of states for Li_2ZrCuO_4 is shown. The valence band has a width of about 7eV, comparable with other chain cuprates and is dominated by Cu and O states, especially at the lower edge of the valence band around -6 eV (bonding states) and at the energy range close to zero (anti bonding states). States of the Zr-O octahedra appear in the middle part of the valence band. Their contribution to the states close to the Fermi energy is negligible.

The well separated states around the Fermi energy are of main interest as they determine the magnetism of the system. These states are dominated by the in-plane orbitals of the CuO_4 plaquettes corresponding to the anti-bonding $dp\sigma$ states (not shown here, compare Ref. [94]). The distortion of the plaquettes from an ideal planar chain geometry does not affect significantly the band characters of the anti bonding $dp\sigma$ states. The hybridization with out-of-plane states is very small and does not differ from compounds with ideal planar CuO_2 chains.

The half filled anti-bonding $dp\sigma$ bands (determining the magnetic exchange) show their main dispersion along the chain direction (Z-Γ) and in the chain plane (Γ-Y, S-X), indicating the leading magnetic exchanges in the layers (compare Fig. 3.12, right). Perpendicular to these directions the dispersion is small, suggesting small exchanges between the layers. To unravel the hierarchy of exchanges in the system as well as to estimate a cut-off for

negligible long range exchanges in further SC calculations evaluating the total values of exchanges, TB calculations are performed.

All obtained transfer integrals larger than 5 meV are summarized in Table 3.2. A sketch of the corresponding exchange paths can be found in App. C.3. We find the main hoppings between NN and NNN along the chains and three considerable inter-chain hoppings in the chain plane. Comparing the SYM results with results from the VCA model, we see that the differences in the hopping integrals are very small and of the same order as the accuracy of the TB fit procedure. This indicates that the chosen structural model for the Li(1) split position is irrelevant for the calculated coupling constants of Li_2CuZrO_4. Taking into account the strong Coulomb repulsion in a model approach, we construct from our TB model a single-band Hubbard model (with a typical value [95] $U_{eff} = 4.2$ eV for edge shared CuO_2 chains) which can be mapped subsequently onto a Heisenberg model. We find $J_1^{AFM} = 1.7 \pm 0.1$ meV for the NN exchange and $J_2^{AFM} = 3.0 \pm 0.1$ meV for the NNN exchange.

To evaluate J_1 and J_2 on a quantitative level (including FM contributions), we performed a series of SC calculations. The comparison of the total energies of these SC with different spin arrangements and a subsequent mapping onto a Heisenberg model leads to a FM NN exchange $J_1^{TOT} = -11.2$ meV and an AFM NNN exchange $J_2^{TOT} = 2.2$ meV. The ground state of the compound is determined by the ratio $\alpha = J_2^{TOT}/J_1^{TOT} = -0.22 \pm 0.03$ that would result in a FM ordered ground state in close vicinity to the QCP ($\alpha = -0.25$). The variation of U_{3d} from 5.5 eV to 8.0 eV in the LSDA+U calculation does not change this behavior qualitatively, although for the smaller U_{3d} values a slightly increased α is obtained in terms of the absolute value. Besides a possible small error in the calculated exchange parameters, the experimentally observed spiral state from NMR data [96] might result due to the sizable inter chain couplings $J_0^y = 4(t_0^y)^2/U_{\text{eff}} \sim 0.6$ meV and $J_2^y \sim 0.6$ meV that both stabilize long range order.

t_i/meV	t_1	t_2	t_0^{ic}	t_1^{ic}	t_2^{ic}
SYM	-42	-56	-26	14	-25
VCA	-44	-55	-25	15	-26
FIC	-86	-92	-49	24	-21

Table 3.2.: Derived transfer integrals using an effective TB model for different structural models. For the corresponding hopping paths see also App. C.3. The choice of the structural model to consider the Li split site has only minor influence (compare VCA and SYM).

Influence of chain distortion

Whereas the different treatment of the Li(1) split position does not influence the band structure and the corresponding magnetic model essentially, the role of the distortion of the CuO_4 plaquettes remains to be addressed: How much does the non-planar geometry of the chains influence the balance of the NN, NNN and inter-chain couplings and the resulting placement of the compound in the J_1-J_2 phase diagram, especially its vicinity to

the QCP? For a fictitious planar chain,[8] changes are expected since a changed Cu-O-Cu bond angle (changed by about 0.8°) will influence J_1^{TOT} and the different orientation of the anti-bonding $dp\sigma$ "molecular orbital" will alter J_2^{TOT}. Since these changes are hardly predictable quantitatively from structural considerations only, we apply our mapping approach also to a fictitious compound with ideal planar CuO_2 chains.

In Fig. 3.12 (right panel) the resulting anti-bonding $dp\sigma$ bands and the related density of states for this fictitious structure are shown. For a planar chain geometry, we obtain an about 50% larger bandwidth, but a very similar shape of the bands compared with the real structure. On first glance, this suggests a scaling of the leading hopping parameters, only. Our TB fit yields nearly a doubling of the hopping integrals as listed in Tab. 3.2, thus a dramatic change of the corresponding exchange terms can be expected. To take into account the large FM contributions to J_1^{TOT}, we carried out LSDA+U calculations for the same SC used before.

Surprisingly, we find a nearly unchanged NN exchange J_1^{TOT}, but only due to the compensation of the increased individual contributions J_1^{FM} and J_1^{AFM}. Since the FM contribution J_2^{FM} to J_2^{TOT} remained small - as for the real structure - it basically scales like $J_2^{AFM} \sim 4t_2^2/U_{\text{eff}}$. Thus, we obtain a large change in J_2^{TOT} and consequently in the frustration ratio for the planar fictitious chains $\alpha_{\text{FIC}} \sim -0.6$. In consequence, the ratio $\alpha = J_2/J_1$ depends strongly on structural details of the local Cu-O environment. This is especially important regarding the vicinity of the system to the QCP. On the other hand this sensitivity of α to the chain buckling may provide the opportunity of manipulating the ground state of the system selectively by substitution or external pressure.

Unfortunately, a planar chain arrangement leads also to a sizable increase in the inter chain coupling. This can be understood as the decrease of buckling increases the inter-chain overlap of the O orbitals belonging to the $dp\sigma$ states. This way, a tendency towards long range order is stabilized, although the quantitative influence of inter-chain couplings to the ground state is sparsely considered in the literature.[97]

Stability of the Li(1) split position

Although the different treatments of the Li(1) split position yield no significant influence on the shape or width of the relevant bands determining the magnetic exchange parameters the split position may influence other properties of the compound. Related to the split position, the local symmetry or disorder could modulate the pitch angle of the helical state or be crucial for the formation of a possible multiferroic phase. Furthermore, ^{7}Li NMR and complex dielectric measurements reveal a glass-like ordering of the Li(1) ions below $T_g = 100\,\text{K}$.[98] Thus, using our SCs simulating different types of Li(1) order, we tackled the questions whether a tendency to a static Li(1) order can be supported by calculations. For the purpose of computational feasibility, we restricted ourselves to a fourfold cell (32 atoms). The comparison of the total energy for the different ordered Li(1) patterns (SYM, S1, S2, S3) favors energetically the high-symmetry model (SYM) with a single Li(1) position (compare App. C.1 and C.2). The second lowest in energy is the structure with an alternating Li(1) displacement along the chain direction (S3). For this Li(1) arrangement, the dependence of the total energy on the Li(1) displacement is depicted in Fig. 3.13 (left). The resulting curve does not indicate a double well potential as expected for a Li(1) split

---

[8]O(1) was placed at (0, 0.228, 0.5). This structutal variation decreases the Cu-O bond length by 0.01Å, and increases the Cu-O-Cu bond angle along the chain direction by 0.8°.
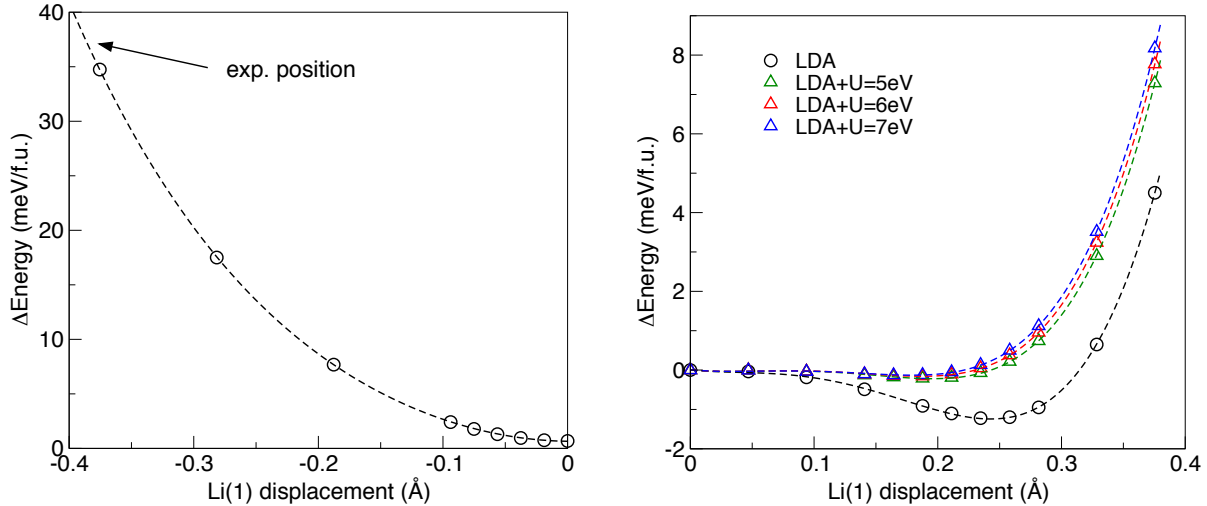
Figure 3.13.: Energy difference depending on the displacement of the Li(1) atom from the high-symmetry position. Left: The displacement of Li, while all other atoms are fixed, favors the high symmetry solution. Right: Displacement of Li and a subsequent relaxation of the surrounding atoms lead to the double minimum in energy expected for a split position.

position, but a minimum around the high symmetry position and a harmonic behavior up to almost 0.3 Å Li(1) displacement. According to our calculations, for the experimentally suggested Li(1) split position (marked by the arrow in Fig. 3.13) only slight anharmonic effects could be expected. To ensure, that the Li(1) order is not driven by correlation effects at the Cu site, LSDA+U calculations were performed showing no significant differences. Thus, calculations with a fixed lattice apart from Li(1) can not support the split position but favor the high symmetry solution. This could have its origin in (i) dynamic effects that violate the adiabatic approximation used in the calculation or (ii) the stabilization of the disordered structure by entropy rather than energy.

To consider a possible correlation effect between the Li(1) site and the surrounding atoms as suggested for the Li(1) and O(1) site by Ref. [98] , we performed a series of calculations relaxing the O sites for different fixed Li(1) positions.

For a first probe we deflect the Li(1) atom along the x axis and relax the O(1) and O(2) positions within the symmetry and space group of the SC S1, as the smallest structural model allowing an individual placement of Li(1). Already the comparison of total energies for this simplified simulation of a correlated Li(1)-O position exhibits a sizable double minimum for a displacement of Li(1) from the high symmetry position by about 0.25 Å. The maximal energy gain between the high symmetry position and the optimal Li(1) displacement is about 1 meV (11 K) in our LDA calculation, much too small to explain the onset of a glass like freezing below 100 K.[98] However, the shape of the characteristic energy potential for the split position depend sensitive on the chosen functional and the exact shift of Li(1). A displacement of Li(1) from the high symmetry towards its fully relaxed position without any symmetry restrictions[9] increases the energy difference significantly.[99] Using

---

[9]This calculations were performed in space group P1, where all atoms have been relaxed simultaneously including Cu, Zr and Li(2).

GGA, well known to describe inter atomic distances more precisely than LDA, obtain the energy minimum close to the experimental observed Li(1) displacement. Preliminary results in our common study yield a maximum energy gain of about 9-12 meV (105-140 K) in line with the experimental evaluated energy scale of 100 K.

Whereas the choice of the Li(1) model can be neglected for the evaluation of the magnetic exchange parameters for a fixed lattice of Li_2ZrCuO_4, this no longer holds for a correlated Li(1)-O(1) position. Since the O(1) site determines the CuO_2 chain geometry, a relaxation of O(1) affects directly the chain distortion, which is crucial for the magnetic ground state. To estimate this indirect influence of the Li(1) split position on the magnetic ground state, we evaluate the modulation of J_1 and J_2 depending on the modulation of the O(1) sites, observed in a fully relaxed structure for the experimental determined Li(1) position. The obtained exchange integrals as a function of the O(1) displacement are depicted in Fig. 3.14. The maximal and minimal displacement of O(1) from the planar chain plane result in a modulation of the frustration ratio of $\alpha = -0.3 \pm 0.1$ (brown circles). Thus, along the chain direction a modulation of the exchange parameters without long range order is expected, complicating the intuitive picture.

Influence of high-pressure

Motivated by the theoretical results revealing the influence of the chain geometry on the NNN exchange and the related change in α, we challenged experimentally the possibility to drive the system closer towards the QCP by high pressure.

Therefore XRD measurements have been performed using a screw type of DAC with methanol/ethanol as pressure transmitting medium. Up to the maximal applied pressure of 15 GPa the crystal structure remains stable. After the integration and a background correction of the collected data, the lattice parameter of Li_2ZrCuO_4 have been determined by a Le Bai fit using the FULLPROF package. Due to the experimental difficulty to resolve the light atoms of the compound next to Zr, we calculated the O position of the crystal structure by a DFT based relaxation, while Li(1) was fixed to the high symmetry position[10].

In Fig. 3.14 the dependence of the experimentally evaluated volume under pressure is illustrated. A slight deviation from an ideal smooth decrease appears in the volume vs. pressure curve around 10 GPa typical for a freezing of the pressure transmitting medium and a loss of hydrostatic conditions. Regarding our combined experimental and theoretical approach to determine the crystal structure of Li_2ZrCuO_4 under pressure, we yield (i) a volume change of about 10%, (ii) a sizable reduction of the chain buckling and (iii) a deviation of the Cu-O-Cu bonding angle less than 1°. Thus, applying pressure allows to influence the deflection of O atoms from the ideal planar chain geometry as the crucial parameter influencing the NN and NNN exchange and thus in consequence determining the formation of the magnetic ground state. For a qualitative relation, we applied the same spin arrangements and SC for the LSDA+U calculation as before. The resulting exchange parameters and their frustration ratio are depicted in Fig. 3.14 as a function of the O displacement together with the values for the experimental crystal structure from Ref. [93], the theoretical estimation of Li(1)-O correlation effects and the fictitious planar chain geometry.[11] The results based on the high pressure data are placed between

---

[10]Neglecting the Li(1)-O correlation effect as a first approximation.

[11]The relation between pressure and the O displacement is almost linear. Compare Fig. 3.14 (left, middle
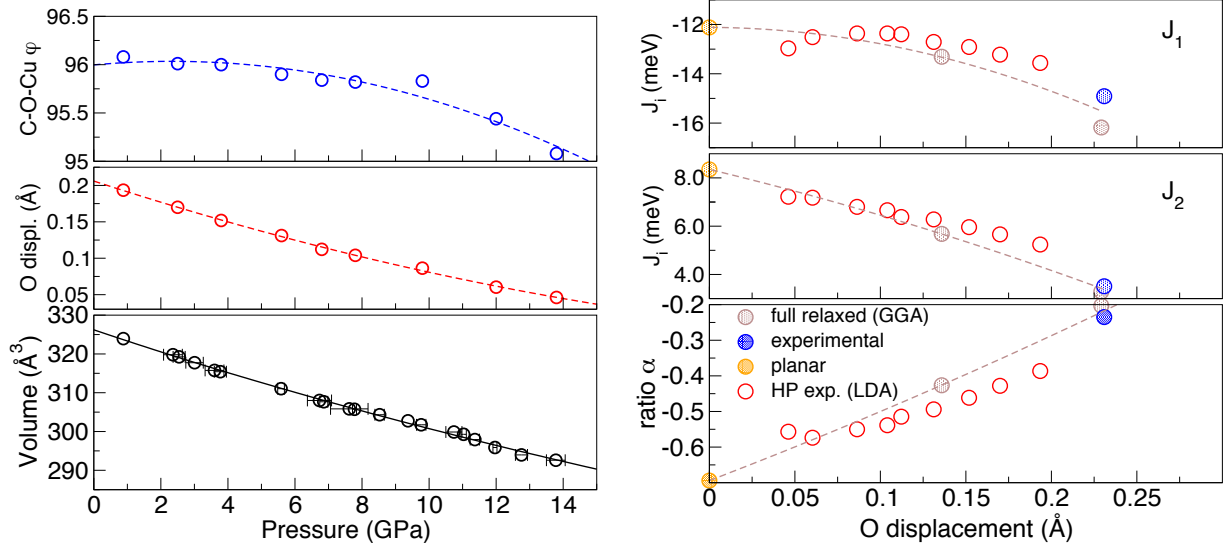
Figure 3.14.: Left: Dependence of the unit cell volume under pressure from XRD measurements. The development of the bond angle and O displacement is derived from the computational relaxed crystal structures based on the experimental results. Right: Calculated exchange integrals and frustration ratio as a function of the O displacement from an ideal, planar chain symmetry.

the experimentally obtained ambient pressure data and the fictitious planar structure. An almost linear dependence can be expected. The choice of the chosen exchange and correlation functional influences the slope and absolute values of exchange parameters sizably. A detailed systematic study including also the Li(1)-O correlation is required. However, external pressure influences the chain buckling and this way allows to tune the system. Since pressure drives the system away from the QCP, a combination of substitution and pressure is suggested. In a first step Zr could be substituted by alternative ions to increase the chain buckling[12], which can be subsequently suppressed by pressure in a controlled way.

Summary

Applying LDA and LSDA+U band structure calculations we obtain a consistent, microscopically based picture in good agreement with cluster calculations (Ref. [94]): (i) Li_2ZrCuO_4 can be understood as a quasi-1D chain compound with FM NN J_1 and AFM NNN J_2 exchange in close vicinity to a QCP. (ii) We find sizable inter-chain couplings that should be relevant for the magnetic ground state of the system, especially due to the vicinity of the system to a QCP where small exchange parameters may strongly influence the balance between the competing ground states. (iii) Calculations for a fictitious structure with planar chains indicate that the balance between J_1 and J_2 depends heavily on structural details, especially on the magnitude of the CuO_2 chain buckling. (iv) This

---

panel).

[12]In analogy to the two compounds $Na_3Cu_2SbO_6$ and $Na_2Cu_2TeO_6$, where the exchange of Sb by Te changes the distortion of the edge shared dimer chain.

also applies for the inter-chain coupling which is strongly increased for the fictitious planar geometry.

Our findings suggest that the buckling of the CuO_2 chain is crucial for the vicinity to the QCP, therefore it should be possible to tune the system towards that point by chemical substitution at the Zr site or by external pressure. The influence of pressure on the chain distortion was proved experimentally by high pressure XRD measurements using a screw type of DAC. On the other hand, it would be desirable to decrease the inter-chain coupling for which the orientation of the CuO $pd\sigma$ orbitals is more relevant than inter-atomic distances according to our results. Thus, a search for good quasi 1D systems should turn towards crystal structures where the chains are arranged in a strongly non-planar pattern. Our simulations indicate that the Li(1) split position has only a negligible direct influence on the spin system, assuming that all other atoms of the structure are fixed to their experimental positions. Within this approximation our calculations do not support the experimentally observed glassy-like order for Li(1) on this split position[98] since it yields a single Li(1) position as most energetically favorable. Taking into account a possible Li(1)-O correlation changes the picture. The relaxation of the neighboring O atoms in the CuO_2 chain for different Li(1) displacement reveals the characteristics of a double well potential in the total energy. First estimations of total energy differences in our ongoing study are in line with the experimentally determined ordering temperature. The influence of correlated Li(1)-O sites on the magnetic model will be addressed in further studies. The main parts of the section are published in Ref. [79] and Ref. [94]. Ref. [79] emphasizes on the vicinity of Li_2ZrCuO_4 to the QCP by a combination of experimental and computational methods. The results of thermodynamic data are evaluated with respect to theoretical results from QCP simulations and DFT calculations. In contrast, Ref. [94] focuses on the microscopic origin and structural peculiarities for the vicinity of the compound to the QCP .

3.1.3. PbCuSO$_4$(OH)$_2$ - magnetic exchange ruled by H

The natural mineral linarite PbCuSO$_4$(OH)$_2$, which has an unusually intense blue color, is closely related to Li$_2$ZrCuO$_4$ in both, its crystal structure and its magnetic properties. Similar to Li$_2$ZrCuO$_4$, linarite consist of chains formed by edge shared CuO$_4$ plaquettes, which differ from an ideal planar geometry, though not by a distortion of the chains, but rather by a folding (see Fig. 3.15). While the low temperature properties of PbCuSO$_4$(OH)$_2$ were earlier described by Baran *et al.* [100] as a quasi one dimensional $J_1 - J_2$ model well in the region of a helical ordered ground state, recent thermodynamical measurements suggest that the system is in close vicinity to a quantum critical point (QCP). The difficulty to settle this controversy between the experimental observation and the earlier suggested model stimulated a reinvestigation of the magnetic ground state for PbCuSO$_4$(OH)$_2$ also in a theoretical study. In addition, recent neutron diffraction (ND) measurements by Schofield *et al.* [101] provide for the first time experimentally determined Wyckoff positions for the two inequivalent H sites. This set of crystallographic data will be named S2 during the following discussion, whereas the crystal structure reported by Effenberger *et al.* [102] based on XRD is called S1. Surprisingly, the new set of crystallographic data, which mainly differ in a changed H position, has strong influence on the electronic structure. Calculating the magnetic ground state of PbCuSO$_4$(OH)$_2$ based on the crystal structures S1 and S2, we obtain two different sets of exchange parameters J_1 and J_2 with significantly different frustration ratio, which in consequence places the system in different regions of the phase diagram. This unexpected strong influence of the H sites onto the magnetic ground state rises the question about the correct crystal structure of linarite and its stability at low temperatures. Since the published crystallographic data in literature can be separated into two sets (represented by S1 and S2), which differ in a slightly different relative placement of the structural units, we start the search for the correct crystal structure from theory. Furthermore the discrepancy between the theoretically optimized and the experimentally obtained H position from neutron data has to be addressed. Our theoretical study was supported by single crystal XRD. To probe the stability of the crystal structure at low temperatures, we performed XRD measurements at the high-resolution beam line ID31 at the ESRF, Grenoble, down to 4 K using a powder sample obtained by grinding a piece of the same crystal as used for the single crystal XRD.

Linarite crystallizes in a monoclinic space group. The general configuration of the crystal structure is depicted in Fig. 3.15. Most relevant for the development of the magnetic ground state is the arrangement and local environment of the magnetically active Cu^{2+} ions. In PbCuSO$_4$(OH)$_2$ Cu is coordinated by a Jahn-Teller distorted O octahedra as present in many cuprates, where the four short bonded O atoms in the equatorial plane of the octahedra with Cu-O distances of about 1.92 to 1.98 Å form CuO$_4$ plaquettes. These CuO$_4$ plaquettes are arranged to edge shared chains with a folding angle of 155° between neighboring plaquettes, while the O of the CuO$_2$ chains form OH groups with the two crystallographically different H atoms. This way, two crystallographic O sites appear along the chains and result in two slightly different Cu-O-Cu bond angles (91° and 94°). These close to 90° angles give raise to large FM contributions to the NN interaction according the GKA rule.[85] Also the folding of chains may reduce the long range AFM interactions due to the unfavorable orientation of interacting orbitals and thus a suppression of the NNN exchange. The individual chains running along the crystallographic y direction form layers in the yz plane. The pronounced tilting of the folded chains against each
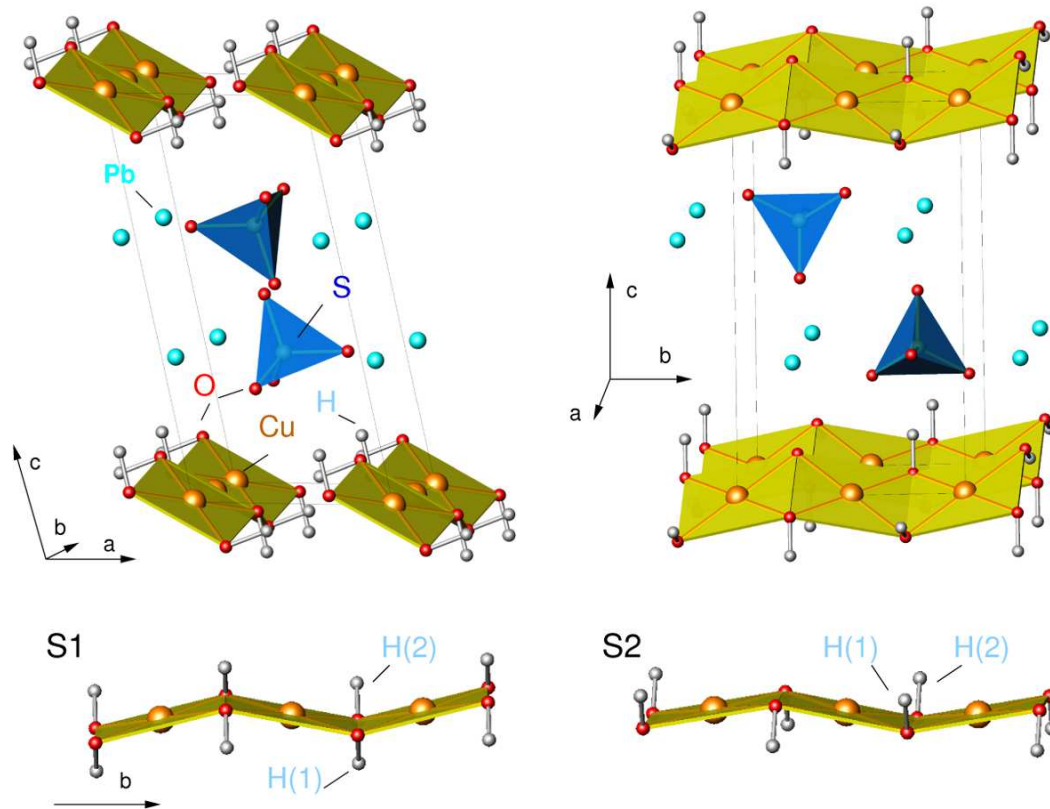
Figure 3.15.: Top: Crystal structure of PbCuSO$_4$(OH)$_2$ containing folded CuO$_4$ chains. The placement of H with respect to the folded chains along b is crucial for the electronic structure. Bottom: Short chain segments with different H sites. The structural model S1 is based on the XRD results from Ref. [102] and computational optimized H positions using the SIESTA package. The H arrangement of S2 results from recent ND experiments Ref. [101].

other suggests the suppression of inter chain couplings within a layer, as the O orbitals of neighboring chains are not placed within the same plane, comparable to the scenario in Li$_2$ZrCuO$_4$. Perpendicular to the chain plane, the layers are well separated by a double layer of SO$_4$ tetrahedra and Pb atoms[13]. The O atoms of the SO$_4$ tetrahedra complement the octrahedral surrounding of Cu.

However, the building units of the crystal structure are very similar in the published crystallographic data, e.g. S-O or Cu-O distances are comparable, the crystal structures from XRD S1 (Ref. [102]) and ND S2 (Ref. [101]) differ in the relative placement of SO$_4$ to CuO$_2$ chains and Pb atoms and the tilting of CuO$_2$ chains.

Former study and new experimental data

The J_1 –J_2 model for PbCuSO$_4$(OH)$_2$ was developed from thermodynamic measurements and a microscopic modeling based on LDA band structure calculation resulting in a FM-NN and AFM-NNN exchange with a frustration ratio of $\alpha = -0.5$.[100] The electronic structure

---

[13]This leads to the large inter layer distance of about 9.7Å

calculations were performed for the crystal structure reported by Effenberger *et al.* [102] (S1) and theoretically optimized H positions using the SIESTA package. FM contributions to the exchange integrals were considered using a semi-empirical renormalization.

The observation of multiferroic behavior in edge shared chain compounds due to symmetry breaking caused by an incommensurate helical order as discussed for LiCuVO$_4$[103], LiCu$_2$O$_2$[104] or CuCl$_2$[105], raised new interest in the family of edge shared chain cuprates and stimulated in many cases a reinvestigation of known compounds. Furthermore, the ground state of PbCuSO$_4$(OH)$_2$ was not yet confirmed by an independent experimental work.

New field dependent thermodynamic measurements [106, 107] for a single crystal suggest a close vicinity of the compound to a QCP. The magnetic susceptibility data show a pronounced maximum at about 5 K, placed even at lower temperatures than the maximum in comparable measurements for Li$_2$ZrCuO$_4$ (compare Fig. 3.16, and Ref. [100]). In addition, specific heat data measured for the same sample in different external fields show a strong field dependence. Whereas the anomaly in C_p at about 2.6 K is suppressed and shifts down with increasing field, the contributions to the heat capacity above 7.5 K grow with increasing external field in close analogy to the field dependence observed for Li$_2$ZrCuO$_4$. Recent NMR and ESR experiments are in line with the magnetic susceptibility data and confirm a T_N of 2.75 K. The evaluation of the Knight-shift as well as the line width broadening in NMR and ESR indicates the onset of magnetic ordering far above T_N suggesting strong frustration and quantum fluctuations [107]. The experimental investigations were impeded by varied impurities occurring in the natural samples. Thus, the present experimental data point to a system close to a QCP while theory places the compound well in the helically ordered phase in a simple $J_1 - J_2$ model (neglecting further exchanges J_3 and J_{ic}) [100]. Therefore, also a theoretical reinvestigation of the compound is of special interest, especially since inter chain couplings could become crucial for this system.

Electronic structure and magnetic model for experimental structures

To gain deeper insight into the magnetism of PbCuSO$_4$(OH)$_2$, we calculated the electronic structure of the compound and developed its magnetic model from a microscopic basis. Especially, the extent of FM contributions to the NN and the influence of chain folding on the NNN exchange were determined using SC calculations.

The atom resolved density of states for S2 is depicted in Fig. 3.16. The valence band shows a width of about 10 eV, slightly broader than in most of the cuprates, while the low lying states between -11 eV and -6 eV are mainly formed by Pb-O and S-O states. Above -6 eV Cu and O states clearly dominate the band structure with an energy difference between the bonding and anti bonding Cu-O $dp\sigma$ states of about 6 eV in perfect agreement with typical edge shared chain cuprates. Furthermore, the anti bonding $dp\sigma$ states, determining the magnetic exchange, are well separated from the rest of the valence band and centered around the Fermi energy ε_F in our LDA calculation. This metallic character of the density of states, in contrast to the insulating behavior of the compound, already suggested from the blue color of the mineral, is a well known short coming of LDA and discussed in detail in Section 2.1.6. Thus, a TB modeling of these anti bonding states will be straight forward. A comparison of the total DOS based on S2 with the total DOS for S1 is given in the inset of Fig. 3.16. Whereas the general structure and shape of the valence band is similar for both structural models, clear differences occur close to the Fermi energy. Since the
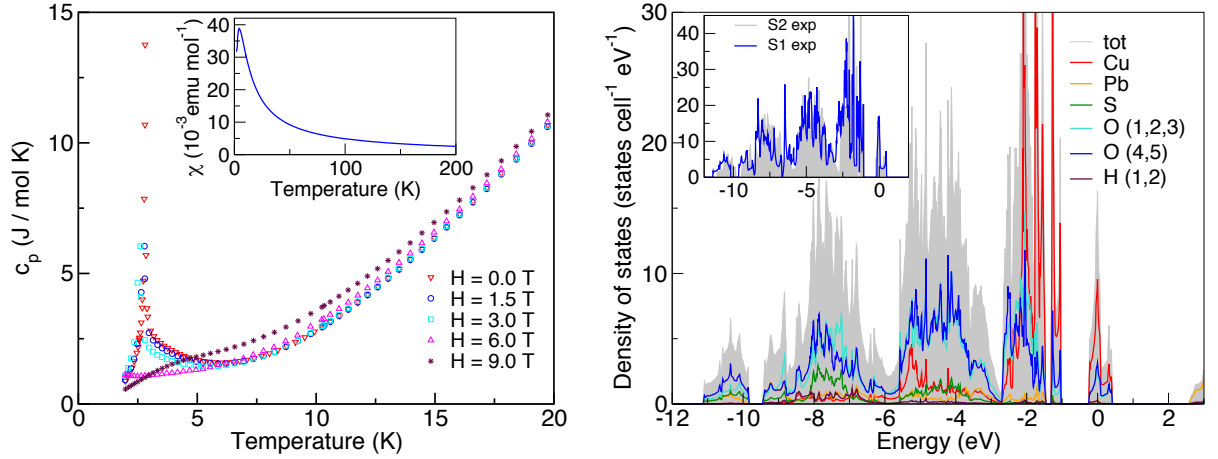
Figure 3.16.: Left: New measurements of the magnetic susceptibility and heat capacity in different fields point to a system in close vicinity to a QCP.[106] Right: Calculated LDA density of states for the experimental crystal structure S2. The anti bonding $dp\sigma$ states are well separated from the rest of the valence band. Inset: Comparison of the total density of states for the experimental crystal structures S1 and S2. The all-over behavior of the valence band is very similar.

magnetic model is determined by the anti bonding $dp\sigma$ states, these states are compared in more detail in the top panel of Fig. 3.16 (left). Besides a downshift of the S2 states by about 0.1 eV compared to S1, the shape of the $dp\sigma$ states shows distinct differences like the double peak structure compared to a single peak in S2 between -0.2 and 0.1 eV. These differences are even better visible in the band structure for both crystal structures depicted in Fig. 3.17, especially close to the Γ or X points and suggest immediately sizable differences in the regime of transfer integrals.

For a qualitative evaluation of these differences, we developed the TB models based on Cu centered WF for S1 and S2. We yield the clear picture of leading transfer integrals t_1 and t_2 along the CuO$_2$ chains for both systems in agreement with the results from Baran *et al.* [100] and the low dimensional behavior of the magnetic susceptibility. The leading exchange paths are illustrated in Fig. 3.18. However, the two systems differ significantly in their inter chain couplings mainly t_0^{ic} (compare Tab. 3.3). Whereas S1 result in $J_0^{ic,S1} = 0.16$ meV applying $J_i = 4t_i^2/U_{\mathrm{eff}}$ and $U_{\mathrm{eff}} = 4$ eV, we obtain a nearly one order of magnitude larger inter chain exchange for S2 with $J_0^{ic,S2} = 1.5$ meV.

To consider the FM contributions, neglected in our effective one band approach, but expected from the crystal structure to the NN and NNN exchange, we performed LSDA+U calculations of SC with different spin arrangements. For S1 we yield $J_1 = -4.5$ meV, $J_2 = 5.4$ meV and a frustration ratio $\alpha^{S1} = -1.2$ (for $U_{3d} = 6$ eV), different from the results of Ref. [100] with $\alpha = -0.5$ based on the same crystal structure but a semi-empirical renormalization to consider the FM contributions. This deviation originates mainly from a much weaker reduction of the NNN exchange in our approach and in consequence a much larger total AFM exchange J_2. On the other hand, our NN exchange J_1 is slightly larger. However, this set of exchange integrals is well inside the helical ordered state and can not explain the strong field dependence of thermodynamic data suggesting a close vicinity to
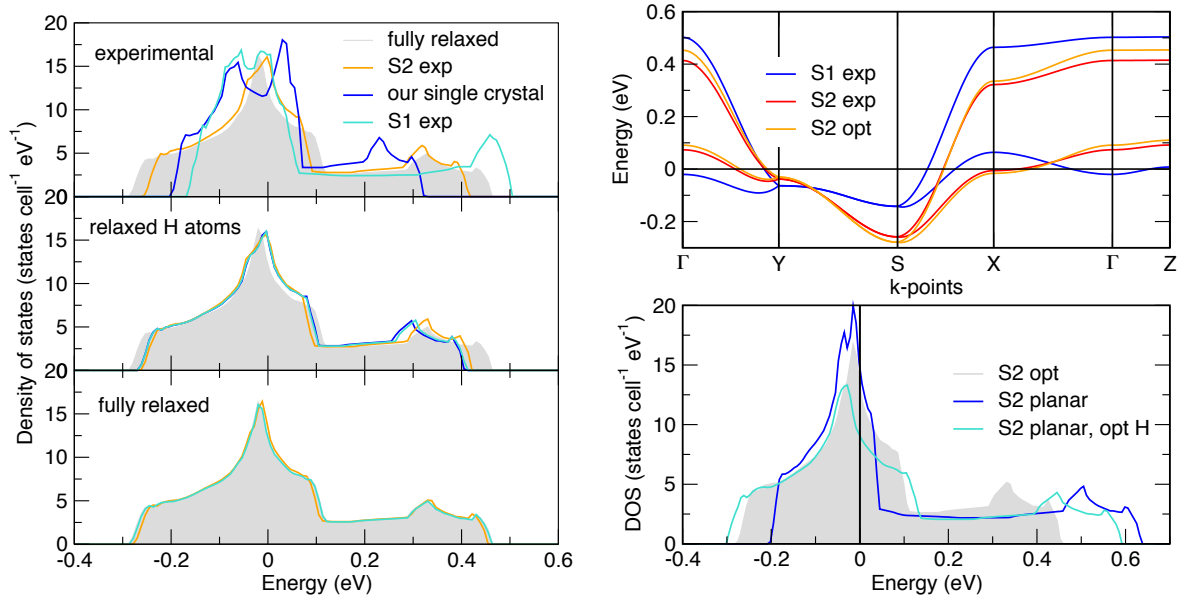
Figure 3.17.: Left: Comparison of the total density of states for the different crystallographic data sets and different relaxation steps. Right: Comparison of the anti bonding $dp\sigma$ bands for the different structural models (top) and influence of chain folding on the $dp\sigma$ states (bottom).

the QCP.

In contrast, S2 yields $J_1 = -13.0\,\text{meV}$, $J_2 = 4.8\,\text{meV}$ and $\alpha^{S2} = -0.37$, much closer to the classical QCP at $\alpha = -0.25$ (with $U_{3d} = 6\,\text{eV}$). The FM contributions to the total exchanges are of the same size as for S1. The comparison of the inter chain exchanges derived from the TB model and the SC calculation show just minor differences confirming no sizable FM contribution to the long range exchanges.

The crucial differences in the frustration ratio for S1 and S2 forces a reinvestigation of the crystal structure as basis for a reliable theoretical description of the compound (compare also App. C.7). A mere comparison of total energies favors the crystal structure S2 from neutron data by $3.6\,\text{eV/cell}$. However, this energetically preference alone is not sufficient as unambiguous criteria to settle the question about the correct crystal structure without an

t_i/meV	t_1	t_2	t_3	t_0^{ic}	t_1^{ic}	t_2^{ic}
S1, exp	104.4	86.9	11.7	12.6	8.3	14.6
S2, exp	70.8	83.6	11.0	39.1	2.4	17.0
S1, relaxed	76.8	90.9	12.2	48.6	2.1	16.2
S2, relaxed	76.2	89.0	11.9	46.0	2.3	16.6
Ref. [100]	130.5	79	9			

Table 3.3.: Calculated transfer integrals derived from a TB fit to the LDA band structure in meV for the experimental crystal structures (exp) and their fully relaxed variants (relaxed) in comparison to the transfer terms reported in Ref. [100].
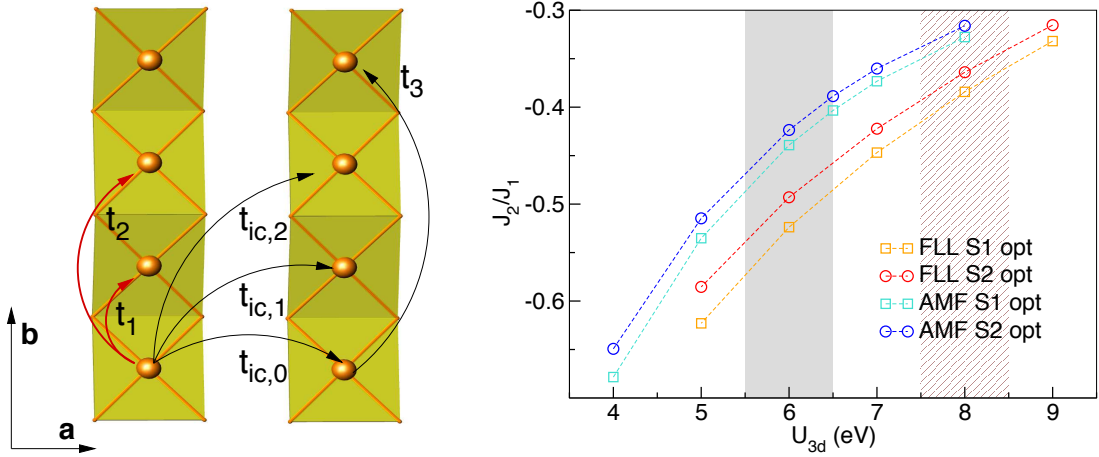
Figure 3.18.: Left: Sketch of leading exchange paths for $PbCuSO_4(OH)_2$ obtained from the
TB model. Right: Influence of U_{3d} on the frustration ratio for the relaxed
crystal structures of S1 and S2 depending on different DCC.

independent support for one of the structural solutions or a detailed analysis of the influence
of structural peculiarities on the magnetic model.[14] Thus, we combined the following
approaches: (i) a theoretical relaxation of the atom sites within the symmetry of the
experimentally determined space group and volume (fixed lattice parameter and monoclinic
angle) by DFT calculations, (ii) single crystal x-ray diffraction measurements and (iii) low
temperature x-ray diffraction measurements using a powder sample to probe the stability
of the crystal structure down to $4.2\,K$ close to the magnetic ordering temperature.

J_i/meV	J_1	J_2	$J_0^{ic} + 2J_2^{ic}$	J_1^{ic}
S1, exp	-4.5	5.4		
S2, exp	-13.0	4.8		
S1, relaxed	-13.0	5.7	1.6	-0.18
S2, relaxed	-13.0	5.5	1.4	-0.17

Table 3.4.: Derived exchange integrals in meV for $U_{3d} = 6\,eV$ from magnetic SC calcula-
tions within the AMF-DCC.

Relaxation and convergency of crystal structures

To tackle the question about the real crystal structure of $PbCuSO_4(OH)_2$ from theory,
we performed a series of calculations relaxing stepwise all atomic sites according to the
symmetry of the space group and with the experimentally determined lattice parameters
starting from the reported crystallographic data from Effenberger *et al.* [102] based on
XRD (S1) and Schofield *et al.* [101] from ND (S2).

---

[14]It could be possible, that both suggested crystal structures are incorrect, and a third structural model
could lead to an even larger energy gain.

The full relaxation of both experimental crystal structures converges into the same solution, where the two H sites are placed close to the experimental refined H sites of S2. This H arrangement, correlated to the folding of CuO_4 chains, is not only more intuitive from structural considerations than the alternating H pattern found from the earlier optimization using the SIESTA package (compare Fig. 3.15), but leads also to an energy gain of almost 4 eV/cell.

The detailed comparison of total energies and the development of the anti bonding Cu-O $dp\sigma$ states for a stepwise relaxation of atoms reveals a crucial influence of the H position on the magnetically active orbitals. The relaxation of H atoms, only, leads to a significant improvement and convergency of the DOS for the different experimental structures, resulting in a nearly identical band shape but a slightly different band width. The total energy for S1 is reduced by 3.9 eV/cell, while the relaxation of H atoms for S2 minimizes the total energy only by 0.12 eV/cell, indicating the close vicinity of the theoretically optimized and experimental refined H sites. The further relaxation of the heavy atoms yield an additional energy gain of about 0.1 eV/cell for S1 and 0.3 eV/cell for S2, respectively and a perfect agreement of the total DOS (compare Fig. 3.16, bottom). Thus, beside the insufficient estimation of the H sites, S1 provides a placement of heavy atoms, namely the relative position of Pb atoms, SO_4 tetrahedra and CuO_4 chains, closer to the theoretically relaxed structure than S2.

Applying the same magnetic SC as before, we obtain a FM-NN exchange $J_1 = -13 \pm 1$ meV, an AFM-NNN exchange $J_2 = 5.5 \pm 1$ meV and $\alpha = -0.4 \pm 0.1$ for the relaxed crystal structure based on $U_{3d} = 6 \pm 0.5$ eV well inside the helically ordered phase. While the choice of the DCC scheme influences the absolute values of the exchange integrals, their ratios remain stable (compare App. C.4 and C.7).

Stability at low temperatures

To ensure that the discrepancies between the experimental data pointing to a close vicinity of the compound to a QCP and the theoretical evaluated magnetic ground state, which places linarite well in the ordered phase (without taking into account strong inter chain frustration), does not originate from a structural phase-transition at low temperatures, we preformed XRD experiments down to 4 K. The measurements were performed at the high resolution beam line ID31 at the ESRF in Grenoble. A comparison of the integrated XRD pattern for the maximal measured temperature difference are depicted in Fig. 3.19. For several reflections a significant splitting is observed (e.g. $2\Theta = 7.5°$ or $10.5°$). These splittings do not indicate a structural phase transition, but rather a separation of peaks consistent with the symmetry of the space group. Thus, down to 4 K the crystal structure of $PbCu_2SO_4(OH)_2$ remains stable regarding our experimental results. A further evaluation of the collected data will not be discussed, since the small changes in the lattice parameter are beyond the reliability of the experiments due to technical problems during the experiment and the quality of the powder sample, which originates from a small pice of the natural mineral (for more details see App. C.6). The refinement of single crystal XRD measurements result in a crystallographic data set (without H sites) close to the data reported by Effenberger *et al.* and agrees well with the theoretically suggested structure.
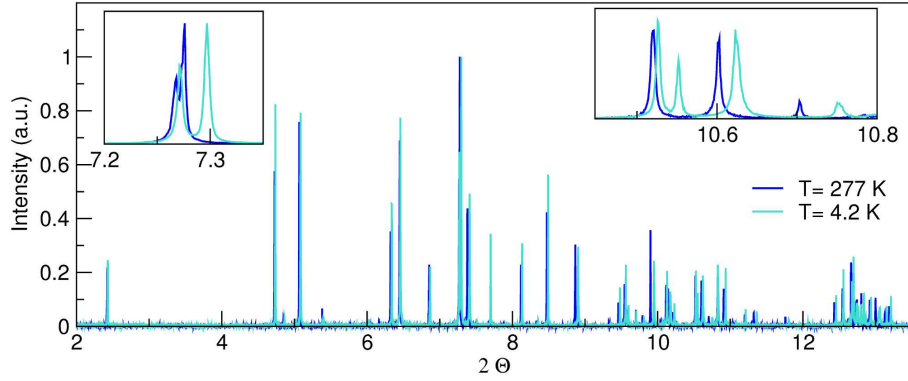
Figure 3.19.: Comparison of the x-ray pattern measured with high resolution for the largest measured temperature difference. The splitting of several peaks, as e.g. observed for the reflection at about $2\Theta = 10.5°$, is not related to a structural phase transition and should be ascribed to the thermal expansion.

Influence of chain folding

To estimate the influence of the chain folding on the magnetic ground state of the system, especially on the NNN exchange, we constructed a fictitious structure containing ideal planar chains and compared its magnetic properties to the real system. The construction of the fictitious $PbCuSO_4(OH)_2$ system was done in two steps. Starting from the fully relaxed structural model S2, the two O sites along the chain are shifted to realize a planar CuO_4 geometry. The new O sites are O(2)(0.2817 1/4 -0.4376) and O(4)(-0.2817 1/4 0.4376). In a second step we optimized the H sites, since the position of H is crucial for the magnetic ground state of linarite as discussed above. The obtained fictitious, planar crystal structure results in a 0.007Å smaller Cu-O distance and a change in the Cu-O-Cu bonding angle by less than 0.5°. The dominant role of the H position in this system is also visible in the comparison of the anti bonding $dp\sigma$ states for the two different construction steps (with and without H relaxation, see Fig. 3.17). The evaluation of the transfer integrals by a fit of the relevant LDA bands using our effective TB model yields $t_1 = 106$ meV and $t_2 = 109$ meV. The long range transfer terms remain nearly unchanged (compare Tab. 3.5). Thus, the folding of CuO_4 chains mainly influences the short range interactions (NN and NNN) as expected. In the fictitious planar geometry t_1 is increased by 30 meV and t_2 by 10 meV, which corresponds to an increase of the AFM contributions by 6 meV and 3 meV for J_1^{AFM} and J_2^{AFM}, respectively. The total exchange integrals estimated from SC calculation for NN and NNN follow a different trend. Whereas the absolute value of J_1 is reduced by 2 meV, the absolute strength of J_2 increases by 3 meV, in accordance with the trend observed in the transfer integrals. In turn, the FM contribution to the total exchange for J_2 is quasi unaffected by the folding of CuO_4 chains, whereas the AFM contribution is sizably suppressed as earlier suggested by Baran *et al.* [100]. For J_1 the chain geometry influences both, FM and AFM contributions, where the change in the FM contribution overcomes the change in the AFM part of the exchange, resulting in a slightly reduced total exchange. Thus, the frustration ratio for the planar structure is enlarged compared to the folded system, driving the system even more away from the classical QCP within a $J_1 - J_2$ model. Thus, $PbCuSO_4(OH)_2$ follows the same trend as Li_2ZrCuO_4 in accordance with

the intuitive picture, that a deviation of the chains from the planar geometry suppresses predominantly J_2 since the orientation of interacting orbitals becomes insufficient.

t_i/meV	t_1	t_2	t_3	t_0^{ic}	t_1^{ic}	t_2^{ic}
S2, relaxed	76	89	12	46	2	17
S2, planar H opt	106	109	14	52	-	10
J_i/meV	J_1	J_2		$J_0^{ic} + 2J_2^{ic}$	J_1^{ic}	
S2, relaxed	-13.0	5.5		1.4	-0.17	
S2, planar H opt	-11.1	8.7		1.7	-0.16	

Table 3.5.: Derived transfer terms from a WF based TB fit on the LDA band structure in comparison to the exchange integrals obtained from magnetic SC calculations.

Summary

We studied the magnetic properties for the natural mineral linarite for the experimental structures reported by Effenberger *et al.* [102] and Schofield *et al.* [101] from a microscopic basis using a combination of band structure and model calculation. Surprisingly, we yield two different sets of exchange integrals placing the system in different regions of the phase diagram. The full relaxation of the atomic sites based on DFT calculation starting from the two experimental crystallographic data sets converge into the same crystal structure. A possible influence of the magnetic ordering on the crystal structure is neglected so far. A full relaxation of the atomic sites including the magnetic order at low temperatures is underway. The comparison of the different structural models reveals that the electronic structure of $PbCuSO_4(OH)_2$ is very sensitive to the exact H position, which in consequence affects the magnetic behavior of the compound. We end up with the picture of a FM NN exchange $J_1 = -13 \pm 1\,\mathrm{meV}$ and an AFM NNN exchange $J_2 = 5.5 \pm 1\,\mathrm{meV}$ for $U_{3d} = 6 \pm 0.5\,\mathrm{eV}$ and small inter chain interactions. The FM contributions were considered explicitly by LSDA+U calculations using magnetic SC, in contrast to the semi-empirical renormalization used by Baran *et al.* [100]. The obtained frustration ratio $\alpha = J_2/J_1 = -0.4 \pm 0.1$ places the system well in the helical ordered phase. Recent thermodynamical data [107] exhibit a typical low dimensional behavior in agreement with our quasi 1D model. The strong field dependence of specific heat, a finger print of the vicinity to a QCP, is most likely driven by the inter layer couplings. A possible structural phase transition as origin for this discrepancy can be excluded down to $4.2\,\mathrm{K}$ by XRD measurements. The influence of the chain folding was studied in detail. In agreement with the trends observed for the related compound Li_2ZrCuO_4, the NNN exchange is suppressed by the deviations from an ideal planar chain geometry, leading to an increase in the absolute value of the frustration ratio. Parts of the section are published in Ref. [107].

3.1.4. CuCl$_2$ and CuBr$_2$ - flipping magnetic orbitals by crystal water

The Cu-halides CuCl$_2$, CuCl$_2$·2H$_2$O, CuBr$_2$, and CuBr$_2$·4H$_2$O are structurally strongly related to the family of cuprates with chains of edge-shared CuO$_4$ units. In these compounds the O atoms of the magnetically active Cu^{2+} plaquettes are exchanged by Cl or Br atoms. The stronger enlargement of the Cl 3p or Br 4p orbitals in the halides compared to the O 2p orbitals in the cuprates causes a significant expansion of the inter atomic distances, however, the local coordination of the Cu^{2+} ions remains very similar. In typical cuprates Cu forms four short Cu-O bonds of about 2.0 Å and two long Cu-O bonds of about 2.5 Å resulting in a distorted octahedral coordination, where the magnetically active orbital is situated in the equatorial plane. In CuCl$_2$, the Cu-Cl distances scale to 2.26 Å (4×) and 2.96 Å (2×), whereas in CuBr$_2$ Cu-Br bond distances of 2.41 Å (4×) and 3.15 Å (2×) are found. This preserved fourfold planar Cu^{2+} coordination suggests a strong analogy of the magnetic exchange mechanism in the halides to the undoped cuprates.

CuCl$_2$ and CuBr$_2$ consist in covalent networks of edge shared CuCl$_4$ plaquettes or CuBr$_4$ plaquettes, respectively. In CuCl$_2$ and CuBr$_2$, the bridging angle along the edge-shared chains between the magnetically active Cu^{2+} and the ligands is 93.6° and 92.0°, respectively and thus very similar to that in the CuO$_2$ chain cuprates. In this family bond angles close to 90° result in FM NN exchange in accordance with the GKA rules. Examples are LiCu$_2$O$_2$ [74, 108, 75] or Li$_2$ZrCuO$_4$ [79] (compare Sec. 3.1.2).

Since in CuCl$_2$ and CuBr$_2$ the chains are arranged in layers similar to the crystal structure of Li$_2$ZrCuO$_4$ and LiCu$_2$O$_2$, a rather weak magnetic exchange between the layers is expected. Even the arrangement of the chains within the layers is very similar. Thus, a quasi 1D behavior might be expected from a mere comparison with these cuprate crystal structures.

Similar to the strong relation of CuCl$_2$ and CuBr$_2$ to the family of edge shared chain cuprates and the strategy to develop the magnetic model for this compounds by a comparison to well known systems, an analog approach may work for the development of the magnetic ground state model for the hydrated compounds CuCl$_2$·2H$_2$O and CuBr$_2$·4H$_2$O. In particular, for compounds that contain crystal water in different amounts, it is a widespread strategy to develop the magnetic model for hydrated variants by transferring the known parameters from related, similar systems in a slightly renormalized form according to the changed distances and/or bond angles.

Although in some cases the topology of the magnetic ion network and the related magnetic properties totally change upon dehydration, like in the case of CuSiO$_3$·H$_2$O [10, 109] and CuSiO$_3$ [48, 110], for most compounds only moderate structural changes with respect to the magnetic network are observed. It is generally assumed that in this case crystal water leads mainly to a modest change of the crystal field for the magnetic ion. In turn, small changes in the crystal field only, would directly suggest a description within the same model with slightly revised parameters [111]. This leads to the common believe that crystal water only plays a minor role regarding the magnetic properties for compounds where the crystal structure is basically preserved upon water intercalation.

Here, in contrast, we show that the hydration of CuCl$_2$ to CuCl$_2$·2H$_2$O fundamentally changes the magnetic properties, although the topology of the covalent Cu-Cl network is seemingly unchanged. Whereas CuCl$_2$·2H$_2$O is a classical three-dimensional (3D) anti ferromagnet (AFM), we establish the dehydrated species as an example for a quasi 1D chain compound with FM nearest neighbor (NN) exchange J_1 and AFM next-nearest neighbor (NNN) exchange J_2. This result can be consistently understood from a reorientation of

the magnetically active Cu orbital driven by the hydration. Earlier studies,[112, 113] that tried to model $CuCl_2$ as a spin 1/2 chain found considerable deviations from a 1D behavior since in these investigations only a NN AFM coupling was considered. A similar scenario is also observed in $CuBr_2$ and its hydrated variant $CuBr_2 \cdot 4H_2O$. The additional crystal water expands the crystal structure even more than in the case of $CuCl_2$. However, the dramatic change of the coupling regime follows the same mechanism.
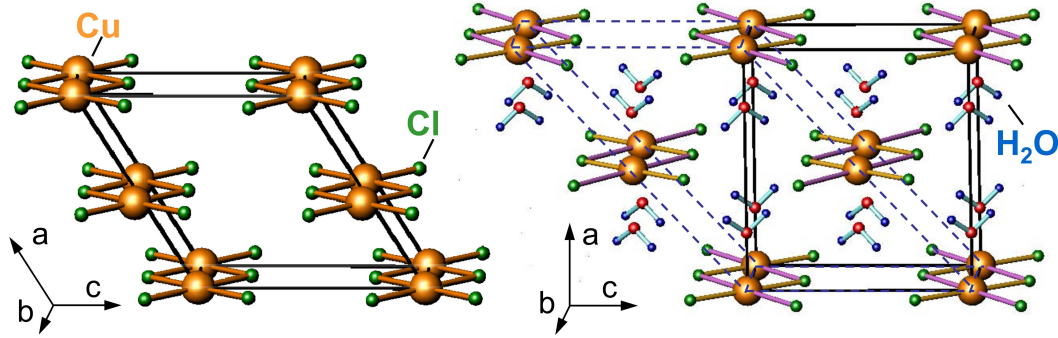
Figure 3.20.: Crystal structure of $CuCl_2$ (left) and $CuCl_2 \cdot 2H_2O$ (right). The crystal water is intercalated between the $CuCl_2$ layers. The dashed line in the $CuCl_2 \cdot 2H_2O$ structure marks the unit cell of the water free $CuCl_2$.

$CuCl_2$ and $CuCl_2 \cdot 2H_2O$

The crystal structure of $CuCl_2$ is presented in Fig. 3.20. Cu and Cl form a covalent network of edge shared $CuCl_4$ plaquettes running along the crystallographic b direction.

When $CuCl_2$ is exposed to moisture, H_2O enters the space between the chain layers, finally forming the fully hydrated $CuCl_2 \cdot 2H_2O$ (Fig. 3.20, right). Although the crystal structure seems very similar at a first glance, the crystal water induces several changes: (i) The interlayer distance increases, (ii) the $CuCl_2$ chains shift with respect to each other and, (iii) the Cu-Cl distances within the chains are modified. Whereas the structural changes can be easily understood by packing and electrostatics (negatively polarized O^{2-} is situated close to the Cu^{2+} ions, H^+ is attracted by Cl^-), the origin of the drastic change of magnetic properties – 1D versus 3D – is far from obvious.

However, a rough evaluation of the thermodynamical data for $CuCl_2$ and $CuCl_2 \cdot 2H_2O$ and a mere comparison of the single crystals indicate immediately the different character of the two compounds. In Fig. 3.21 pictures of small sample pieces for the hydrated and dehydrated variant, which differ already in color and morphology, are shown together with the results of the magnetic susceptibility measurements. (Details about synthesis, characterization and thermodynamic measurements are given in the Appendix A)

The magnetic susceptibility of $CuCl_2$ exhibits a broad maximum at $T_{max} \approx 75$ K as a fingerprint of quasi 1D behavior. The absence of an impurity related Curie tail at low temperatures indicates the high quality of the sample. An AFM Curie-Weiss temperature $\Theta_{CW} = 107$ K has been extracted from the high temperature region. A sharp kink at $T_N = 24$ K (see Fig. 3.21 and inset $d\chi/dT$) followed by a rapid drop of χ indicates a magnetic phase transition as earlier suggested [112] and confirmed by specific heat data (see Ref. [114]).
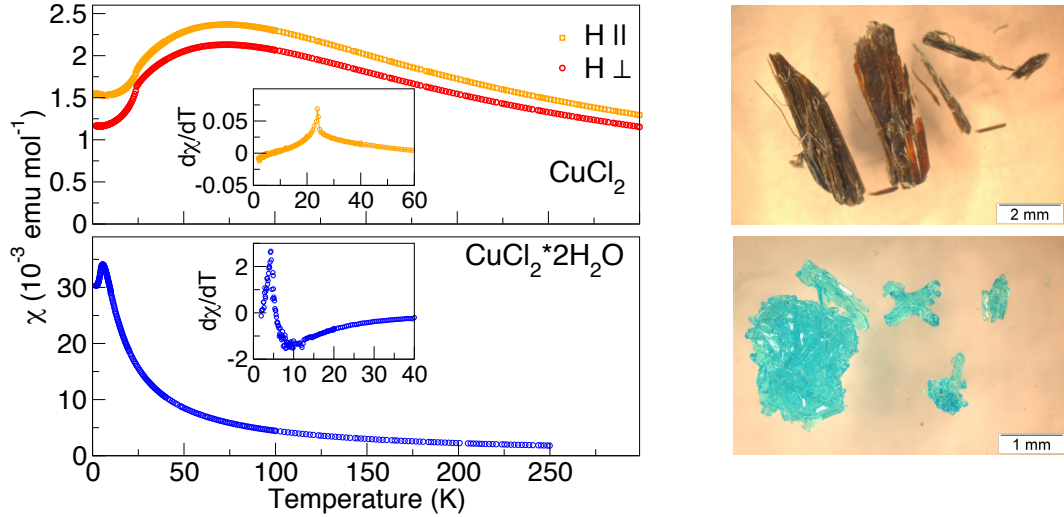
Figure 3.21.: Left: Magnetic susceptibility for single crystal $CuCl_2$ (top) and $CuCl_2 \cdot 2H_2O$ (bottom) powder. While $CuCl_2$ shows a typical low dimensional behavior, $CuCl_2 \cdot 2H_2O$ is a classical three dimensional system. The sharp peaks in the derivatives (insets) indicate the ordering temperatures. Picture according to Ref. [114]. Right: The small sample pieces differ already in color and shape ($CuCl_2$, top; $CuCl_2 \cdot 2H_2O$, bottom).

In contrast to the quasi 1D susceptibility of $CuCl_2$, the hydrated system shows an increasing susceptibility down to low temperatures right above the AFM phase transition at $4.3\,\mathrm{K}$, in perfect agreement with earlier measurements [115, 116]. A Curie-Weiss temperature $\Theta_{CW} = 5.3\,\mathrm{K}$ has been evaluated indicating weak AFM interactions.

The essentially different character of the susceptibility of both compounds points to a changed regime of exchange couplings rather than to a mere re-scaling according to the modified atomic distances. To construct an appropriate microscopic model based on the relevant interactions we perform *ab-initio* electronic structure calculations, as successfully demonstrated earlier for the closely related CuO_2 chain compound family.

The total and atom resolved LDA densities of states (DOS) for both compounds are depicted in Fig. 3.22. On a coarse energy scale both systems are similar, the contribution of the additional H states to the valence region is negligible. Both compounds show half-filled, well separated anti-bonding bands at the Fermi level. This metallic character is a well known shortcoming of the LDA and is described in detail in Sec. 2.1.6.

A closer inspection of the DOS and the related band structure reveals two important differences: (i) Whereas the width of the anti-bonding band in $CuCl_2$ is $0.8\,\mathrm{eV}$ – rather typical for 1D edge-shared CuO_2 chains [15] – the bandwidth in $CuCl_2 \cdot 2H_2O$ is reduced by more than a factor of three to about $0.25\,\mathrm{eV}$ (compare Fig. 3.22). (ii) The magnetically active anti-bonding band in $CuCl_2$ is formed exclusively by Cu-Cl $dp\sigma$ states corresponding to the bonds pictured in Fig. 3.20. In contrast, for $CuCl_2 \cdot 2H_2O$ the O $2p$ orbitals that are directed towards the Cu contribute significantly to this band. This leads to the formation of a new $dp\sigma$ orbital perpendicular to the original ones. The related $CuCl_4$ or $CuCl_2O_2$

---

[15]For comparison, $CuGeO_3$ shows a bandwidth of $0.95\,\mathrm{eV}$ for the anti-bonding band, $CuSiO_3$ about $0.65\,\mathrm{eV}$ and $LiCuVO_4$ about $0.7\,\mathrm{eV}$.
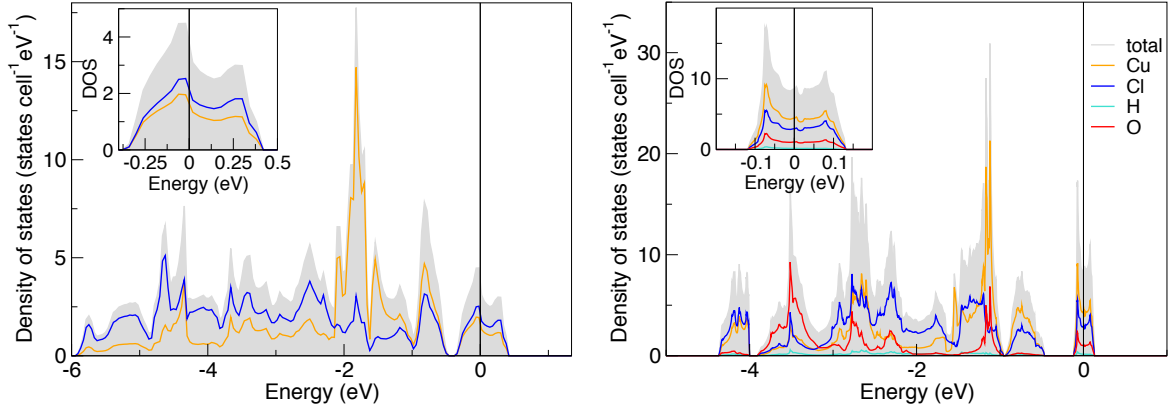
Figure 3.22.: Calculated atom resolved density of states for $CuCl_2$ (left) and $CuCl_2 \cdot 2H_2O$ (right). The width of the antibonding Cu-O $dp\sigma$ states differ considerable for the two compounds. O from the crystal water contribute to these states in the case of $CuCl_2 \cdot 2H_2O$.

plaquettes are shown in Fig. 3.24. These plaquettes, relevant for the magnetic couplings, form edge-shared chains in $CuCl_2$, whereas they are disconnected in the hydrated system.
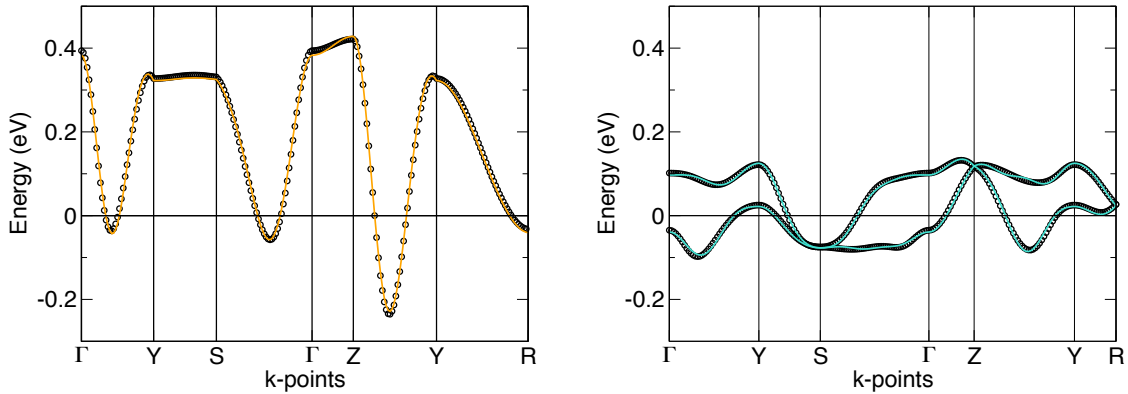

Figure 3.23.: LDA band structure (black circles) and derived TB fits (solid lines) for $CuCl_2$ (left) and $CuCl_2 \cdot 2H_2O$ (right). While $CuCl_2$ shows large dispersion along the chain direction, the dispersion is reduced and more three dimensional for $CuCl_2 \cdot 2H_2O$. The two bands for $CuCl_2 \cdot 2H_2O$ originate from the two Cu atoms per primitive cell.

Naturally, this "orbital switching" induced by the crystal water implies a change of the coupling regime from 1D to 3D. To study these changes on a quantitative level, we constructed a TB model (for the main transfer path see App. C.9) for both compounds and fitted it to the relevant LDA bands (Fig. 3.23). The leading transfer integrals t_i are given in Table 3.6. The calculated t_i confirm the intuitive picture that corresponds to Fig. 3.24: $CuCl_2$ shows quasi 1D dispersion along the chain with dominating NNN hopping t_2, and a considerably weaker coupling between the chains, while the coupling between adjacent layers is very small. On the other hand, the changed plaquette arrangement in $CuCl_2 \cdot 2H_2O$,

t_i/meV	t_1	t_2	t_1^{ic}	t_2^{ic}	t_1^{il}
$CuCl_2$	34	117	61	-19	8
$CuCl_2 \cdot 2H_2O$	17	6	4	16	20

Table 3.6.: Calculated leading hopping integrals t_i for the effective TB model. The related transfer paths are shown in App. C.9. Whereas in $CuCl_2$ the transfer terms along the chain direction dominate, $CuCl_2 \cdot 2H_2O$ exhibits strongly reduced terms.

induced by the crystal water, leads to a strongly reduced band width and correspondingly small isotropic (3D) transfer integrals (Table 3.6).

Mapping the effective TB model via a Hubbard model onto a Heisenberg model, as described before, leads to the AFM exchange constants $J_i = 3 - 5$ K for the three leading couplings in $CuCl_2 \cdot 2H_2O$ based on the reasonable range of $U_{\text{eff}} = 3.5 - 4$ eV.[16] These J's are perfectly in line with the experimentally observed $T_N = 4.3$ K as could be expected for an almost isotropic 3D coupling.

For $CuCl_2$, the leading NNN t_2 results in $J_2^{AFM} = 160 - 180$ K. Although of the correct order of magnitude compared to T_{max} and Θ_{CW}, this would clearly exceed the "overall AFM coupling" in the compound without additional FM interactions. Since sizable FM contributions to the NN exchange are expected from the close to 90° angle along the edge shared chains, we apply LSDA+U calculations for different spin arrangements in magnetic super cells (SC) for a quantitative estimate of the FM contributions to the leading J's.

Mapping the resulting total energy differences to the Heisenberg model, we obtain the following total exchange integrals for $U_{3d} = 7 \pm 0.5$: $J_1 = -(150 \pm 10)$ K, $J_2 = 155 \pm 25$ K and $J_1^{ic} = 35 \pm 5$ K. Within the error bars, the latter two agree very well with the J values calculated from the corresponding t's of the TB approach,[17] indicating that FM contributions beyond NN are rather small. In contrast, we find a large FM contribution of about 175 K to J_1 as expected from the Cu-Cl-Cu bond angle of 93.6°. The size of the FM contribution to J_1 fits well to related edge-shared CuO_2 chain compounds.

The obtained leading exchange interactions confirm the intuitive picture of a quasi 1D chain model compound with small inter-chain coupling, very similar to $LiCu_2O_2$ [74, 108, 75]. Therefore, the magnetic ground state is mainly determined by the ratio $\alpha = J_2/J_1$ of the frustrating main interactions along the chains. For $CuCl_2$, we find $\alpha = -(1.0 \pm 0.1)$ and predict a ground state well in the helical ordered region of the J_1–J_2-phase diagram.

For an independent evaluation of the leading exchange interactions the magnetic susceptibility $\chi(T)$ was simulated within a spin-1/2 J_1–J_2 Heisenberg model for various J_2/J_1 ratios, using the transfer-matrix density-matrix renormalization-group and exact diagonalization techniques. Rather typical for the J_1–J_2 Heisenberg model [108, 75], two possible solutions were obtained: an (i) AFM-AFM solution ($\alpha = +3.0$ with $J_1 = 120$ K and $J_2 = 40$ K) and a (ii) FM-AFM solution ($\alpha = -1.5$ with $J_1 = -90$ K and $J_2 = 135$ K). The FM-AFM solution (ii) is in rather good agreement with our DFT results, while the AFM-AFM solution (i) can be disregarded due to the close to 90° Cu-Cl-Cu bond angle. In

---

[16]$U_{\text{eff,Cl}} < U_{\text{eff,O}}$ as effective Cu-Cl orbitals are stronger expanded in space.
[17]This good agreement justifies *a posteriori* the transfer of the U_{eff} and U_{3d} values from the CuO_2 chain compounds.
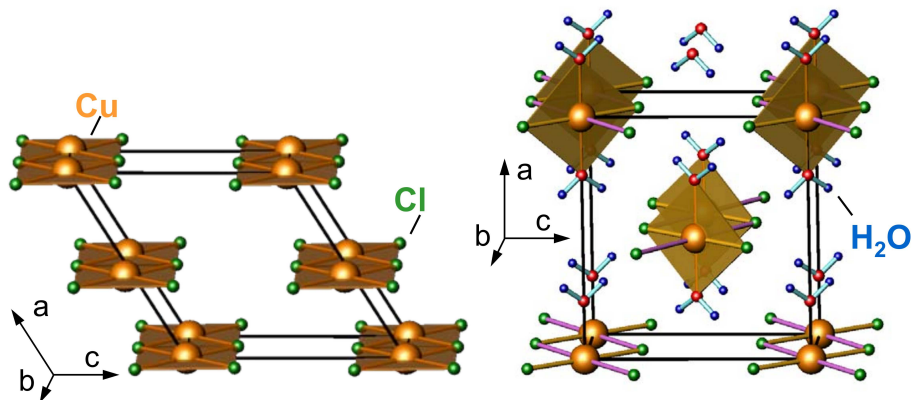
Figure 3.24.: Sketch of the magnetically active $pd\sigma$ plaquettes for $CuCl_2$ (left) and $CuCl_2 \cdot 2H_2O$ (right). Whereas these orbitals form quasi 1D edge shared chains in $CuCl_2$, the plaquettes in $CuCl_2 \cdot 2H_2O$ are isolated resulting in weak, but 3D interaction.

addition, a recent study based on neutron scattering, thermodynamic measurements and DFT calculations confirmed the helical ordered state for $CuCl_2$.[117]

The dramatic effect of the dehydration of $CuCl_2 \cdot 2H_2O$ certainly raises the question whether this is really a typical dehydration process or if the involvement of the crystal water related oxygen in the magnetic exchange via covalent Cu-O bonds is an indication for a chemical reaction on a different energy scale. The experimentally determined dehydration enthalpy $\Delta H^0_{\text{dehyd.}} = 117\,\text{kJ/mol}$ of $CuCl_2 \cdot 2H_2O$ is a typical (small) value for this class of materials [118, 119]. Our *ab-initio* estimate for the dehydration enthalpy yields $\Delta H^0_{\text{dehyd.}} = 95\,\text{kJ/mol}$ which is in quite good agreement with the measured value, provides additional confidence to the reliability of the calculational procedure.

$CuBr_2$ and $CuBr_2 \cdot 4H_2O$

The compound $CuBr_2$ crystallizes in close analogy to $CuCl_2$ forming edge-shared $CuBr_4$ chains along the y-direction with an about 2° smaller Cu-Br-Cu bonding angle along the chains. Due to the larger ionic radius of Br compared to Cl the Cu-Br bonding distances are enlarged to 2.96Å compared to 2.41Å for Cu-Cl in $CuCl_2$, which in consequence results in larger lattice parameters. The more extended character of Br suggests stronger inter-chain exchanges already from structural considerations.

Under hydration $CuBr_2$ absorbs four molecules crystal water per unit cell forming $CuBr_2 \cdot 4H_2O$. As in $CuCl_2$, the crystal water intercalates between the chain layers causing similar changes of the crystal structure. In particular (i) the inter layer distance is expanded significantly by the double layer of H_2O molecules, (ii) the $CuBr_4$ chains shift against each other and (iii) the Cu-Br bond distances are modulated along the chains. Since the exact determination of the position of H atoms (in vicinity to Br) from XRD is rather challenging and the experimental crystal structure prevents unusual short O-H distances, we relaxed the atomic sites of H with respect to the total energy starting from the experimental data set. Our calculations converge into a structure with typical inter atomic distances, namely Cu-O =2.03 Å, Cu-Br= 2.38 Å / 2.98 Å, O-H$_{mol.}$=1.0 Å within the water molecule and typical the

O-H distances for the hydrogen bridges of O-H$_{hb}$=1.66Å. The change in the local Cu coordination under hydration is comparable to the changes in the Cl compound. CuBr$_2$·4H$_2$O forms two short and two elongated Cu-Br bonds and a new covalent Cu-O bond. Thus, half of the crystal water binds covalent to the Cu^{2+} as observed in CuCl$_2$·2H$_2$O, while the remaining crystal water molecules are placed in between the former chain layers (compare Fig. 3.25). The strong analogy of the crystal structure of Br compounds to the Cl variants suggests a similar mechanism under hydration and a dramatic change of the magnetic properties by the switching of magnetic active orbitals.
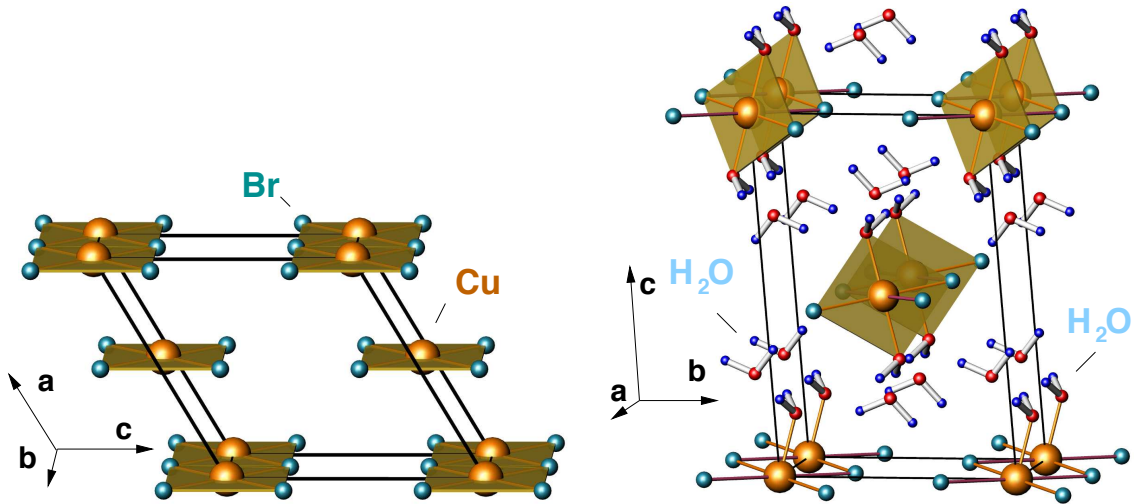
Figure 3.25.: Crystal structure of CuBr$_2$ (left) and CuBr$_2$·4H$_2$O (right). The water intercalation changes the local Cu environment and results in a flipping of magnetic active orbitals in analogy to the hydration of CuCl$_2$.

Already the mere comparison of the total density of states, depicted in Fig. 3.26, reveals strong similarities in the electronic structure between the two halides. The valence band of CuBr$_2$ shows a very similar shape compared to CuCl$_2$ with an about 0.5 eV smaller valence band width. The anti bonding $dp\sigma$ states are slightly broadened ($w \sim 0.9$ eV) and formed by Br and Cu states. When moisture enters the compound the valence band changes its shape significantly. We found a much more structured density of states from strongly narrowed bands, where the width of the anti bonding $dp\sigma$ states is drastically reduced by nearly a factor of four ($w \sim 0.25$ eV). The atom resolved density of states exhibits strong contributions from O(1) (covalent bonded H$_2$O) to the anti bonding $dp\sigma$ states and support the picture of orbital switching. The evaluation of the orbital resolved density of states (not shown) confirms the formation of the new magnetically active orbitals CuBr$_2$O$_2$ perpendicular to the CuBr$_4$ plaquettes in CuBr$_2$. Thus, the system changes from an edge shared chain system into a 3D network of isolated plaquettes. Contributions from the interlayer H$_2$O can be neglected close to the Fermi energy ε_F.

The drastic change of the system under hydration affects also the band structures. Beside the strong reduction of the band width, already observed in the density of states, the system changes its character from a quasi 1D behavior to a 3D coupled system. The pronounced dispersion along the CuBr$_4$ chain direction with flat bands between the chain layers is strongly suppressed and changed into weak, but comparable dispersion along all
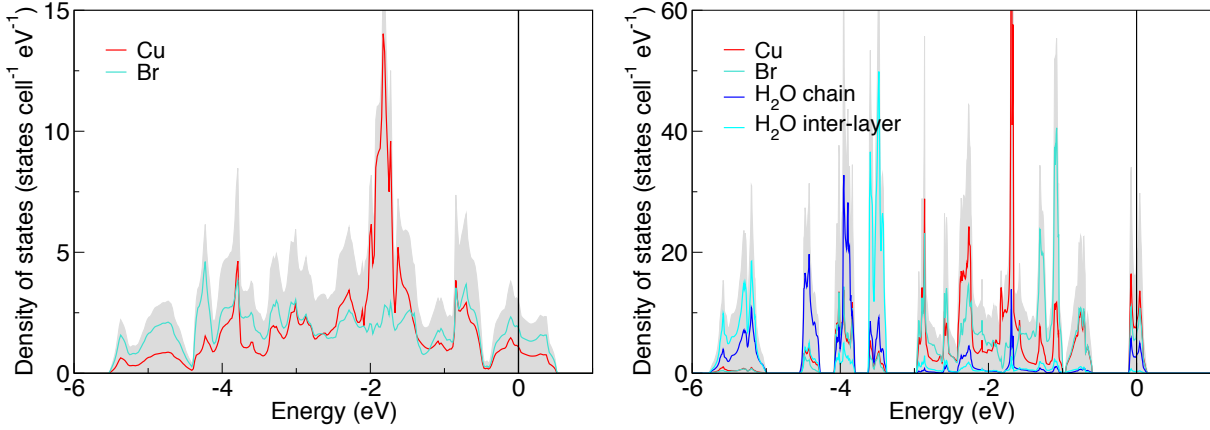
Figure 3.26.: LDA density of states for $CuBr_2$ (left) and $CuBr_2 \cdot 4H_2O$ (right). The width of the anti bonding $dp\sigma$ states changes dramatically under hydration. For $CuBr_2 \cdot 4H_2O$ states from the covalently bonded H_2O contribute to these states, while states from the inter layer H_2O can be neglected.

crystallographic directions. The change is directly reflected in the transfer integrals of the two compounds derived from the fit of an effective TB model onto the relevant bands. The obtained transfer integrals are listed in Tab. 3.7. For $CuBr_2$ the leading hopping term t_2 appears along the chain direction together with a sizable inter chain hopping between the chains t_0^{ic}. For $CuBr_2 \cdot 4H_2O$ the transfer integrals are strongly suppressed, in line with the quasi isotropic and reduced band width. The leading term t_1^{ic} is smaller by more than factor of three compared to the leading hopping term t_2 in $CuBr_2$, which corresponds to a factor of ten in the AFM part of the exchange integrals regarding $J^{AFM} \sim 4t^2/U_{eff}$. Mapping the effective TB model via a Hubbard model onto a Heisenberg model leads to the AFM exchange integrals. For $CuBr_2 \cdot 4H_2O$ we obtain $J_1^{ic} = 25 - 21\,\mathrm{K}$ for the leading exchange integral in the physical relevant range of $U_{eff} = 3 - 3.5\,\mathrm{eV}$. The 3D character of the coupling regime can be understood from the orientation of magnetically active orbitals and of the H_2O molecules.

For $CuBr_2$ we obtain an AFM contributions to the exchange integrals of $J_2^{AFM} = 250 - 290\,\mathrm{K}$ and $J_0^{ic} = 77 - 90\,\mathrm{K}$. The NN exchange J_1 is determined by the competition of FM and AFM contributions, expected from the vicinity of the Cu-O-Cu bonding angle along the chains to 90° in $CuBr_2$. Therefore, an estimation of J_1 from the TB model only will not resemble the physical picture of the NN exchange. To consider FM contributions to the exchange integrals, we performed LSDA+U calculations of magnetic SC. The comparison of the total energies for different collinear spin arrangements and the subsequent mapping onto a related Heisenberg model yields $J_1 = -110 \pm 6\,\mathrm{K}$, $J_2 = 350 \pm 11\,\mathrm{K}$, $J_{ic} = 140 \pm 50\,\mathrm{K}$ and $\alpha = -3$ for $U_{3d} = 6 \pm 1\,\mathrm{eV}$, placing the system well in the helical ordered phase.[18] Next to the magnetic interactions along the structural chains, $CuBr_2$ shows a sizable inter chain exchange within the chain plane. The increase of the magnetic interaction between the chains is in line with the stronger expansion of Br orbitals compared to Cl.

Since $CuBr_2 \cdot 4H_2O$ contains two types of crystal water, the (i) H_2O molecules intercalated

---

[18]The reduced effective correlation $U_{eff} = 3 - 3.5\,\mathrm{eV}$ suggested by the expansion of Br orbitals is justified by the good agreement between TB and LDA+U results.
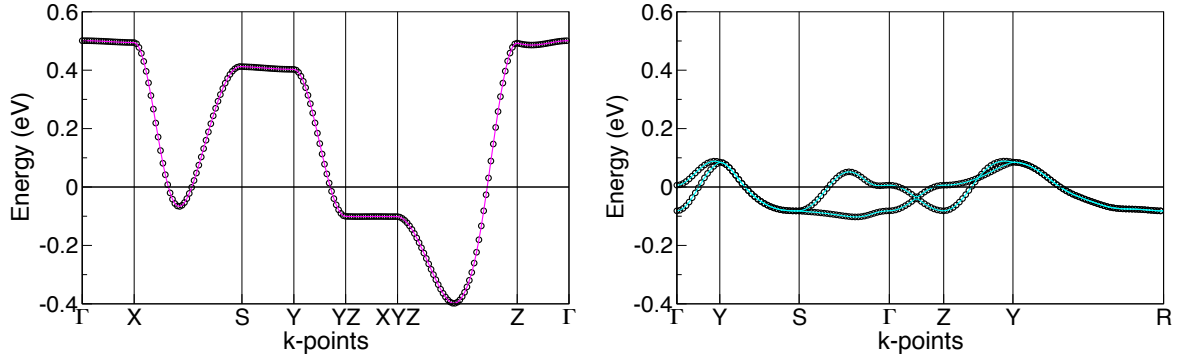
Figure 3.27.: Comparison of the band structure for $CuBr_2$ (left) and $CuBr_2 \cdot 4H_2O$ (right). The hydration lead to a strong reduction of the band width and a change from a quasi 1D behavior to isotropic 3D dispersion.

t_i/meV	t_1	t_2	t_3	t_0^{ic}	t_1^{ic}	t_0^{il}	t_1^{il}
$CuBr_2$	47	136	34	76	29	10	5
$CuBr_2 \cdot 4H_2O$	-	11	-	11	39	-	9

Table 3.7.: Calculated leading hopping integrals t_i for the effective TB model.

between the chain layers and (ii) H_2O, which binds covalently to Cu forming new $CuBr_2O_2$ plaquettes, the evaluation of the dehydration enthalpy of this system allows an estimate of the energy scale for the dehydration process, independent from the type of crystal water. The calculations yields $\Delta H_{\text{dehyd.}}^0 = 208 \, \text{kJ/mol}$ for four H_2O, in perfect agreement with the energy scale of dehydration enthalpy of $CuCl_2$ with 96 kJ/mol for two H_2O. Furthermore, the system enables us to separate the enthalpy contribution for the different types of crystal water for a direct comparison of their energy scale.

Unfortunately, the hydrated variant $CuBr_2 \cdot 2H_2O$ is not observed experimentally. Thus, an fictitious system was constructed by removing the inter layer H_2O in $CuBr_2 \cdot 4H_2O$ and optimized the crystal structure with respect to the total energy. In our calculations we follow two optimization strategies: (i) an optimization of the unit cell volume and a subsequent relaxation of atomic sites and (ii) a relaxation of atomic sites followed by the optimization of the unit cell volume. The resulting crystal structures are slightly different after the first iteration step[19]. Nevertheless, the present accuracy is sufficient for a rough estimate of the energy scales related to the dehydration processes.

The optimization of the fictitious crystal structure of $CuBr_2 \cdot 2H_2O$ results not only in a scaling of inter atomic distances within the symmetry of $CuBr_2 \cdot 4H_2O$, but causes a relative change of the inter atomic arrangement, in particular a rotation of the $CuBr_2O_2$ plaquettes (compare Fig. 3.28). This rotation of the $CuBr_2O_2$ units, which can be understood in terms of electrostatics, leads to an energy gain of 1.7 eV/(f.u.) and a significant change in the DOS (see App. C.9).

This structural change for $CuBr_2 \cdot 2H_2O$ impedes the separation of dehydration enthalpy

---

[19]Further iteration steps for a fully converged crystal structure are planed in our ongoing study.
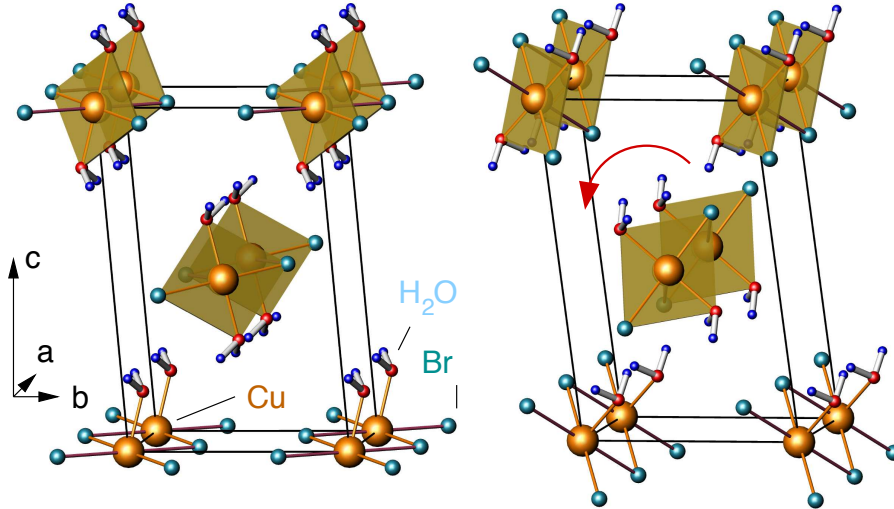
Figure 3.28.: Construction of the fictitious crystal structure of $CuBr_2 \cdot 2H_2O$. The relaxation of O, Br and H atoms leads to a rotation of the $CuBr_2O_2$ plaquettes.

for the two types of crystal water, but at the same time elucidate, why the $CuBr_2 \cdot 2H_2O$ variant is not observed experimentally. The stepwise evaluation of the dehydration enthalpy (following (i) and (ii)) requires the rotation of the $CuBr_2O_2$ plaquettes as crucial precondition for the formation of the $CuBr_2 \cdot 2H_2O$ phase. However, the calculated enthalpy is very small (42kJ/mol per two H_2O) and not sufficient for a stabilization of the phase for macroscopic time scales. Following the energy balance between the different phases

$$CuBr_2 \cdot 2H_2O \rightleftharpoons 1/2(CuBr_2) + 1/2(CuBr_2 \cdot 4H_2O)$$

$CuBr_2 \cdot 2H_2O$ decomposes into $CuBr_2$ and $CuBr_2 \cdot 4H_2O$. The estimated enthalpy for the phase separation is 63kJ/mol corresponding to two H_2O molecules.

Summary

We studied the magnetic ground state of the Cu^{2+} halides $CuCl_2$ and $CuBr_2$ in comparison to their hydrated variants. Our study provides a consistent explanation for the fundamentally different magnetic properties of $CuCl_2 \cdot 2H_2O$ and $CuCl_2$ as well as $CuBr_2 \cdot 4H_2O$ and $CuBr_2$, respectively.

Whereas $CuCl_2 \cdot 2H_2O$ is a quite isotropic 3D AFM with small exchange couplings due to the orientation of neighboring isolated $CuCl_2O_2$ plaquettes, $CuCl_2$ can be well understood in terms of a 1D FM-AFM J_1–J_2 chain model. This extension of the original critically discussed 1D AFM-NN only model [112] re-establishes the pronounced 1D nature of the magnetism in $CuCl_2$. The dramatic change of magnetic properties between both compounds can be traced back to a switching of the magnetically active orbital induced by crystal water. From our combined electronic structure and model calculation we predict a helical ground state and possibly multiferroic behavior for $CuCl_2$ driven by strong in-chain frustration originating from FM nearest neighbor and AFM next-nearest neighbor exchange interactions. This prediction is supported by the results of QMC simulations of the experimental susceptibility. The helical ground state of $CuCl_2$ and the appearance of

multiferroic behavior was recently confirmed by independent studies.[117, 105]

The magnetic properties of the related compounds $CuBr_2$ and $CuBr_2 \cdot 4H_2O$ can be understood in close analogy to the Cl compounds. The edge shared chain compound $CuBr_2$ can be described by a 1D FM-AFM J_1–J_2 chain model with a rather strong inter-chain coupling compared to $CuCl_2$ (due to the larger extension of the Br $4p$ orbitals). For the hydrated variant $CuBr_2 \cdot 4H_2O$, which contains covalently bonded H_2O molecules as observed in $CuCl_2 \cdot 2H_2O$, and H_2O molecules intercalated between the layers, the magnetic properties change totally, resulting in a weakly coupled 3D AFM. This significant difference of the magnetic ground state originates in a flip of the magnetically active orbitals similar to the effect in the Cl compounds. A detailed evaluation of hydration enthalpies implies the instability of $CuBr_2 \cdot 2H_2O$ with respect to a disproportionation reaction into $CuBr_2$ and $CuBr_2 \cdot 4H_2O$.

Our study reveals that crystal water can have crucial influence on the electronic and magnetic properties of low dimensional magnets. More general, our work emphasis that a transfer of model parameters from seemingly closely related systems is rather dangerous. The unaware neglect of this fact will lead to an - at best - inaccurate description of the physical properties in many cases. Parts of the section are published in Ref. [114].

3.1.5. Na$_3$Cu$_2$SbO$_6$ and Na$_2$Cu$_2$TeO$_6$ - alternating chain systems

Closely related to systems with edge shared chains are materials containing structural dimer chains formed by Cu$_2$O$_6$ units. These crystal structures often stabilize alternating chains or magnetic dimer states at low temperatures with a characteristic spin gap behavior. Based on simple structural consideration the alternating chain model $J_{1a} - J_{1b}$ usually provides a natural opportunity to describe the magnetic ground state of such compounds following the alteration in the crystal structure. For the limiting case $J_{1a} \gg J_{1b}$ the alternating chain model converges into the dimer model. However, the microscopic analysis of the coupling regime for such systems revealed in several cases, that the structural and magnetic dimers do not coincide, since the AFM coupling within the structural dimers is compensated by sizable FM contributions. The recently studied compound Na$_3$Cu$_2$SbO$_6$ [120] contains such structural dimer chains and shows a pronounced spin gap behavior at low temperatures. The alternating chain model is suggested by several independent studies, but the ratio and nature of the alternating couplings is still under debate demonstrating the difficulty to establish reliable models for new compounds.[4, 121, 5, 122]

Motivated by the controversial reports about the magnetic ground state of Na$_3$Cu$_2$SbO$_6$ based on both, experimental and theoretical studies, we develop the magnetic model of Na$_3$Cu$_2$SbO$_6$ and the strongly related compound Na$_2$Cu$_2$TeO$_6$ [123] from microscopic grounds using our DFT based model approach. In more detail, we investigate the influence of the structural differences and the octahedral ionic groups on the magnetic ground state for the two compounds. Especially the distortion of dimer chains is discussed with respect to its influence on the frustration ratio α motivated by the strong influence of the chain geometry on the magnetic properties in Li$_2$ZrCuO$_4$ (see Sec. 3.1.2). The interpretation of the magnetic susceptibility data for Na$_3$Cu$_2$SbO$_6$ within the alternating chain model demonstrates the difficulty to distinguish between two different sets of parameters, which is even more problematical as the magnetic susceptibility data are sensitive to subtle changes in the O stoichiometry and site occupation. The combination of our theoretical results with thermodynamic measurements and QMC simulations resolves the controversy about the magnetic ground state in Na$_3$Cu$_2$SbO$_6$ and allows to illustrate an unambiguous evidence for the FM-AFM scenario by the comparison of the simulated momentum-resolved spectrum (based on our microscopic model) to the recently published inelastic neutron scattering data.

The small green crystals of Na$_3$Cu$_2$SbO$_6$ contain pairs of slightly distorted, edge shared CuO$_4$ plaquettes forming structural dimers with a Cu-O-Cu bonding angle of 95°. The dimers are arranged into chains along the crystallographic b axis connected by the equatorial plane of SbO$_6$ octahedra (compare Fig. 3.29, right panel). The apical O of the CuO$_6$ octahedra realize a linking to the next Cu$_2$O$_6$ dimer chain. In this way layers are generated, which are separated by Na atoms (compare Fig. 3.29, left panel). The crystal structure of Na$_2$Cu$_2$TeO$_6$ is (quasi) isostructural. Substituting Sb by Te leads to a stronger distortion of the Cu$_2$O$_6$ dimer chains and a reduction of Na atoms between the layers in agreement with the additional electron of Te compared to Sb.

Experimental results and suggested models

In accordance with the crystal structures the magnetic models of Na$_3$Cu$_2$SbO$_6$ and Na$_2$Cu$_2$TeO$_6$ have been discussed as quasi one-dimensional alternating chain systems. But up to now, the
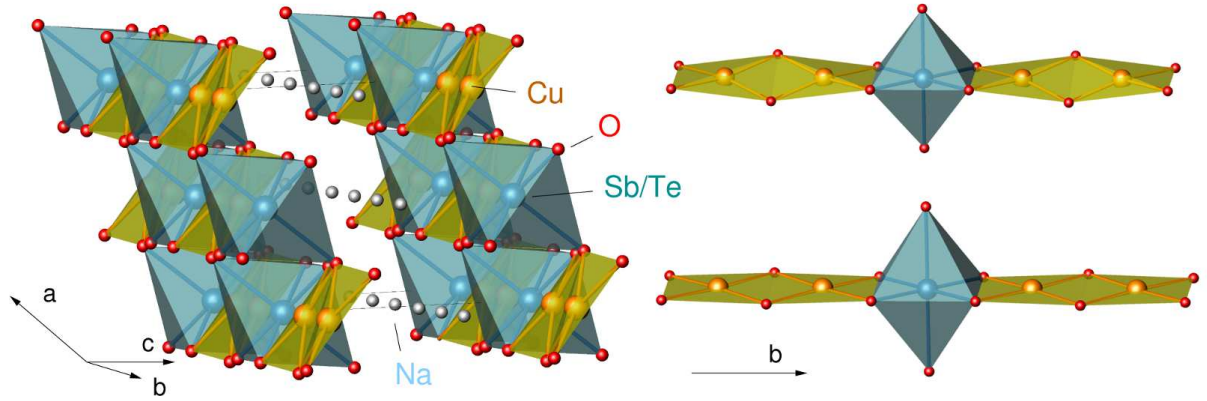
Figure 3.29.: Left: Crystal structure of $Na_3Cu_2SbO_6$. The compound contains distorted Cu_2O_6 dimers interconnected to chains by SbO_6 octahedra. This structural dimer chains run along the b-axis. Right: Short dimer chain segments for the real (distorted) chain (top) and an ideal planar chain geometry (bottom).

nature of the alternating couplings is still controversially discussed. Whereas S. Derakhshan *et al.* [4] suggest an AFM-AFM coupling along the dimer chains from a combination of evaluating magnetic susceptibility data and a NMTO down-folding method, the analysis of thermodynamical measurements from Y. Miura *et al.* [121] and the electronic structure calculations by H.-J. Koo *et al.* [5] support a FM-AFM scenario. A later study of Y. Miura *et al.* [122] based on inelastic neutron scattering supports the FM-AFM model for $Na_3Cu_2SbO_6$ but with a changed ratio of the alternating exchange integrals. In contrast, the AFM-AFM scenario for $Na_2Cu_2TeO_6$ gains additional support from reported NMR and magnetic susceptibility data by Morimoto *et al.* [124] and a combined study, including magnetic susceptibility data and DFT based extended Hueckel calculations by Xu *et al.* [123]. As both scenario, the AFM-AFM and FM-AFM model, are supported by several experimental and theoretical works, an unambiguous criteria to settle the debate is still missing.

The magnetic susceptibility for $Na_3Cu_2SbO_6$ is depicted in Fig. 3.30. The measurements were performed in a magnetic field of $0.04\,T$ and show a typical low dimensional behavior with a broad maximum around $T_{max} = 95\,K$. A Curie-Weiss fit above $200\,K$ yields an AFM $\Theta_{CW} = 50 \pm 10\,K$. Below $18.5\,K$ impurities give rise to an upturn of the magnetic susceptibility.

Since the symmetry of the crystal structure suggests an alternation of the relevant exchange couplings within (J_{1a}) and between (J_{1b}) the structural Cu_2O_6 dimers and in accordance with the recent studies, an alternating chain model was chosen for the evaluation of exchange parameters from the magnetic susceptibility. Quantum Monte Carlo (QMC) simulations of the magnetic susceptibility fitted to the experimental data result in two sets of parameters, describing the measurements with nearly the same accuracy, but belonging to different parts of phase diagram (compare Fig. 3.30). The two obtained parameter sets are listed in Tab. 3.9.

The excellent agreement of the FM-AFM and AFM-AFM solution with the experimental data does not allow to distinguish between the two scenario based on the magnetic susceptibility data alone. In addition, the situation becomes even more ambiguous as the exact

O stoichiometry and site occupation are sensitive to the sample preparation affecting the shape of the magnetic susceptibility curve. The obtained differences between the QMC simulations based on the FM-AFM and AFM-AFM scenario tend out to be smaller than differences in the magnetic susceptibility by different samples (see Fig. 3.30, right). The crucial influence of the sample treatment can already be seen from the different color of powder samples (compare Fig. 3.32). Thus, the independent development of the magnetic model by theory or additional experimental measurements are strongly required.
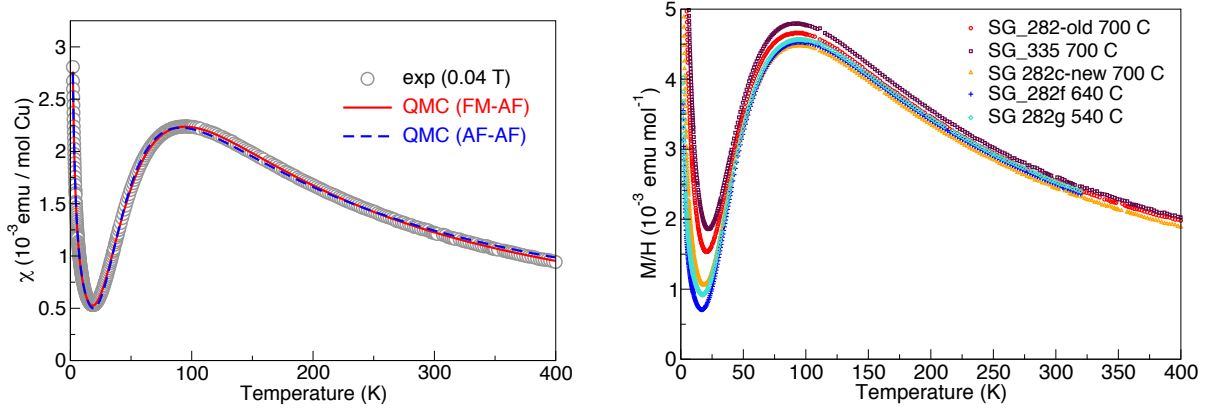
Figure 3.30.: Thermodynamic measurements for $Na_3Cu_2SbO_6$: Left: Comparison of the magnetic susceptibility together with QMC simulations for the FM-AFM and AFM-AFM alternating chain model. Both models fit the experimental data with the same accuracy. Right: Magnetic susceptibility measured for different powder samples. The different sample treatment affects the magnetic susceptibility significantly. The deviations originating from a different sample treatment exceed the differences between the two fitted models.

Electronic structure and magnetic model

Motivated by the controversial reports about the magnetic ground state of the strongly related compounds $Na_3Cu_2SbO_6$ and $Na_2Cu_2TeO_6$ and the difficulty to establish unambiguously their magnetic model from theory and thermodynamical data, we performed electronic structure calculations and developed their magnetic ground state from microscopic origin. The obtained density of states for $Na_3Cu_2SbO_6$ and $Na_2Cu_2TeO_6$ are depicted in Fig. 3.31. Both compounds show a rather similar valence band with respect to its width and shape. The density of states of $Na_3Cu_2SbO_6$ is clearly dominated by Cu and O states down to -5.5 eV, while contributions from Na and Sb can be neglected in this energy range. Centered around -6 eV, contributions from Sb atoms, which connect the structural Cu_2O_6 dimers in the crystal structure, hybridize significantly with the Cu-O states. In the case of $Na_2Cu_2TeO_6$, a similar admixture of Te states at the lower edge of the valence band is observed, although this part of the density of states is separated and shifted down in energy by about 1 eV compared to $Na_3Cu_2SbO_6$, in line with the additional valence electron of Te compared to Sb.

At the upper edge of the valence band, around the Fermi energy, a well separated block of Cu-O states appears for both compounds. These states can be assigned to the anti
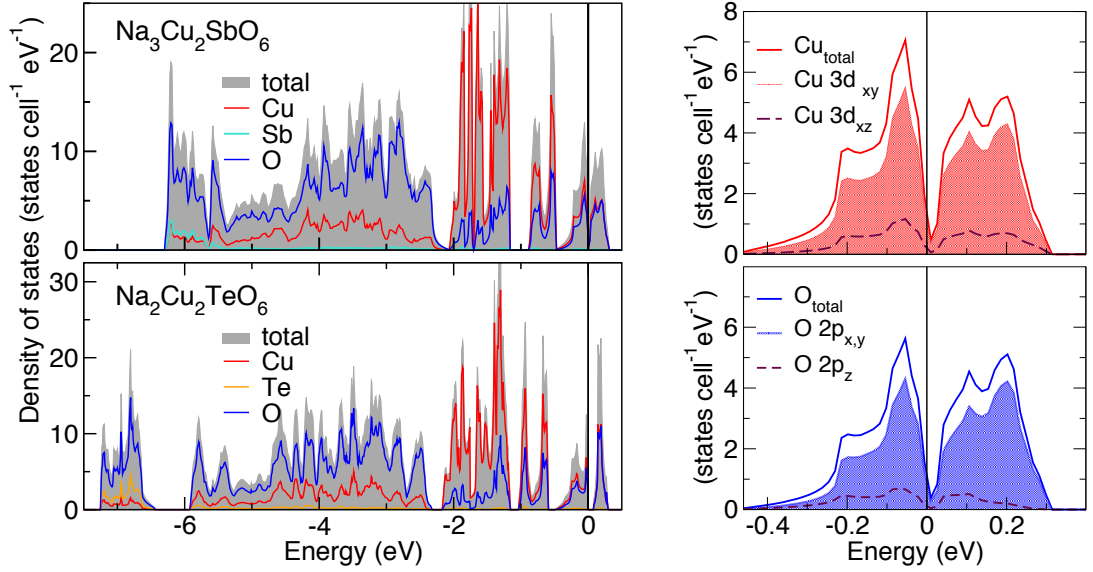
Figure 3.31.: Left: Atom resolved LDA density of states for $Na_3Cu_2SbO_6$ (top) and $Na_2Cu_2TeO_6$ (bottom). Right: Orbital resolved density of states close to the Fermi energy for $Na_3Cu_2SbO_6$ exemplary. Despite the chain distortion, this states are clearly dominated by anti bonding Cu-O $dp\sigma$ character.

bonding $dp\sigma$ states by an analysis of the orbital resolved density of states, which are shown in Fig. 3.31 (right panel) for $Na_3Cu_2SbO_6$ exemplarily. A relaxation of the experimental crystal structure leads to a small energy gain of $33\,meV/f.u.$ for $Na_3Cu_2SbO_6$, while the changes in the crystal structure are negligible. In contrast, a relaxation of the atomic sites in $Na_2Cu_2TeO_6$ lowers the energy by $130\,meV/f.u.$ and results mainly in a change of the chain buckling. Since also the anti bonding $dp\sigma$ states are influenced by the relaxation, we derived the magnetic properties for both, the experimental and relaxed crystal structure of $Na_2Cu_2TeO_6$.

The distortion of the Cu_2O_6 dimers from an ideal planar geometry has just minor influence on the anti bonding $dp\sigma$ states. Although contributions from hybridization with out-of plane states appear, applying an effective TB model is still valid, since this contributions are small compared to the pure anti bonding $dp\sigma$ states.

A mapping of the related LDA bands allows to estimate the magnitude, range and hierarchy of the hopping parameters of the system and thus supports a microscopic insight into the coupling regime. Therefore we fitted the LDA band structure by an effective TB model using a least square fitting routine. We obtain perfect agreement of the TB fit to the LDA calculations, which is shown in Fig. 3.32 for $Na_3Cu_2SbO_6$ exemplarily together with a sketch of the leading hopping paths. The obtained parameters for the leading transfer terms are given in Tab. 3.8.

In both systems the dominant interaction appear along the chains between the structural dimers. Our analysis yields $t_{1b} = 127\,meV$ for $Na_3Cu_2SbO_6$ and $t_{1b} = 162\,meV$ for $Na_2Cu_2TeO_6$, respectively. The intra-dimer hopping $t_{1a} = 60\,meV$ for $Na_3Cu_2SbO_6$ and $t_{1a} = 16(43)\,meV$ for the experimental (relaxed) structure of $Na_2Cu_2TeO_6$ are smaller by more than a factor of 2. In addition we find further inter-chain couplings to neighboring dimer-chains with in a layer comparable to the coupling strength of t_{1a}. Since for the
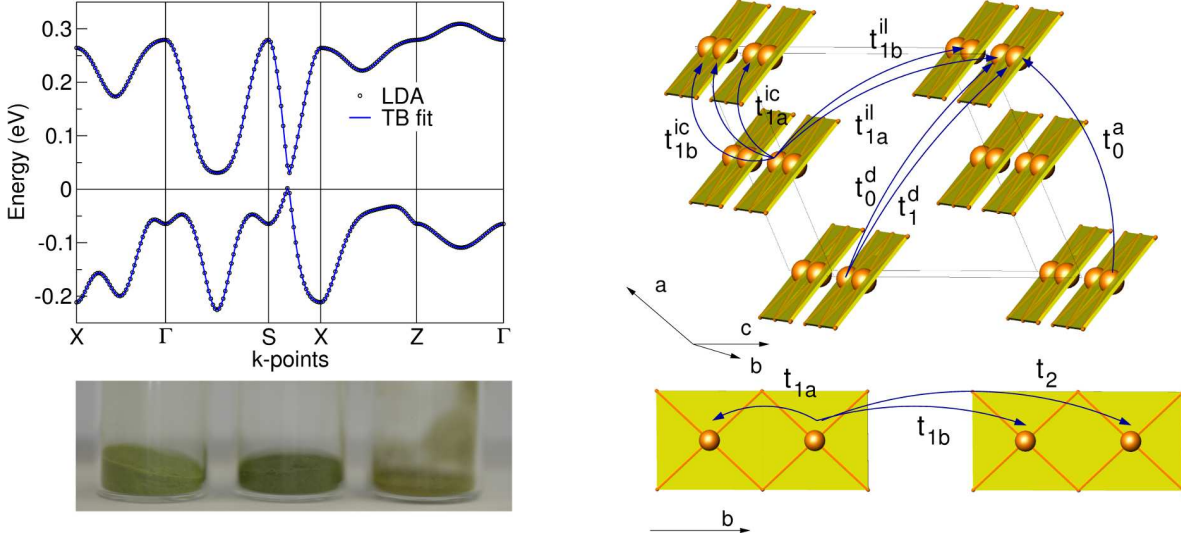
Figure 3.32.: Left: Comparison of the LDA band structure with the bands obtained from the TB model fit (top). The powder samples of different treatment show slightly different colors. Right: Sketch of transfer paths considered in the TB model.

t_1/meV	$\mathbf{t_{1a}}$	$\mathbf{t_{1b}}$	t_2	t_{1a}^{ic}	t_{1b}^{ic}	t_{1a}^{il}	t_{1b}^{il}	t_0^d	t_1^d	t_0^a
Sb exp	**60.6**	**127**	18.2	-27.8	17.0	5.8	-6.6	21.8	-4.6	17.4
Sb planar	**45.3**	**119**	22.4	-7.9	9.4	14.9	-18.8	30.1	-13.2	-
Te exp	**15.6**	**162**	16.4	-38.5	24.7	2.8	2.5	13.7	-	25.5
Te relaxed	**42.5**	**152**	17.3	-42.4	26.3	3.4	3.9	14.5	-	23.1
Te planar	**27.3**	**152**	29.3	-12.6	12.4	14.1	-15.9	26.0	-11.8	1.2

Table 3.8.: Comparison of derived transfer terms in meV from the fitted TB model.

magnetic intra-dimer exchange J_{1a} FM contributions are expected, an expansion of the magnetic model based on the hopping terms only is clearly necessary. However, taking into account the strong Coulomb repulsion in a model approach, we map the effective TB model onto a Hubbard model and subsequently onto a Heisenberg model for the low-lying magnetic excitations. With a typical value of $U_{\text{eff}} = 4\,\text{eV}$ for edge-shared CuO_2 chains we estimate the anti ferromagnetic part of exchange integrals $J_{1b}^{AFM} = 16\,\text{meV}$ and $J_{1a}^{AFM} = 4\,\text{meV}$ for $Na_3Cu_2SbO_6$ and $J_{1b}^{AFM} = 26\,\text{meV}$ and $J_{1a}^{AFM} = 2\,\text{meV}$ for $Na_2Cu_2TeO_6$ (realxed), respectively, regarding the relation $J_{ij}^{AFM} = 4t_{ij}^2/U_{\text{eff}}$.

The applied effective TB approach supports a microscopic insight into the coupling regime, but disregards the FM contribution to the exchange integrals, which in turn are expected inside the structural dimers of the compounds due to the Cu-O-Cu bonding angle close to 90°. To estimate the total exchange integrals including both, FM and AFM contributions, we performed LSDA+U calculations of magnetic SCs. The comparison of the total energies for different collinear spin arrangements and the further mapping onto a Heisenberg model results in the FM NN exchanges $J_{1a}^{TOT} = -12 \pm 2\,\text{meV}$ inside the structural dimers for

$Na_3Cu_2SbO_6$ and $J_{1a}^{TOT} = -11 \pm 2\,meV$ for $Na_2Cu_2TeO_6$ (relaxed structure), respectively, based on $U_{3d} = 6 \pm 1\,eV$. For the NNN exchange, between the structural dimers, we find $J_{1b}^{TOT} = 13 \pm 4\,meV$ for $Na_3Cu_2SbO_6$ and $J_{1b}^{TOT} = 17 \pm 6\,meV$ for the (relaxed) $Na_2Cu_2TeO_6$. All further exchange integrals between different chains and layers are smaller than $1\,meV$ (for details see App. C.14). Compared to edge shared chain cuprates the dimer compounds $Na_3Cu_2SbO_6$ and $Na_2Cu_2TeO_6$ exhibit a rather strong influence of the Coulomb repulsion U_{3d} and the DCC on the exchange integrals. However, the magnetic ground state of a $FM - AFM$ alternating chain is preserved for the wide range of U_{3d} from 4-9 eV and both DCC (compare Fig. 3.34).

Thus, we end up with the physical picture of alternating $FM-AFM$ chains for $Na_3Cu_2SbO_6$ with exchange integrals of nearly the same magnitude but different sign (FM-intra-dimer exchange and AFM inter-dimer exchange) while for $Na_2Cu_2TeO_6$ the alternating chains $FM-AFM$ are modified with an about two times larger AFM exchange between the structural dimers. Comparing the resulting model of $Na_3Cu_2SbO_6$ with $\alpha = J_{1a}/J_{1b} = -0.93$ based on our DFT calculation with the two solutions from our HTSE and QMC simulation fitting the experimental obtained magnetic susceptibility, we find a good agreement for the FM-AFM solution with $\alpha = -1.23 \pm 0.02$. The evaluated exchange integrals are listed in Tab. 3.9.

In comparison with earlier DFT based studies, our $FM-AFM$ model is in agreement with the theoretical results from Koo et al.[5] based on a SC mapping comparable to this study, but yielding a sizable difference in the frustration ratio α. For $Na_3Cu_2SbO_6$ we obtain $\alpha = -0.93$ much closer to the experimentally evaluated $\alpha = -1.25$ than $\alpha = -0.48$ in Ref. [5]. This discrepancy in the ratios of the theoretical studies holds also for $Na_2Cu_2TeO_6$ with $\alpha = -0.62$ compared to $\alpha = -0.3$ from Ref. [5]. In contrast the study of Derakhshan et al.[4] conclude an AFM-AFM scenario from their down folding procedure. Although our model is in contradiction to their magnetic ground states, the comparison of our pure AFM parts of exchange integrals (derived from the TB model) with the parameters presented by Derakhshan et al.[4] differ just by few percent.

Influence of the chain geometry

For a deeper understanding of the underlaying mechanism, we tried to unravel the origin for the differences in the frustration ratio for $Na_3Cu_2SbO_6$ and $Na_2Cu_2TeO_6$. The two related compounds differ not only by their connecting ions, but also by details of their chain geometry, in particular the size of the deviation of O from the ideal planar chain geometry and several interatomic distances. Comparing the band structure for both compounds the anti bonding $dp\sigma$ band differ in their band width, while the shape is rather similar. In contrast, changing the chain geometry from the experimental observed distortion to an ideal planar chain within one compound the band width is rather stable while the shape changes sizable (compare X-Γ or X-Z in Fig. 3.33 for $Na_3Cu_2SbO_6$ exemplarily). The additional electrons of Te compared to Sb and a changed number of Na atoms can be excluded as agent for the differences, since comparing the electronic structure for Te and Sb within the same structure using the VCA lead to nearly identical behavior (shape and bandwidth of anti bonding $dp\sigma$ bands are preserved, compare App. C.12).

For a more qualitative evaluation of the influence of the different parameter we developed the magnetic ground state for fictitious variants of the Te and Sb compound consisting ideal, planar chains. From our LSDA+U calculations with $U_{3d} = 6 \pm 1\,eV$ we obtain

Na$_3$Cu$_2$SbO$_6$	model	J$_{1a}$/K	J$_{1b}$/K	α=J$_{1a}$/J$_{1b}$
LSDA+U	FM-AFM	-140 ± 20	151 ± 46	-0.93
HTSE	FM-AFM	-205	170	-1.21
QMC	FM-AFM	-216	173	-1.25
Ref. [4]	AFM-AFM	22	169	0.13
Ref. [5]	FM-AFM	-165	345	-0.48
Ref. [121] (exp)	FM-AFM	-165	209	-0.79

Na$_2$Cu$_2$TeO$_6$	model	J$_{1a}$/K	J$_{1b}$/K	α=J$_{1a}$/J$_{1b}$
LSDA+U (exp.)	FM-AFM	-117 ± 29	233 ± 70	-0.76
LSDA+U (rel.)	FM-AFM	-122 ± 23	198 ± 70	-0.62
Ref. [123]	AFM-AFM	13	127	0.1
Ref. [4]	AFM-AFM	2	212	0.01
Ref. [5]	FM-AFM	-158	516	-0.3
Ref. [121] (exp)	FM-AFM	-272	215	-1.27

Table 3.9.: Leading exchange integrals, derived from our approach in comparison to earlier studies.

J$_{1a}$ = -19.5 ± 4.5 meV and J$_{1b}$ = 11 ± 3 meV for Na$_3$Cu$_2$SbO$_6$ and J$_{1a}$ = -27 ± 7 meV and J$_{1b}$ = 18 ± 4 meV for Na$_2$Cu$_2$TeO$_6$, respectively. The dependence of the exchange integrals for the planar systems on the Coulomb repulsion U_{3d} is depicted in Fig. 3.34 in comparison to the experimental crystal structures.

We reveal an intimate interplay of different structural parameter, namely the chain distortion and inter atomic distances. The distortion of the dimer chains influences mainly the intra-dimer exchange J_{1a}, since the local environment of J_{1b} remains basically unchanged by shifting the O(1) atoms into the chain plane. This relation follows the intuitive picture, since the local environment between the structural Cu$_2$O$_6$ dimers is stabilized by the equatorial plane of the connecting Te/SbO$_6$ octahedra. On the other hand both intra- and
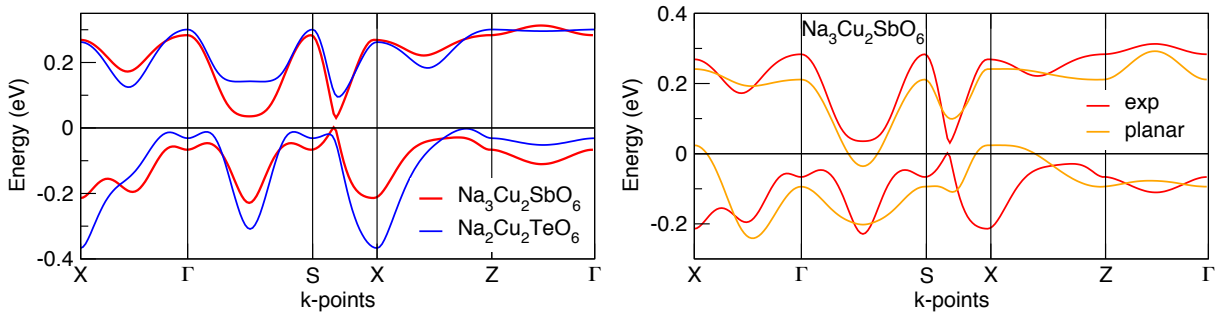

Figure 3.33.: Left: Comparison of the band structure for the two compounds Na$_3$Cu$_2$SbO$_6$ and Na$_2$Cu$_2$TeO$_6$. To separate structural effects from electronic contributions the influence of varying the chain geometry (right) or exchanging the connecting ion (left) is depicted for Na$_3$Cu$_2$SbO$_6$.
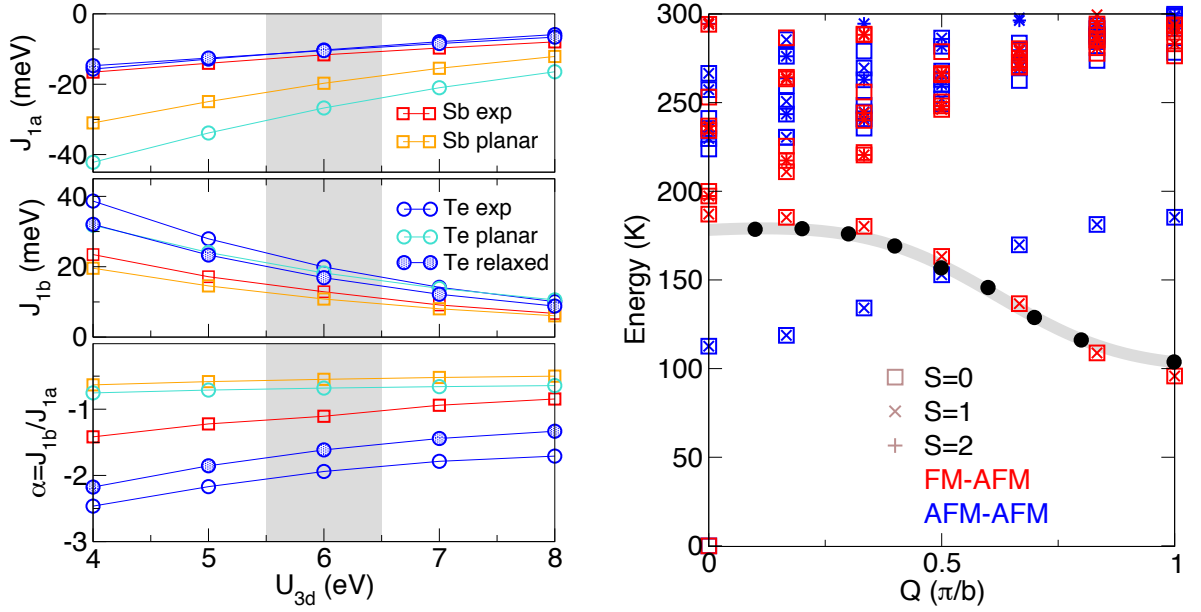
Figure 3.34.: Left: Calculated frustration ratios $J_{1b}/J_{1a} = \alpha$ as function of the Coulomb repulsion U_{3d} for different structural models for the two compounds. Right: Low energy excitation spectra for the alternating Heisenberg chain of N=24 sites, based on the two QMC solutions (FM-AFM and AFM-AFM). Note the different trend of dispersion for the low lying excitation branch between the two solutions. Experimental data from Ref. [122] are shown by black, filled circles.

inter-dimer exchanges depend on the inter-atomic distance, different in the two variants, which give raise to a different strong hybridization between the orbitals.

Regarding our results, the inter-dimer exchange J_{1b} is ruled by simple distance effects (compare e.g. O-O in Tab. 3.10). The shorter inter atomic distances in $Na_2Cu_2TeO_6$, e.g. the Cu-Cu inter-dimer or the O-O distance, lead to larger exchange integrals compared to the Sb compound. The results from SC calculation and TB model follow the same trend. The distortion of the chain has only minor influence.

In contrast, the intra-dimer exchange J_{1a} is determined by a subtle balance between distance and distortion effects. The two experimental crystal structures of Te and Sb result in a nearly identical values of exchange parameter by the cancelation of both effects. While the shorter inter-atomic distances in the Te compound raises the magnetic exchange, it is suppressed at the same time by the stronger distortion of chains and thus the inappropriate orientation of interacting orbitals compared to the Sb compound. The pure distance effect on J_{1a} becomes obvious comparing the exchange integrals for the structures with planar chain geometry. The shorter distances in Te lead to larger magnetic exchanges in analogy to the trend in J_{1b}. The influence of the chain distortion is visible comparing the differences between the exchange integral for $Na_3Cu_2SbO_6$ in the experimental and planar geometry. The deviation of O from ideal planar chain suppresses J_{1a}. In line with this observation, we found an even larger difference between the magnetic exchange of the experimental and planar geometry in $Na_2Cu_2TeO_6$ caused by the significantly stronger distortion of chains. The equidistant increase of J_{1a} for $Na_3Cu_2SbO_6$ from the experimental to the planar geom-

3. Low dimensional magnets

	Cu-Cu (NN) [Å]	Cu-Cu (NNN) [Å]	Cu-O-Cu [°]	O-O [Å]	Cu-O [Å]	δO [Å]
Sb exp	2.96	5.91	95.27	2.94	2.02/2.00	0.39
Sb planar	2.96	5.91	94.22	2.94	2.02/2.02	0
Te exp	2.89	5.78	91.95	2.83	1.97/2.01	0.58
Te relax	2.86	5.82	92.9	2.92	1.95/1.97	0.53
Te planar	2.86	5.82	95.2	2.92	1.95/1.93	0

Table 3.10.: Comparison of representative inter atomic distances for the different structures. The deviation of O atoms from the ideal planar chain geometry is given explicitly by δO.

etry (distortion effect) and $Na_2Cu_2TeO_6$ planar (distance effect) crystal structure suggests, that both effects are of similar strength. The influence of the chain distortion in comparison to related edge shared and dimer chains are discussed in Sec. 3.2.

The magnetic ground state, influenced by frustration ratio J_{1b}/J_{1a}, is mainly determined by the distortion of chains due to the cancelation of the distance effect.

The chain distortion also influences the hierarchy of inter-chain exchanges. While in the experimental structure the long range exchanges beyond t_{1a} and t_{1b} mostly appear inside the layers of the ab-plane, in the planar system the coupling between the layers is strengthened due to the orientation of the O orbitals (compare ts in Tab. 3.8 or Js in App. C.14).

Summary

In a joint experimental and theoretical study we developed the magnetic ground state of the two strongly related dimer-chain compounds $Na_3Cu_2SbO_6$ and $Na_2Cu_2TeO_6$. Combining thermodynamic measurements, QMC simulations, DFT based electronic structure and model calculations we demonstrated that the two compounds are best described by means of a FM-AFM alternating chain model. QMC simulation of the magnetic susceptibility yield two possible solution for the magnetic ground state of $Na_3Cu_2SbO_6$, an AFM-AFM and FM-AFM solution, due to the symmetry of the Hamiltonian itself. A decision based on thermodynamic data alone is ambiguous. Therefore, we evaluated the low temperature magnetic properties of $Na_3Cu_2SbO_6$ and $Na_2Cu_2TeO_6$ from a microscopic basis using an effective TB model on top of electronic structure calculation together with LSDA+U calculation of magnetic SC. We unravel the clear picture of FM-AFM alternating chains in line with the close to 90° Cu-O-Cu bonding angle within the structural dimers of the crystal structure. For $Na_3Cu_2SbO_6$ a frustration ratio of $\alpha = J_{1a}/J_{1b} = -0.93$ is obtained in good agreement with the FM-AFM solution from QMC simulation (we follow the definition of α established in earlier publications). The alternating FM-AFM chain in $Na_2Cu_2TeO_6$ is modified by a stronger inter-dimer exchange and an frustration ratio of $\alpha = -0.62$.

Since most of the earlier studies establish their magnetic models for the two compounds in a similar way, combining results from magnetic susceptibility experiments and DFT based calculations, we expand our study by the simulation of the low energy neutron spectra, this way resolving the ambiguity between the FM-AFM and AFM-AFM scenario ultimately. The related calculation of the excitation spectrum E(Q) exhibits a well separated dispersion branch for the lowest energy excitation (compare Fig. 3.34, right). This brach follows a

significantly different behavior for the FM-AFM and AFM-AFM solution. The sines-like dispersion of the FM-AFM model follows perfectly the experimental data from inelastic neutron scattering measurements reported by Miura *et al.* [122], while the AFM-AFM model leads to a cosine behavior and can clearly ruled out.

To unravel the difference in α between $Na_3Cu_2SbO_6$ and $Na_2Cu_2TeO_6$ influence of structural peculiarities on the magnetic properties was systematically investigated. We found a subtle balance of distortion and distance effects. Whereas mostly J_{1a} (intra-dimer exchange) is modulated by the chain distortion, the change of the chain buckling has only minor influence on J_{1b} (inter-dimer exchange), since the local environment of the interacting orbitals remains unchanged. However, for the formation of the ground state, the distortion of chains is the crucial parameter since distance effects cancel out.

3.1.6. $Cu_2(PO_3)_2CH_2$ - magnetic vs. structural dimers

Related to the alternating chain compounds $Na_3Cu_2SbO_6$ and $Na_2Cu_2TeO_6$ is the spin 1/2 compound $Cu_2(PO_3)_2CH_2$, which contains structural Cu_2O_6 dimers and exhibits a spin gap at low temperatures. But in contrast to the latter two compounds, the Cu_2O_6 dimers in $Cu_2(PO_3)_2CH_2$ are strongly distorted and linked in a three dimensional fashion by $PO_3CH_2PO_3$ units. The eight inequivalent Cu atoms per unit cell (from four inequivalent dimer chains) with slightly different distances and relative arrangement result in a diversity of different exchange paths. However, in contrast to the structural complexity the magnetic susceptibility of $Cu_2(PO_3)_2CH_2$ shows a characteristic low dimensional behavior. To develop a reliable magnetic model for this rather complicated structure, we combined nuclear magnetic resonance (NMR) and nuclear quadrupole resonance (NQR) spectroscopy, magnetic susceptibility, specific heat, and high field magnetization measurements together with extensive electronic structure calculations and QMC simulation. This combination of independent methods allowed to develop a consistent physical picture, even for this rather complex system including (i) local distortion around the magnetic ion sites, (ii) competing ferro- and antiferromagnetic interactions due to the vicinity of the Cu-O-Cu bond angle to 90°, and (iii) numerous inequivalent super exchange pathways. In this section we will focus on the computational results. The experimental results can be found in detail in Ref. [125] and are shortly summarized. We obtain the picture of coupled alternating chains formed by weakly coupled magnetic dimers, which surprisingly do not coincide with the structural dimers as one may expect in a naive approach. Such a difference between structural and magnetic dimers was already observed in $VO(HPO_4)\cdot H_2O$.[126]

The crystal structure of $Cu_2(PO_3)_2CH_2$ contains pairs of strongly distorted edge-sharing CuO_4 plaquettes connected with each other by $PO_3CH_2PO_3$ units (compare Fig. 3.35). These structural Cu_2O_6 dimers with Cu-O-Cu bond angles of 101° and 94° form chains along the crystallographic b direction. Regarding the dimers and their arrangement, the crystal structure of $Cu_2(PO_3)_2CH_2$ strongly resembles the compounds $Na_3Cu_2SbO_6$ and $Na_2Cu_2TeO_6$.

Experimental results

Also the magnetic susceptibility depicted in Fig. 3.36 bears similarities to $Na_3Cu_2SbO_6$. It shows a typical low dimensional behavior with a broad maximum at about $45\,K$ and a strong decrease at low temperatures indicating a spin gap. The sizable upturn at lowest temperatures can be ascribed to impurities and point defects. In contrast to the interpretation of magnetization data by Barthelet *et al.* [127], we do not observe any signature of a magnetic ordering in the susceptibility data down to $1.8\,K$. The absence of long range magnetic ordering is in addition supported by our specific heat measurements, which exhibits no anomaly at low temperature.[125] A Curie-Weiss fit to the magnetic susceptibility in the range of $120\,K$ to $400\,K$ results in a large Curie-Weiss temperature $\Theta_{CW} = -78\,K$ and $\mu_{eff} = 2.05\mu_B/Cu$. Assuming a dimer model, motivated by the structural dimers present in the compound, does not allow to describe the susceptibility data with reasonable accuracy. The obtained Bleaney-Bowers fit including a Curie term for the defects and a constant χ_0, results in addition in very low g-values, incompatible with usual Cu^{2+} magnetism (see green dots in Fig. 3.36, left panel). Since the temperature dependence of the Knight shift from NMR measurements is in very good agreement with the magnetic susceptibility data, the deviation of the dimer fit from the experimental data cannot be assigned to impurities
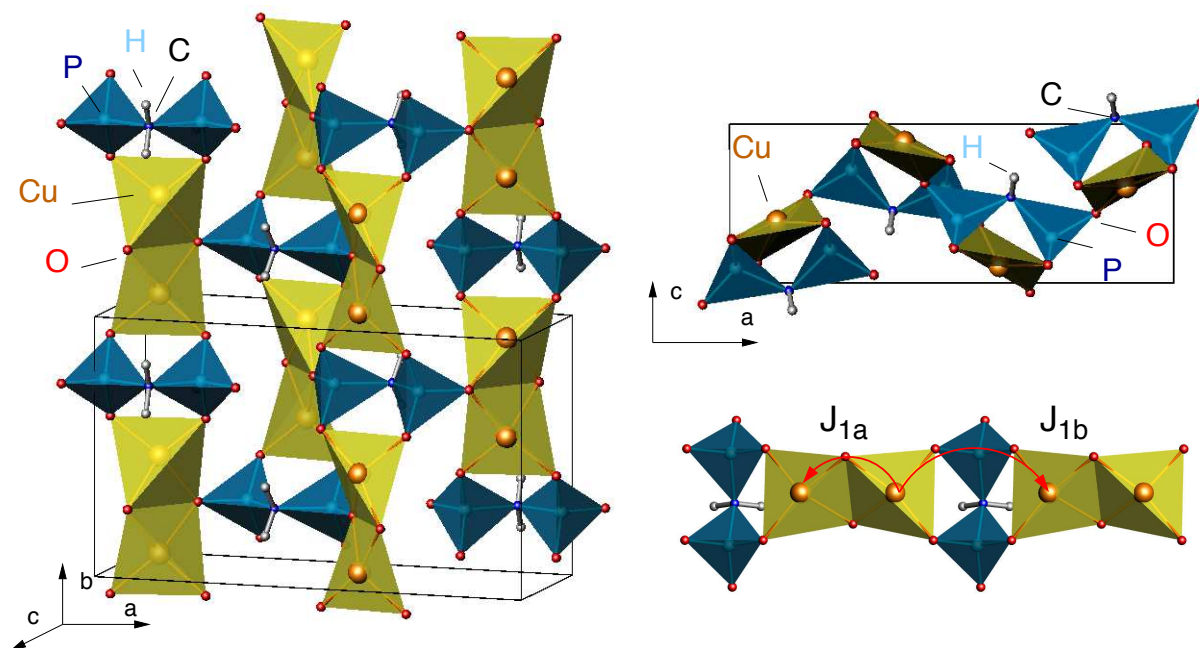
Figure 3.35.: Crystal structure of $Cu_2(PO_3)_2CH_2$ with distorted Cu_2O_6 dimers, which are connected via methylene diphosphonate $PO_3CH_2PO_3$ units with two crystallographically inequivalent P positions. The differences in the inter chain linking leads to a variety of inequivalent exchange paths with slightly different distances.

or the presence of a second phase. However, stimulated by the chain-like feature in the crystal structure, the model can be expanded by an additional coupling, leading to an alternating chain model. A corresponding fit using the alternating chain model leads to a considerable improvement, resulting in a spin gap of about 30 K, slightly depending on the method of its evaluation. NQR measurements of the spin lattice relaxation time exhibit an activation law behavior that can be described with a spin gap of about 24 K in very good agreement with the above mentioned value.

To challenge the idea of a coupled alternating chain model and to gain deeper insight into the microscopic interactions, we applied our computational approach combining a TB modeling with super cell (SC) calculations using LSDA+U.

Electronic structure and microscopic modeling

To get microscopic insight into the electronic structure, the relevant orbitals and main interaction paths, density functional band structure calculations were carried out. In Fig. 3.36 (right) the atom resolved density of states (DOS) is shown. The valence band of $Cu_2(PO_3)_2CH_2$ has a width of about 10 eV and splits in clearly separated parts, which can be assigned to the states of the different structural building blocks. Between -5 eV and 1 eV the states are dominated by the CuO-plaquette states. The lower lying states between -5 eV and -7.5 eV and between -8 eV and -10 eV originate mainly from PO_3 and CH_2 contributions. The contributions of P, C and H states in the energy range from -1 eV to 0.4 eV and are negligible.
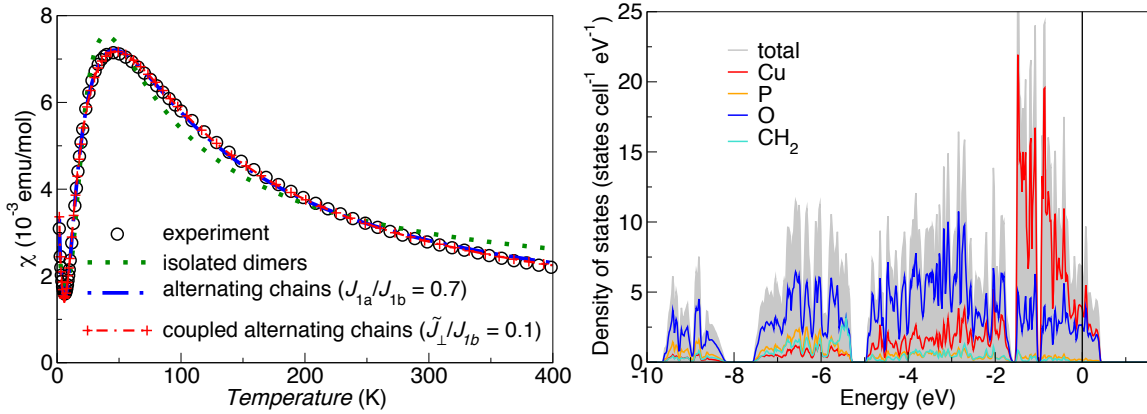
3. Low dimensional magnets

Figure 3.36.: Left: Measured magnetic susceptibility together with different model fits. The simple dimer model shows sizable deviations from the experimental data. The expansion of the model improves the quality of the fit. Right: Calculated LDA band structure. The anti bonding $dp\sigma$ states overlap with the lower part of the valence band.

Most important for our study are the anti bonding Cu-O $dp\sigma$ states as they are responsible for the magnetic properties of the system. In many cuprate systems with planar (like LiCuVO$_4$[76] or CuGeO$_3$[80]) or quasi-planar (like PbCuSO$_4$(OH)$_2$ in Sec. 3.1.3 or Li$_2$ZrCuO$_4$ in Sec. 3.1.2) Cu-O coordination these states are well separated from the lower lying states of the valence band. In these cases, the derivation of the relevant effective TB model is rather simple. However, in Cu$_2$(PO$_3$)$_2$CH$_2$ the situation is more complex: the separated band complex above $-1\,$eV (see Figs. 3.37) contains 24 bands instead of the expected 8 anti bonding bands according to 8 Cu atoms per unit cell. Although the Cu-O $dp\sigma$ states dominate the higher lying bands (between $-0.4\,$eV and $0.4\,$eV, see left panel of Fig. 3.37), they show a sizable mixing with the non-bonding bands at lower energies. This can also be seen from the orbital resolved DOS (compare Ref. [125]) where the Cu and O $dp\sigma$ states spread out to lower energies and, at the same time, the highest antibonding bands show a corresponding admixture of other Cu and O orbitals. The underlying reason for the unusually strong admixture of non-planar orbitals is the rather strong distortion of the CuO$_4$ plaquettes which even renders the assignment of the Cu-O $dp\sigma$ states a bit ambiguous.

To remove the ambiguity in the selection of the relevant bands applying a least-squares TB fit procedure, we calculate the TB model parameters from the calculated Wannier functions (see Fig. 3.38). In Fig. 3.37 (right), the resulting TB bands (blue) are presented together with the LDA band structure (gray). In line with the above mentioned hybridization, the higher lying TB bands agree quite well with the underlying LDA bands, whereas a sizable deviation is observed at lower energies. With a resulting band width of about $1\,$eV for the effective one-band model, Cu$_2$(PO$_3$)$_2$CH$_2$ shows a rather typical value compared to related compounds with isolated CuO$_4$ plaquettes as Sr$_2$Cu(PO$_4$)$_2$ (band width $w \sim$ $0.7\,$eV [1]), Bi$_2$CuO$_4$ ($w \sim 1\,$eV [128]) or the dimer-chain compound Na$_3$Cu$_2$SbO$_6$ ($w \sim$ $0.7\,$eV Sec. 3.1.5 and Ref. [5]). On the other hand, one should keep in mind that, despite the rather good matching of the TB model to the LDA bands, the accuracy of an effective
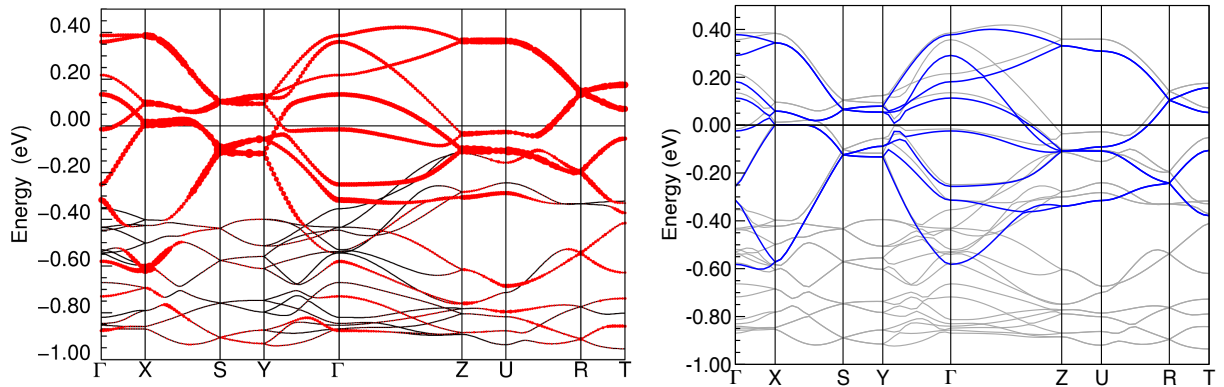
Figure 3.37.: Left: Calculated band structure and characters of Cu-O $dp\sigma$ states. The distortion of plaquettes causes a strong hybridization at the lower end of the antibonding $dp\sigma$ band. Right: Calculated band structure in comparison with the bands derived from a WF based TB model.

one-band model is limited due to the sizable hybridization with other Cu-O orbitals not included in this model. Although in principle the agreement of the TB bands with the LDA calculation could be improved by an extension to a multiband model, we restrict our investigation to an effective one-band approach for the sake of simplicity and easy interpretation.

The resulting leading hopping integrals t_i from the Wannier function based TB model are pictured in Fig. 3.38. We find a clear regime of interactions where the leading transfer terms are the nearest neighbor (NN) intra-dimer hopping $t_{1a} = 103$ meV and the NN inter-dimer hopping $t_{1b} = 92$ meV along the dimer chain direction. In addition, smaller inter-dimer couplings of the order of 50 meV perpendicular to the dimer chain with partial frustrating character are obtained. Due to the low symmetry of the distorted plaquette network (different orientation of the plaquettes), several only slightly different hopping terms are obtained. For simplification, they can be represented by the effective (averaged) parameters $\tilde{t}_i$ in good approximation (see Fig. 3.38).

Considering only the low lying spin excitations, we map the obtained transfer integrals via a Hubbard to a Heisenberg model. Applying $U_{\text{eff}} = 4.5$ eV we obtain $J_{1a}^{\text{AF}} = 9.5$ meV and $J_{1b}^{\text{AF}} = 7.5$ meV for the leading couplings along the chains. To simplify the picture further, for the smaller, frustrating inter-chain couplings an averaged coupling $\tilde{J}_{\perp}^{\text{AF}} \sim 1$ meV can be introduced (see Fig. 3.38) since the couplings $\tilde{J}_i^{\text{AF}}$ are of rather similar size. Thus, the LDA based TB model results in a picture of coupled, alternating AFM chains with an alternation parameter $\alpha = J_{1a}/J_{1b}$ of the order of 1.

Although the TB model provides considerable microscopic insight into the coupling regime, one should be aware that its further mapping onto a Heisenberg model yields only the AFM part of the exchange integrals. This is especially important for Cu-O-Cu bonds close to 90° that are present in our compound inside the structural dimers. According to the Goodenough-Kanamori-Anderson rules,[85] a sizable ferromagnetic (FM) contribution J_{1a}^{FM} to the total intra-dimer exchange J_{1a} can be expected.
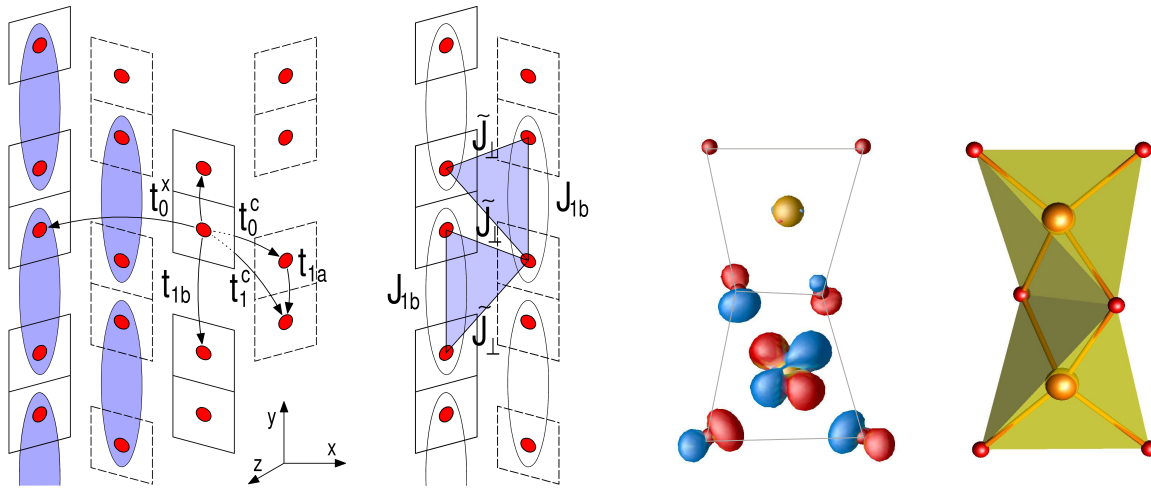
600

Figure 3.38.: Left: Main transfer integrals between Cu atoms from the TB model. Magnetic and structural dimer do not coincide. The effective frustrating interchain coupling between the dimers is illustrated by triangles. Right: Cu centered Wannier function with Cu $3d(x^2 - y^2)$ character together with the corresponding structural Cu_2O_6 dimer.

FM contribution by LSDA+U

Based on the knowledge of the short range character of the leading magnetic interactions in $Cu_2(PO_3)_2CH_2$, we carried out LSDA+U calculations for SC with different spin arrangement. Mapping the total energies of these SC onto a Heisenberg model we can estimate total exchange integrals including both FM and AFM contributions. Different magnetic solutions have been obtained from self-consistent calculations choosing different initial spin configurations. As result, we find $J_{1a} \sim 0.5\,\mathrm{meV}$ and $J_{1b} \sim 6\,\mathrm{meV}$ for $U_d = 7.5\,\mathrm{eV}$. This underlines the relevance of FM contributions to the intra-dimer exchange ($J_{1a}^{\mathrm{FM}} \sim -9\,\mathrm{meV}$), whereas for the inter-dimer exchanges J_{1b} and $\tilde{J}_\perp$ FM contributions are of minor importance ($J_{1b}^{\mathrm{FM}} \sim -1.5\,\mathrm{meV}$). From the LSDA+$U$ calculations, we estimate an average (effective) coupling $\tilde{J}_\perp = 1\,\mathrm{meV}$ between the dimer chains [20] in agreement with $\tilde{J}_\perp^{\mathrm{AF}} \sim 1\,\mathrm{meV}$ from the TB based results.

From these results a rather surprising picture arises: the compound can be understood as a system of interacting AFM dimers, but the magnetic and structural dimers do *not* coincide (compare Fig. 3.35 and Fig. 3.38). In addition, the weaker inter-dimer coupling between the chains will be frustrated (see Fig. 3.38, triangles in the right panel). The change of the appropriate magnetic model using a TB based approach only and combining it with LSDA+U results emphasizes the importance of the combined approach, since otherwise contradicting results can be obtained for this type of systems.[5, 4]

The effect of orbital mixing, observed in the LDA and LSDA+U results, is also reflected in a large experimentally measured electric field gradients (EFG). The good agreement

---

[20]We obtained $J_\perp$ by averaging the calculated individual exchange integrals. All calculated individual contributions are of similar size between 1...2 meV, but have a rather large error bar ($\sim 50\%$) due to the small energy differences and the computationally limited size of super cells.

of calculated EFG with the measured quadrupole frequencies supports independently the reliability of our DFT calculation.

Summary

In a joint experimental and theoretical study we developed the magnetic model for the rather complex spin 1/2 system $Cu_2(PO_3)_2CH_2$, which can be described in good approximation as coupled alternating AFM Heisenberg chains. Although the structural Cu_2O_6 dimers present in this compound may on first glance suggest a strong magnetic interaction within these dimers, our study can consistently assign the leading exchange to an antiferromagnetic inter-dimer coupling. The reliability of the suggested unexpected scenario is based on a variety of independent experimental and theoretical methods: (i) magnetic susceptibility, (ii) specific heat, (iii) NMR, (iv) NQR and (v) high-field magnetization measurements that are accompanied by (vi) density functional band structure calculations and (vii) quantum Monte-Carlo simulations to provide microscopic insight into the origin of the magnetic interactions. The evaluation of the magnetic susceptibility, specific heat, NMR and NQR data suggest an alternating Heisenberg model to describe the low temperature properties of $Cu_2(PO_3)_2CH_2$.

To challenge the suggested model and to evaluate the main magnetic interaction paths, DFT based band structure calculations were carried out. The combination of a TB model based on Wannier functions for the relevant anti bonding bands with LSDA+U total energy calculations for SC with different spin arrangements leads consistently to an alternating chain model. However, the DFT calculations result in sizable, frustrated couplings between the alternating chains. For the sake of simplicity of the corresponding magnetic model, these individual couplings are represented by an effective frustrating inter-chain exchange that is about 5 times smaller than the leading coupling along the chains. Surprisingly, this leading antiferromagnetic exchange corresponds to the coupling between the structural Cu_2O_6 dimers. The coupling within these dimers is strongly reduced due to sizable ferromagnetic contributions. Our findings underline the impending danger to obtain an inappropriate magnetic model based on over simplified structural considerations, i.e. regarding inter-atomic distances, only. The reliability of the first-principles calculations is supported by the theoretically evaluated electric field gradient, which is in good agreement with the measured quadrupole frequency.

Quantum Monte-Carlo simulations, that are in line with the proposed model of coupled alternating chains, complement our study. Simulating the high field magnetization curve using QMC calculations, reveals that the suggested inter-chain coupling leads to a considerable improvement with respect to the measured data, especially in the vicinity of the spin gap. The results of the section are published in Ref. [125], where NMR, NQR and high field magnetization experiments are discussed in more detail together with the results of QMC simulations.

However, the low temperature behavior of the NMR spectra (the two P sites become equivalent) raised our interest in the stability of the crystal structure at low temperatures, additionally motivated by the structural transition at low temperatures for compounds containing a similar Cu coordination. Thus we performed XRD experiments at the high resolution beam line ID31at the ESRF. Unfortunately, the evaluation of the collected data reveal inconsistencies, most likely related to a change/deconvolution of the powder sample by the intensity of the beam during the measurements (see also App. C.13). Further studies

are on the way following a new data acquisition strategy. Also preliminary high pressure experiments have been performed at the ID09 of the ESRF using a screw type DAC with ethanol/methanol as transition medium (compare App. C.13). Up to $10\,\mathrm{GPa}$ no general symmetry transition is observed. The spectra show a strong broadening. In an ongoing computational study, we probe the internal parameter of the crystal structure based on the obtained high pressure lattice parameter considering magnetic ordering or distortion effects beyond the ambient pressure symmetry. The strongly distorted Cu dimers and its complicated 3D coupling suggest a high sensitivity on pressure, which consequently would change the local Cu coordination and which can give raise to unexpected influence on the magnetic properties.

3.1.7. Cu_2PO_4OH - orbital order between dimers and chains

The spin $1/2$ compound Cu_2PO_4OH attracts large interest not only by its unusual crystal structure containing a combination of edge shared CuO_4 chains linked by Cu_2O_8 dimers, but also exhibiting a spin gap at low temperatures. Whereas the spin gaps in $Na_3Cu_2SbO_6$, $Na_2Cu_2TeO_6$ or $Cu_2(PO_3)_2CH_2$ can be ascribed to the formation of alternating Heisenberg chains in accordance with the structural dimer chains present in this compounds, the origin of the spin gap in Cu_2PO_4OH is not obvious from a structural point of view.

Recently, a combined experimental and theoretical study suggested a tetramer model as the magnetic ground state for Cu_2PO_4OH based on the assumption of the cancelation of FM and AFM contribution to the exchange integrals along the edge shared chains.[129] This model allows to fit the magnetic susceptibility data, which shows a typical low dimensional behavior, in the whole temperature range from 1.8 to $300\,K$. A spin gap of about $140\,K$ was evaluated from the susceptibility data. In line with the tetramer model, no long range ordering is observed down to $1.8\,K$ in specific heat measurements. The spin gap behavior of Cu_2PO_4OH was supported by an independent NMR study. The experimental temperature dependence of the Knight-shift was described according the earlier suggested tetramer model.[130] However, the suggested tetramer model is rather counter intuitive with respect to the distinct quasi 1D characteristics of many edge shared chain compounds. Furthermore, the difficulty to establish a reliable magnetic model based on a fitting approaches only, leads to misleading conclusions in the past due to the intrinsic symmetry of the Hamiltonian itself.

Stimulated by the interesting crystal structure and the suggested contra intuitive model, we performed electronic structure calculation to develop the magnetic model of Cu_2PO_4OH from microscopic grounds.

The compound Cu_2PO_4OH crystallizes in a orthorhombic space group with two inequivalent Cu sites. The Cu(1) atoms are coordinated in a distorted O octahedron with two long Cu-O bonds (2.39Å) and four short Cu-O bonds (1.96Å ($2\times$) and 1.98Å ($2\times$)) typical for many cuprates. The CuO_4 plaquettes of the equatorial plane form planar, edge-shared chains along the c-axis. In contrast, the Cu(2) sites are surrounded by five O atoms with two shorter Cu-O distances of about 1.95 Å and three longer Cu-O bonds (about 2.04 Å) forming a trigonal bipyramid coordination. This unusual coordination occurs also in Cu_2OSeO_3.[131] In Cu_2PO_4OH a pair of CuO_5 bipyramids is always combined to a dimer by sharing an edge. In the compound both inequivalent Cu sites are in a Cu $3d^9$ state and magnetically active, in contrast to $NaCu_2O_2$, where the different Cu coordination involves one magnetically active Cu^{2+} and one non magnetic Cu^+ site.[132]

Along the a-axis the edge shared chains are connected by the dimer units at every second O atom along the chain direction. This way buckled layers in the ac-plane are formed, which are linked by PO_4 tetrahedra. In addition H atoms bind to the connecting O atoms between chains and dimers. Since in $PbCuSO_4(OH)_2$ the H position influences the magnetic exchange crucial (see Sec. 3.1.3), we relaxed the H sites in Cu_2PO_4OH and compared their influence on the electronic structure and the magnetic ground state. The relaxation leads to an energy gain of $0.47\,eV$/cell (4 f.u.), but the resulting exchange integrals show no significant differences for the experimental determined and relaxed H positions (compare App. C.22).

The alternating linking by dimers along the chain direction suggests strait forward the formation of alternating exchanges along the edge shared chains. The estimation of the
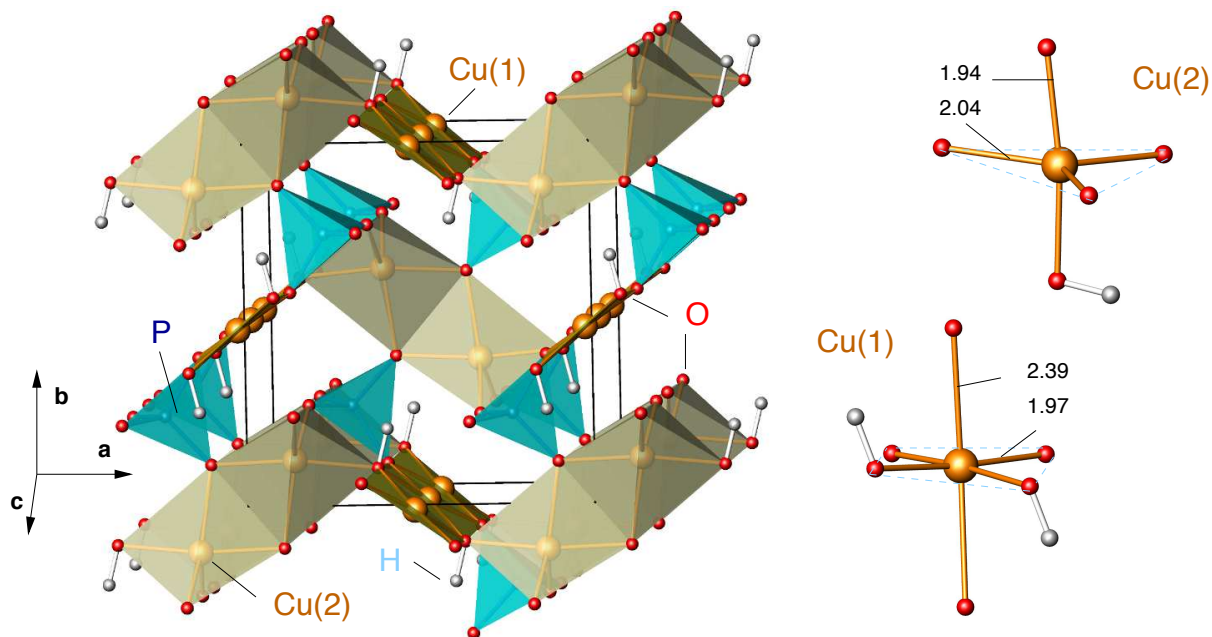
Figure 3.39.: Left: Crystal structure of the spin gap compound Cu_2PO_4OH. The compound contains two different types of Cu atoms. Cu(1) forms edge-shared CuO_4 chains connected by Cu(2)-dimers. This dimers are formed by two edge-shared trigonal bipyramids. Right: Local coordination of Cu(1) and Cu(2).

exchanges via the dimers between the chains is far from trivial. A similar connection between chain-like motives is realized in the natural mineral dioptase [133], where spiral chains are coupled by dimers.[21] In this case the magnetic ground state of the compound was determined by an FM intra-dimer (inter-chain) and an AFM intra-chain exchange. In contrast to dioptase, the chains in Cu_2PO_4OH show an edge shared symmetry with close to 90° Cu-O-Cu bonding angles giving rise to competing FM and AFM contributions and impeding a reliable estimation of the exchange integrals from structural consideration only. In particular the following bond angles appear in the crystal structure: A Cu(2)-O-Cu(2) bond angle within the dimer units 100.27°, two slightly different Cu(1)-O-Cu(1) angle along the chains 96.57° and 96.79°, and the Cu(1)-O-Cu(2) angle between dimers and chains 122.93°.

Electronic structure

To gain deeper insight and develop the magnetic model of Cu_2PO_4OH from a microscopic basis, we calculated the electronic structure of the compound within the LDA. The obtained density of states of the valence band is depicted in Fig. 3.40. Cu_2PO_4OH shows a band width of about 10.5 eV, slightly larger compared to many cuprates. The valence band contains sizable contribution from PO_4 states in the low lying energy region between -8 and -2.5 eV. The OH states appear as narrow bands close to -8 eV. The contributions from

---

[21]The local coordination of Cu within the dimer is different in dioptase compared Cu_2PO_4OH. In dioptase the dimers are formed by planar Cu_2O_6 units.

O and Cu states are present in the whole valence range, while above -2.5 eV especially the contributions from Cu states clearly dominate. Thereby both Cu sites contribute nearly to the same amount. In contrast to many edge shared chain compounds, the Cu-O states close to the Fermi energy, ruling the magnetic properties of the system, show no clear separation from the rest of the valence band. The projection of the density of states onto the local coordinate system of Cu(1) (local x-axis along the chain direction) reveals typical Cu $3d_{xy}$[22] character for the half filled states in the LDA DOS. In contrast the orbital resolved DOS for Cu(2) (within in the local coordinate system of Cu(2)) shows a clear Cu $3d_{3z^2-r^2}$ half filled band, where the Cu $3d_{3z^2-r^2}$ states are oriented along the short Cu-O bonds in the CuO_5 bipyramids. Thus, the orbital resolved DOS point to orbital order in the system.

To generate different solutions and probe the stability of a possible orbital order in the system Cu_2PO_4OH, we performed several calculations starting from different occupation matrices, regarding different occupations of Cu 3d orbitals. We were able to stabilize different orbital patterns. The Cu(1) $3d_{xy}$ and Cu(2) $3d_{3z^2-r^2}$ configuration is energetically favored. The half occupation of $3d_{xy}$ for both Cu sites increases the total energy by 0.5 eV/Cu. This large energy gain between different configurations of orbital occupation allow to separate the orbital degree of freedom from the magnetic coupling in the compound, since the two effects act on different energy scales. A similar approach hase been applied to compounds with orbital degrees of freedom to probe the orbital ground state (see Ref. [134, 135, 136]). As expected, LSDA+U calculations result in a gapped density of states for the ground state orbital occupation and a FM ordering (see App. C.15).
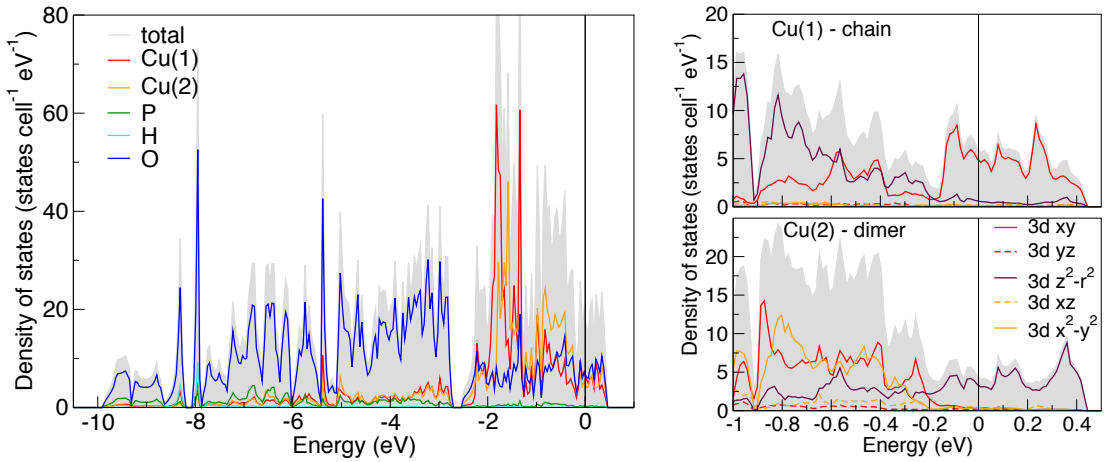

Figure 3.40.: Left: Calculated atom resolved density of states for Cu_2PO_4OH. Right: Orbital resolved density of states close to the Fermi energy for the two different Cu sites. Whereas Cu(1) is dominated by usual Cu $3d_{xy}$ states, the dimer Cu(2) shows nearly pure Cu $3d_{3z^2-r^2}$ character in the relevant energy range.

Although the magnetically active states overlap with the rest of the valence band in the DOS, the band characters for Cu(1) $3d_{xy}$ and Cu(2) $3d_{3z^2-r^2}$ states (depicted in Fig. 3.41) show well localized bands in the band structure. The half filled Cu(1) and Cu(2) states exhibit only a small mixture into other, overlapping states close to ε_F, e.g., with the four

---

[22]The Cu $3d_{xy}$ orbital corresponds to the Cu $3d_{x^2-y^2}$ orbital in the former systems, since the local coordinate system runs here along the chain direction.

overlapping bands of Cu(2) $3d_{xy}$ states in the energy range from -0.1 eV to 1.0 eV (compare also App. **??**). At the lower edge of the anti bonding $dp\sigma$ states the hybridization increases and band characters start to spread out. Since these effects are small, it is possible to determine the band width w of the anti bonding $dp\sigma$ states allowing a rough estimate for the leading exchanges in the system. We obtain $w = 1.3$ eV for Cu_2PO_4OH, a bit larger than the band width $w = 1$ eV of $Cu_2(PO_3)_2CH_2$ (compare Sec. 3.1.6), containing distorted dimer chains coupled in a 3D arrangement, or $w = 0.8$ eV of dioptase [133], with dimer coupled helical chains from CuO_4 plaquettes. On the other hand, the band width is clearly smaller than corner shared systems with typical band width of $w = 2.5$ eV for Sr_2CuO_3[91].
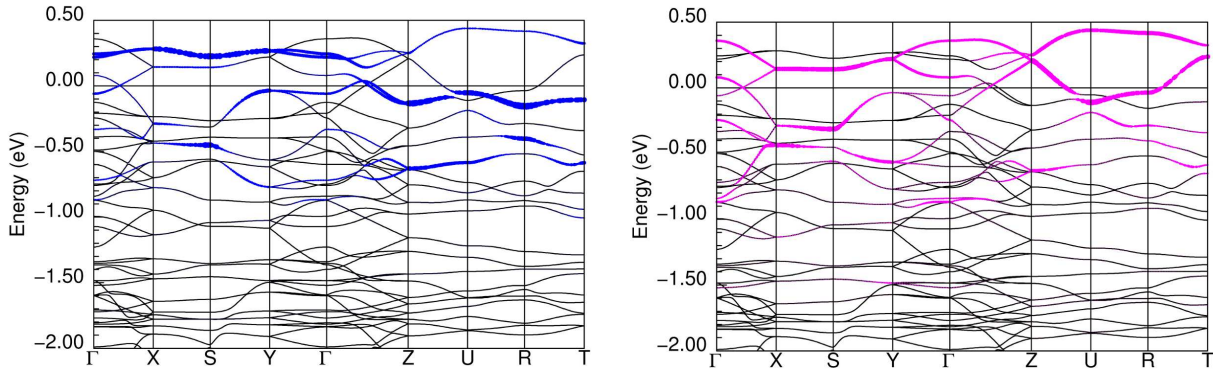

Figure 3.41.: Calculated band structure and band characters of Cu-O $dp\sigma$ states for Cu(1) (left) and Cu(2) (right). Whereas Cu(1) exhibits mainly dispersion along the chain direction, the dispersion of the Cu(2) related bands has a more two dimensional character. For both Cu sites the inter layer dispersion is suppressed.

Furthermore, the different character of the two Cu sites is reflected in a weak hybridization of Cu(1) and Cu(2) states at the upper edge of the anti bonding $dp\sigma$ states and a different characteristic dispersion for Cu(1) and Cu(2). The bands mainly formed from Cu(1) show a clear chain like (quasi one-dimensional) behavior. Especially the upper Cu(1) band between 0.5 eV and -0.2 eV has a considerable dispersion along the CuO_4 chain direction ($\Gamma - Z$) and flat bands along the other directions. In contrast, the bands originating mainly from Cu(2) are characterized by a more 2D dispersion and a stronger splitting according the number of inequivalent Cu(2) atoms per unit cell.[23] Nevertheless, the dispersion along the b-axis is in general suppressed, suggesting weak coupling in direction perpendicular to the buckled ac-planes formed by chains and dimers.

Developing the magnetic model

For a quantitative picture from microscopic grounds we mapped the eight bands around the Fermi energy, corresponding to the eight inequivalent Cu sites of the unit cell, onto an effective one-band TB model based on Cu centered Wannier functions with Cu $3d_{xy}$ character for Cu(1) and Cu $3d_{3z^2-r^2}$ character for Cu(2), respectively.

---

[23]In Cu_2PO_4OH we found four inequivalent Cu(2) sites (corresponding to two inequivalent dimers) and four inequivalent Cu(1) sites per unit cell.

The resulting fit is in rather good agreement with the LDA band structure (see Fig. 3.42, left). The obtained WF, depicted in Fig. 3.43, visualize the orbital ordering of the system. We yield four dominant transfer terms: the intra-dimer transfer t_d, an alternating transfer along the CuO$_4$ chain $t_{1a,b}$ and an inter-dimer-chain transfer t_{cd} (compare Tab. 3.11). Surprisingly, further transfer integrals along the quasi 1D chain, especially the NNN transfer term t_2 present in typical quasi 1D systems are strongly suppressed. The sizable inter-dimer hopping terms are in line with the orientation of the Cu(2) $3d_{3z^2-r^2}$ orbitals. Transfer terms smaller than 20 meV are not listed explicitly.
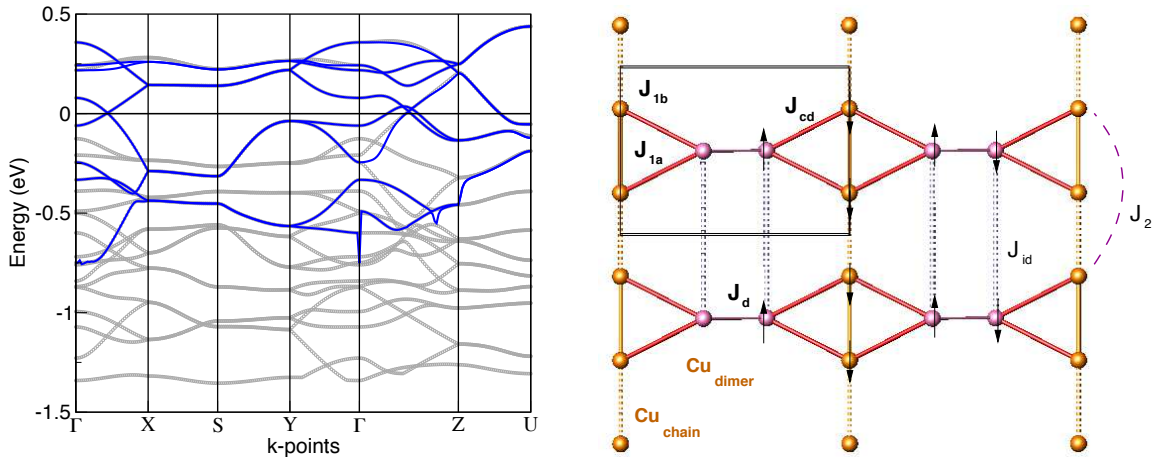

Figure 3.42.: Left: LDA band structure and derived bands from a WF based TB model fit, considering Cu(1) $3d_{xy}$ orbitals and Cu(2) $3d_{3z^2-r^2}$ orbitals. Right: Derived magnetic model. The suggested tetramer model is expanded by several further couplings. However, the tetramer model can be considered as intuitive, minimum model, although the size of the spin gap is strongly influenced by the additional interactions.

Following our subsequent mapping approach, from an effective TB model via a Hubbard model onto a Heisenberg model, we can reveal the AFM parts of exchange parameters for Cu$_2$PO$_4$OH$_2$. Using a standard value for the effective correlation within the CuO$_4$ units $U_{eff} = 4.0$ eV we estimate $J_{cd}^{AFM} = 198$ K, $J_d^{AFM} = 233$ K, $J_{1a}^{AFM} = 148$ K and $J_{1b}^{AFM} = 35$ K. Since the AFM exchange integrals are proportional to t_{ij}^2, all further exchanges are smaller than 10 K corresponding to 5% of the leading exchange and can be neglected in first approximation. Only the inter layer transfer t_{ild} between two dimers yields an AFM exchange integral of 26 K.

t_i/meV	t_{cd}	t_d	t_{1a}	t_{1b}	t_2	t_3	t_{ic}	t_{idz}^0	t_{ild}	t_{idx}	t_{idz}^1
t_i	130	141	113	57	18	22/6	22	32	47	24	23

Table 3.11.: Leading coupling terms for Cu$_2$PO$_4$OH derived from the WF based TB approach.

However, the vicinity of several Cu-O-Cu bonding angles to 90°, present in the crystal structure of Cu$_2$PO$_4$OH, require a careful consideration of FM contributions to the exchange

parameters. Therefore, we performed super cell calculation of different spin arrangements based on LSDA+U calculation which naturally contains both, AFM and FM parts to the exchange. The comparison of total energies yields $J_{cd} = 197\,\mathrm{K}$ as the dominant interaction in the compound, whereas the inter-dimer and inter-chain exchanges are strongly reduced by FM contributions. We obtain $J_d = 42\,\mathrm{K}$, $J_{1a} = -33\,\mathrm{K}$ and $J_{1b} = -29\,\mathrm{K}$ for $U_{3d} = 6\,\mathrm{eV}$ applied to both Cu sites. Neither the variation of U_{3d} in the physically relevant range from 4-8 eV nor the choice of the DCC influences the ground state qualitatively (compare App. C.22). Considering the different expansion of the magnetic orbitals for Cu(1) and Cu(2) by a 2 eV stronger Coulomb repulsion U_{3d} for Cu(2) compared to Cu(1) influences mainly the intra-dimer exchange, which is further reduced. The changed balance of leading exchanges strengthens this way further the dominant character of J_{cd}. On the other hand, long range exchanges between the $3d_{3z^2-r^2}$ orbitals are increased with increasing correlation, where their sum can be estimated to $47 \pm 20\,\mathrm{K}$ for $U_{3d,3z^2-r^2} = 6 - 10\,\mathrm{eV}$. The optimization of the H sites has only minor influence on the exchange integrals in contrast to $PbCu_2SO_4(OH)_2$. However, the surprisingly strong reduction of exchange integrals by FM contribution leads in first approximation to the simple picture of one dominant exchange, consistent with the suggested tetramer or spin square model.
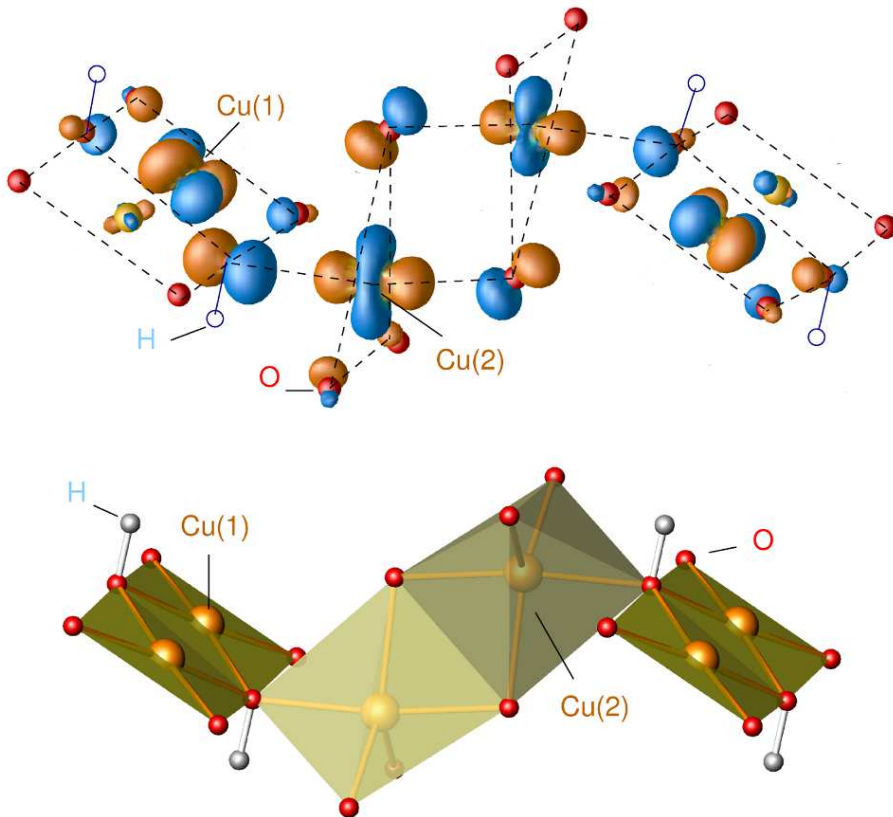

Figure 3.43.: Orbital order in Cu_2PO_4OH visualized by the calculated Wannier functions for the two different Cu sites. Whereas the Cu(1) atoms along the edge shared chains exhibit typical (xy) character, the trigonal bipyramid coordination of Cu(2) results in $(3z^2 - r^2)$ symmetry.
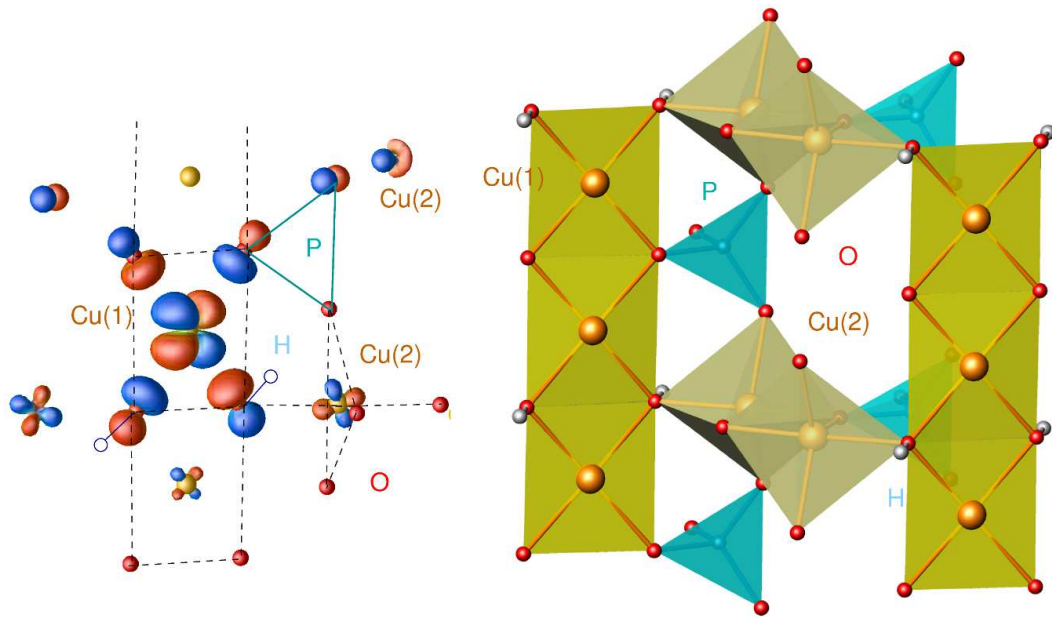
Figure 3.44.: Cu centered Wannier function for Cu(1): The extension of the WF along the edge shared chain is asymmetric in line with the alternating coupling strength between neighboring Cu(1) sites. The strong coupling to the Cu(2) sites is mediated by the O connected to H.

Summary

In this study we combined electronic structure and model calculations to develop the magnetic ground state of Cu_2PO_4OH, which crystalizes in an unusual crystal structure containing edge shared CuO_4 chains linked by structural Cu_2O_8 dimers. The differences in the local Cu coordination, "4+2" and "2+3", influence the crystal field splitting and give rise to orbital order in the system. The magnetic and orbital degrees of freedom can be decoupled and considered independently, since the energy scale of the processes is strongly different (5800 K/Cu from orbital order and about 200 K/Cu magnetic coupling).

Using a WF based TB model to derive the magnetic properties of the system from a microscopic basis we obtain four dominant transfer terms: (i) two along the edge shared chains, (ii) one inside the dimer and (iii) one between chains and dimers. The exchange integrals along the edge shared chain and inside the structural dimers are strongly suppressed by strong FM contributions compensating the AFM driven terms. The exchange along the edge shared chains alternates in line with the crystal structure. We end up with the picture of a dominant AFM inter-dimer-chain exchange $J_{cd} = 197$ K. The next exchange integrals are smaller by a factor of five. Thus, our calculations support the tetramer model suggested earlier [129], also it should be considered as a minimal model, since the pure tetramer model overestimates the size of the spin gap $\Delta \sim J = 190$ K compared to $\Delta = 140$ K from thermodynamic data. This difference elucidate the importance of additional couplings in the system, which strengthens long range order and suppress the size of the spin gap. A detailed studies to unravel role of smaller couplings is required.
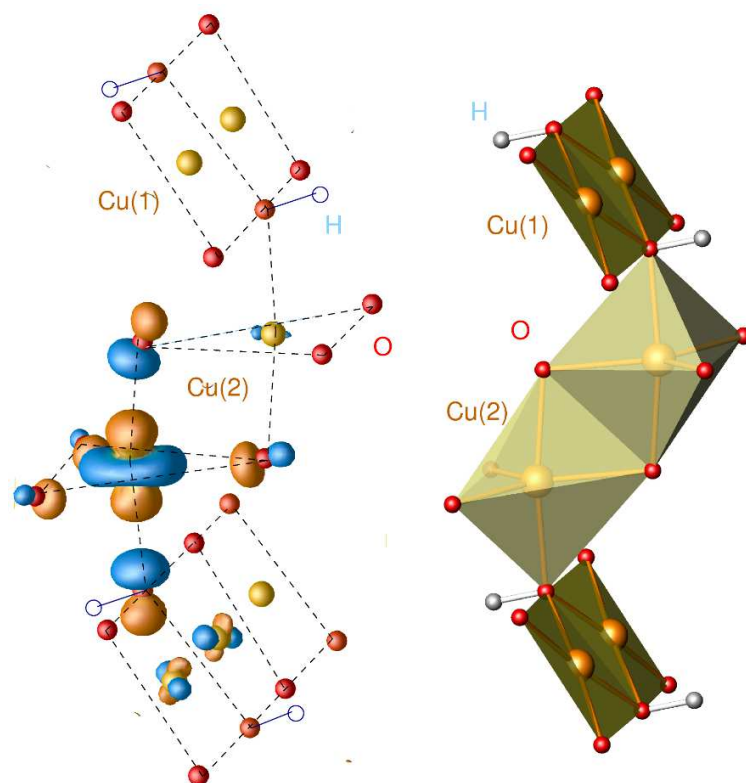
Figure 3.45.: Cu centered WF for Cu(2) with clear $(3z^2 - r^2)$ character. The WF show a sizable extension to the neighboring edge shared CuO_4 chain, whereas the coupling to the second Cu(2) of the structural dimer is strongly suppressed.

3.1.8. $A_2\mathbf{Cu}E\mathbf{O}_6$ - an new family of spin 1/2 square lattice compounds

The compounds, discussed so far, all contained chain-like structural motives, where the leading exchanges in most cases appeared along the structural chains. The magnetic properties of these systems were described in good approximation by quasi 1D $J_1 - J_2$ models or $J_{1a} - J_{1b}$ alternating chain models. Already the seemingly simple quasi 1D $J_1 - J_2$ model attracts much interest due to its fascinating phase diagrams driven by magnetic frustration. In the quasi one dimensional systems, the frustration originates from competing NN and NNN interactions along the chains as discussed in detail e.g. for Li_2ZrCuO_4 (Sec. 3.1.2) or $PbCuSO_4(OH)_2$ (Sec. 3.1.3). A two dimensional variant of a $J_1 - J_2$ Heisenberg model are square lattice systems, where frustration rises in the presence of sizable AFM NN and NNN exchanges (compare Fig. 3.1 and Fig. 3.47). In this case, the NN exchange J_1 along the side of the square lattice and the NNN exchange J_2 along the diagonal of the square lattice can not be fulfilled at same time, in analogy to the competition of NN and NNN in the 1D-chain geometry. The phase diagram of the $J_1 - J_2$ square lattice model involves three ordered phases, (i) a ferromagnetic (FM), (ii) a Neel antiferromagnetic (N-AFM) (checkerboard) and (iii) a columnar antiferromagnetic (C-AFM) phase.[137, 138, 139] A schematic phase diagram is depicted in Fig. 3.47. These ordered phases are separated by two critical regions, where exotic ground states including a spin-liquid phase are still under debate. The unusual physics in close vicinity to the quantum critical regions stimulated many experimentalists to search for real materials close to this phase regions to challenge the theoretical predictions. Recently, detailed studies about the interplay of structural peculiarities and magnetic properties of many V based square lattice compounds have been reported.[140] Here we focus on the Cu based square lattice compounds A_2CuEO_6 (A=Sr, Ba and E=Te, W).[141] This new family of distorted double perovskites realizes an ideal square lattice geometry in combination with a sizable variety of its connecting ions. Thus, a systematic investigation of the magnetic properties of these compounds depending on the connecting ions could be the basis for a purposive substitution driving the system close to the critical region.

Expectations are raised further by comparing the measured magnetic susceptibility data for the four compounds of the family. Beside the characteristic broad maximum in the susceptibility, pointing to the low dimensional behavior of the compounds (in line with a square lattice model), the position of the maxima in the susceptibility differ considerable (see Tab. 3.13). A Curie Weiss fit to the high temperature region for these materials yields $\theta_{CW} > 0$ for all four compounds, suggesting predominant AFM interactions in the systems. This first evaluation of thermodynamic data suggests that the compounds are placed at different regions of the phase diagram, as important precondition for tuning the system by substitution.

The compounds of the A_2CuEO_6 family crystallize in a double perovskite structure.[141] The planar CuO_4 units form an ideal square lattice within the xy-plane (compare Fig. 3.46). This isolated CuO_4 plaquettes are connected by the equatorial plane of Te/W-O octahedrons. The next, shifted square lattice layer along the z-axis is linked by Sr and Ba atoms, respectively.

Electronic structure

To get deeper insight and to unravel the origin of the different properties of the four compounds we performed electronic structure calculation and developed the magnetic model
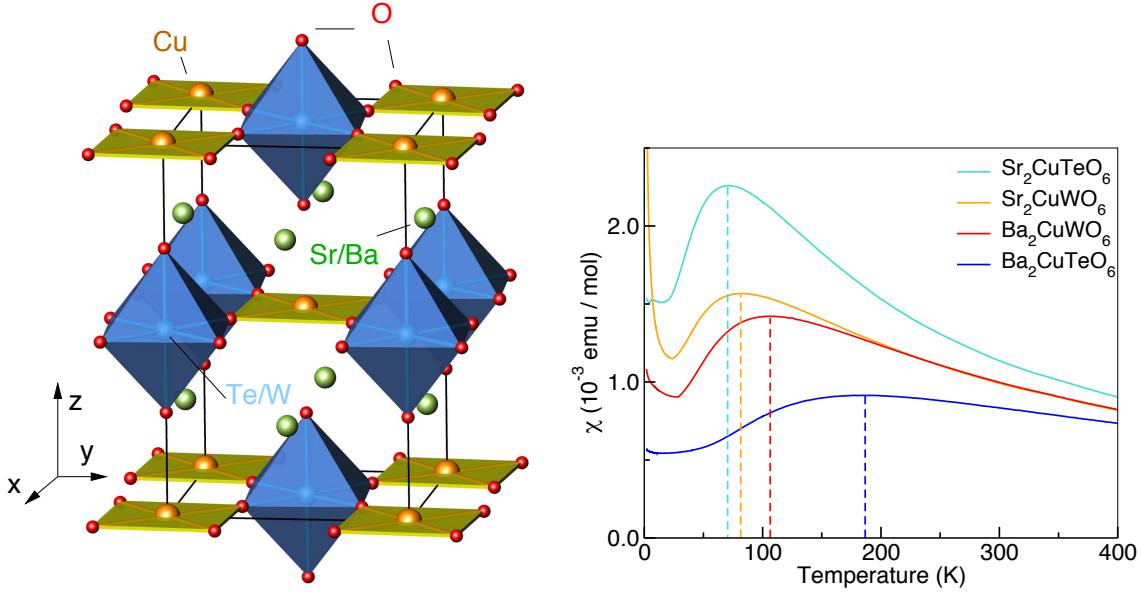
Figure 3.46.: Left: Crystal structure of A_2CuEO_6. The compound family forms an ideal square lattice geometry with localized spin 1/2. Right: Comparison of the experimental magnetic susceptibility. All compounds show low dimensional behavior and dominant AFM interactions, but differ in the position of the susceptibility maximum.

from a microscopic basis.

Comparing the density of states for the four compounds we find significant differences and can separate the systems into two groups: the Te containing compounds and the W compounds, whereas the exchange of Ba by Sr has just minor influence on the electronic structure. The atom resolved density of states for the four compounds are depicted in Fig. 3.48. All compounds show a valence band, which is dominated by Cu and O states, with a typical width of about $7.5 - 8\,\mathrm{eV}$, similar to many cuprates. The main contributions from Sr/Ba-O and and Te/W-O states appear at the lower edge of the valence band. From -4 eV to the Fermi energy ε_F their contributions to the DOS are negligible. While for Sr_2CuTeO_6 the states close to ε_F are well separated from the rest of the valence band, such a separation is missing in Sr_2CuWO_6. A similar trend is observed for the Ba containing compounds. However, evaluating the orbital resolved density of states for both systems reveals nearly pure Cu-O anti bonding $dp\sigma$ character at the upper edge of the valence band, close to ε_F. These states, determining the magnetic exchange in the compound, show a band width of about $w = 0.6\,\mathrm{eV}$ for Sr_2CuTeO_6 ($w = 0.7\,\mathrm{eV}$ for Ba_2CuTeO_6, respectively) in accordance with many edge shared chain compounds. In contrast, the W compounds exhibit a strong broadening of the anti bonding $dp\sigma$ states, resulting in a more than two times broader width of $w = 1.5\,\mathrm{eV}$ for Sr_2CuWO_6 ($w = 1.3\,\mathrm{eV}$ for Ba_2CuWO_6, respectively) and no clear separation from the lower lying states. The significant difference of the electronic structure for the Te and W compounds is even more obvious comparing the band structures. The anti bonding $dp\sigma$ bands exhibit not only a different width, but also a totally different shape (compare Fig 3.49). Following the dispersion along $\Gamma - X$ or $M - \Gamma$ this discrepancy is connected to the different sign of the transfer integrals, e.g., at
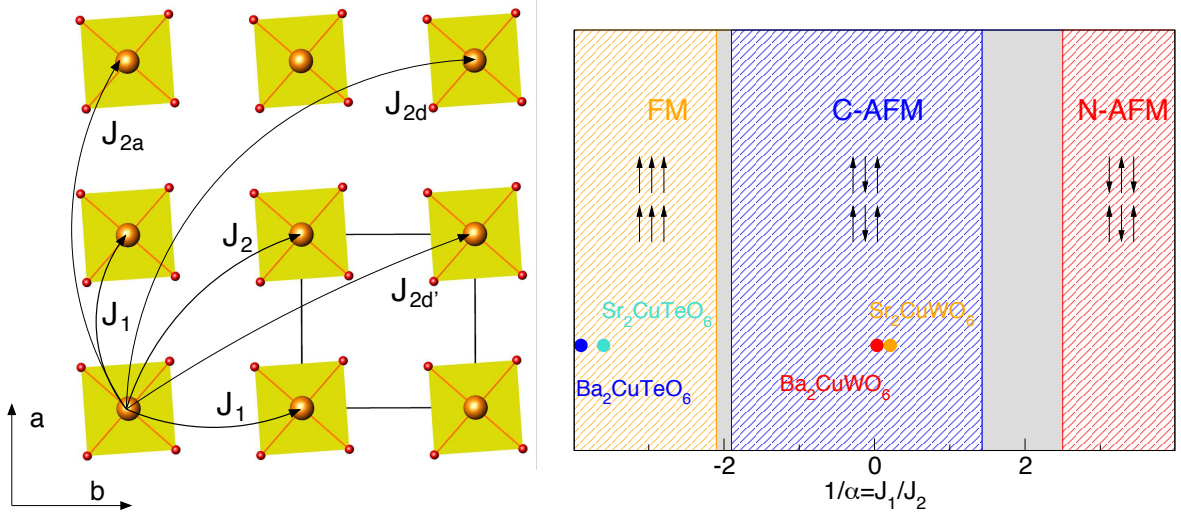
Figure 3.47.: Left: Sketch of the leading transfer paths considered in the TB model. Right: Schematic phase diagram of the $J_1 - J_2$ square lattice model according Ref. [138]. The quantum critical regions between the ordered phases attract always great interest and are present under debate.[139]

the Γ-point or M-point, for the Te and W compounds. This differences in the symmetry of the dispersion suggests directly a different symmetry of the coupling regime. However, both systems show a 2D character with flat bands perpendicular to the square lattice plane. Although in the W compounds the gap between anti bonding $dp\sigma$ states and the rest of the valence band is closed, the development of an TB model should be unambiguous, since nearly no hybridization with lower states occur. This can be concluded from the good localization of the anti bonding $dp\sigma$ bands, e.g., for Sr_2CuWO_6 depicted in Fig. 3.49, where a band crosses the $dp\sigma$ band close to ε_F (along $\Gamma - Z$) without mixing into this states. Surprisingly, small hybridization effects appear for the Te compound. A small part of the band character in Sr_2CuTeO_6 spreads out to the lower lying Cu $3d_{3z^2-r^2}$ bands at the M-point. This effect is much stronger for Ba_2CuTeO_6, although the states around ε_F are rather well separated.

Magnetic model

To evaluate the influence of the different symmetry on the magnetic ground state, we developed an effective TB model for the four square lattice compounds. The resulting fits are in good agreement with the LDA band structure. The obtained transfer integrals are listed in Tab. 3.12.

For all compounds we obtain two leading transfer integrals t_1 and t_2, in line with a square lattice model. The Te compounds are characterized by a leading hopping along the edges of the square lattice t_1, whereas the W compounds show dominant exchange along the diagonals t_2. The different symmetry of the two subgroups, concluded already from the differences in the band dispersion, are directly reflected in the different sign of transfer terms. As a further difference between the two systems, the W compounds show a pronounced 2D character with suppressed hopping terms perpendicular to the square lattice plane, whereas the Te containing compounds exhibit a sizable coupling between the dif-
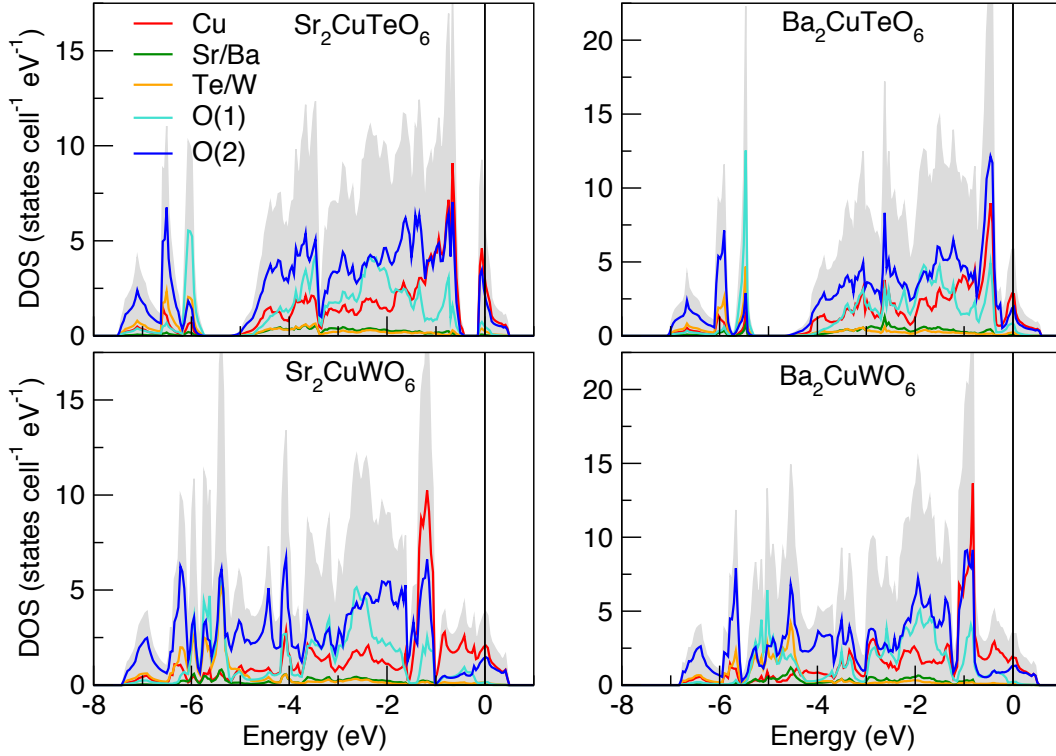
Figure 3.48.: Atom resolved density of states for the family of A_2CuEO_6 compounds. For all compounds the valence band is dominated by Cu and O states. The W containing systems show a strong broadening of the anti bonding $dp\sigma$ states.

ferent layers (compare Tab. 3.12). For Ba_2CuTeO_6 the inter-layer terms reach 10% of the leading transfer term. This is of comparable strength than the further hopping terms within the square lattice plane beyond t_1 and t_2 in the W compounds.

To ensure that the low temperature magnetism of the compounds is not significantly affected by neglected FM contributions, we performed LSDA+U calculations for J_1 and J_2 using different magnetic super cells (SC). Regarding our results, the LSDA+U calculations confirm the hierarchy of exchange integrals derived from the TB approach with a dominant AFM NN exchange J_1 for the Te compounds (along the the edges of the square lattice), in contrast to the dominant AFM NNN exchange J_2 for the W systems (along the diagonals of the square lattice). In particular, we obtain $J_1 = 100\,\mathrm{K}$ and a small FM $J_2 = -3\,\mathrm{K}$ for Sr_2CuTeO_6, which results in a frustration ratio of $\alpha = J_2/J_1 = -0.03$. For Ba_2CuTeO_6 the

t_i [meV]	t_1	t_2	t_{2a}	t_{2d}	$t_{2d'}$	t_c	t_{ca}	t_{cd}
Sr_2CuTeO_6	50	45	1	3	4	12	-8	4
Ba_2CuTeO_6	73	20	8	-2	1	12	-14	12
Sr_2CuWO_6	-66	-134	-2	-9	-5	0	0	0
Ba_2CuWO_6	-27	-137	-1	-8	-7	0	0	0

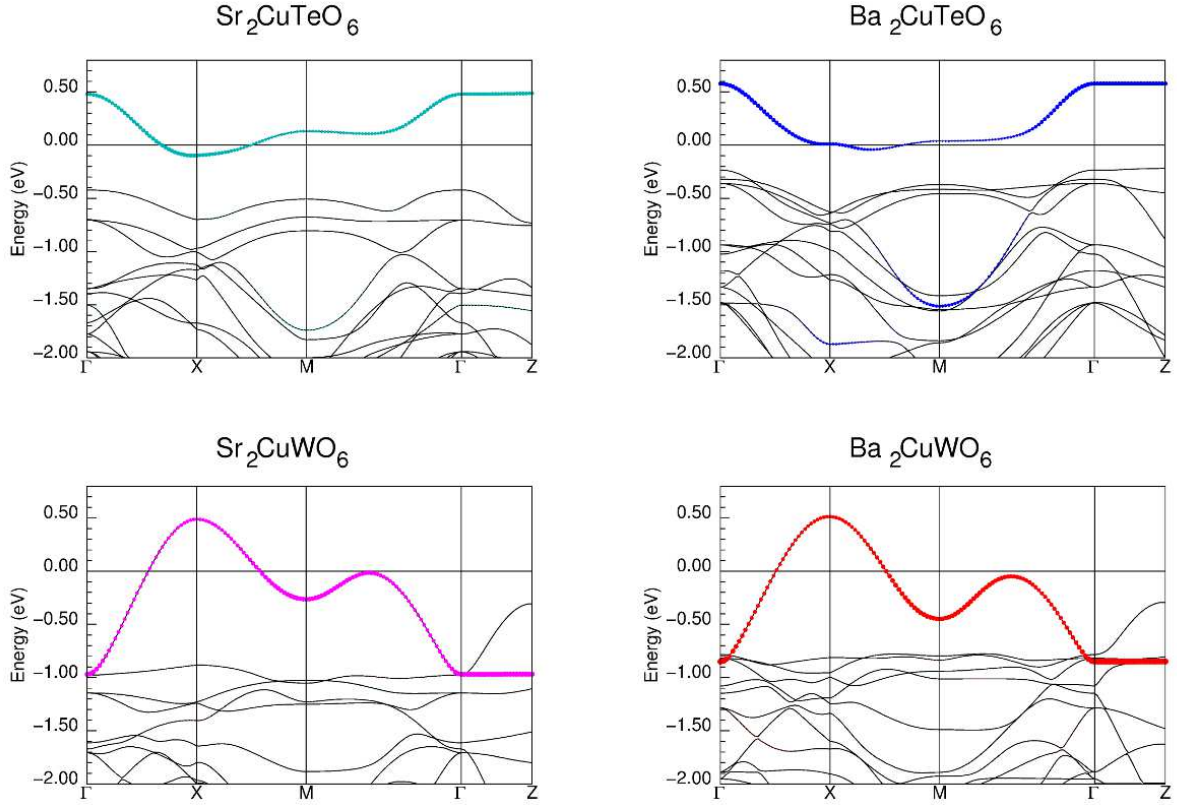Table 3.12.: Derived transfer integrals from Wannier function based TB model.

Figure 3.49.: Band structure with band characters of the magnetically active, anti bonding $dp\sigma$ CuO_4 orbitals. The band width and shape differ dramatically for Te and W compounds, while the substitution of Sr by Ba has only minor influence.

frustration ratio $\alpha = -0.009$ is even smaller with $J_1 = 216\,\mathrm{K}$ and $J_2 = -2\,\mathrm{K}$. Both Te systems are placed well in the N-AFM phase (compare Fig. 3.47). For the W compounds our calculations yield a small $J_1 = 4\,\mathrm{K}$ and a dominant $J_2 = 122\,\mathrm{K}$ for Ba_2CuWO_6 resulting in $\alpha = 30.5$, whereas the exchange integrals reach $J_1 = 25\,\mathrm{K}$ and $J_2 = 119\,\mathrm{K}$ for Sr_2CuWO_6 with $\alpha = 4.76$. Thus, we end up with a C-AFM order for the W containing materials.

Comparing these results with the exchange parameters obtained from the TB model, we find an overestimation of exchange integrals by the TB approach for the W compounds by nearly a factor of two. In contrast, the exchange integrals for the Te compounds are strongly underestimated using our TB fitting procedure. Whereas the overestimation of the magnetic coupling strength by the TB model can be understood by neglecting FM contributions, the underestimation of the exchange integrals in the Te compounds comes as a surprise. Keeping in mind the spread out of band character at the M-point, which is especially strong for Ba_2CuTeO_6, we refitted the LDA bands allowing the WF to expand more in energy. This leads to a significant increase of t_1 towards the results from LSDA+U SC calculations. This crucial influence of hybridization effect on the transfer terms is rather unexpected, since a similar spread out of band weights, was earlier observed in $AgCuVO_4$ or $Cu_2(PO_3)_2CH_2$, but exhibited only moderate influence. In addition, taking into account correlation, will shift the bands in energy this way suppressing the hybridization naturally. The important role of hybridization effect from Cu $3d_{x^2-y^2}$ into Cu $3d_{3z^2-r^2}$ for Ba_2CuTeO_6

is further pointed out, comparing the trend of the exchange integrals derived from TB and SC calculations. For Ba_2CuTeO_6 the TB model derived exchange integrals are not only much too small, but also violate the general trend of/between the systems. A detailed study expanding the effective one-band model to a two band model, taking into account the Cu $3d_{3z^2-r^2}$ orbitals explicitly within the TB model, is strongly required.

Compound	Ba_2CuTeO_6	Sr_2CuTeO_6	Ba_2CuWO_6	Sr_2CuWO_6
T_{max} [K]	(≤ 400)	77	180	189
θ_{CW} [K]	188	71	107	81
HTSE				
J_1 [K]	196	69	3	7
J_2 [K]	-5	-18	116	93
TB				
J_1 [K]	62	30	8	50
J_2 [K]	5	23	218	209
LSDA+U				
J_1 [K]	216	100	4	25
J_2 [K]	-2	-3	122	119

Table 3.13.: Comparison of J_1 and J_2 derived from different theoretical approaches together with the characteristic temperatures from magnetic susceptibility data for the compound family A_2CuEO_6. While the results from LSDA+U, and the evaluation of the thermodynamic measurements give a consistent picture, the exchange integrals for the Te compounds derived from the TB approach are far smaller.

For an independent evaluation of the exchange parameter QMC simulations and a HTSE of the magnetic susceptibility were performed. The evaluation of the magnetic susceptibilities is not ambiguous resulting in multiple parameter sets, which fit the experimental data with the same accuracy. However, always one of the parameter sets agrees well with the corresponding model derived from our LSDA+U approach. The parameters are given in Tab. 3.13.

These results are supported further by the recent evaluation of the magnetic models for Sr_2CuTeO_6 and Sr_2CuWO_6 using neutron scattering.[142] The derived propagation vectors are in perfect agreement with the N-AFM and C-AFM ground state of Sr_2CuTeO_6 and Sr_2CuWO_6, respectively. Furthermore, pronounced interlayer coupling for the Te compounds, which is of the order of 10 K, is also supported. However, the origin for the different inter-layer coupling regimes is up to now unclear.

In contrast, the underlying mechanism of the different character for the in-plane coupling regimes for the Te and W containing compounds is revealed by the comparison of the Cu centered WF for Sr_2CuTeO_6 and Sr_2CuWO_6, depicted in Fig. 3.50, exemplarily. Immediately the different symmetry and thus the different coupling paths becomes obvious. In the W compounds the magnetic exchange between two Cu atoms is mediated by the O atoms via the W ion along the diagonal of the square lattice. The exchange path is in line with the d-like symmetry of the W orbitals. In contrast, the exchange path in the Te compounds reflects the p-like symmetry of Te orbitals resulting in an effective transfer

along the edges of the square lattice.

Since the exchange path of the magnetic interaction is connected to the symmetry of the transferring ion, a substitution to tune the system close to the critical region between C-AFM and N-AFM order will fail conceptional. The mixing of an exchange between d- and p-like character is impossible and will lead at least to a phase separation.
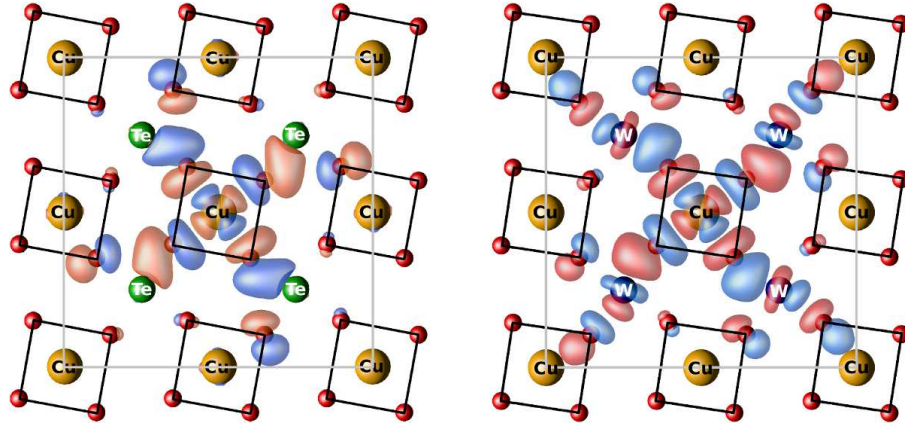

Figure 3.50.: One-band Wannier functions with $3d(x^2 - y^2)$ character for Sr_2CuTeO_6 (left) and Sr_2CuWO_6 (right). The coupling regime changes from p-like to d-like symmetry.

Summary

Combining DFT based electronic structure and model calculations we investigated the magnetic ground state of the new family of spin $1/2$-square lattice compounds A_2CuEO_6 (A=Sr, Ba and E=Te, W). Regarding our calculations all systems can be consistently described within the 2D J_1-J_2 square lattice model. We reveal a significant difference between the Te and W containing members of the compound family. The Te compounds exhibit their dominant exchange J_1 along the edges of the square lattice, resulting in a N-AFM ground state. In addition sizable inter layer couplings appear in these systems. In contrast, we found a leading exchange J_2 along the diagonals of the square lattice for the W compounds suggesting a C-AFM ordering at low temperatures. The coupling between the layers is strongly suppressed and can be neglected, in first approximation. As origin for the opposite coupling regime within the square lattice plane, we detect the symmetry of interconnecting ions as crucial parameter. An analysis of the different exchange paths from microscopic grounds using Cu centered WF, reveals a pronounced expansion of the Wannier orbitals along the edge of the lattice in accordance with the p-symmetry of Te and follow the d-symmetry in the case of an interconnecting W atom (along diagonals). This mechanism, renders the idea of a purposive substitution of the two systems impossible, to drive the compounds closer to the quantum critical region. Based on our experience we started the investigation of E =U and E =Os containing members of the A_2CuEO_6 compound family [143, 144], which could act as alternative substitution variants. In an ongoing study, especially the influence of possible relativistic effects on the coupling regime will be studied.

Our LSDA+U results are in perfect agreement with the obtained models from HTSE of the magnetic susceptibility and recent neutron diffraction experiments. The maximum in the magnetic susceptibility T_{max} and Θ_{CW} follow the same trend than the leading exchange integrals (compare Tab. 3.13). The only exception from the rather consistent picture are the exchange integrals derived from the TB approach for the Te compounds. Especially Ba_2CuTeO_6 exhibits a four times smaller J_1^{AFM} compared to the LSDA+U result, which can be related to the hybridization into lower lying states at the M-point. An expansion of the effective one-band model is required to follow the question, which underlying mechanism is limiting the applicability of our approach. The strong influence of hybridization effects between Cu $3d_{x^2-y^2}$ and Cu $3d_{3z^2-r^2}$ orbitals to the leading exchange integrals for Ba_2CuTeO_6 will be studied explicitly. However, while the coupling regime within the square lattice plane can be understood by the symmetry of interconnecting ions, the origin for the different inter layer couplings remains an open question, which will be addressed in further studies.

3.2. General trends and relations

In the last section we studied different cuprates and halides with emphasis on the magnetic properties of these materials and a reliable description of their ground state. The comparison of our computational results with experimental data and their generally good agreement reveal the power of present day electronic structure calculations. However, the theoretical approach depends on several parameters which are not known exactly. In this section we try to reveal the influence of the unknown Coulomb repulsion U_{3d} and the double counting correction (DCC) on the calculated properties for the investigated compounds. In our comparative study we follow the question whether we can deduce general trends for the family of edge shared cuprates and halides. In addition, the influence of structural peculiarities like distortion, exchanged ligands in the magnetically active CuX_4 building blocks or the crucial Cu-O-Cu bond angle are discussed focusing on possible general relations, possibly allowing reliable predictions on structural considerations or in turn a purposive modification of compounds by substitution.

3.2.1. Approximation for the treatment of strong correlation

For a series of edge shared chain and dimer chain compounds we investigated the influence of the Coulomb repulsion U_{3d} on the magnetic ground state, in particular their leading exchange integrals J_1 and J_2, or J_{1a} and J_{1b}, respectively. The obtained dependencies for a variation of U_{3d} in the physical relevant range from $4 - 8\,\text{eV}$ (within the AMF DCC) are depicted in Fig. 3.51. Foremost, we found a general decrease of the absolute strength of magnetic exchanges with increasing correlation U_{3d}. This relation is coherent with the intuitive expectations, since a stronger correlation suppresses the probability of two electrons occupying one orbital simultaneously and thus any effective exchange process.

In more detail, the NNN exchange, J_2 for the edge-shared chain compounds and J_{1b} for the dimer chain compounds (inter-dimer exchange), shows for all compounds a similar behavior. In first approximation, the behavior of J_2 and J_{1b}, respectively, is inversely proportional to U_{3d}. We observe a distinct separation between the compounds containing edge shared chains like $LiCuVO_4$, Li_2ZrCuO_4 and $PbCuSO_4(OH)_2$ (for all $J_2 \leq 12\,\text{meV}$, compare Fig. 3.51) and the structural dimer compounds $Na_3Cu_2SbO_6$, $Na_2Cu_2TeO_6$ and $Cu_2(PO_3)_2CH_2$, where the latter systems show a significant stronger NNN exchange. Comparing the exchange path for NNN interaction in edge-shared and dimer chains, the NNN distance between the Cu^{2+} ions are comparable, but in the case of the edge-shared chain systems the interacting Cu atoms are separated by other interstitious Cu atom, while the Cu sites in the dimer compounds are interconnected by non magnetic sites, in particular the equatorial plane of SbO_6 or TeO_6 octahedra (compare Fig. 3.29) or even $PO_3CH_2PO_3$ units (see Fig. 3.35).

While the significant increase of the corresponding exchange in $Sr_2Cu(PO_4)_2$,[47] an edge shared chain compound where every second plaquette is missing (resulting in a chain formed by isolated plaquettes), is well established, the increase of J_{1b} in the dimer compounds comes as a surprise. However, the replacement of a magnetically active ions by a non-magnetic ion in between the interacting Cu^{2+} atoms strengthens the exchange in these cases. (For a direct comparison of the chain geometries and NNN exchange paths see App. C.18.)

Besides the separation into edge shared and dimer chain compounds, the comparison of

the NNN exchange exhibits a strong dependance on the Cu^{2+} ligands. Comparing the resulting curves for the edge shared cuprates with the edge shared halides (triangles in Fig. 3.51), we found an increase of the magnetic exchange connected to the expansion of the magnetically active orbital.

While we yield $J_2 = 6.5\,meV$ for $LiCuVO_4$, where the Cu atoms interact via the O $2p$ orbitals, we obtain more than a doubling of $J_2 = 17\,meV$ for the magnetic exchange transferred by the Cl $3p$ orbitals in $CuCl_2$. The even larger Br $4p$ orbitals in $CuBr_2$ result in $J_2 = 30\,meV$ (all values given for $U_{3d} = 6\,eV$). The bond angle Cu-X-Cu (X =O, Cl, Br) has only minor influence on J_2, different to J_1.
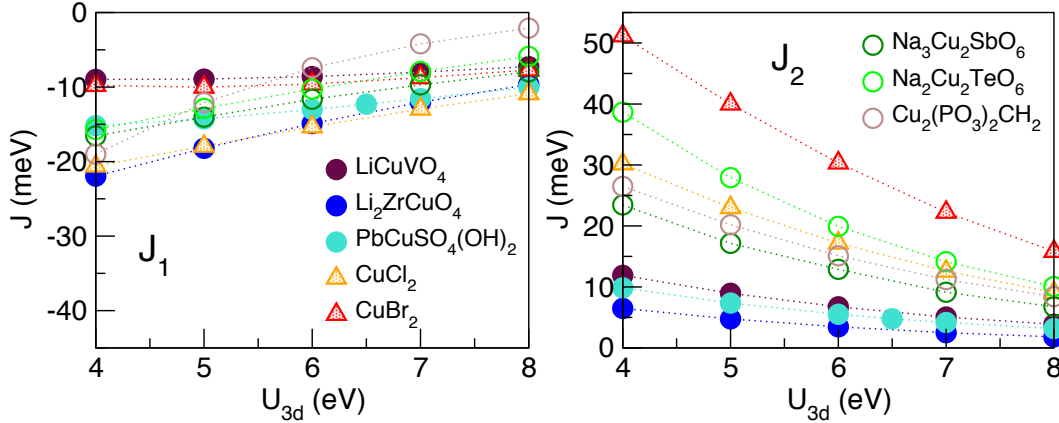

Figure 3.51.: Influence of the Coulomb repulsion U_{3d} on the leading exchange integrals of cuprates containing edge shared chains (filled circles) or structural dimer chains (open circles) and edge shared halides (triangles). While the NNN exchange J_2 (J_{1b}) exhibits a clear trend, the behavior of the NN interaction J_1 (J_{1a}) is more complex.

In contrast to the rather simple trends of the NNN exchange, the dependance of the NN exchange (J_1 in edge shared chains and J_{1a} intra-dimer interaction in dimer chain compounds) on the correlation U_{3d} is much more complex and follows no clear trend: (i) We can exclude a simple Cu-ligand distance effect comparing J_1 for $PbCuSO_4(OH)_2$ and Li_2ZrCuO_4, where J_1 is enlarged for Li_2ZrCuO_4 although the inter atomic Cu-O distances are increased by $0.1\,Å$. (ii) As a second parameter, the deviation of the O from an ideal planar chain geometry Δx and thus the chain distortion can be ruled out as solely parameter by comparing $LiCuVO_4$ ($\Delta x = 0$) with Li_2ZrCuO_4 ($\Delta x = 0.23\,Å$) and $Na_3Cu_2SbO_6$ ($\Delta x = 0.39\,Å$). The absolute values of J_1 do not follow the trend observed for the O displacement Δx. (iii) Further, we can exclude the Cu-O-Cu bonding angle as the only crucial parameter, comparing $Na_2Cu_2TeO_6$ ($\gamma = 92°$) with Li_2ZrCuO_4 ($\gamma = 94°$) and $LiCuVO_4$ ($\gamma = 95.5°$). While the Cu-O-Cu bonding angle increases continuously between these compounds, the NN exchange J_1 does not follow the same trend. (iv) Finally, we do not even observe a clear relation between J_1 and the ligands of the CuX_4 units. While the expansion of interacting orbitals increases from O via Cl to Br, $LiCuVO_4$ and $CuBr_2$ exhibit a rather similar NN exchange, in contrast to the much larger absolute values of J_1 observed for $CuCl_2$.

Taking into account these observation, the dependance of J_1 cannot be ascribed to a single parameter. Instead, our study suggests a subtle interplay of all these effects (inter atomic

distances, chain distortion, ligands and Cu-O-Cu bonding angle), which influence the orientation, expansion and energy of interacting orbitals and thus their hybridization strength. In addition, crystal field effects will affect the hybridization of states. In conclusion, a prediction of J_1 based on structural motives is far from trivial.

However, the dependance of the frustration ratio $\alpha = J_2/J_1$ (or $\alpha = J_{1b}/J_{1a}$, respectively), determining the magnetic ground state of a system, on the correlation U_{3d} is again fairly similar for all compounds (compare Fig. 3.52 left panel). The frustration ratio decreases with increasing U_{3d}, which is in line with the stronger dependance of the NNN exchange on the correlation compared to the NN interaction, since the NN exchange is not only determined by the transfer processes $J \sim t^2/U_{eff}$, but by an additional Hunds coupling. Only two systems, $CuBr_2$ and the strongly distorted dimer compound $Cu_2(PO_3)_2CH_2$, deviate from the general trend in a first evaluation. In the case of $CuBr_2$, this deviation can be traced back to a mere scaling effect related to the larger frustration ratio. The normalized frustration ratio α/α_0 with $\alpha_0 = \alpha(U_{3d} = 6\,eV)$ is in line with the trends of other cuprates and halides (see Fig. 3.52 right panel). Thus, only the deviation of $Cu_2(PO_3)_2CH_2$ from the general trend remains. This compound shows even the opposite behavior in the trend of the normalized ratio. Since $Cu_2(PO_3)_2CH_2$ crystallizes in a complex crystal structure giving rise to a variety of slightly different, inequivalent inter chain couplings, we averaged these interactions to an effective inter chain coupling, which is of similar size than J_{1a}. Therefore, the accuracy of the developed model should be improved, before the compound can be established as an exception from the general trend observed in all other compounds. To settle this question, further studies are needed.
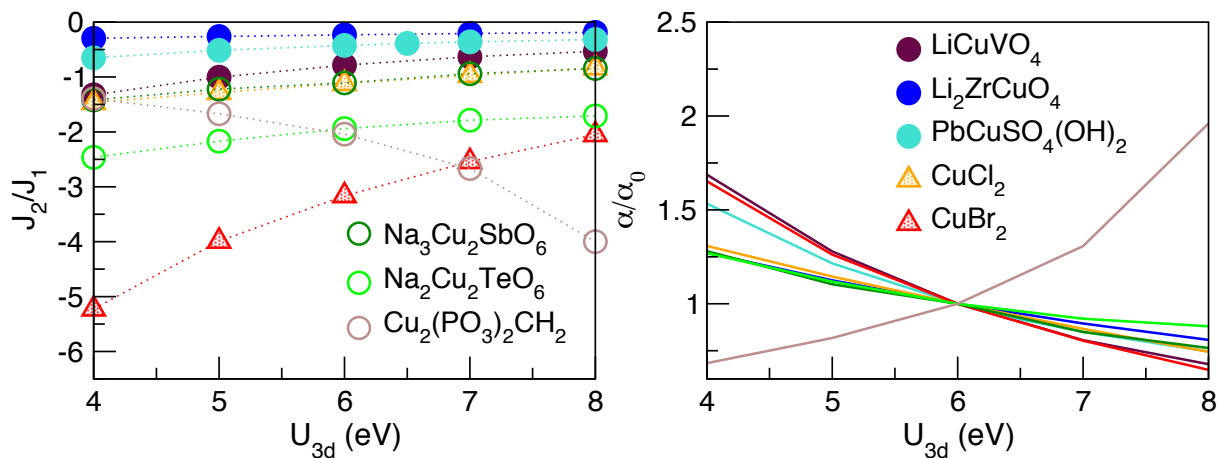

Figure 3.52.: Influence of the Coulomb repulsion U_{3d} on the frustration ratio α. The normalized frustration ratio α/α_0 with $\alpha_0 = \alpha(U_{3d} = 6\,eV)$ exhibits a very similar behavior for all compounds with the only exception of $Cu_2(PO_3)_2CH_2$.

It was recently shown, that the results of LSDA+U calculations depend not only on the specific choice of U_{3d} but can also be sensitive to the choice of the double counting correction (DCC). Especially in the family of vanadates the DCC can have a dramatic effect.[145] For $CdVO_3$ different DCC lead not only to a scaling of the calculated exchange parameters, but even to a change in their sign.

For most compounds investigated in this work, the different DCC yield mostly adequate results with minor influence on the frustration ratio, only. While the absolute values of

exchange integrals are changed, we observe a nearly perfect agreement for the frustration ratios (see App. C.17). Only small deviations occur for LiCuVO$_4$ and CuCl$_2$. In contrast, the DCC has considerable influence for CuBr$_2$ and Cu$_2$(PO$_3$)$_2$CH$_2$. Nevertheless, for all examples, the magnetic ground state is robust against the choice of the DCC.

To deduce any general relation for the influence of the DCC is far from trivial. In many cases a simple shift of U_{3d} between the AMF DCC and FLL DCC by 1.5- 2 eV yields nearly identical results. However, for systems with strongly distorted (non planar) Cu coordination (as in Cu$_2$(PO$_3$)$_2$CH$_2$), for systems where more than two Cu atoms are connected to the ligand (e.g. azurite [146]), for compounds with a strong covalent bonding of Cu^{2+} to its ligand (as in CuBr$_2$) or for systems with short Cu-ligand distances (e.g. in several vanadates [145]) the DCC has considerable influence. Comparing these examples ligand field effects seems to be a crucial parameter. However, extended studies are required for the development of any general relation to predict the influence of the DCC on the properties of a certain material.

3.2.2. Structural elements

In order to tune the physical properties of a compound by the intended modification of its crystal structure, we tried to separate the influence of different structural peculiarities on the magnetic properties. Based on these experiences, a modification of the low temperature magnetism of cuprates by selective substitution or pressure could become predictable.

In Fig. 3.53 the influence of the chain distortion on the frustration ratio for different U_{3d} is depicted. However, the comparison of the distorted edge shared chain compounds Li$_2$ZrCuO$_4$ and PbCuSO$_4$(OH)$_2$ and the distorted dimer-chain compounds Na$_3$Cu$_2$SbO$_6$ and Na$_2$Cu$_2$TeO$_6$ with their ideal planar variants exhibit opposite trends.

The development of the NNN exchange J_2 for Li$_2$ZrCuO$_4$ and PbCuSO$_4$(OH)$_2$ is rather intuitive. In the experimentally observed distorted chain geometry, the interacting orbitals are oriented within different planes, impeding the respective transfer path via the O ligands and this way suppressing J_2. The orientation becomes more favorable within the ideal, planar chain geometry, where the magnetic active orbitals lay within the same plane supporting the transfer processes. In contrast to the increased NNN interaction, the NN exchange J_1 is reduced in the planar systems, especially for small correlations. A possible scenario for this trend is a strengthening of the Hunds coupling in the non planar geometry resulting in three partially filled O orbitals (in contrast to the two partially filled orbitals in the ideal planar system), which all contribute to an effective FM coupling. Especially for small correlation, this effect has a sizable influence due to a stronger Cu-O hybridization. Nevertheless, the frustration ratio is shifted towards larger values for the fictitious planar compounds.

The trend observed for the dimer compounds Na$_3$Cu$_2$SbO$_6$ and Na$_2$Cu$_2$TeO$_6$ depending on the distortion is significantly different. The NNN exchange J_{1b} between the structural dimers remains nearly unchanged since the distortion does not affect the local surrounding between the magnetically active Cu atoms. The slight reduction of J_{1b} in the planar compounds (opposite trend compared to the chain compounds) originates mainly from changed inter atomic distances (compare discussion in Sec. 3.1.5). In contrast to the edge shared systems, the NN exchange J_{1a} in the dimer compounds is enlarged for the planar structures. Although at first glance counter intuitive, this trend follows the same scenario as described above. For the distorted structure all three orbitals at the O site are partially
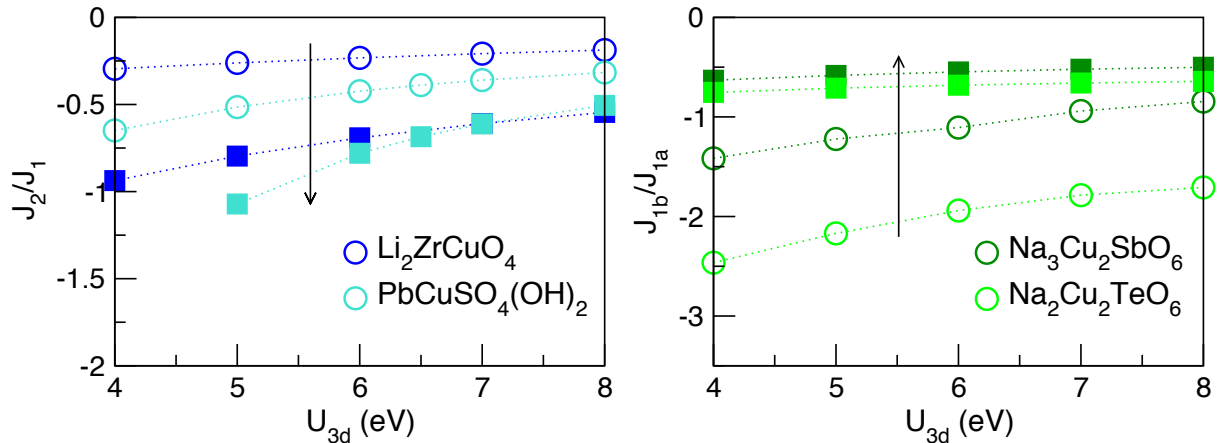
Figure 3.53.: Influence of the Coulomb repulsion U_{3d} on the frustration ratio α for compounds with different strong distortion of the CuO_4 plaquettes. The relation between the shift of α and the strength of distortion for edge shared chain systems is the opposite for structural dimer chain compounds. (distorted structure=circles, planar geometry = squares)

filled, but with the difference that the O $2p_z$ orbital couples directly to the neighboring chain in line with the O $2p_z$ and Cu $3d_{3z^2-r^2}$ character in the orbital resolved density of states for $Na_3Cu_2SbO_6$ (compare Fig 3.31). For the planar system, the exchange along z is suppressed resulting in a stronger hybridization with the planar O orbitals.

As a second structural element, we investigated the role of the Cu-O-Cu bonding angle, bridging two magnetic active Cu^{2+} ions along the edge shared units. In many cases the GKA rules, which predict an AFM NN exchange for bond angle of 180° and FM NN exchange for bond angles of 90°, allow a first (often convincing) estimation of the magnetic exchange integrals. In accordance with the GKA rule many cuprates with typical bonding angles between 92° and 95° show FM NN interaction like $LiCuVO_4$ or Li_2CuO_2, while the famous spin Peierls compound $CuGeO_3$ with an bonding angle of 98.4° is determined by an AFM NN exchange. Thus, in real compounds, crystal field effects and bond angles between the "limiting" cases of 180° and 90° complicate the picture and impede a straight forward prediction. The dependance of J_1 on the bond angle was investigated earlier for $CuGeO_3$ based on cluster calculation without considering crystal field effects.[147] To gain deeper insight into the influence of the bond angle on the exchange interactions, as a precondition to develop a more precise description, we carried out a systematic study.

Therefore, we varied the bonding angle of several edge shared compounds for a fixed Cu-O (or ligand) distance and calculated the leading exchanges J_1 and J_2 using LSDA+U calculations of magnetic super cells.

We restricted the variation of the Cu-O-Cu bonding angle for fixed Cu-O distance to an angle range from 75° to 110° due to strong, unphysical hybridization effects of the ligands hampering the results for smaller and larger values, respectively. For bond angles smaller than 90° the CuO_4 plaquettes are deformed from an ideal square geometry into rectangles, where the short edge of the rectangle runs along the chain direction. This way the O atoms along the chain direction come closer and closer, resulting in an increase of J_2, until far too short inter atomic distances cause exaggerated direct ligand-ligand interactions.

In the case of bond angles larger than 90°, the CuO$_4$ plaquettes are deformed along the opposite direction (the short edge of the rectangle runs now perpendicular to the chain direction). Thus, the ligands perpendicular to the chain direction come significant closer influencing the exchange interactions in a complex way. For CuCl$_2$ and CuBr$_2$, with their stronger extension of ligand orbitals, the range of a reliable bond angle variation is even stronger restricted. We exclude bond angles larger than 100° from our comparative study (grey shadowed). For the cuprates similar effects seems to appear for bond angles smaller than 80°. In consequence, also these regions are excluded (grey shadowed).

In Fig. 3.54 the change of the chain geometry together with the Cu centered Wannier functions for CuBr$_2$ are depicted, exemplarily.

The deformation of the plaquettes affects not only the intra chain geometry, but also the inter chain distances. To exclude artificial effects on the derived parameter we checked the influence of a modified inter chain distance on the leading exchange integrals. For the two limiting cases, CuF$_2$ and CuBr$_2$, with a minimal and maximal expansion of Cu^{2+} ligands, we observe only small deviations (compare App. C.10 and C.11).
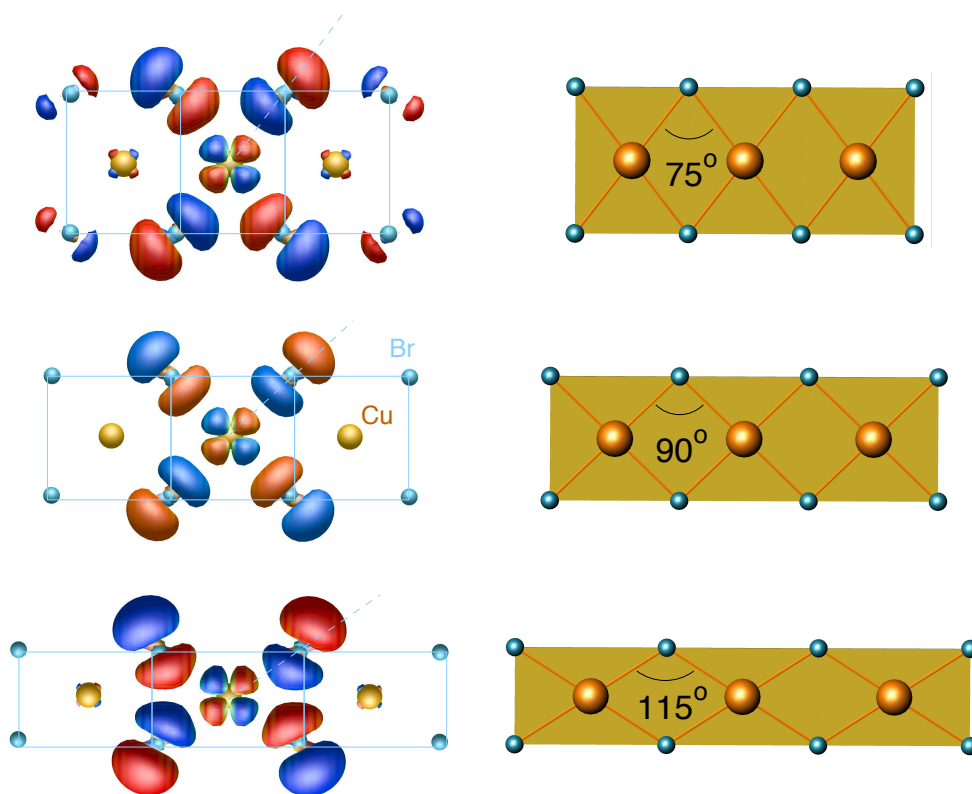

Figure 3.54.: Comparison of the Cu centered WF of CuBr$_2$ for different Cu-Br-Cu bond angles. Since the Cu-Br distance is fixed during the angle variation, the chain geometry becomes rectangular distorted, resulting in extremely short Br-Br distances along (75°) and perpendicular (115°) to the chain direction. For small angles the WF show a strong extension to neighboring Br atoms along the chain.

Unfortunately, varying the Cu-O-Cu bonding angel for a fixed Cu-O distance in a solid,

affects at the same time several other inter-atomic distances. Since their impact on the probed exchange integrals, e.g. by a changed crystal field, is hard to predict, we compared our calculated parameter derived for the solid with cluster calculation using well converged chain segments. Already for cluster sizes of few Cu atoms we obtain a surprisingly good agreement of the leading exchanges J_1 and J_2 tested for $CuCl_2$, $CuBr_2$ and a fictitiouse isostructural system CuF_2.[148][24]

Besides the family of edge shared halides, we included Li_2CuO_2 and $NaCu_2O_2$ [132] as representatives of typical edge shared cuprates in our comparative study. These systems contain only few additional (inter chain) ions in a simple geometry to avoid as much as possible effects from energetically unfavorable distortion of structural building blocks beyond the CuO_4 chain. Finally we considered $CuGeO_3$ in our investigation allowing to compare our results with earlier studies. The variation of the Cu-O-Cu bond angle in $CuGeO_3$ was realized in two ways: (i) First, we varied the chain geometry (changed bonding angle, but fixed Cu-O distance) in a way, that the relative placement and inter atomic distances of the connecting GeO_4 tetrahedra remain unchanged. In consequence, the orientation of neighboring chains differs. (ii) Alternatively, we substituted the GeO_4 tetrahedra by Sr atoms. This way, the effects from the relative shift of the building blocks and the influence of the crystal field can be estimated.

In Fig. 3.55 the dependance of the leading exchange integrals on the the Cu-O-Cu bond angle is depicted. While the trend in the NN exchange J_1 is more complex, the NNN exchange J_2 exhibits simple relations. First, the strength of J_2 depends strongly on the expansion of the ligands (from Br (4p)- Cl (3p)- O (2p)- F(2p)) as one expects from an intuitive picture. Secondly, J_2 scales with the distance, already obvious following J_2 from 75° to 100° where the NNN distance change from about $3.0\,\text{Å}$ to $4.0\,\text{Å}$ for $CuBr_2$, exemplarily. Only, the artificial $CuGeO_3$ system, where the connecting GeO_4 tetrahedra are substituted by Sr, shows an unusual behavior at low bonding angles. The changes in the crystal structure hinders the NNN exchange for small angles, originating from a changed transfer path and most likely a changed crystal field. At the same time, a strong increase of the inter chain exchange is observed (not shown).

Comparing the NN exchange J_1 for all investigated compounds, the derivation of a common relation between the bonding angle and magnetic exchange is at least difficult. For most compounds, J_1 transforms from a FM to AFM interaction by changing its sign for large bonding angle. Exceptions are the two halides $CuCl_2$ and $CuBr_2$. For Cu-X-Cu bond angle above 100° the NN exchange J_1 turn down, since the ligands along the edge of the distorted CuX_4 ($X =$Cl, Br) plaquettes come far too close. In accordance, the down-turn for $CuBr_2$, exhibiting a stronger expansion of $4p$ orbitals in space compared to the $3p$ orbitals of $CuCl_2$, occurs earlier. The maximal FM couplings appear at 78° and 85° for $CuCl_2$ and $CuBr_2$, respectively. The fictitious system CuF_2, with its well localized F $2p$ ligand states, show a smooth behavior in the whole range of bond angles. We found a maximal FM exchange close to 90° and a change from a FM to AFM coupling at about 100°.

The change from FM to AFM exchange for the edge shared cuprates Li_2CuO_2 and $NaCu_2O_2$ appears close 100° (difference smaller than 2°), similar to the observation for CuF_2. How-

---

[24]At ambient condition, CuF_2 crystallizes in the same type of crystal structure like CuO. To unravel the influence of the Cu^{2+} ligands on the magnetic exchange in a systematic way, we constructed an artificial CuF_2 system isostructural to the chain compounds $CuCl_2$ and $CuBr_2$ and optimized the lattice parameter. The crystallographic data are given in App. B.9.
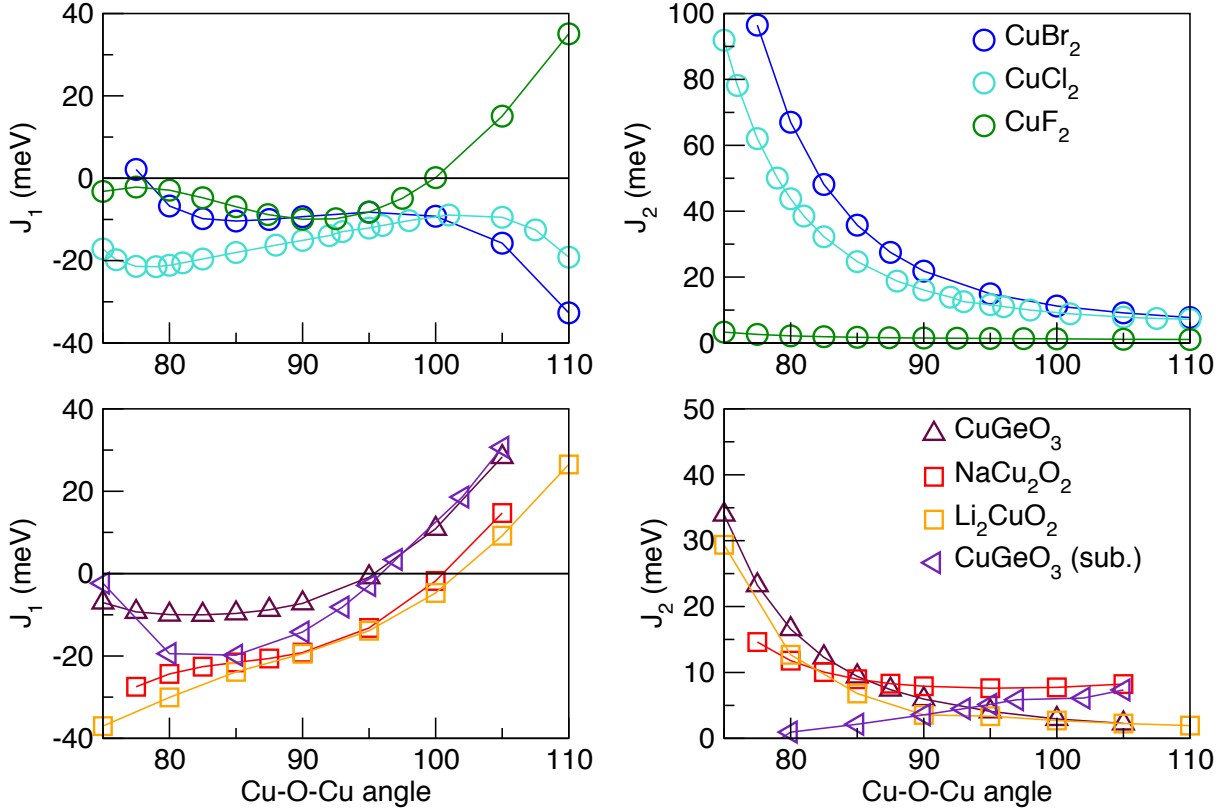
Figure 3.55.: Influence of the bridging angle to the leading magnetic exchange interaction for Cu^{2+} compounds with edge shared chain geometry. Whereas the trend in J_2 are rather intuitive, the behavior of J_1 is more complex.

ever this compounds show no absolute maxima in their FM exchange.

In contrast, the transition from FM to AFM in $CuGeO_3$ is shifted to sizable smaller boning angle. For the real crystal structure of $CuGeO_3$ and its substituted variant, J_1 changes sign at about 96°. The whole trend of J_1 is in good agreement with the study of Braden *et al.* [147], where the influence of the bond angle was evaluated by cluster calculations.

To gain deeper insight into these differences, we systematically compared the (i) AFM and FM parts of the exchange integrals derived from our TB model approach in comparison with the results from LSDA+U SC calculations and (ii) the orbital occupation of the bridging ligands for all compounds under consideration.

The AFM parts of the exchange integrals for the cuprates are depicted in Fig. 3.56 (right panel). They consistently exhibit a minimum around 85° in agreement with the earlier reported angle dependence in $CuGeO_3$ [147]. For the halides the minimum is shifted to larger angles and appears around 90° or at even slightly larger angles (see Fig. 3.57, right panel). However, we excluded the angle region above 100° for $CuCl_2$ and $CuBr_2$ in our study, since in this region exaggerated effects from ligand-ligand interactions due to the too short interatomic distances along the chain direction give raise to unphysical contributions.

Comparing the FM parts of exchange integrals for all compounds no simple trend becomes obvious at first glance. But relating the FM parts of exchange integrals to the p-orbital occupation of the ligands elucidate a consistent picture.
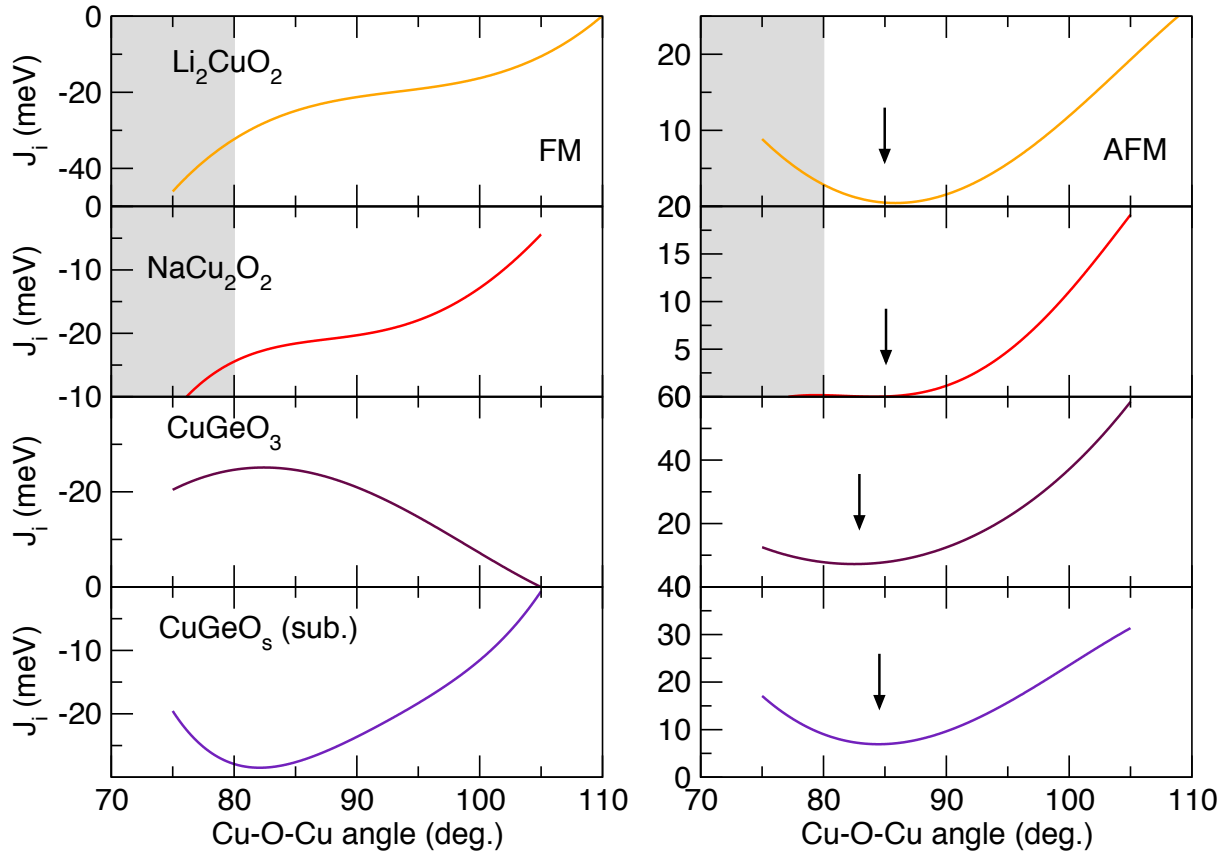
Figure 3.56.: Influence of the Cu-O-Cu bond angle on the FM (left) and AFM (right) contribution to J_1 for different cuprates. The AFM part is derived using an WF TB model approach, whereas the FM contributions are obtained by the difference to the LSDA+U SC calculations according $J_{FM} = J_{TOT} - J_{AFM}$.

The p-orbital occupation of the ligands within the CuX_4 plaquettes as function of the bridging angle is depicted in Fig. 3.58. For a projection of the LSDA+U density of states we chose a local coordinate system where x' runs along the chain direction and z' perpendicular to the chain plane. For all compounds the p_z orbital is almost fully occupied and quasi constant for the whole range of varied bond angles. Only the occupation of Op_z for NaCu$_2$O$_2$ is sizably reduced in accordance with the crystal structure, where non magnetic CuO$_2$ units connect the edge shared CuO$_4$ chains along z.

All compounds exhibit the same general trend: the occupation of p_y orbitals increases for an increasing bond angle, while at the same time the p_x states become depopulated. This trend is in line with the example of the orbital occupation of O in the limiting case of Sr$_2$CuO$_3$, containing corner shared chains with bond angles of 180° and $p_x = 0.7$, $p_y = 0.9$ and $p_z = 0.86$. For all compounds the experimental bond angle is indicated by a dashed line. Consistently it appears in a range where p_y is slightly stronger occupied compared to p_x. The only exception is CuGeO$_3$ with an opposite balance between p_x and p_y.

The p-orbital occupation of ligands is influenced by the crystal field (ligand field) and ligand-ligand interactions. Without this two effects, an equivalent occupation of p_x and p_y around 90° is expected and a maximal FM exchange for 90° due to the cancelation of any
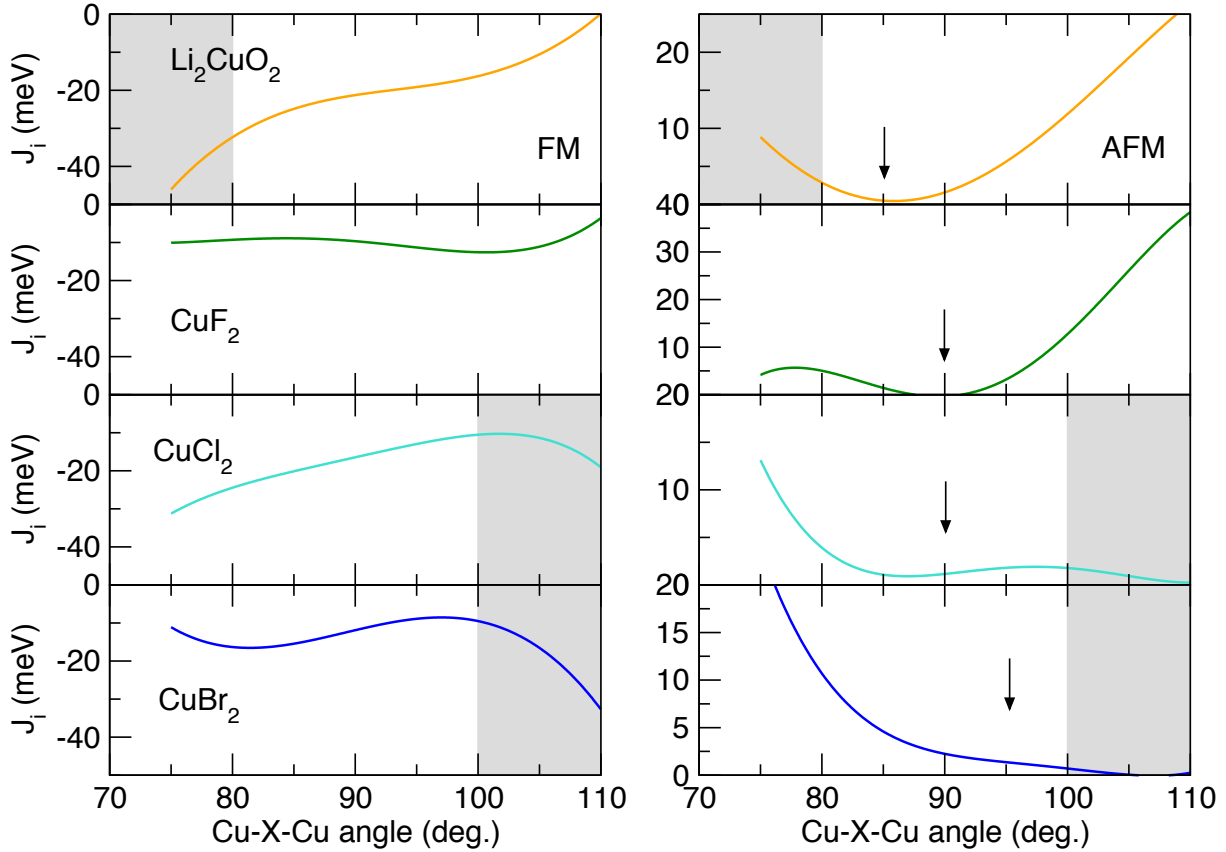
Figure 3.57.: Influence of the Cu-X-Cu bond angle on the FM (left) and AFM (right) contribution to J_1 for different halides and Li_2CuO_2. The AFM part is derived using an WF TB model approach, whereas the FM contributions are obtained by the difference to the LSDA+U SC calculations according $J_{FM} = J_{TOT} - J_{AFM}$.

AFM contributions in accordance with the Hunds rules.

For the cuprates Li_2CuO_2 and $NaCu_2O_2$ we found the crossing point of p_x and p_y occupation close to 90°. In contrast, this point is shifted towards bond angles larger than 100° for $CuGeO_3$, where strong crystal field effects are expected due to the interconnecting GeO_4 tetrahedrons. Substituting this building blocks by Sr atoms reduces the crystal field effects and the crossing point between p_x and p_y occupation appears slightly below 90° similar to Li_2CuO_2 and $NaCu_2O_2$.

For the halides, where the bridging O atoms are replaced by F, Cl or Br, the ligand-ligand interactions are modified. Especially for Cl and Br with their stronger expansion of $3p$ and $4p$ states such effects become important. As a consequence, the point of equal occupation of p_x and p_y orbitals is significantly shifted to smaller bond angles. The ligand-ligand interaction of orbitals perpendicular to the chain direction has a stronger influence on the orbital occupation than ligand-ligand interaction along the chain.

Although the orbital occupation of ligands is not understood in all details, its connection to the FM parts of exchange integrals becomes obvious. In all cases, the maximal, reliable FM contribution appears close to the point, where p_x and p_y are occupied equally. In the
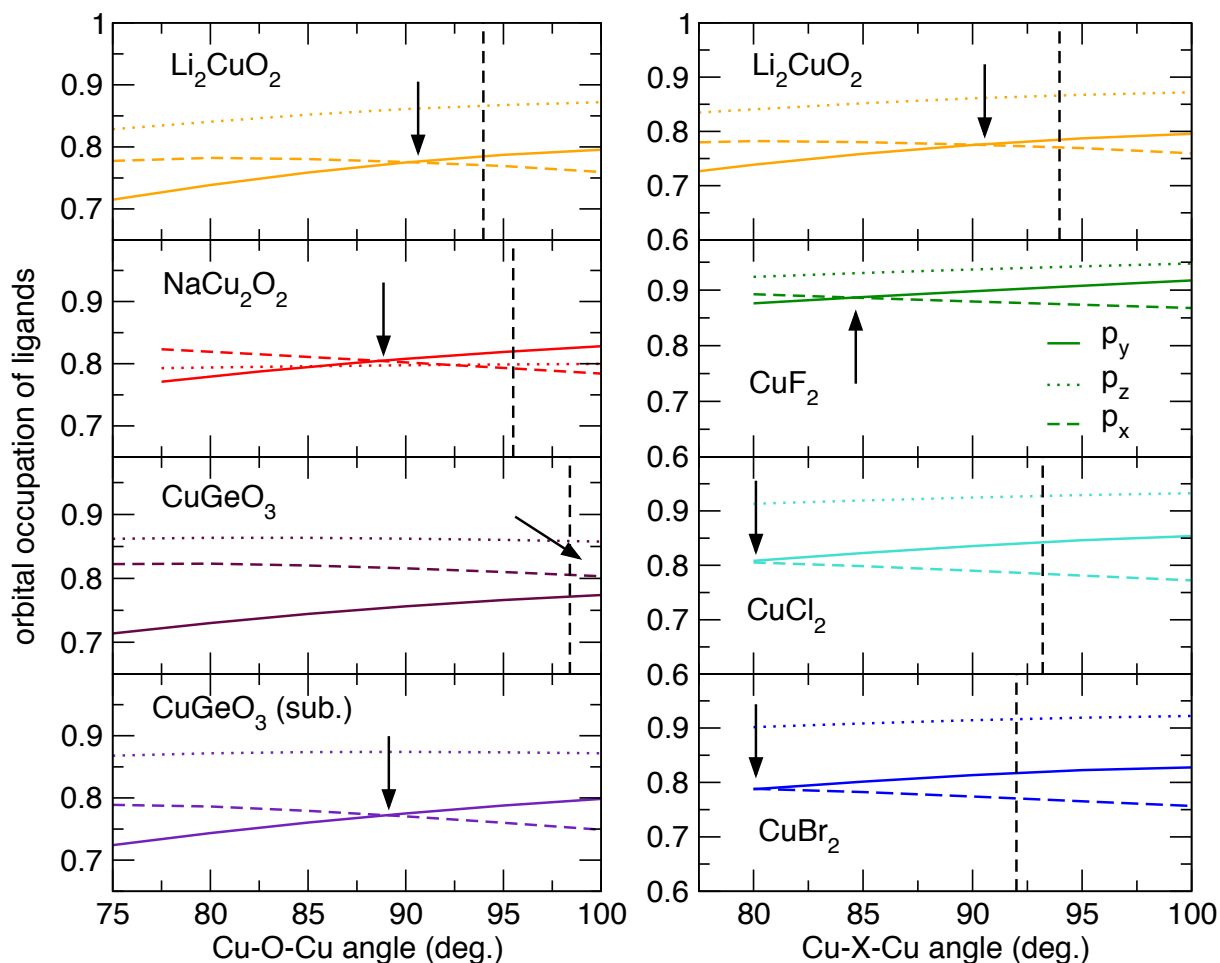
Figure 3.58.: Development of the p-orbital occupation of ligands within the CuX_4 plaquettes ($X =$O, Cl, Br, F) for different bond angles. Crystal field effects and ligand-ligand interaction influence the position of an equal occupation between p_x and p_y orbitals (arrows). The experimental bond angles are indicated by dashed lines.

case of Li_2CuO_2 and $NaCu_2O_2$ it is the inflection point close to 90°. For $CuGeO_3$ this point is expected for angels above the studied angle range, but for the Sr substituted variant the crossing point and the maximal FM contribution coincide. For the halides maximal FM interactions take place at small bridging angles. The down turn of the calculated behavior above 100°, described to unphysical effects originating from distorted plaquette geometry, appears at a similarly unbalanced orbital occupation than in the cuprates for small angles.

Summary

To conclude, our systematic study illustrates the complex balance between a variety of parameter influencing the magnetic exchange interactions in this class of materials. However, the derived trends are rather robust against the specific treatment of strong correlation for the investigated compounds, in particular U_{3d} and the DCC. On the other hand, to derive any general rules for the relation between the leading exchange integrals J_1 and

J_2 to structural peculiarities is a sever challenge. Whereas the long range interactions containing J_2 are mostly related to distance effects, modulated by the orbital extension of ligands, the coupling strength of J_1 sensitively depend on a variety of different parameters. Distance effects, orbital extension of ligands, crystal field effects, distortion and changed bond angles influence the NN exchange in a complex way. Comparing the influence of chain distortion for several compounds reveals consistently a suppression of the magnetic long range couplings, if the interacting orbitals are not placed within the same plane, whereas distortion mainly tunes the FM contribution to the exchange for J_1 in a non trivial way. The systematic study of the leading exchange integrals with respect to a variation of bond angles found a subtle balance of crystal field and ligand-ligand effects to J_1, whereas J_2 follows similar distance effects than mentioned above. The trend of FM contributions to J_1 can be connected to the orbital occupation of ligands, whereas the strength of AFM parts are rather similar in all compounds and in line with an earlier study of $CuGeO_3$. However, these findings are still far too crude to develop magnetic models for new compounds from structural consideration, only. An expansion of our approach to multi band models is required to further separate the individual contributions to the exchange process and to unravel a microscopic picture for the underlying mechanism ruling J_1.

4. Magnetic intermetallic compounds under extreme conditions

In the last chapter we combined DFT based electronic structure and model calculations to describe the magnetic properties of low dimensional materials containing well localized magnetic moments. The developed and refined magnetic models, derived from microscopic grounds, allow in all cases a conclusive interpretation of the experimental observations, although the investigated materials are ruled by strong correlations, which are still challenging for present day DFT calculation.

The successful application of our theoretical approach to strongly correlated systems, suggests an even unpretentious description and modeling of magnetic properties for intermetallic compounds. Since this work was developed in the Max Planck Institute for Chemical Physics of Solids, an institute with special emphasis on the physics and chemistry of intermetallic compounds, the close neighborhood to experimentalists stimulated several common projects. In the next section, examples of this common investigations are presented, which were motivated and further developed by the close interplay of theory and experiment during the period of this thesis.

These studies benefit from the unique experimental opportunities and large experience within the class of intermetallic compounds present in the institute. The theoretical calculations do not only describe the experimentally observed phenomena in a realistic way, but also demonstrate the predictive power of present day DFT calculations. In the presented cases, the theoretical predicted phenomena and developed models were challenged experimentally using state of the art techniques of modern synchrotron facilities.

In particular, we studied the close interplay of magnetism and structural phase transition in the two itinerant systems YCo_5 and $SrFe_2As_2$ and the compound series $EuPd_3B_x$ containing well localized moments. All systems show a structural phase transition induced by pressure and/or doping, but the respective driving forces are different. We identified a magnetic instability, the formation of new bonds and a valence transition as underlaying mechanism for the onset of the phase transitions, for YCo_5 (Sec. 4.1.1), $SrFe_2As_2$ (Sec. 4.1.2) and $EuPd_3B_x$ (Sec. 4.2.1), respectively.

4.1. Itinerant magnets

4.1.1. YCo$_5$ - a direct proof for a magneto elastic transition by XMCD

Recently, a new type of electronically driven phase transition was reported for the itinerant ferromagnet YCo$_5$.[49, 149] At high pressure the compound shows an isomorphic lattice collapse connected to a sudden change of its magnetic moment. Electronically driven phase transitions resulting in an isomorphic lattice collapse had already been observed earlier in Ce metal or SmS with a volume reduction of about 15% under pressure. Whereas in these examples the volume instability is connected to an altering contribution of $4f$ electrons to the chemical bonding [150, 151] or to a change in the valence state [152], respectively, the intermetallic compound YCo$_5$ exhibits a stable valence. Furthermore, DFT based calculations point to a magnetic mechanism as driving force for the phase transition in YCo$_5$ and classify the phase transition as an electronic topological transition.[49, 149] Motivated by these studies, we tried to provide a direct experimental evidence for this magneto-elastic transition.

A direct way of detecting a magnetic instability that is coupled to the lattice degrees of freedom would require measuring a magnetization related parameter under applied pressure. Due to the very high transition pressure of about 20 GPa, such measurements are a severe technical challenge. However, we succeeded to provide direct experimental evidence for the magnetic nature of the observed phenomenon based on X-ray magnetic circular dichroism (XMCD) measurements for the Co K-edge under pressures up to 22.5 GPa. The experiments were accompanied by DFT calculations that link the observed sudden decrease of the Co $4p$ polarization to the drop of the Co $3d$ magnetic moments. The obtained temperature dependent transition pressure is in perfect agreement with the earlier reported XRD results;[49] its zero-temperature extrapolation matches the calculated value. As expected within the proposed itinerant magnetism scenario, the critical pressure decreases with temperature.

YCo$_5$ crystallizes in the CaCu$_5$ structure type (see inset Fig. 4.2) with the hexagonal space group $P6/mmm$. All atoms occupy special positions (Y $1a$, Co $2c$ and $3g$). For a given volume, according to a certain experimental pressure, the c/a ratio as the only free structural parameter was optimized with respect to the total energy. The obtained dependance of the c/a ratio on the unit cell volume shows a clear discontinuity between 74 and 72 Å^3. The related volume collapse of 1.3%, estimated from the equation of states of the low- and high pressure phase, is accompanied by a sudden drop of the Co moment (compare Fig. 4.1, left and Ref. [49]). An evaluation of the calculated density of states (DOS) gains more insight into the underlying mechanism of this effect. Exemplarily the corresponding DOS for two volumes well below and above the transition are depicted in Fig. 4.1. At ambient pressure, YCo$_5$ is an archetypal strong ferromagnet exhibiting a full polarization of the Co $3d$ majority states. According to Ref. [49] a singularity in the electronic density of states (DOS) moves through the Fermi energy with increasing pressure (decreasing volume) (arrows in Fig. 4.1, right) and results in a sudden depopulation of anti bonding majority states. At this point, the energy gain due to an increase of chemical bonding overcomes the magnetic exchange interaction, causing a strong reduction of the ferromagnetic moment and at the same time a pronounced anomaly in the lattice parameter. This volume instability was experimentally confirmed by XRD measurements under high pressure. Although good agreement between the calculated and the measured transition pressure was obtained eval-
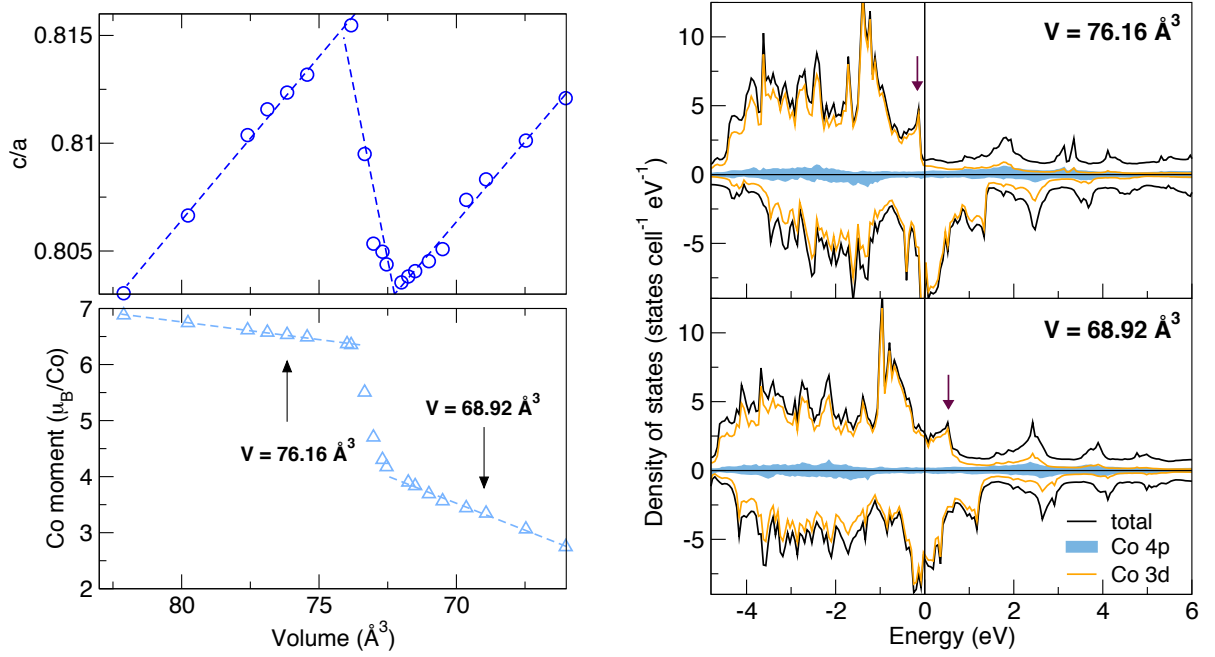
Figure 4.1.: Left: Optimized ratio c/a for different volumes (top) and development of the Co moment (bottom) for YCo_5. The collapse of the unit cell volume (discontinuity in c/a) coincides with a pronounced change of the Co magnetic moment. Right: Calculated total density of states in comparison to the Co $4p$ states for large and small volumes (low and high pressure). The arrow denotes the van Hoven singularity responsible for the transition.

uating the structural change, a direct proof of the magnetic origin for this phase transition is still missing.

X-ray magnetic circular dichroism (XMCD) under pressure

In order to give such a direct evidence we performed x-ray absorption spectroscopy (XAS) and XMCD measurements at the energy dispersive XAS beam-line ID24 of the ESRF using the setup reported in Ref. [153], upgraded with a He cryostat especially designed for high pressure magnetic measurements. Unfortunately, the strong absorption of the diamonds at low X-ray energies inhibits the collection of XMCD spectra at the Co L-edges ($2p - 3d$). Therefore, we performed our measurements at the alternative Co K edge (7 709 eV, 1s-4p) [153]. This unfavorable change from the L- to K-edge impedes the measurements, since the Co magnetic moment is mainly determined by the polarization of Co $3d$ states (corresponding to the L-edge), whereas the measurements at the K-edge mainly probe Co $4p$ states. These states follow the polarization of Co $3d$ states by hybridization effects, but exhibit a much smaller contribution to the DOS. However, we used a membrane type non-magnetic Cu-Be DAC equipped with 1.2 mm perforated anvils in order to reduce the absorption[1]. Due to the very small XMCD cross section of the order 10^{-3} of the absorption jump at the $3d$ transition metal K-edges, the detection of the weak XMCD

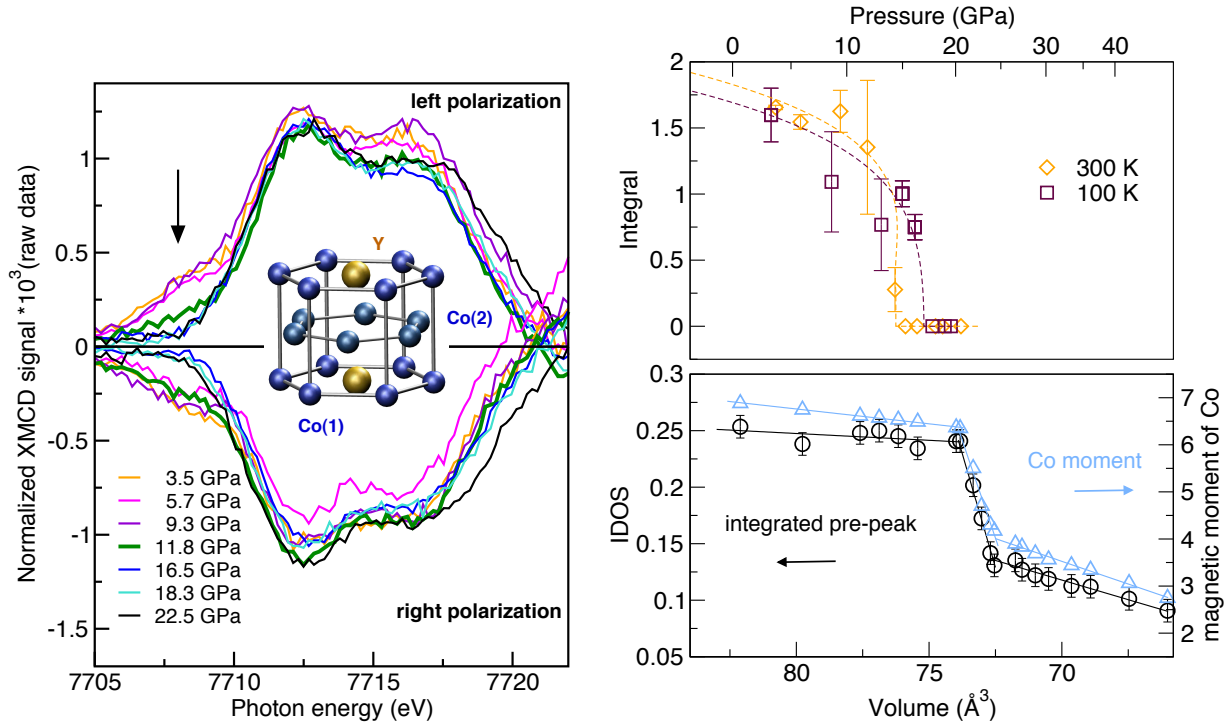[1]The transmission through a pair of 1.2 mm diamonds at the Co K-edge is about 1.6%.

Figure 4.2.: Left: Normalized room temperature XMCD spectra measured for selected pressures up to 22.5 GPa. A low energy shoulder of the signal disappears with increasing pressure (black arrow). Inset: Crystal structure of YCo_5. Right: Comparison of experimental and theoretical development of the XMCD signal-shoulder under pressure. Top: Integral of the first Gaussian peak used to model the pre-peak region of the experimental signal. Bottom: Calculated integrated DOS of the XMCD pre-peak together with the calculated magnetic moment of Co.

signal nonetheless remains a demanding experimental challenge.

The normalized (and background corrected) room temperature XMCD spectra, measured for increasing pressure in both polarization directions, are shown in Fig. 4.2 (left). The good agreement between both helicities indicates reliability and reproducibility of the measured XMCD signal. Ambient-pressure data on the closely related $LaCo_5$ show a similar shape of the XMCD spectrum [154]. The most characteristic change of the signal under pressure is the disappearance of the low energy shoulder between 7 705 and 7 710 eV (arrow in Fig. 4.2). For pressures below about 10 GPa, the spectra remain almost unchanged, containing two main peaks and a shoulder at low energies. Increasing the pressure above about 10 GPa causes a rapid decrease of the intensity for this pre-peak (shoulder) until it is fully suppressed at pressures higher than 15 GPa. This suppression threshold is close to the critical pressure of the structural phase transition observed in the XRD experiment [49], indicating an intimate relation of both phenomena. The pressure induced change of the spectra is fully reversible.

Development of the electronic structure under pressure

To confirm the direct relation between the magnetic and structural transition, we calculated the total and the partial Co 4p density of states together with the related spin polarizations for the entire measured pressure range.[2] Fig. 4.1 (right) shows exemplarily the corresponding curves for two volumes well below and above the transition. According to Ref. [49], this transition is characterized by a sudden shift of a Co 3d-related van-Hove singularity across the Fermi level (arrows in Fig. 4.1, right). The Co 4p density of states is rather small, and a change of these states is hardly visible at first glance. Thus, it is more instructive to look at the difference between the majority and minority spin DOS. Fig. 4.3 (left) shows the corresponding Co 4p polarization, which is directly related to the measured XMCD signal, in comparison to the total polarization. To present the Co 4p data together with the much larger total polarization dominated by Co 3d contributions, the Co 4p data had to be multiplied by a factor of five. Already by a first evaluation, the low pressure Co 4p polarization is clearly larger than that of the high pressure phase. The contributions of the two different Co sites are rather similar.
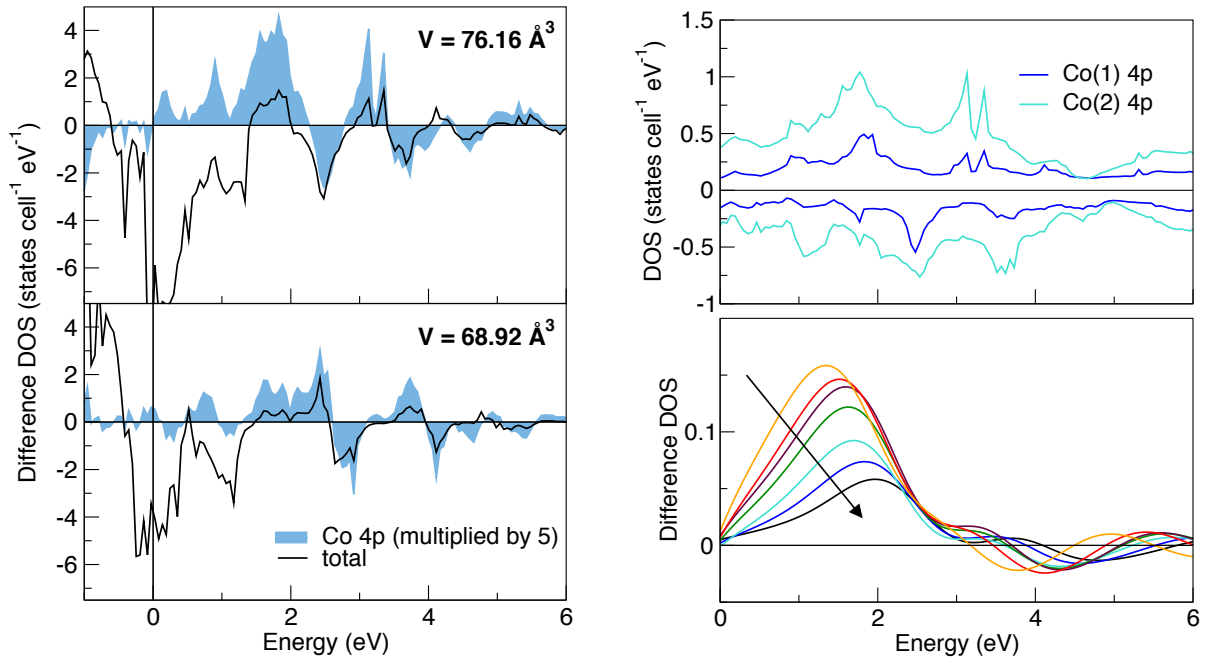

Figure 4.3.: Left: Spin polarization given by the difference of majority and minority DOS for the low and high pressure phase. Right: Unoccupied DOS for the two different Co sites in the energy range of the XMCD signal shoulder. (top). Calculated Co 4p polarization above the Fermi energy, broadened with the experimental resolution of 1.3 eV. The direction of increasing pressure is denoted by the arrow (bottom).

Corresponding analyses were carried out for several different pressures up to 50 GPa. The resulting Co 4p polarization were broadened with the experimental resolution of 1.3 eV,

---

[2]To probe the transition directly at the *L*-edge was hindered by the strong absorption of diamonds in the relevant energy range.

see Fig. 4.3 (right, lower panel). The most prominent first peak in the polarization of the unoccupied Co $4p$ states between the Fermi level and 2.5 eV is monotonically decreasing with increasing pressure. Structures at higher energy merely oscillate, so that the integrated polarization is not very sensitive to the chosen upper bound. The lower panel of Fig. 4.2 displays the calculated integral of the Co $4p$ polarization taken between the Fermi level and 5 eV (black circles), error bars indicating the range of values obtained by shifting the upper integration limit between 4 eV and 6 eV. The variation of the broadening between 0.7 eV and 1.5 eV does not change the picture qualitatively. For comparison, the total magnetic spin moment of Co is shown (blue triangles). We found that the polarization of the lowermost *unoccupied* $4p$ states closely follows the trend set by the total spin polarization of the *occupied* Co states. This allows us to consider the integrated XMCD signal, which has its origin in the polarization of the unoccupied $4p$ states, as an indicator for the behavior of the total Co spin moment. Considering possible effects from spin-orbit coupling, we performed full relativistic calculations and analyzed the polarization of the Co $4p$ states according to the selection rules from the respective orbital resolved density of states. After a broadening of this data we found the same dependence as observed in the scalar relativistic calculations (compare App. C.20). However, whereas the behavior of the pre-shoulder can be modeled consistently by our the electronic structure calculations, the origin for the higher energy region needs a further study.

$p_{c,I}/(GPa)$	XMCD	XRD	Theor.
300 K	13 ± 1	12.8 ± 0.5	-
100 K	17 ± 1.5	18 ± 2	-
0 K	19 ± 2	20.5 ± 2.5	21 ± 2

Table 4.1.: Transition pressures $p_{c,I}$ from XMCD, XRD and theoretical calculations for different temperatures. The experimental values are linearly extrapolated to $T = 0\,\mathrm{K}$ for a direct comparison.

To evaluate quantitatively the evolution of the low energy shoulder with pressure, we fitted the XMCD signal between 7705 eV and 7721 eV with three Gaussian peaks. The top panel of Fig. 4.2 shows the pressure dependence of the area of the first Gaussian peak (corresponding to the shoulder at $\sim$ 7708 eV in the experimental signal), averaged over the two helicities at room temperature and at 100 K (error bars indicate the spread of values between the two helicities). For pressure higher than 13 GPa at room temperature the whole XMCD signal can be reproduced with only two peaks at higher energy and the integral in Fig. 4.2 has accordingly been put to zero. Consequently, the steep decrease of the integrated signal around 13 GPa indicates a sudden reduction of the Co spin moment, as discussed above. This transition is shifted to about 17 GPa at 100 K. Both values coincide within the error bounds with the isomorphous structural transitions observed in high-pressure XRD experiments [49, 149] (see Tab. 4.1). In turn, a related zero-temperature extrapolation meets the theoretically predicted transition pressure.

Summary

To summarize, combining electronic structure calculations and high-pressure XMCD experiments, we provide direct evidence for the magneto-elastic origin of the isostructural

phase transition under pressure of YCo$_5$ for the first time. The driving force of this transition between two different ferromagnetic phases is related to a van Hove singularity in the DOS, mainly formed by Co $3d$ states, crossing the Fermi energy. The dramatic change in the electronic structure causes a reorganization of the Fermi surface topology for the majority spin channel. This electronic topological transition directly links the volume collapse to the drop of the magnetic moment. The structural transition under pressure was already confirmed by XRD measurements.[49] Here, we probed the change of the magnetic moment under pressure by XMCD experiments. Since a direct observation of the Co $3d$ polarization at the L-edge is hindered by the opaque diamonds of the pressure cell in the relevant energy range, we alternatively probed the magnetism of the system by evaluating the Co $4p$ states at the K-edge, which follow the trend of Co $3d$ states by hybridization effects. The collected spectra exhibit a reversible change of the pre-peak of the signal under pressure. Electronic structure calculations allow to assign this shoulder to the Co $4p$ states and reproduce the experimentally observed trend under pressure. The evaluated critical pressure is in perfect agreement with the transition pressures derived from the previous XRD measurements and the theoretical calculation. However, up to now our calculations succeeded only to model the low energy region of the XMCD signal. Full relativistic calculations yield the same picture. In an ongoing study we try to develop the simulation of the full signal. The results of the section will be published in Ref. [155].

4.1.2. SrFe$_2$As$_2$ - symmetry-preserving lattice collapse

The unexpected discovery of superconductivity in Fe-based pnictides raised enormous interest in the whole solid state community and stimulated numerous experimental and theoretical studies to find new ways to increase the superconducting transition temperature. Most of the new compounds discovered in the past three years can be grouped into five families: REOFeAs/AFeAsF – 1111 (RE=rare earth, A= alkaline earth); AFe$_2$As$_2$ – 122 (A=alkaline earth or divalent rare earth); AFeAs – 111 (A=alkaline metal); FeSe(Te) – 11; PFe$_2$As$_2$ – P22 (P= perovskite oxide). A common structural feature of the parent compounds is a FeAs building block separated by different spacer layers (compare Fig. 4.4). The thickness of the spacer layer governs the dimensionality of the electronic structure and influences the onset of the superconducting phase.[156] The families of Fe-pnictides show rich phase diagrams and a strong interplay of the crystal structure, magnetism and superconductivity. The details and peculiarities of these phase diagrams as phase boundaries or coexistence regions still stimulate extensive studies during the search for the underlying mechanism of the superconductivity in this new type of superconductors.

The undoped Fe-pnictides crystallize in a tetragonal crystal structure. At low temperatures a phase transition appears from the tetragonal to an orthorhombic symmetry which is accompanied by an ordering of the Fe moments in an antiferromagnetic stripe type ordering. This phase is the so-called spin density wave (SDW) phase. The suppression of the lattice distortion and magnetic order of the SDW can result in the onset of superconductivity. This can be realized by hole doping, electron doping, isovalent substitution and pressure pointing to the intimate correlation of structural peculiarities, magnetism and superconductivity in this family of compounds. However, in contrast to doping and substitution, pressure allows to modify the system without a change of the electronic structure by additional charges or drastic changes of the local crystal fields.

Experiments have shown great success in the enhancement of sample quality and the controlled manipulation of T$_c$ by substitution and doping. But still there exist other challenges to be addressed, like the possible coexistence of magnetism and superconductivity. Although theory successfully describes the general trends, it struggles with different problems: Band structure calculations allow for example a successful description of the tetragonal to orthorhombic structural distortion as well as the development of the magnetic moment under doping and pressure. Unfortunately, DFT fails in the reliable determination of the As z position and thus, the As-Fe bond length. Furthermore, the nature of the Fe moment is discussed controversially, which exhibits neither a clear itinerant nor localized character. Thus, the origin and underlying mechanism responsible for the superconductivity in the family of Fe-pnictides is far from being understood and is still fueling continuing discussions.

Here, we focus on the pressure dependance of the crystal structure of SrFe$_2$As$_2$, a member of the family of 122 compounds. This compound exhibits the magneto-structural transition into the SDW phase at about 205 K at ambient pressure [157]. Using LDA band structure calculations, the stability of the SDW and the influence of pressure and doping was investigated in detail.[158] For SrFe$_2$As$_2$, calculations as a function of reduced volumes witnesses a break down of the Fe moment and a transition from a SDW orthorhombic phase to a collapsed tetragonal phase with a small anomaly in the c/a ratio which strongly depends on the optimization procedure. On the experimental side, combining electrical resistivity and x-ray diffraction measurements under high pressure reveal a downshift of
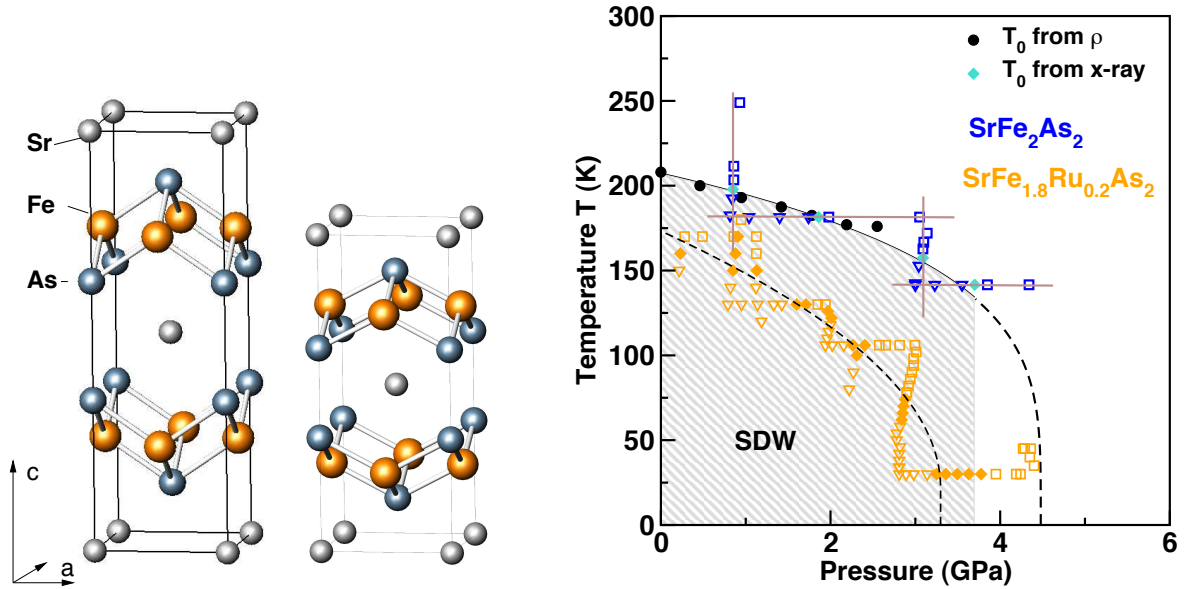
Figure 4.4.: Left: Crystal structure of the tetragonal (T) and collapsed tetragonal (cT) phase of $SrFe_2As_2$. The tetragonal phase exhibits the $ThCr_2Si_2$ structure type, while the cT phase realizes the $BaCu_2P_2$ structure type. Right: Influence of hydrostatic and chemical pressure at T_0 derived from X-ray diffraction - transition from the tetragonal to the orthorhombic distorted phase.

T_0 with increasing pressure.[159] Besides, Ru doping on the Fe site allows to suppress magnetic ordering and shifts T_0 towards lower temperatures. The destabilization of the magnetic order for strong Ru doping was shown by magnetization, electrical resistivity and specific heat measurements and suggests that Ru substitution can be considered as "chemical pressure".[39] In line with this concept recent (preliminary) high pressure x-ray data show a considerable downshift of T_0 for 10% Ru substitution (see Fig. 4.4, right).

Isostructural phase transition from the tetragonal to a collapsed tetragonal phase

However, many of the high pressure experiments were focused on the suppression of the SDW and the onset of superconductivity. Recently, pressure induced isostructural transition from a paramagnetic tetragonal (T) to a collapsed tetragonal (cT) phase have been reported for several members of the 122 family indicated by a drastic change of the c/a ratio.[160, 161, 162] For $CaFe_2As_2$ this collapse is suggested to be controlled by the Fe spin, concluded from DFT calculations.[163, 160] Furthermore a theoretical study based on molecular dynamics for AFe_2As_2 compounds reveal a similar scenario for the pressure-driven transition from the SDW into a non magnetic cT phase.[164] On the other hand, T-cT transition have been reported earlier in many RET_2P_2 (RE=rare earth, T= transition metal, P=group 13 or 14 element) compounds depending on the combination of rare earth and transition metal atom, e.g., $SrFe_2As_2$ crystallizes in a tetragonal phase (or $ThCr_2Si_2$ structure type), whereas $LiCu_2P_2$ shows a collapsed tetragonal structure. The significantly different P-P distances along the tetragonal c axis is ascribed to a subtle interplay of different contributions to the bonding situation.[165] Since many of these compounds show neither magnetic ordering nor superconductivity, these results put the dominant role of

magnetic ordering into question. Therefore, we decoupled the T-cT transition in $SrFe_2As_2$ from the ordering of Fe moments and investigated the influence of pressure independently from the Fe spins. We performed high pressure experiments at room temperature well above any magnetic or superconducting transitions. In our calculations we neglected the spin degree of freedom (non magnetic, LDA calculations) to closely mimic the experimental scenario. Our study resulted in the picture of a bonding driven phase transition (which will be described in detail in the next sections), in contrast to the scenario of a strong coupling of the Fe ordering to the transition as suggested in literature.[163, 160, 164]
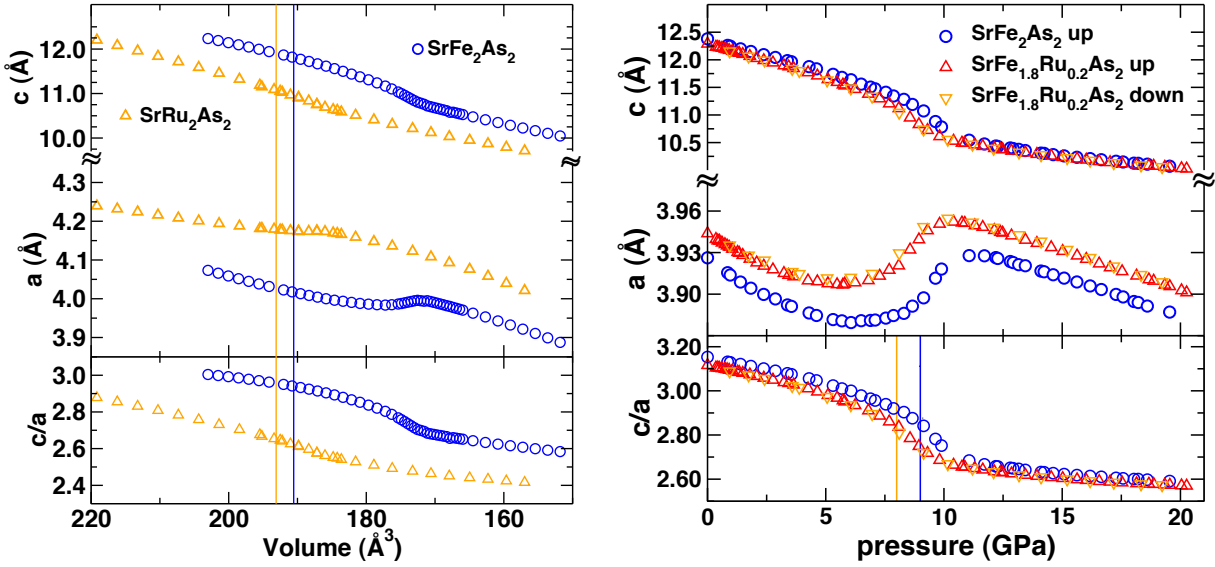

Figure 4.5.: Left: Calculated, optimized lattice parameter and ratio for decreasing volume within LDA for $SrFe_2As_2$ and $SrRu_2As_2$ using the experimental, ambient pressure As z coordinates. The experimental volume at ambient pressure are marked by vertical lines. Right: Measured lattice parameter and ratio for $SrFe_2As_2$ and $SrFe_{1.8} Ru_{0.2}As_2$. The critical pressure for the transition is denoted by vertical lines in the c/a ratio. 10% Ru substitution results in a down shift of about 1 GPa for the critical pressure.

Influence of pressure and Ru substitution

To simulate the influence of pressure on $SrFe_2As_2$, we optimized the c/a ratio for different volumes and evaluated the dependance of the lattice parameters c and a. The resulting dependance using the LDA functional and a fixed, experimental As z-position are depicted in Fig. 4.5. Our calculations found a considerable drop in the c/a ratio (blue circles). Whereas the c axis monotonously decreases, the a axis shows an anomalous increase close to the structural instability. The theoretical determined transition pressure evaluated from the derivative of a Murnaghan-Birch equation of states fitted to the the high and low pressure phase is $p_c^{DFT} = 11 \pm 1$ GPa. Using the GGA functional result in essentially the same findings with respect to the position of the transition and the strength of the anomaly (see App. C.19). The full optimization of the crystal structure, including theoretical optimized As z-position for different volumes, smoothens the signature of the transition and shifts p_c

to larger values. The influence of the As z-position on the transition is not surprising, since DFT fails in accurately reproducing the experimental Fe-As bond length even at ambient pressure.[166, 167] Comparing the calculated equilibrium volume for $SrFe_2As_2$ obtained using LDA and GGA with the experimental value, both approaches underestimate the equilibrium volume by 17% and 10%, respectively. These observations are in contrast to the well known underestimation by LDA calculation and overestimation by GGA of the volume by few percent as compared to experiments. Up to now there is no conclusive explanation for these findings established. However, the formation of a nematic order, which is unaccessible using present-day DFT tools, gains more and more acceptance.[168]

To tackle the question about the nature of the T to cT transition from experiments, we performed high pressure x-ray diffraction measurements up to 20 GPa at ID09 of the ESRF using a membrane type of DAC and He as pressure transmitting medium to ensure hydrostatic conditions. After integration and a background correction, the lattice parameters were determined by a Le Bail fit. The obtained lattice parameters exhibit the same behavior like our electronic structure calculations. We observed a continuos decrease of the c and a axis up to around 7 GPa, followed by an anomalous increase of the a axis from 7 to 11 GPa, whereas above 11 GPa both lattice parameters decrease continuously again. This behavior results in a sudden drop of the c/a ratio in agreement with the theoretical results and a significant change of c/a from 2.86 to 2.65 (corresponding to a volume collapse of about 5%). The transition pressure is estimated to be $p_c^{XRD} = 10 \pm 1$ GPa in excellent agreement with the DFT derived value.

To probe the concept of chemical pressure by Ru substitution, we applied our theoretical approach to the compound $SrRu_2As_2$. As $SrRu_2As_2$ shows no magnetic moments at ambient conditions (room temperature and ambient pressure) it allows to develop a pure chemical picture of the transition. At ambient pressure $SrRu_2As_2$ crystalizes in a quasi collapsed tetragonal phase close to the onset of the phase transition. Therefore, the effect of pressure in our calculations is much smaller. Nevertheless, an anomaly in the c/a ratio is visible (compare Fig. 4.5, orange triangles). To challenge the concept of chemical pressure by Ru substitution experimentally, a sample with 10% Ru substitution was pressurized with the same setup. The amount of Ru substitution was restricted to 10% to minimize disorder effects. $SrFe_{1.8}Ru_{0.2}As_2$ exhibits the same characteristic dependance of the lattice parameters, but the critical pressure was shifted down by about 1 GPa supporting independently that Ru substitution acts as chemical pressure.

As-As bond formation

As both, experiments and calculation, reveal the T to cT transition to be independent from magnetic ordering, this raises the obvious question regarding the driving force of the phase transition. Following the idea of Hoffmann and Zheng about the formation and breaking of inter-layer bonds within the family of compounds crystalizing in the $ThCr_2Si_2$ structure type,[165] we evaluate the dependance of the As-As inter-layer distance under pressure. In Fig. 4.6 the As-As distances under pressure based on the experimentally refined crystal structures (including a refinement of the As z position) are shown (blue circles). We found a sudden reduction of the As-As inter-layer distance at $p_c = 10 \pm 1$ GPa which coincides with the collapse of the c/a ratio. Interestingly, $SrFe_2As_2$ exhibits clearly a stronger shortening of the inter layer distance as caused by a mere change of the lattice parameter, visible by the comparison of the As-As distance based on the change of the c axis
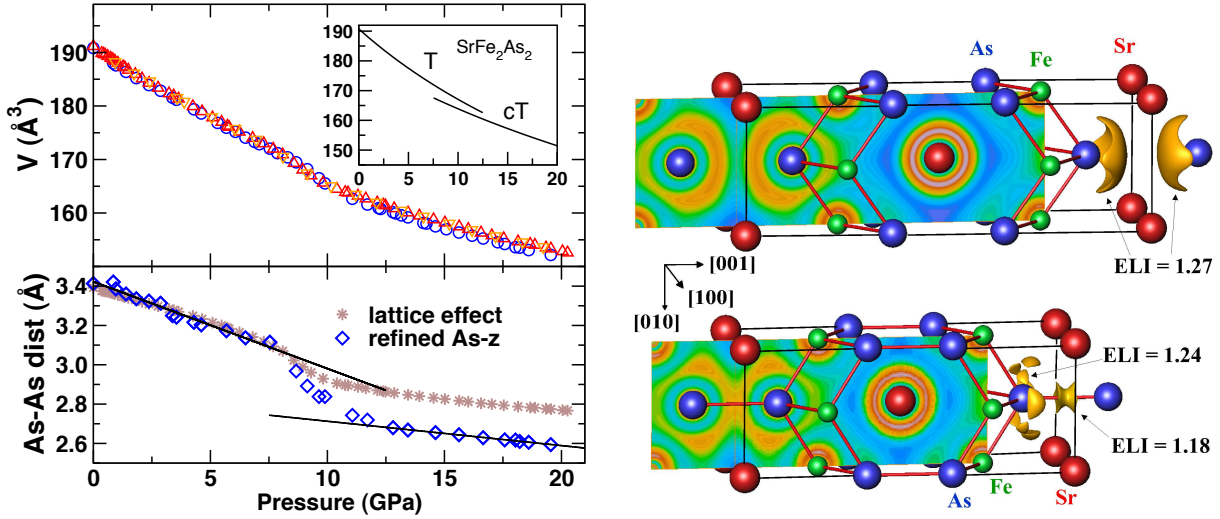
Figure 4.6.: Left: Experimental observed volume dependance (top) and fitted Murnaghan-Birch equation of states for for the tetragonal (T) and tetragonal collapsed (cT) phase (inset, top). As-As distances obtained from a full refinement of the internal As z position for $SrFe_2As_2$ in comparison to As-As distances based on the As z coordinates from ambient pressure. Right: Electron localizability indicator (ELI) for the T and cT phase. The shortening of As-As distance is accompanied by the formation of As-As interlayer bonds visualized by the pronounced ELI-D maximum between the two As sites sitting on top of each other along the c axis. Picture according to Ref. [169]

only (brown stars in Fig. 4.6) with the full relaxed structure (blue circles in Fig. 4.6). This collapse of the As-As distance from 3.41 Å (at ambient pressure) to 2.59 Å (at the highest measured pressure of 19.6 GPa) point to the formation of As-As inter layer bonds. The As-As distance in the high-pressure phase is only slightly larger than the single bond distance of 2.52 Å in α-As.[170] The collapse of the lattice and a possible As-As bond formation is also reflected in an about 25 GPa larger bulk modulus for the cT phase compared to the T phase. Whereas we obtain a bulk modulus of about $B_0 = 64$ GPa in the T phase from a fit to the experimental data by the Murnaghan-Birch equation of states (fit from ambient pressure down to 8.6 GPa), the formation of inter-layer bonds impedes the compressibility in the cT phase which result in a sizable increase of $B_0 = 90$ GPa (fit from 11.0 GPa to 19.5 GPa).

The evaluation and comparison of the band structure and band characters for the bonding and anti bonding As-As states for both phases supports this picture (compare Fig. 4.7).[3] Under pressure, parts of the anti bonding As $4p_z$ bands are shifted towards higher energies, above the Fermi level, whereas the bonding states remain nearly unchanged. In consequence, the depopulation of anti bonding states increases the As-As bond strength. For a more quantitative measure of the bonding strength the number of excess electrons

---

[3]The band characters of the bonding and anti bonding As-As inter site states were obtained by a projection of the band structure onto inter-site As z states between two As atoms sitting on top of each other along the z axis. The combination of $\phi_\sigma = \frac{1}{\sqrt{2}}(\phi_1 - \phi_2)$ and $\phi_{\sigma^*} = \frac{1}{\sqrt{2}}(\phi_1 + \phi_2)$ results in bonding and anti bonding characters.

was evaluated, which can be determined by the difference of occupied bonding states and occupied anti bonding states. For the ideal case of fully occupied bonding states and unoccupied anti bonding states the number of excess electrons is two. A further occupation of anti bonding states would decrease the number of excess electrons down to zero for the case of fully occupied anti bonding states and a break down of the bonding. For $SrFe_2As_2$ we found a clear increase of the number of excess electrons from 0.4 for the T phase to 1.0 for the cT phase in line with a strengthening of the As-As bonds.
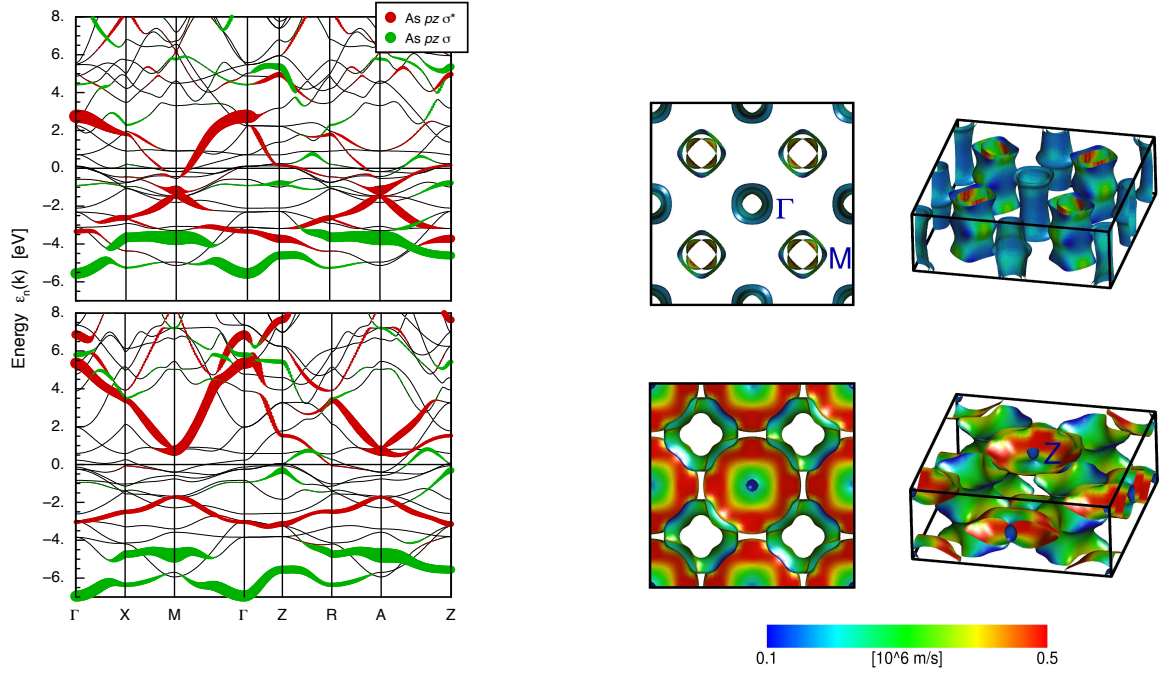

Figure 4.7.: Left: Band characters of bonding (green) and anti bonding (red) combination of inter-site As $4p$ states for the tetragonal (top) and collapsed tetragonal (bottom) phase. In the cT phase one of the anti bonding bands becomes depopulated. Right: Fermi surface for the tetragonal (top) and collapsed tetragonal (bottom) phase. The structural transition has a crucial influence on the Fermi surface topology.

Further electronic structure calculations for the T and cT phase reveal a strong influence of the changed bonding situation on the Fermi surface topology and plasma frequencies (the ratio of in-plane to out-of-plane frequencies λ changes from 3 (T) to 0.7 (cT)) of the compound and a change of the system from a quasi 2D system into a quasi 3D system (for details see Ref. [169]). This is mostly related to the depopulation of the anti bonding As-As $4p_z$ band, which hybridize with Fe $3d_{x^2-y^2}$ states, and the corresponding shift above the Fermi energy. Thus, a Fermi surface vanishes in the cT phase compared to the T phase. As a consequence, the Fermi surface topology changes dramatically. Although the structural transition is independent from the ordering of Fe moments, the dramatic changes in the electronic structure can in turn impact physical properties, such as the magnetism or superconductivity of the compound.

Our results are in line with calculations in real space investigating the chemical bonding in the two phases of $SrFe_2As_2$. In contrast to our calculations in k-space the study in real space allow to visualize the bond formation in a unique way and support an intuitive picture. Therefore the electron localizability indicator (ELI) was evaluated according to Ref. [171] with an ELI module implemented within the FPLO program package.[172] The topology of ELI was analyzed using the program BASIN [173] with consecutive integration of the electron density in basins, which are bound by zero-flux surfaces in the ELI gradient field, allowing to assign an electron count for each basin. The ELI-D distribution for the ambient condition T phase is shown in the upper panel of Fig. 4.6 (right), results for the high pressure cT phase are depicted in the lower panel of Fig. 4.6 (right). For the T phase we observe two distinct maxima in the ELI-D between the two As atoms along the z axis (isosurface $\Upsilon = 1.27$) pointing to the absence of an As-As bond. In the cT phase we found one pronounced maximum by the concentration of ELI-D close to the middle point of the As-As contact, illustrating the formation of an As-As bond (isosurface $\Upsilon = 1.18$). Thus, this change from two separated maxima into one distinct maximum between the two As sites is a clear fingerprint for the formation of a new As-As bond.

Summary

To summarize, we investigated in a joint experimental and theoretical work the influence of hydrostatic and chemical pressure on $SrFe_2As_2$ and found an isostructural phase transition from a tetragonal (T) into a collapsed tetragonal (cT) phase. Combining DFT based electronic structure calculations for k- and real-space properties with high-pressure XRD experiments up to $20\,GPa$ at room temperature, we obtained a consistent picture.
For the onset of the phase transition we obtained a critical pressure of about $p_c^{XRD} = 10 \pm 1\,GPa$ from X-ray diffraction measurements in good accordance with our LDA calculations $p_c^{DFT} = 11 \pm 1\,GPa$. The downshift of p_c by about $1\,GPa$ for a sample with 10% Ru substitution supports the concept of chemical pressure by Ru substitution. Our results exclude a dominant role of magnetic ordering of Fe spins to the isostructural, symmetry preserving collapse, since we found the structural phase transition independent from any magnetic ordering. Detailed analysis of the bonding scenario in both, k- and real-space, revealed the formation of As-As inter layer bonds as the driving force of the transition with large influence on the electronic structure. In the ambient pressure T-phase, covalent bonded Fe-As layers are separated by large Sr^{2+} cations. The large As-As interlayer distance is dominated by geometric reasons. The predominant ionic interactions between the rigid Fe-As layers and Sr cations make the material soft along the stacking c axis. Thus, applying pressure leads to a decrease of the distance between the layers and therefore the As-As distance. When a critical orbital overlap of the As $4p$ orbitals is reached, the bonding interactions promptly dominate and the phase transition occurs. Electronic structure calculation suggest a scenario where the stabilization of As-As bonding states at the same time stabilizes As-Fe anti bonding states. As a consequence, the As-Fe bonds become weaker and the lattice parameter a increases whereas c decreases at the phase transition. Such a scenario was earlier studied and observed in several phosphorus-based compounds.[174, 175] The results of this section were already published in Ref. [169].

4.2. Localized magnets

4.2.1. EuPd$_3$B$_x$ - valence transition under doping and pressure

Valence instabilities observed in rare-earth (RE) $4f$ systems have attracted huge interest in the past. In solids RE metals are mostly trivalent in the standard state. In fact, Eu and Yb are the only lanthanide metals which are divalent in their elemental metallic standard state as well as in some alloys and intermetallic compounds. In that case their crystal chemistry is typically strongly influenced by the large radii of the ions. In addition, the physical properties of Eu are significantly different in the two states, namely Eu^{2+} (S = 7/2, L = 0) carrying a high magnetic moment (J = 7/2) compared to Eu^{3+} (S = 3, L = 3, J = L - S = 0) with a non magnetic ground state and low-lying excited magnetic states. Thus, not only the crystal chemistry depends crucially on the $4f$ valence, but also the related electronic and physical properties.

In many cases, a deviation from the typical trivalent state of the RE component can already be suspected from a deviation of the unit cell volume of a specific compound from the expected volume decrease within the RE compound series according to the lanthanide contraction rule. The valency of several RE species in a compound is determined by many factors like the local environment (determining the crystal field splitting), the electronegativity and concentration of the alloying partners [176, 177, 178] in the compound as well as external parameters like temperature, pressure and magnetic field.[179] Therefore, a typical approach to study RE valence changes is the successive variation of these relevant factors in a systematic way.

In particular, the insertion of boron in cubic REPd$_3$ compounds had been studied by Dhar *et al.* systematically using x-ray diffraction (XRD) and magnetic susceptibility measurements.[180, 181] An increase of the lattice parameters under B insertion was observed for the RE series REPd$_3$B$_x$ as reported in Ref. [180]. Above a certain concentration x, depending on the RE metal, a further increase of the B content leaves the lattice parameter unaffected. In addition, for RE = Eu and Yb a pronounced anomaly in the lattice parameters was found compared to the other RE compounds. This peculiarity lead to further studies on the Eu compound based on Mössbauer and x-ray absorption near-edge-structure (XANES) spectroscopy,[182, 183, 184] reporting a decrease of the mean Eu valence ν for $x > 0.25$ connected with the formation of a heterogeneous mixed valence state including the stoichiometric compound EuPd$_3$B. Furthermore, for LaPd$_3$ no variation of the lattice parameter was observed at all, up to the fully stoichiometric LaPd$_3$B [180].

Stimulated by the difficulties to interpret these effects based on the reported data, (as, e.g., the critical B concentration for the transition is inconsistent) a recent study investigated the electronic structures of intermetallic borides REPd$_3$B$_x$ within the density functional theory using the LSDA+U and coherent potential approximation (CPA) for the whole series from RE= La to Lu as a function of the boron content.[185] Surprisingly, the calculated lattice parameter obtained for all REPd$_3$B compounds are significantly higher than the experimental lattice parameters, questioning the reported synthesis of stoichiometric compounds REPd$_3$B. In this context, it was shown unambiguously by detailed experimental studies that boron cannot be inserted into LaPd$_3$ under equilibrium conditions. Instead, in a sample with nominal LaPd$_3$B stoichiometry, the precipitation of LaB$_6$ crystals in a LaPd$_3$ matrix was observed.

The impossibility to insert B in the LaPd$_3$ compound enforces the question, whether similar
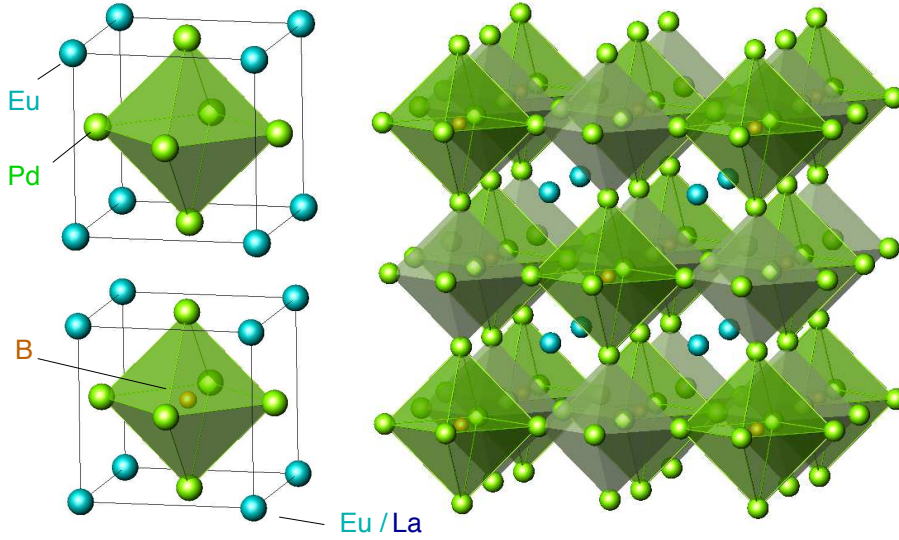
Figure 4.8.: Left: Crystal structure of $EuPd_3$ (top) and $EuPd_3B$ (bottom). Whereas B insertions fills the Pd-octahedra, La is substituted at the Eu site. Right: Experimentally observed super structure for $EuPd_3B_{0.5}$.

effects also appear in the other compounds of the series, resulting in a partial insertion of B, only. Thus, the inconsistent reports about valence changes could have their origin in different sample compositions.

In order to clarify this issue, we reinvestigated in a joint experimental and theoretical work a large series of $EuPd_3B_x$ and $GdPd_3B_x$ compounds. Careful synthesis and characterization based on a combination of XRD, metallography, energy- and wave-length dispersive x-ray spectroscopy as well as chemical analysis could establish the range of existence for $EuPd_3B_x$ up to $x \leq 0.53$ and $x \leq 0.42$ for the $GdPd_3B_x$ compounds, respectively. Furthermore, our electronic structure calculation predict a valence change of $EuPd_3B_x$ above a critical B content $x_c = 0.19$ from a non-magnetic Eu^{3+} state into a magnetic Eu^{2+} state which is related to a discontinuity of the lattice parameter. In contrast, the $GdPd_3B_x$ system with a stable Eu^{2+} state exhibits an almost linear increase of the lattice parameter following Vegards law. However, being aware that present day DFT calculation have still difficulties with respect to the description of strong correlated systems and disorder, we probe our theoretical results by XRD, XAS and thermodynamic measurements. The experimental data confirm the theoretical prediction of a valence transition and find an excellent agreement of x_c for the onset of the transition, but classify the transition as a formation of a heterogeneous mixed valence state changing the mean Eu valence from Eu^{3+} ($x \leq 0.2$) towards $Eu^{2.5+}$ for $x = 0.5$.

The observed close interplay of the Eu valence state and the discontinuity in the unit cell volume under B substitution raises the question, if the valence transition is driven by the mere change of inter atomic distances, by the B chemistry or ruled by the valence electron count. Thus, we investigated the influence of high pressure to $EuPd_3B_x$ compounds with fixed B content above the transition. Regarding our calculations we observe a subtle interplay between doping and volume effects, while the disorder of the system is less relevant. XAS and XRD measurements under high pressure show, that applying pressure can reverse

the effect only partially, driving the magnetic Eu^{2+} state towards the non-magnetic Eu^{3+} state and thus pointing to an important contribution of the B atom to the valence transition. Finally, the systematic, theoretical investigation of the related series of Eu$_{1-x}$La$_x$Pd$_3$ compounds allow to separate effects caused by the B chemistry from pure electron doping effects and supports the predominant role of charge doping as origin for the onset of the valence transition.

Eu valence under B substitution - theory

To investigate a possible valence instability in the EuPd$_3$B$_x$ compounds depending on the B content x, LSDA+U calculations for the two ordered extreme cases $x = 0$ and $x = 1$ were carried out. However, EuPd$_3$B represents a fictitious compound since no complete occupation of the B position can be experimentally achieved (see below). A discussion of the underlying crystal structure as well as preferential site occupation by the B atoms has been given in a previous publication.[185] The resulting densities of states (DOS) are depicted in Fig. 4.9. In both compounds the valence band is mainly formed by (non polarized) Pd $4d$ states. The contributions from Pd $5p$ and $5s$ as well as Eu $5d$ and $6s$ states are very small and can be neglected. The B states in EuPd$_3$B appear below -5 eV. Thus, the main differences between both compounds are due to the Eu $4f$ states and the placement of the Fermi energy.

The strongly localized $4f$ states yield sharp peaks in the density of states. For EuPd$_3$ we find these peaks in the majority channel at the lower end of the valence band and an unoccupied $4f$ state at about 1 eV above the Fermi energy. In the minority spin channel all $4f$ states are unoccupied as expected. Evaluating the occupation of the $4f$ orbital, EuPd$_3$ is in a $4f^6$ state. Since the valence band is unpolarized, a non-magnetic ground state can be expected due to the Hund's rules ($J = L - S = 0$).

In EuPd$_3$B, connected with the insertion of B, the $4f$ states of the majority spin channel become fully occupied. These strongly localized states are placed at about -1 eV. The $4f$ states of the minority spin channel remain unoccupied and are shifted upwards to 10.5 eV, according the energy difference $\Delta E \sim U + I$ from the on-site repulsion U and the exchange split I (compare the energy difference of the unoccupied majority and minority $4f$ states in EuPd$_3$ and EuPd$_3$B, see Fig. 4.9, left). This results in a magnetic Eu $4f^7$ state.

Following the question, how the $4f$ occupation develops with x in more detail, we model a successive insertion of B from EuPd$_3$ to EuPd$_3$B using CPA calculations. While the disorder of the insertion is covered by the CPA, a possible dynamic mixed valence scenario for Eu cannot be simulated, since a fractional occupancy of orbitals is suppressed by the LSDA+U approach, which favors full polarization. Furthermore, the combination of the LSDA+U and CPA method results in a complex potential surface with several local minima, causing difficulties to find the correct global minimum. Considering the difficulty of multiple solutions (depending on numerical parameters in the CPA approach), we compared LSDA+U results for the ordered structures ($x = 0, x = 0.5$ and $x = 1$) with the corresponding BEB [186] results and with CPA calculations for similar concentration ($x = 0.01$, $x = 0.5$ and $x = 0.99$). The obtained DOS show only minor differences at the lower end of the valence band and in the unoccupied states (see Fig. 4.10, left). Comparing optimized lattice parameters using the different approaches leads essentially to the same results. Thus, the CPA approach is well controlled and yields justified results.

We optimized the crystal structure (equivalent to the optimization of the cubic lattice
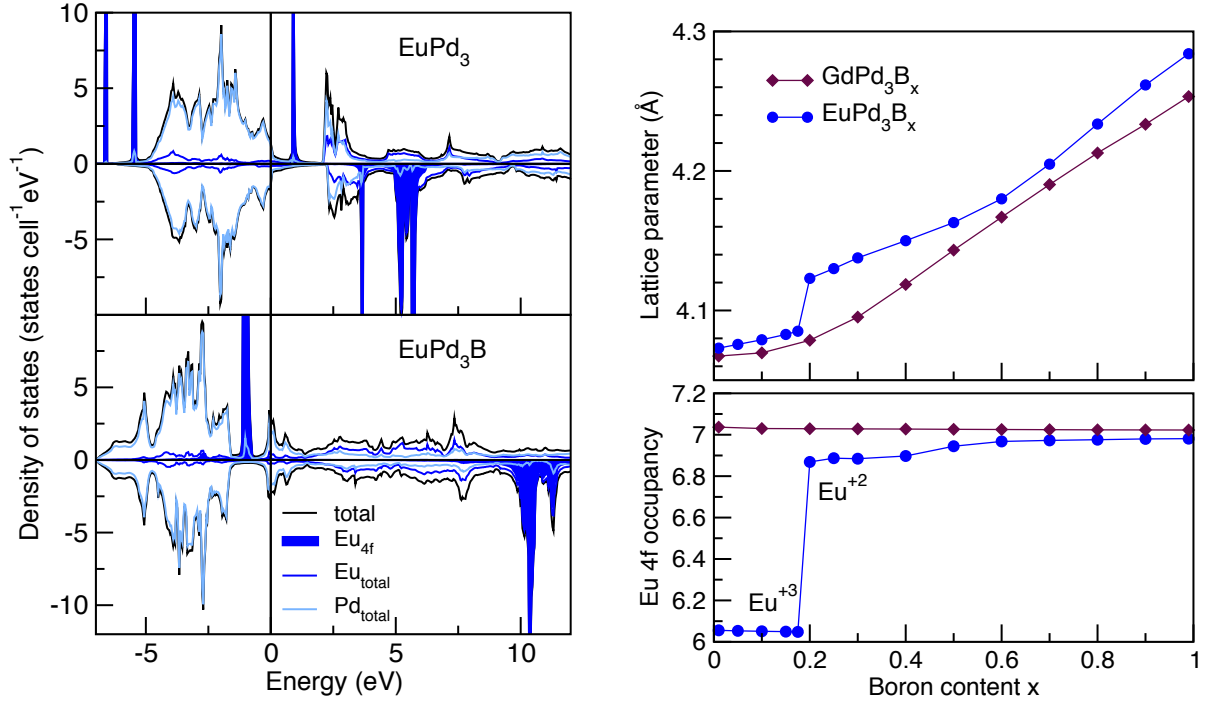
Figure 4.9.: Left: Calculated density of states for $EuPd_3$ (top) and $EuPd_3B$ (bottom). Beside the $4f$ states, $EuPd_3$ shows a symmetric density of states for the two spin channels. In $EuPd_3B$ the majority spin channel shows fully occupied $4f$ states. Right: Optimized cubic lattice parameter and $4f$ occupation as function of the B content for $EuPd_3B_x$ and $GdPd_3B_x$. In $EuPd_3B_x$ the lattice parameter shows a jump at $x \approx 0.2$. For the same B content a change from a trivalent to a divalent Eu state is observed.

parameter as the only free parameter) for several different B concentration and evaluated the electron population of the Eu states. The dependence of the lattice parameter a on the B content x (see Fig. 4.9, right) shows a sudden increase of the lattice parameter at $x_c^{DFT} = 0.19 \pm 0.02$. This anomaly of the lattice parameter corresponds to a volume change of about 2.6% and is accompanied by a drastic change of the Eu $4f$ occupation from the trivalent to the divalent state. In contrast, the reference system $GdPd_3B_x$ with a half filled $4f$ shell, shows a stable $4f^7$ state under B insertion and a smoothly increasing lattice parameter as one might expect from Vegard's law.

Eu valence under B substitution - experiment

Being aware of the aforementioned shortcoming of present day DFT calculation to describe strong correlated systems, in particular with intermediate or mixed valence states, we challenge our theoretical prediction of a valence transition in $EuPd_3B_x$ for $x_c^{DFT} \geq 0.19 \pm 0.02$ by an extended experimental study. Altogether, the experimental investigation confirm the valence transition of Eu upon B insertion in $EuPd_3B_x$. However, instead of a transition from a purely trivalent into a divalent state, a transition into a heterogeneous mixed valence state as reported earlier by S. K. Dhar *et al.* was observed [182]. The careful synthesis and characterization of more than 20 (10) Eu (Gd) compounds with different B
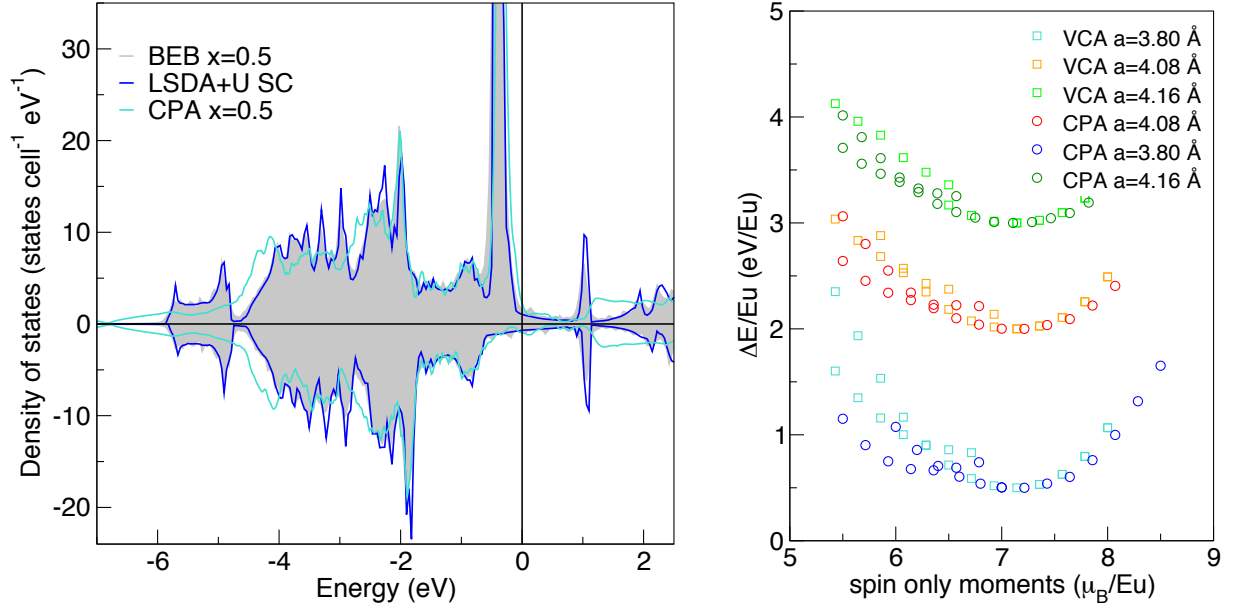
Figure 4.10.: Left: Calculated density of states for $EuPd_3B_{0.5}$ applying different approximations to model the partial occupation of the B site. The good agreement of the different approaches justify the reliability of the CPA calculations. Right: Fixed spin moment calculation for $EuPd_3B_{0.3}$ for three different volumes using the CPA and VCA approach to model the partial B site occupation. Independent from the approximation we found two distinct minima in the fix spin moment calculation.

content allow to determine precisely the existence range of $EuPd_3B_x$ up to $x \leq 0.53$ and $x \leq 0.42$ for the $GdPd_3B_x$ compound (see Fig. 4.11, left). For higher B concentration the lattice parameters stay constant and additional phases precipitate, which is mainly EuB_6, similar to the formation of LaB_6 in $LaPd_3B_x$ or GdB_6, respectively. Our results are in good agreement with recent studies on phase equilibria in the ternary system Eu-Pd-B and of $GdPd_3B$ solid solution by A. Pandey *et al.* and O. Sologub *et al.*.[188, 187] The relevant lattice parameters as a function of the B content are included in Fig. 4.11 for comparison. In contrast, the results from an earlier study by Dhar *et al.* deviate significantly, suggesting an overestimation of the B content in the real samples by referring to the nominal B concentration. Details on the characterization and a further comparison of different studies as well as the formation of a super structure in $EuPd_3B_x$ for B concentration above $x = 0.35$ are discussed in Ref. [189]. Consistent with the calculations, the XRD data show an anomaly of the lattice parameter for $EuPd_3B_x$ at $x_c^{XRD} = 0.22 \pm 0.02$, indicating the onset of the valence transition, while for $GdPd_3B_x$ continuously increasing lattice parameters are found. However, a less pronounced anomaly compared to the theoretical predicted jump in the lattice parameter is observed, namely a kink between two regions of linear behavior.

To ensure that this lattice anomaly is related to the suggested valence change, XAS experiments at the Eu L_{III} edge were performed. The measurements with varying B content assign the kink to the onset of a transition into a mixed valent Eu state. An evaluation of the critical B content resulted in $x_c^{XAS} = 0.22 \pm 0.03$ which is in excellent agreement
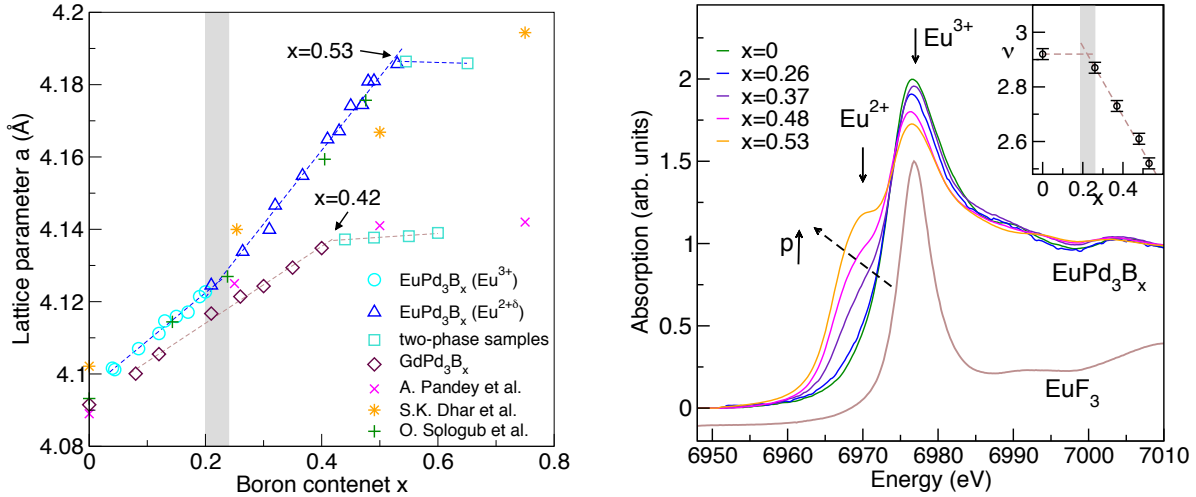
Figure 4.11.: Left: Experimental obtained lattice parameter versus B content x for $RE\text{Pd}_3\text{B}_x$ (RE=Eu, Gd). For the Eu compound series a pronounced kink in the dependance of the lattice parameter at $x = 0.2$ appears. For comparison the experimental results from Ref. [182, 187, 188] are included. Samples with $x = 1$ reported by S. K. Dhar *et al.* and A. Pandey *et al.* are not shown. Right: Measured EuL_{III} XAS spectra for different EuPd$_3$B$_x$ compounds in comparison to the reference compound EuF$_3$. The ratio of contributions originating from Eu^{3+} and Eu^{2+} changes with increasing B concentration.

with the results from XRD and band structure theory. Moreover, temperature dependent measurements of compounds with a fixed B content above the transition allow to classify the system as a heterogeneous mixed valence system, in line with the observation of two Mössbauer lines by Dhar *et al.*[182]. Furthermore, magnetic susceptibility and specific heat measurements support the mixed valence state also for higher B concentration.

The theoretical and experimental results give a consistent picture. The insertion of B induces a valence change accompanied by a lattice anomaly in the series of EuPd$_3$B$_x$ compounds. Since the substitution of B changes different parameter at the same time, in particular the unit cell volume, the number of valence electrons and the crystal field, the driving force for the onset of the transition remains unclear. To unravel the underlaying mechanism and separate effects caused by a change of the crystal structure from effects of the B chemistry, high pressure experiments for compounds above the transition are performed, following the question if the valence state can be reversed.

Eu valence under high pressure - theory

To elucidate the origin of the valence transition in EuPd$_3$B$_x$ we try to separate the effects caused by a change of the unit cell volume from the effect of B substitution to the Eu valence state. Thus the influence of volume changes on the Eu valence state was investigated starting from electronic structure calculation. While pressure can be simulated easily by a variation of the unit cell volume, the modeling of the Eu valence state is more challenging. Unfortunately, it is not possible to simulate directly the mixed valence state observed in the experiments, as the LSDA+U method favors full polarization and suppresses this

way a fractional occupation of the Eu $4f$ states. However, it is possible to stabilize Eu $4f$ occupations close to the two limiting cases of 6 and 7 μ_B/Eu in the majority spin channel. Starting from this two solutions we performed fixed-spin moment calculations for compounds with fixed B concentration and varied the volume of the unit cell[4]. As the spin only moment of this calculations are related to the Eu $4f$ occupation and therefore to the valence state of Eu, the interplay of volume and $4f$ charge effects can be studied. The comparison of the total energies yield the more stable configuration for a specific B content volume combination. In Fig. 4.12 the dependance of the total energy from the spin-only moment for four compounds with different B content is depicted. While in the case of EuPd$_3$ the two branches of the energy curves regarding the two limiting Eu $4f$ occupations are clearly visible (arrows in Fig. 4.12), the stabilization of the Eu $4f^6$ phase is more and more suppressed with increasing B content and restricted to smaller spin only magnetic moments.
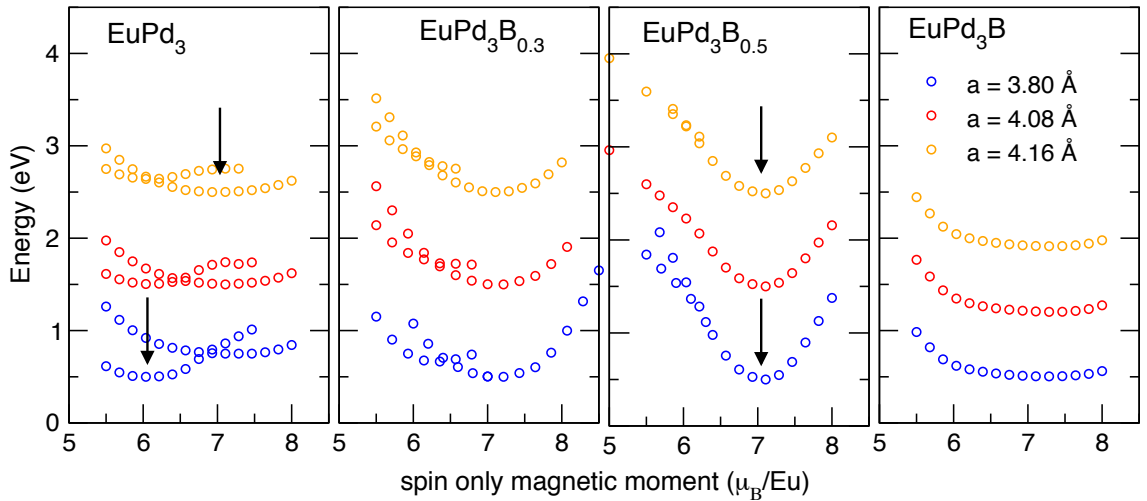

Figure 4.12.: Fixed spin moment calculations for compounds with different B content under pressure (different volumes): The total energy differences for the ordered structure EuPd$_3$ and the fictitious compound EuPd$_3$B are based on LSDA+U calculations. For $x = 0.32$ and $x = 0.5$ the disordered B site is simulated by CPA. This results are checked to the energy dependence using the VCA approximation (compare Fig. 4.10). For $x = 0.5$ additional super cell calculations using LSDA+U with an ordered B arrangement based on the experimental observation were performed. The total energies are given relatively to the corresponding minimum. The arrows denote the absolute minima.

In more detail, we find a subtle balance between the Eu^{3+} and Eu^{2+} state for EuPd$_3$ in its optimized equilibrium volume ($a = 4.08$Å, see left panel of Fig. 4.12, middle graph). The energy difference of the two solutions is less than $4\,\text{meV}$/Eu. Applying pressure, simulated by a reduction of the unit cell volume, clearly stabilizes the Eu^{3+} state by an energy

---

[4]We change the unit cell volume corresponding to a change in the lattice parameters from 3.80Å to 4.16Å. This volume range corresponds to a change in the lattice parameter from about 0.3Å smaller than the optimized lattice parameter for the B free compound EuPd$_3$ to the optimized volume for EuPd$_3$B$_{0.5}$ with nearly maximal B concentration.

difference of about 0.25 eV/Eu. On the other hand, if the unit cell volume is expanded by the same volume difference, the Eu^{2+} state becomes energetically preferred. Thus, regarding our calculations, the valence state of Eu in $EuPd_3$ exhibits a clear volume effect. In the case of $EuPd_3B_{0.3}$ with an B content just above the onset of the valence transition, the two solutions are still well pronounced. Although their total energy shifts against each other under pressure, the decrease of the unit cell volume does not change the global energy minimum and the Eu^{2+} state remains stable for the whole volume range, in contrast to the behavior of $EuPd_3$. This stabilizing effect of the B substitution to the Eu^{2+} state is strengthened further with increasing B substitution. While for $EuPd_3B_{0.5}$ the metastable solution of Eu^{3+} can be obtained only for spin-only moments below 6 μ_B/Eu with a sizable energy difference to the Eu^{2+} state, $EuPd_3B$ converges always into the single solution of Eu^{2+} (compare right panel of Fig. 4.12).

To ensure that the observed effects are independent from a specific approximation to model the B site, the results using the LSDA+U (for x =0, 0.5, 1), VCA and CPA approach were checked and compared carefully with each other (see Fig. 4.10, differences between different approximations for x =1, 0, 0.5 are even smaller.). From their good agreement we conclude, that the magnetic properties of the compound depend sensitively on the B content, but not on the particular B order, in contrast to an earlier study, where the Eu valence instability was connected to an anisotropic B environment.[190]

Our calculations yield a clear volume effect to the Eu valence state of the $EuPd_3B_x$ compounds, although a change of the preferred Eu $4f$ occupation is only observed for $EuPd_3$. Beside this volume dependance, the substitution of B strongly stabilizes the Eu^{2+} state. However, the difficulty to describe the heterogeneous mixed valence state of Eu by the LSDA+U approach in a realistic way requires experimental support for a reliable picture.

Influence of pressure on Eu valence - experiment

The demonstrated interplay between the occupation of the Eu $4f$ states and the unit cell volume regarding our calculation proposes to tune the Eu valence state by pressure for a fixed B concentration, or even to reverse the phase transition.

As a direct probe of the Eu valence state XAS under pressure was carried out for $EuPd_3B_{0.48}$ above the valence instability with a mean valence $\nu = 2.63(2)$ at ambient pressure. The obtained experimental data are depicted in Fig. 4.13 (left). For ambient pressure, the measured spectrum at the L_{III} edge exhibits a main peak centered at 6976.5(5) eV corresponding to Eu^{3+} states and a shoulder, at about 8 eV lower in energy, originating from Eu^{2+} states in good agreement with earlier measurements [189] and the heterogeneous mixed valence state of the compound.

The stepwise increase of pressure reduces the intensity of the shoulder significantly, though it is not suppressed totally. For pressures up to 25 GPa, the pure Eu^{3+} state as present in the compounds $EuPd_3B_x$ with $x \leq 0.2$, cannot be achieved. $EuPd_3B_{0.48}$ remains in a mixed valence state but with an clearly enlarged mean valence of $\nu = 2.68(2)$ (p =24 GPa). This process is reversible by decreasing pressure (compare Fig. 4.13, left inset).

For the compound $EuPd_3B_{0.32}$, much closer to the onset of the valence transition, the two valence states should be closer in energy according to our DFT calculations ($EuPd_3B_{0.3}$ exhibits a second local minimum in the energy versus moment curve and smaller energy differences between the Eu $4f^6$ and $4f^7$ states compared to $EuPd_3B_{0.5}$) and thus more sensitive to pressure. Unfortunately, the detection of any definite valence change under

pressure for such small B contents was beyond the resolution of the experimental set up. The contribution of Eu^{2+} states to the XAS spectrum for ambient pressure are too small to allow a reliable observation of the transition as the small differences are of the same size than the background fluctuations.[5]

Applying pressure drives the Eu^{2+} states in $EuPd_3B_{0.48}$ towards Eu^{3+} in a continuos way, in analogy to the continuos valence transition under B substitution.[189] For pressures up to 25 GPa the mixed valence state for $EuPd_3B_{0.48}$ cannot be reversed completely, raising the question whether this observation is due to the limit of applied pressure or impeded by an intrinsic property of the compound.
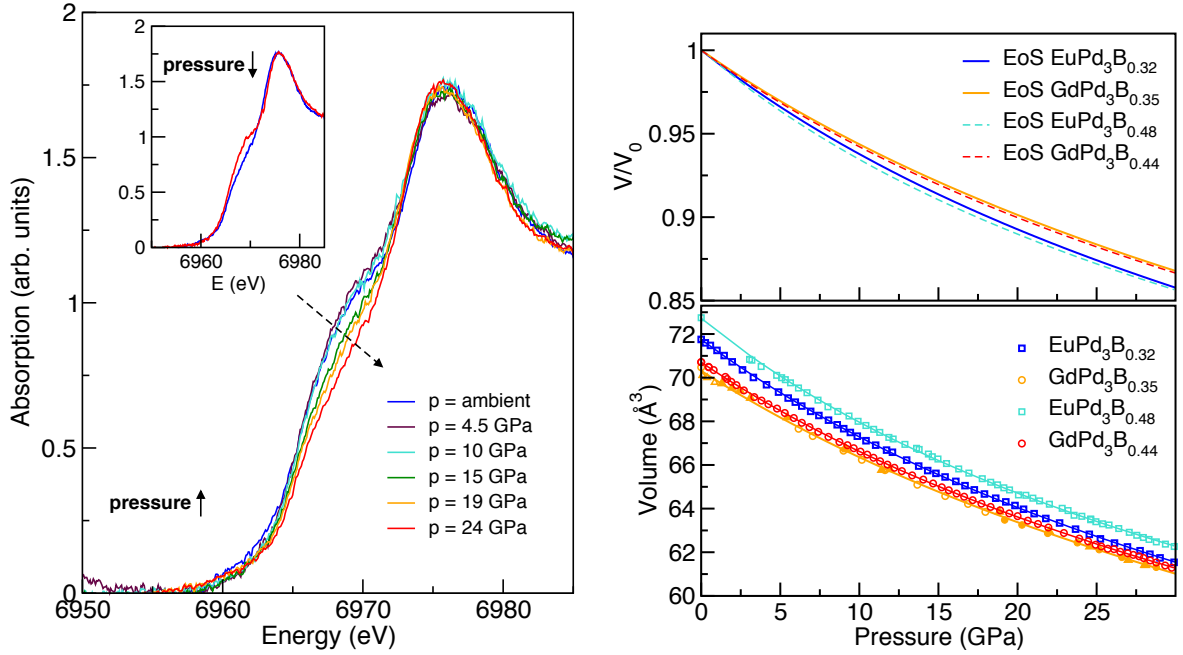

Figure 4.13.: Left: Measured x-ray absorption for pressures up to 25 GPa for $EuPd_3B_{0.48}$ well above the valence transition. Applying pressure only partially suppresses the low energy shoulder of the signal. Right: Measured equation of states for $EuPd_3B_{0.32}$ and $EuPd_3B_{0.48}$ above the onset of the valence transition and related Gd-reference compounds with comparable B content. The experimental data were fitted by the Murnhagan-Birch equation of states. The Eu compounds exhibit a softer pressure dependence than the Gd compounds pointing to a valence instability.

To estimate the pressure required to restore the equilibrium volume for the pure Eu^{3+} state of the reference system $EuPd_3$, and to ensure the stability of the crystal structure upon pressure, we performed XRD measurements at high pressure. The experiments were additionally motivated by the corresponding XRD experiments under B substitution, which allowed the indirect observation of the valence transition by a pronounced kink in the plot of the lattice parameter vs. boron content (compare Fig. 4.11).

---

[5]The detection of the small changes of the mean valence for the small sample size and non ideal hydrostatic pressure condition on DAC limit the resolution of the experiment.

For pressures up to $30\,\mathrm{GPa}$ no general structural changes were observed for $\mathrm{EuPd_3B_{0.32}}$ and $\mathrm{EuPd_3B_{0.48}}$, respectively.[6] The measured and refined data are shown in Fig. 4.13 (right). To evaluate the equation of states we fitted the experimental yield volume-pressure dependance by an inverse Murnaghan-Birch equation of states (EoS)

$$V(p) = V_0 \cdot \left(\frac{B_0' \cdot p}{B_0} + 1 \right)^{-1/B_0'}$$

with the bulk modulus B and the compressibility B_0'. The obtained EoS follows perfectly the experimental data in the whole pressure range with $B = 130\pm5$ and $B_0' = 4.7\pm1$, typical for 3D systems (see Fig. 4.13 and Tab. 4.2). Any direct structural anomaly indicating a valence instability is absent, in contrast to the pronounced kink in the dependance of lattice parameters under B substitution discussed above (see also Ref. [189]).

Being aware of the experimental difficulty to resolve the small effects expected from a partial change of the valence states only, in combination with the high pressure method, we compared the results for $\mathrm{EuPd_3B_x}$ with the pressure-behavior of $\mathrm{GdPd_3B_x}$ ($x = 0.35, 0.44$) compounds, which are used as reference systems with half filled $4f$ shell and therefore a stable valence state. Evaluating the EoS for the $\mathrm{GdPd_3B_x}$ compounds we receive an increased $B_0 = 145 \pm 5$ and a similar $B_0' = 4.8 \pm 1$ (compare Tab. 4.2, [7]).

The direct comparison of the normalized EoS for both systems (compare inset of Fig. 4.13) exhibits clearly the smaller bulk modulus for the $\mathrm{EuPd_3B_x}$ compounds compared to the reference systems independent from differences in the B content. This trend is also found independently from a theoretical estimate of B_0 based on our DFT calculations, although calculations result in 1% smaller equilibrium volumes V_0 and 10% larger B_0 in line with the well-known problem of over-binding in LDA. The evaluation of EoS from our theoretical data were obtained by a Murnaghan-Birch equation of states fitted to the calculated volume vs. energy curve

$$E(V) = \frac{B_0 \cdot V}{B_0'} \left[\frac{(V_0/V)^{B_0'}}{B_0' - 1} + 1 \right] + C$$

The softer pressure dependence for the $\mathrm{EuPd_3B_x}$ ($x \geq 0.32$) compounds compared to the Gd reference systems, equivalent to the smaller bulk modulus, is assigned to the valence instability.

Furthermore, the derived EoS allow to evaluate the volume change of the compounds for the applied pressure range. For a pressure of $30\,\mathrm{GPa}$ the volume for the $\mathrm{EuPd_3B_x}$ compounds decreases by about 14%, which is more than twice the volume difference observed under B insertion from $\mathrm{EuPd_3}$ to $\mathrm{EuPd_3B_{0.53}}$.[8] Considering the volume change as the driving force of the valence transition, a pure $\mathrm{Eu^{3+}}$ valence state is already expected for pressures of about at most $10\,\mathrm{GPa}$ in contrast to the experimental observations. Thus, the valence

---

[6]Small asymmetric peak shapes for $\mathrm{GdPd_3B_{0.35}}$ indicate possible structural distortions or the formation of a super structure. The evaluation of the half peak width for different representative peaks for the whole pressure range exhibits no systematic development. So an ambiguous assignment of the modulated peak shapes to a clear origin is not possible. However, the deviation of the unit cell volume based on different structural models are below the experimental resolution and only slightly influence the accuracy of the yielded parameter from the fitted EoS.

[7]The structural refinement of the Gd reference system has a sizable hysteresis influencing the accuracy of the equation of states, resulting in larger error bares.

[8]Volume difference from 4% from theory and 6% from XRD.

EuPd$_3$B$_x$	V_0	B_0	GdPd$_3$B$_x$	V_0	B_0
theo			theo		
$x=0.3$	70.92	139$\pm$2	$x=0.35$	69.2	168$\pm$1
$x=0.5$	72.17	145$\pm$1	$x=0.45$	70.45	168$\pm$1
exp			exp		
$x=0.32$	71.73	133$\pm$1	$x=0.35$	70.3	152$\pm$10
$x=0.48$	72.72	125$\pm$3	$x=0.44$	72.72	145$\pm$1

Table 4.2.: Obtained parameters from least square fits of a Murnaghan-Birch EoS to the experimental data and calculated volume energy relation. The subtle balance of the two minima and their anharmonic behavior in the calculated curve for $x = 0.3$ impedes the fitting and results in slightly larger error bars. The increased uncertainty in the experimental parameter for GdPd$_3$B$_{0.35}$ originates from a small hysteresis of the measurements.

state of EuPd$_3$B$_x$ is predominantly ruled by the inserted B, while volume effects have minor influence. This findings are in agreement with the trends obtained from DFT calculations, where in the case of EuPd$_3$ the volume has a sizable influence of the preferred valence state, while the insertion of B stabilizes the Eu^{2+} state significantly.

The predominant role of B substitution to the valence transition raises two possible mechanisms influencing the system: (i) the covalent B chemistry or (ii) a charge doping effect due to the insertion of additional valence electrons. Our theoretical study of the related system Eu$_{1-x}$La$_x$Pd$_3$ supports the scenario of charge doping as the origin for the valence instability (see below).

Eu valence under La doping

Recently, a similar valence instability, as found in the system EuPd$_3$B$_x$, was observed for the compound Eu$_{0.4}$La$_{0.6}$Pd$_3$ where the influence of chemical pressure on the Eu valence state was investigated by susceptibility and XRD measurements.[191] While the substitution of Eu by La changes the "non magnetic" EuPd$_3$ into an "magnetic" Eu$_{0.4}$La$_{0.6}$Pd$_3$, comparable to the effect of B substitution in EuPd$_3$B$_x$ for $x \geq 0.2$, no valence change or lattice expansion was found for the substitution of Eu by Ce. Applying our calculational approach, we find a stable Eu^{2+} state for Eu$_{0.4}$La$_{0.6}$Pd$_3$ in agreement with the reported experiments. But as La and B are inserted at different crystallographic sites in the systems Eu$_{1-x}$La$_x$Pd$_3$ and EuPd$_3$B$_x$, respectively, the valence instability should be independent of the boron site occupation and respective bond formation.

For a more detailed analysis we simulated the gradual substitution of Eu by La using the LSDA+U+CPA approach analogue to the case of B substitution. In Fig. 4.14 (left) fixed spin moment calculations for two different volumes are shown. In both cases the different La contents strongly influence the balance between the Eu^{2+} and Eu^{3+} state. For a reduced volume the increasing La content changes the global energy minima from 6 to 7μ_{B}/Eu, clearly stabilizing the Eu $4f^7$ state for a La concentration of $x \geq 0.4$. For the experimentally observed volume of Eu$_{0.4}$La$_{0.6}$Pd$_3$, a global energy minimum around 7 μ_{B}/Eu is stable independent from the La content. Nevertheless, the energy difference between local minima and therefore the Eu $4f^6$ and Eu $4f^7$ state changes significantly

depending on the La content.

Systematic calculations for the whole substitution series of $Eu_{1-x}La_xPd_3$ compounds resulted in a sudden change of the optimized lattice parameters for a critical La concentration $x \approx 0.4$. As in the $EuPd_3B_x$ series, this discontinuity of the volume is connected to a sudden change in the occupation of the Eu $4f$ majority spin channel (see Fig. 4.14, right). Since the number of additional electrons per Eu site is basically the same in both systems, this result supports independently the predominant role of charge doping for the Eu valence change. In the case of $EuPd_3B$ the system gains 3 valence electrons compared to $EuPd_3$. For a critical B content of $x_c = 0.2$ the valence transition sets in for 0.6 additional electrons per Eu site. Substituting La in $Eu_{1-x}La_xPd_3$ not only increases the number of valence electrons but also reduces the number of Eu sites. Based on one additional valence electron per substituted La atom, the critical La concentration of $x_c = 0.4$ is shared by 0.6 Eu sites, resulting in 0.67 additional valence electrons per Eu site.
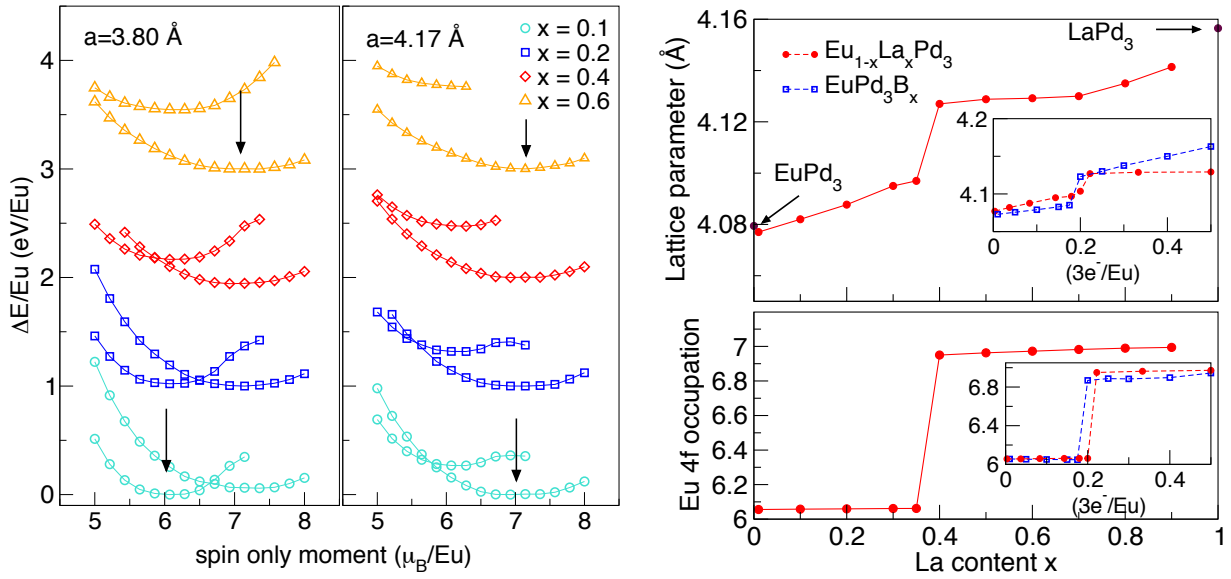
Figure 4.14.: Left: Fixed spin moment calculation for $Eu_{1-x}La_xPd_3$ depending on the unit cell volume for two different La concentrations. Right: Optimized lattice parameter and Eu $4f$ occupation for different La contents in $Eu_{1-x}La_xPd_3$. Insets: Comparison to the development of $EuPd_3B_x$ for different B contents. The data are related to the same number of additional electrons per Eu site.

Summary

In this joint theoretical and experimental investigation we combined DFT based electronic structure calculations with X-ray absorption and X-ray diffraction measurements at high pressures to elucidate the driving force of the valence transition in the system $EuPd_3B_x$, which stimulated many studies in the past. In the series of $EuPd_3B_x$ ($0 \leq x \leq 0.53$) compounds, a valence transition from Eu^{3+} towards Eu^{2+} into a heterogeneous mixed valence state was observed with increasing B content, where the onset of the transition at $x_c = 0.2$ yields a pronounced lattice anomaly. The strong interplay of the Eu valence state and the crystal structure raised the question whether this transition is driven by (i) the

change in the volume, (ii) the chemistry of boron or by (iii) the electron count. Since the substitution of B into the system influences several parameters simultaneously, in particular the crystal structure and the number of valence electrons, the underlying mechanism is not obvious. Furthermore the separation of the relevant parameters is impeded as substitution usually induces at the same time disorder and changes of the local crystal field due to local distortion. However, also theory cannot solve the problem unambiguously as a mixed valence state cannot be simulated in a standard DFT approach. Thus, we applied a combination of different techniques to unravel the contributions of the different effects on the valence transition.

To estimate the pure volume effect (i) on the Eu valence state high pressure experiments for samples with a fixed B content above the transition have been performed. The results of the XAS measurements yield a sizable influence of pressure on the Eu valence, although the mixed valence state can be reversed only partially for pressures up to $25\,\mathrm{GPa}$. The observed valence change of Eu is confirmed by XRD experiments under pressure. The evaluation of the obtained equation of states for two $\mathrm{EuPd_3B_x}$ ($x = 0.32$, 0.48) and two Gd-reference ($x = 0.35$, 0.44) systems with a stable $4f$ configuration result in a significantly smaller bulk modulus for the Eu compounds indicating the valence change. However, the critical volume for the transition (corresponding to $x = 0.2$ at ambient pressure) is already reached at about $10\,\mathrm{GPa}$. This leads to the picture that the volume change (i) is of minor importance for the transition. This conforms with the electronic structure calculations that point to a much stronger influence of the B insertion than a mere increase of the volume. The relevance of the remaining parameters ((ii) boron chemistry vs. (iii) electron count) could be separated by a systematic theoretical study of the series $\mathrm{Eu_{1-x}La_xPd_3}$, where a similar valence change for $x = 0.6$ was reported recently [191]. The calculations indicate a valence transition in $\mathrm{Eu_{1-x}La_xPd_3}$ for $x_c^{La} \geq 0.4$ which corresponds surprisingly well with the electron count per Eu for the critical B concentration $x_c^B = 0.2$. Consequently this leads to the conclusion that the valence transition of $\mathrm{EuPd_3}$ derived compounds is of essentially electronic origin and ruled by the number of additional valence electrons. A detailed experimental study of the $\mathrm{Eu_{1-x}La_xPd_3}$ system to challenge the theoretical prediction is under way. The results of this section are published in Ref. [189] and Ref. [192].

5. Summary and outlook

In this work, DFT based electronic structure calculations, model calculations and various experiments were combined to investigate the close interplay of crystal structure and magnetic properties of solids. Our study demonstrates that present day band structure calculations can successfully describe the electronic and magnetic properties of real materials, like intermetallic compounds containing rare earth elements, or insulating transition metal systems, both exhibiting strong electronic correlations in the $4f$ or $3d$ states, respectively. Effects like vacancies, substitutional disorder, impurities or split positions, which often have a crucial influence on the physical properties of real materials, can be considered with sufficient accuracy in many cases, leading to a realistic description of many phenomena and even developing predictive power. Applying model approaches on top of these electronic structure calculations provides microscopic insights, which allow to unravel underlying mechanisms of the subtle interplay between crystal chemistry and physical properties of real materials.

The combination of this ab-initio approach with quantum Monte-Carlo simulations and various, independent experimental methods probing macroscopic and microscopic properties, such as thermodynamic measurements, high field magnetization, nuclear magnetic resonance or electron spin resonance experiments allowed to develop reliable pictures of new and rather complex materials in close cooperation with experimentalists. In turn, this close interplay of experimental and theoretical studies allowed to refine the developed magnetic models and broadened the experience in the investigated classes of materials. In this sense, the systematic variation of intrinsic parameters by substitution or of extrinsic factors, like magnetic field, temperature or pressure is an efficient way to probe the derived models. Especially pressure allows a continuos change of the crystal structure on a rather large energy scale without the chemical complexity of substitution, thus being an ideal tool to consistently alter the electronic structure in a controlled way.

Using our theoretical approach - DFT electronic structure and model calculations - combined with experimental measurements, we studied the magnetism of low dimensional transition metal and intermetallic compounds with respect to the intimate interplay between their crystal and electronic structure. Whereas in the first part of this work the main purpose was to develop reliable magnetic models of low dimensional magnets, in the second part we studied the influence of pressure on the electronic structure of several intermetallic compounds and challenged our theoretical predictions by state of the art experiments using synchrotron radiation.

In more detail, the first part of this thesis is focused on the magnetic ground states of spin 1/2 transition metal compounds which show fascinating phase diagrams with many unusual ground states, including various types of magnetic order like helical states exhibiting different pitch angles, driven by the intimate interplay of structural details and quantum fluctuations. The exact arrangement and the connection of the magnetically active building blocks within these materials determine the hybridization, orbital occupation, and orbital orientation, this way altering the exchange paths and strengths of the magnetic interaction within the system and consequently being crucial for the formation of the respective

ground states.

The physics of these compounds can often be understood by the reduction of their complex magnetic interactions to more simple models. The investigated chain or square lattice compounds can be sufficiently well described by quasi 1D or 2D $J_1 - J_2$ Heisenberg models, while the studied dimer chain compounds result in alternating $J_{1a} - J_{1b}$ Heisenberg chains, in good approximation. The small inter chain couplings J_{ic} can often be considered as perturbation with respect to the leading couplings, shifting the ordering temperature or changing details of the ordering, e.g., influencing the pitch angle. Exceptions are compounds close to QCP, where J_{ic} can have a dramatic influence due to the cancelation of the leading interactions of the system.

The strong correlations of Cu $3d$ states in these materials have been considered in two different ways: (i) In a model approach adding the strong correlation "a posteriori" or (ii) performing LSDA+U calculations, which contain the strong Coulomb repulsion within the Cu $3d$ orbitals in a mean field way. To elucidate the magnetic ground state of the studied compounds, we mapped the relevant states of the LDA band structure onto an effective TB model and subsequently, including the correlation, via a Hubbard model onto a Heisenberg model to evaluate not only the hierarchy of exchange processes, but also to estimate the AFM parts of exchange integrals. In addition, we performed magnetic super cell calculations within the LSDA+U approximation and mapped the total energies onto related Heisenberg models to derive the total coupling strength of the leading exchange interactions including both, FM and AFM contributions. This combination of methods allowed to develop a comprehensive picture of the magnetic ground state, providing deep microscopic insight and a reliable estimate of the main interactions as preconditional input for numerical simulations of macroscopic properties.

The spin 1/2 transition metal compounds, which have been investigated in this work, illustrate the great variety of interesting phenomena, fueling the huge interest in this class of materials. We focused on cuprates with magnetically active CuO_4 plaquettes, mainly arranged into edge sharing chain geometries. The influence of structural peculiarities, as distortion, folding, changed bonding angles, substitution or exchanged ligands were studied with respect to their relevance for the magnetic ground state.

In particular, we classified the recently synthesized compound $AgCuVO_4$ as an example "in between" the two archetypes of corner- and edge shared chains. The systematic study of Li_2ZrCuO_4 elucidated the subtle balance of exchange interactions in vicinity to a quantum critical point and suggested the suppression of effective inter chain exchanges by the chain distortion as crucial parameter for the classification of the compound with respect to the phase diagram. Furthermore, we revealed the influence of ligand field effects on the magnetic ground state by the strong dependance of magnetic interactions from details of the crystal structure, such as the position of H atoms in $PbCuSO_4(OH)_2$, or the flipping of magnetic active orbitals upon hydration in the halides $CuCl_2$ and $CuBr_2$. We raised unambiguous criteria to settle the controversy about the magnetic ground state of the two spin gap compounds $Na_3Cu_2SbO_6$ and $Na_2Cu_2TeO_6$, which form quasi one dimensional alternating FM-AFM chains. We succeeded to develop the magnetic ground state of the spin gap compounds $Cu_2(PO_3)_2CH_2$ and $Cu_2PO_4CH_2$, both exhibiting rather complex crystal structures. Whereas $Cu_2(PO_3)_2CH_2$ can be described by coupled alternating Heisenberg chains, the magnetic ground state of $Cu_2PO_4CH_2$ is determined by an unusual orbital order of two inequivalent Cu sites. Finally, the comparative study of the new family of spin 1/2 square lattice compounds A_2CuEO_6 (A=Sr, Ba, E=Te, W) has elucidated a crucial

influence of the orbital symmetry of non magnetic spacer ions between the magnetically active units on the coupling regime of the system.

Besides the detailed description of the magnetic ground states of selected compounds, we attempted to unravel the origin for the formation of a particular magnetic ground state by deriving general trends and relations for this class of compounds. Details of the correlation treatment, determined by the Coulomb repulsion U_{3d} and the applied double counting correction within the LSDA+U approach, can become important for compounds with strong ligand field effects, whereas for the compounds investigated in this work such effects have minor impact. Evaluating the influence of chain distortion and of a change of the Cu-O-Cu bond angle has provided simple trends, but no unambiguous rules, which would allow the reliable prediction of magnetic ground states from simple structural considerations, only.

In general, our approach resulted in a reliable and accurate description of leading exchange interactions for real materials exhibiting localized spin 1/2 magnetism based on strong correlations. However, several questions remain open and will be addressed in further studies:

To gain more experience considering correlation effects within LSDA+U calculations for real materials, the unknown parameter U and J for specific compounds should be determined from theoretical grounds using constraint LDA calculations. Alternative approaches are the application of hybrid functionals or quantum chemical schemes for clusters. Linked to the LSDA+U calculation, an extended study of the double counting correction is required to elucidate the relevance, applicability and limitation of the chosen correction to a specific compound. For a deeper insight into the relation between individual parameters of the crystal structure, e.g., the Cu-O-Cu bond angle, and physical properties in the family of Cu^{2+} materials, the comparative, systematic investigations should be extended. Using multi-band studies and extended Hubbard models, the individual contributions to the exchange processes can be analyzed and further separated into the transfer terms between single orbitals. Furthermore, new experiments under pressure are proposed to drive $J_1 - J_2$ systems trough the phase diagram according the theoretical predictions. Preliminary results for Li$_2$CuO$_2$ suggest such a series of phases for the experimentally accessible pressure range and are recommended to be probed by neutron scattering experiments under pressure. Finally, the influence of orbital degrees of freedom on the magnetic ground state rises wide interest and stimulates the search for new materials, exhibiting an intimate interplay between orbital and spin degrees of freedom, to study their fascinating physics in more detail and to unravel the underlaying mechanisms.

In the second part of this work we presented the results of joint theoretical and experimental studies for intermetallic compounds, all exhibiting an isostructural phase transition under pressure. Many different driving forces for such phase transitions are known like quantum fluctuations, valence instabilities or magnetic ordering. The combination of extensive computational studies with state of the art experiments using synchrotron radiation reveals completely different underlaying mechanisms for the phase transitions in the investigated compounds.

For the itinerant system YCo$_5$, electronic structure calculations predicted an isostructural phase transition under pressure driven by a magneto elastic effect. Whereas the structural transition under pressure was already confirmed by high pressure XRD, a direct proof of the magnetic origin for this phase transition was still missing. In our study, we combined XMCD experiments under high pressure with DFT based electronic structure calculations

and succeeded to give a direct evidence of the magnetic character of the driving force responsible for the observed phase transition. A similar magnetic origin for the onset of a structural collapse under pressure was recently suggested for $SrFe_2As_2$, a member of the new family of high temperature iron-arsenide superconductors. According the results of our combined study, the suggested scenario is incorrect, since the structural transition is decoupled from magnetic order in the system. Instead, an electronic structure based bonding analysis in real- and k-space together with XRD experiments under high pressure, revealed the formation of new inter layer As bonds as the driving force in this system.

At last, we focused on the close interplay of the crystal structure and the magnetism in $EuPd_3B_x$. The magnetism of this compound series depends on the Eu valence, which is determined by the localized $4f$ states of the system. Upon B substitution, a lattice anomaly accompanied by a change of the Eu valence state was predicted by electronic structure calculations and confirmed by a combination of XRD and XAS experiments. Temperature dependent XAS measurements classified the Eu valence state as a heterogenous mixed valence state. Applying pressure reversed the transition only partially, excluding a pure volume effect. Probing in a systematic way the influence of structural degrees of freedom and the B chemistry by applying electronic structure calculations, XRD and XAS under pressure, we have demonstrated that the number of valence electrons is the crucial parameter for the onset of the transition. The theoretical investigation of the related system $Eu_{1-x}La_xPd_3$ supports the developed picture and predicts a similar valence transition within this compound series.

This shows, that DFT electronic structure calculations do not only describe insulators in a realistic way, but also intermetallic compounds with different character of their valence electrons. Whereas the correct treatment of weakly correlated itinerant systems could be expected, the consistent modeling of rather complex systems, including strong correlation and substitutional disorder, came as a surprise. The perfect agreement of several theoretical predictions and experimental results demonstrated the predictive power of such combined approaches.

Further studies are required to challenge the predicted phase transition for the $Eu_{1-x}La_xPd_3$ compound series. XRD and XAS experiments for samples with different La content are under way. Motivated by recent reports about a doping induced tetragonal collapse for compounds of the 122 family, electronic structure calculations applying various approximations were started. The preliminary data show encouraging results. Finally, our approach should be applied to even more complex systems, where both itinerant and local moments appear in one compound as in the ferrimagnet $EuFe_4As_{12}$. This material exhibits an ordering temperature T_c of about 150 K, while the closely related compounds $CaFe_4Sb_{12}$ and $SrFe_4Sb_{12}$ show strong magnetic fluctuations, only. Preliminary results from XAS experiments under pressure as well as electronic structure calculations point to a subtle interplay of the Eu valence and Fe magnetism in $EuFe_4As_{12}$.

This thesis demonstrates on a series of complex compounds that the combination of abinitio electronic structure calculations with numerical simulations and with various experimental techniques is an extremely powerful tool for a successful description of the intriguing quantum phenomena in solids. This approach is able to reduce the complex behavior of real materials to simple, but appropriate models, this way providing a deep understanding for the underlaying mechanisms and an intuitive picture for many phenomena. In addition, the close interaction of theory and experiment stimulates the improvement and refinement

of the methods in both areas, pioneering the grounds for more and more precise descriptions. Further pushing the limits of these mighty techniques will not only be a precondition for the success of fundamental research at the frontier between physics and chemistry, but also enable an advanced material design on computational grounds.

A. Technical details

AgCuVO$_4$

The electronic structure calculation were performed using the full potential local orbital scheme FPLO in its versions FPLO7.00-28, FPLO8.50-32 (WF module) and FPLO9.00-33 (to relax atomic sites). The obtained electronic structure using different versions were compared carefully to ensure accuracy. For the the scalar relativistic calculation the exchange and correlation potential of Perdew and Wang was chosen. We used a k-mesh of 343 points in the irreducible part of the Brillouin zone to ensure the convergency of the total energy. To consider the strong correlation within the Cu $3d$ states, we performed LSDA+U calculation and varied U_{3d} in the physically relevant range from $5 - 7\,\text{eV}$. Alternatively, we developed a TB model based on the LDA band structure and considered the strong correlation in a model approach by the mapping of the TB model via a Hubbard model onto an Heisenberg model. The parameters of the TB model were obtained by (i) a least square fit of the LDA bands along high symmetry paths (ii) and using a Cu-centered WF based fitting implemented in FPLO8.50-32.

High pressure X-ray diffraction measurements were performed at the beam line ID09 at the ESRF, Grenoble using a screw type of DAC with methanol/ethanol as pressure transmitting medium. The powder sample was pressurized up to $7.5\,\text{GPa}$. The pressure was determined by the ruby fluorescent method. After the integration of the collected powder pattern by the FIT2D package and a background correction, the lattice parameter were obtained by a Le Bai fit using the FULLPROF program. The internal atom positions were determined computational by relaxing the different atom sites within the symmetry of the space group (FPLO9.00-33). The synthesis, characterization and thermodynamical measurements of the AgCuVO$_4$ powder sample were performed by A. Möller (Universität Köln/University of Houston), J. Jainski (Universität Köln) and W. Schnelle (MPI CPFS, Dresden). For details see also Ref. [87].

Li$_2$ZrCuO$_4$

The electronic structure calculations were performed with the full potential local orbital scheme FPLO in its versions FPLO5.00-19 and FPLO7.00-28. In the scalar relativistic calculations the exchange and correlation potential of Perdew and Wang was used.[20] We also applied the general gradient approximation (GGA) (Perdew-Burke-Ernzerhof[21]) for the exchange and correlation potential to check whether this influences the LDA results. Neither for the band structure nor for the total energy differences we found any significant changes. For the basis within FPLO5.00-19 the following states were taken into account: Cu $(3s3p)/4s4p3d$, Li $1s/(2s2p)+3d$, O $(2s2p3d)$, Zr $(4s4p)/(5s5p4d)$ (notation: *semi-core states / valence states*). The Cu $3s3p$, Li $1s$ and Zr $4s4p$ states were treated as semi-core states due to the large extension of their wave functions. The unoccupied states Li $2p3d$, O $3d$ and Zr $5p$ were considered as hybridization states to complete the basis. All lower laying

states were treated as core states. To ensure accuracy of the total energy 300 k-points in the irreducible part of the Brillouin zone were used.

To model the Li(1) split position of the system, we employed the virtual crystal approximation (VCA) and coherent potential approximation (CPA). Alternatively super cells with different Li(1) orders have been studied. The different Li pattern can be found in the App. C.1, C.2. To treat the strong on-site Coulomb repulsion for Cu $3d$ orbitals explicitly, the L(S)DA + U method with U_{3d} in the representative range from $5.5\,\text{eV}$ to $8.0\,\text{eV}$ and a fixed $J = 1\,\text{eV}$ for the intra atomic exchange have been used.

To consider possible correlation effects between the Li(1) site and the surrounding atoms we probed the stability of the Li(1) split position by relaxing the surrounding O position for different fixed Li(1) sites using FPLO9.00-33 within the LDA, LSDA+U, GGA and GGA+U approach. The relaxation was performed within different space groups and shifting Li(1) along different paths. The presented energy dependance are preliminary results within an on-going project together with A. A. Tsirlin (MPI CPFS, Dresden).

High pressure XRD measurements have been performed at the ID09 of the ESRF in Grenoble for a powder sample (synthesized by A. A. Tsirlin, MPI CPFS, Dresden). A screw type of DAC with ethanol/methanol as pressure transmitting medium was used. Pressures up to $15\,\text{GPa}$ were achieved. The collected powder pattern were integrated using the FIT2D package. After a background correction the lattice parameter were determined by a Le Bai fit using the FULLPROF program. The internal parameters were evaluated computational by the full relaxation of atomic sites within the symmetry of the space group and a fixed Li(1) site (fixed to the high symmetry position) using FPLO9.00-33 based on different functionals (LDA, LDA+U, GGA and GGA+U). The observed trend of the crystal structure under pressure is independent from the chosen functional. See also Refs. [94] and [79] for further experimental details.

PbCuSO$_4$(OH)$_2$

Electronic structure calculations were performed using the full potential local orbital scheme FPLO within the version FPLO9.00-33. For the scalar relativistic calculation the exchange and correlation potential of Perdew and Wang was chosen. To ensure accuracy 518 k-points in the irreducible part of the Brillouin zone were considered.

The crystal structure of PbCuSO$_4$(OH)$_2$ was relaxed step wise starting from the two experimental data sets S1 from Ref. [102] and S2 from Ref. [101]. A fictitious planar structure was constructed starting from the fully relaxed crystal structure of S2 by placing the O(2) atoms to (0.2817, 1/4, -0.4376) to realize an ideal planar chain geometry. Afterwards the H atoms were allowed to relax.

For the development of the magnetic model the LDA band structure was fitted using a WF based TB model. In addition super cell calculation with different collinear spin arrangements were performed using the LSDA+U approach within the two double counting correction schemes AMF and FLL. The Coulomb repulsion U_{3d} was varied within the physical relevant range from 4-8 eV for AMF and 5-9 eV for FLL, respectively.

Low temperature XRD measurements down to $4\,\text{K}$ for a powder sample were performed at the high resolution beam line ID31 at the ESRF in Grenoble using a wave length of $\lambda = 0.39987\text{Å}$. The collected data were integrated on a 0.001 "grit" and refined using the FULLPROF package. The peak profile was characterized by very narrow and partially

asymmetric peak shapes. A displacement and a asymmetry parameter have been considered during the refinement. Due to technical problems the same powder sample was measured during two different beam times. A kink in the a and c axis was observed at about $50\,\mathrm{K}$ in the first run of experiments. Unfortunately, the anomaly in the experimental data coincided with a break of several hours of the experiment due to technical reasons during the beam line operation. In the refined lattice parameter from a second run of XRD experiments at the same beam line and with the same powder sample the anomaly is vanished (compare Fig. C.6 in the Appendix). However, the refinement of the lattice parameter and atomic sites is impeded by several impurities of the natural sample as e.g. quartz. Furthermore, the integrated pattern show distinct asymmetric peak shapes and a broadening of the peaks at low angles.

Thermodynamic measurements were performed by W. Schnelle (MPI CPFS, Dresden) for a powder sample. Single crystal XRD measurements at room temperature were done by H. Borrmann (MPI CPFS, Dresden). All samples in our study originate from the same pice of natural linarite.

CuCl$_2$ and CuBr$_2$

For the electronic structure calculation FPLO7.00-28 within the local (spin) density approximation (L(S)DA) was applied. In the scalar relativistic calculations the exchange and correlation potential of Perdew and Wang was chosen [20]. To consider the strong electron correlations for the Cu $3d^9$ configuration, we use the LSDA+U [37] approximation varying U_{3d} in the physically relevant range from $4 - 8\,\mathrm{eV}$ (AMF) and 5–$9\,\mathrm{eV}$ (FLL). The LDA results were mapped onto an effective tight-binding model (TB) and subsequently onto a Hubbard and a Heisenberg model.

For CuBr$_2 \cdot$ 4H$_2$O the experimental crystal structure was relaxed computational using FPLO9.00-33 within the symmetry of the space group and fixed experimental lattice parameter. The crystal structure of the fictitious system CuBr$_2 \cdot$ 2H$_2$O was constructed following two routes: (i) a volume optimization and a subsequent relaxation of the atomic positions and (ii) first a relaxation of the atomic sites followed by a volume optimization. After the first iteration step, the two routes result in slightly different crystal structures with a total energy difference of about $26\,\mathrm{meV/cell}$. Further iteration steps are required. The preliminary crystal structure of CuBr$_2 \cdot$ 2H$_2$O is given in App. B.11.

For a systematic investigation of the influence of the Cu-O-Cu bonding angle to the NN and NNN exchange integrals we varied the crystal structure of CuCl$_2$, CuBr$_2$ and an isostructural, fictitious CuF$_2$ by changing the Cu-O-Cu angle from $75°$ to $110°$ for constant Cu-Cl, Cu-Br or Cu-F distance. The influence of a changed distance to the neighboring chain was tested.

Exact diagonalization (ED) of the J_1–J_2 Heisenberg Hamiltonian has been performed on $N = 16$ sites clusters using the ALPS code [193] by O. Janson (MPI CPFS, Dresden). The low-temperature behavior of the magnetic susceptibility has been simulated using the transfer-matrix density-matrix renormalization-group (TMRG) method [194].

Polycrystalline CuCl$_2$ was prepared by dehydration of CuCl$_2$·2H$_2$O under vacuum at $390\,\mathrm{K}$. Single crystals were grown by chemical transport in a temperature gradient from $650\,\mathrm{K}$ to $575\,\mathrm{K}$ with AlCl$_3$ as transport agent. The chemical characterization of CuCl$_2$·2H$_2$O and of the CuCl$_2$ crystals was carried out by X-ray powder diffraction, DSC/TG-methods and

chemical analysis (M. Schmidt, MPI CPFS, Dresden).

The heat of dehydration was determined by DSC. Based on five independent measurements, the heat of dehydration is $\Delta H_{\mathrm{dehyd.}}^0 = (117\pm2)\,\mathrm{kJ/mol}$ at $400\,\mathrm{K}$ (S. Hoffmann, MPI CPFS, Dresden).

Magnetization was measured in a SQUID magnetometer $(1.8 - 300\,\mathrm{K})$ in magnetic fields up to $7\,\mathrm{T}$. Heat capacity was determined by a relaxation method in the same temperature range up to $\mu_0 H = 9\,\mathrm{T}$ (W. Schnelle, MPI CPFS, Dresden). See also Ref. [114].

Na$_3$Cu$_2$SbO$_6$ and Na$_2$Cu$_2$TeO$_6$

For the electronic structure calculation the full potential local orbital scheme FPLO8.50-32 was used. In the scalar relativistic calculations the exchange and correlation potential of Perdew and Wang has been applied.[20] To ensure accuracy 470 k-points in the irreducible part of the Brillouin zone were taken into account.

LSDA+U calculations of super cells with different spin arrangements were performed, treating the strong Cu $3d$ correlations in a mean field way. For the double counting correction (DCC) the two limiting cases, the around mean field (AMF) approximation and the fully localized limit (FLL), were applied. The on-site Coulomb repulsion U_{3d} was varied in the physical relevant range from 4–8 eV for the AMF-DCC and from 5–9 eV for the FLL-DCC, respectively, while the intra-atomic Hunds coupling I_{3d} was fixed to 1eV.

To separated structural and ionic effects on the magnetic properties of Na$_3$Cu$_2$SbO$_6$ and Na$_2$Cu$_2$TeO$_6$ the virtual crystal approximation (VCA) was applied. The atomic sites of Na$_3$Cu$_2$SbO$_6$ and Na$_2$Cu$_2$TeO$_6$ were relaxed within the symmetry and lattice parameter of the experimental crystal structure using FPLO9.00-33. Only for the Te containing compound sizable difference are observed. The obtained crystal structure is given in App. B.14. For the structural variants of the two compounds with ideal planar chain geometry O(2) was fixed to (.2069 0.5 -.225) for Na$_3$Cu$_2$SbO$_6$ and O(2) to (.19058 1/2 .2156) for Na$_2$Cu$_2$TeO$_6$, respectively.

Polycrystalline samples of Na$_3$Cu$_2$SbO$_6$ were prepared by solid state reaction (by S. Golbs and M. Schmidt, MPI CPFS, Dresden). The determined lattice parameter of the green powder a=5.676 Å, b = 8.860 Å, c = 5.833 Å and β= 113.33° are in good agreement with earlier studies.[120] The thermodynamic measurements were performed by W. Schnelle (MPI CPFS, Dresden).

To connect theoretical and experimental results, high-temperature series expansion (HTSE) of an alternating Heisenberg chain comprising two inequivalent NN couplings J_{1a} and J_{1b} were performed by O. Janson (MPI CPFS, Dresden). The magnetic susceptibility and the lowest-lying $S_z = 0$, $S_z = 1$ and $S_z = 2$ excitations of a neutron spectrum were computed using the ALPS package by Quantum Monte-Carlo simulations.[193]

Cu$_2$(PO$_3$)$_2$CH$_2$

For the electronic band structure calculations a full potential non-orthogonal local-orbital minimum-basis scheme within the LDA was used. To treat the short C-H distance (0.96Å) the version FPLO6.00-24, with its double numerical basis for the valence states was used. In the scalar relativistic calculation the exchange and correlation functional of Perdew and Wang has been applied.[20]

To study the magnetic properties of the system we mapped the local (spin) density approximation (L(S)DA) band structure onto an effective one band tight binding model (TB) based on Cu-site centered Wannier functions. Strong correlations were included by mapping the TB model onto a Hubbard model and subsequently onto a Heisenberg model. In addition, LSDA+U [37] calculations of super cells with various collinear spin arrangements have been carried out. To approximate the strong Coulomb repulsion at the Cu $3d$ orbitals in a mean field way a Coulomb parameter $U_{3d} = 4\text{--}8\,\text{eV}$ within the AMF DCC and $U_{3d} = 5\text{--}9\,\text{eV}$ for the FLL DCC were used. The onsite exchange was fixed to $J = 1\,\text{eV}$.

Quantum Monte-Carlo (QMC) simulations were performed by O. Janson (MPI CPFS, Dresden) on a cluster of $N = 480$ spins $S = 1/2$ (12 coupled chains of 40 sites each) using the ALPS code.[193]

The presented magnetic susceptibility and Knight-shift (line-shift) experiments for a powder sample were performed by W. Schnelle (MPI CPFS, Dresden) and A. A. Gippius (Moscow State University). Further experimental data as heat capacity, magnetization in high magnetic field or from nuclear quadrupole resonance measurements are presented and discussed in detail in Ref. [125].

Preliminary high pressure experiments were performed up to 10 GPa at ID09 at the ESRF, Grenoble using a screw type of DAC and methanol/ethanol (4:1) as pressure transmitting medium. The pressure was determined by the ruby luminescent method. We observe a strong broadening of the powder rings with increasing pressure. In consequence, the individual reflections overlap significantly impeding the refinement of the crystal structure. However, no significant structural transition appear. The evaluated lattice parameter are given in App. Table C.4. The atomic positions will be determined computational by relaxing the atomic sites with and without considering magnetic ordering of the system in an ongoing study. Room temperature, high resolution XRD data collected at ID31 at the ESRF Grenoble support the refinement of the high pressure data. First low temperature measurements at the high resolution beam line ID31 at the ESRF were performed down to 4 K. Unfortunately, the evaluation of the collected and integrated powder pattern show some inconsistencies most probably related to the reaction of the sample within the high intensity of the beam. The powder sample exhibits visible change in color in the region of the beam spot (compare App. Fig. C.13).

Cu$_2$PO$_4$OH

Electronic structure calculation were performed using the full potential local orbital scheme FPLO within its version FPLO8.50-32 and FPLO9.00-33. For the scalar relativistic calculation the exchange and correlation potential of Perdew and Wang was chosen. To ensure accuracy 343 k-points in the irreducible part of the Brillouin zone were taken into account. The theoretical optimization of H positions (starting from the experimental crystal structure) leads to an total energy gain of 0.47 eV/cell (4.f.u.). Comparing the magnetic properties for the experimental and optimized structure reveals only minor differences. We yield an optimized H site of (-0.0734, 0.2885, 1/2).

For the evaluation of band characters and the construction of WF functions the following local coordinate systems were chosen: Cu(1) (Cu- chain) x'= (0 0 1) and z'= (0.68 1 0); Cu(2) (Cu-dimer) x'= (0 0 1) and z'=(1 0 0).

The orbital occupation was probed by evaluating the density matrix. A half filled Cu(1)

$3d_{xy}$ and Cu(2) $3d_{3z^2-r^2}$ were stabilized giving raise to orbital order in the system. Stabilizing a half filled Cu(1) $3d_{xy}$ and Cu(2) $3d_{xy}$ orbital leads to an energy difference of $0.5\,$eV.

The strong correlation in the Cu $3d$ states were considered within the LSDA+U approach. We varied U_{3d} from 4–8 eV for AMF and from 5–9 eV for FLL, respectively. To consider the different character of xy and $3z^2 - r^2$ orbitals a $2\,$eV stronger correlation was applied to the $3z^2 - r^2$ states.

A$_2$CuEO$_6$

In this common project with O. Janson (MPI CPFS, Dresden) the electronic structure calculation were performed using the full potential local orbital scheme FPLO within its version FPLO8.00-25. For the scalar relativistic calculation the exchange and correlation potential of Perdew and Wang was chosen. To ensure accuracy we considered 242 k-points in the irreducible part of the Brillouin zone.

To develop the magnetic model from microscopic grounds, we mapped the relevant states of the LDA band structure onto an effective TB model using Cu centered WF. The strong correlation of the Cu $3d$ orbitals was considered in a model approach by the subsequent mapping of the derived TB model onto an Hubbard model. Alternatively, the strong Coulomb repulsion was taken into account by LSDA+U calculation with $U_{3d} = 6.5\,$eV within the AMF DCC.

Samples were prepared by R. Nitzsche, M. Schmidt and A. A. Tsirlin (MPI CPFS, Dresden). Magnetic susceptibility measurements were performed by W. Schnelle (MPI CPFS, Dresden). The QMC calculation of a J_1-J_2 model to simulate the magnetic susceptibility by a high temperature series expansion (HTSE) was done by O. Janson (MPI CPFS, Dresden). Neutron diffraction experiments for Sr$_2$CuTeO$_6$ and Sr$_2$CuWO$_6$ were carried out by A. A. Tsirlin (MPI CPFS, Dresden) at the ILL Grenoble.

Systematics

For the systematic study of the NN and NNN exchange integrals on the Cu-O-Cu bonding angle γ of the edge shared chain compounds we varied γ from 75° to 110° at the same time fixing the Cu-O distance.

We started from the crystal structure of Ref. [195] for LiCuVO$_4$ exhibiting an experimental observed bonding angle of about 95.98°. The crystal structure data of Li$_2$CuO$_2$ were taken from Ref. [196]. The crystallographic data for NaCu$_2$O$_2$ (according to Ref. [132]) were slightly modified resulting in a constant Cu-O distance and a single bonding angle of 95.54° along the chain direction. Therefore, O(1) and O(2) were shifted to (0.15455 1/4 0.11) and (0.58505 1/4 0.11), respectively. The investigation of the famous Spin Peierls system CuGeO$_3$ with an Cu-O-Cu bonding angle of 98.41° were based on the experimental crystal structure according Ref. [197]. For the CuF$_2$ we constructed an artificial crystal structure in analogy to the crystal structure of CuCl$_2$ and CuBr$_2$.[1] The optimization of the volume leads to $a = 5.6883\,$Å, $b = 2.9427\,$Å, $c = 5.2609\,$Å and $\beta = 127°$. As reference system for a Cu-O-Cu bonding angle of 180° Sr$_2$CuO$_3$ from Ref. [199] was chosen.

---

[1]In nature CuF$_2$ crystallizes in the same type of crystal structure than CuO [198].

The LSDA+U calculation during the angle variation were performed for $U_{3d} = 7\,\mathrm{eV}$ and $I_{3d} = 1\,\mathrm{eV}$ within the AMF-DCC. The integrated orbital resolved density of states were calculated within a Cu centered local coordinate system, where x' runs along the chain direction and z' perpendicular to the chain plane.

YCo$_5$

For the spin polarized electronic structure calculation we chose the full potential local orbital scheme FPLO within its version FPLO5.00-19 with all numerical parameters according to Ref. [149], where extensive convergence tests have been carried out.

The results (density of states) were checked carefully against the new version FPLO9.00-33 with its double numerical basis. To simulate the experimental XMCD spectra we calculated the polarization of Co states and broadened it by 1.3 eV close to the experimental resolution. To consider a possible strong influence of spin-orbit coupling, full relativistic calculation were performed (for the projection on orbital resolved DOS a modified version FPLO9.03-37 was applied). The obtained polarization (summed up following the selection rule for dipolar excitation) show the same trends like the scalar relativistic calculation.

We performed Co K-edge (7 709 eV) X-ray absorption spectroscopy (XAS) and XMCD measurements at the energy dispersive XAS beam-line ID24 of the ESRF using the setup reported in Ref. [153], upgraded with an He cryostat especially designed for high pressure magnetic measurements. Circular polarization was attained with a diamond quarter wave plate. The sample was pressurized within a membrane type non-magnetic Cu-Be DAC and inserted in a 0.7 T magnetic field parallel to the x-ray beam. The cells were equipped with 1.2 mm perforated anvils in order to reduce the absorption. The samples were synthesized by U. Schwarz (MPI CPFS, Dresden).

Data for pressures up to 22.5 GPa were collected along two isotherms, at room temperature and at 100 K, using methanol/ethanol (4:1) and nitrogen, respectively, as pressure transmitting media. The pressure was measured using the ruby fluorescence method [55] and the temperature was monitored by a sensor placed on the copper sleeve hosting the cell. For each pressure point, the XMCD spectrum was obtained by accumulating 100 data acquisitions. The applied magnetic field was flipped between each of the successive absorption spectra recordings, while keeping the helicity fixed. Always, a second XMCD spectrum was measured with the inverse helicity. The measured spectra were deconvoluted by three gaussian. Since the small, low energy shoulder fall below a threshold it was consequently set to zero.

See also Ref. [155].

SrFe$_2$As$_2$

In this common project with D. Kasinathan (MPI CPFS, Dresden) the electronic structure calculation were performed using the full potential local orbital scheme FPLO9.00-24 within both, local density approximation (LDA) and as well as generalized gradient approximation (GGA). The crystal structures are optimized at different levels to investigate or isolate effects that may depend sensitively on certain structural features. The full-relaxation of the unit cell involves optimizing the c/a ratios in addition to relaxing the As-z position.

Samples were prepared by A. Leithe-Jasper (MPI CPFS, Dresden). X-ray diffraction measurements (XRD) were performed at the high-pressure beam-line ID09 of the ESRF up to 20 GPa at room temperature for $SrFe_2As_2$ and $SrFe_{1.8}Ru_{0.2}As_2$. For best possible hydrostatic conditions we used a membrane type of diamond anvil cell (DAC) with helium as pressure transmitting medium. The pressure was determined using the ruby fluorescence method. The measured powder rings were integrated using the program FIT2D. After a background correction the lattice parameters were refined with the FULLPROF package. In addition, for selected pressure points, the As z positions were determined starting from the results of our Le Bai fits without considering any further displacement parameters.

The calculation of the band characters for bonding and anti-bonding combinations of inter-site As $4p$ states were realized by K. Koepernik (IFW, Dresden) by an unreleased version of the FPLO scheme. Calculations in real-space were performed by Yu. Grin (MPI CPFS, Dresden). For details see also Ref. [169].

$EuPd_3B_x$

Since $EuPd_3B_x$ asks for the combination of the LSDA+U and the CPA approach to ensure an appropriate description of the rather complex system, including strong correlations and substitutional disorder, we used the full potential local orbital scheme FPLO in its version FPLO5.00-19.

In the scalar relativistic calculations the exchange and correlation potential of Perdew and Wang was chosen.[20] As basis set the following semicore / valence and polarization states were taken into account: Eu $(4d4f5s5p)/(6s6p5d)$, Pd $(4s4p)/5s5p4d$ and B $2s2p3d$. All lower lying states were treated as core states in a fully relativistic way.

To take into account the strong correlation in the Eu $4f$ shell in a mean field like approximation we performed LSDA+U calculations[37] with the on-site Coulomb repulsion $U = 8\,eV$ (in the atomic limit for the double counting scheme) and the on-site exchange $J = 1\,eV$. This correspondes to the Slater parameters $F_0 = 8\,eV$, $F_2 = 11.91\,eV$, $F_4 = 7.96\,eV$ and $F_6 = 5.89\,eV$ typical for $4f$ elements.[31] The variation of U between 6 eV and 8 eV and J between 0 eV and 1 eV does not change the results qualitatively (see App. C.21).

To model the gradual, disordered insertion of B from $EuPd_3$ to $EuPd_3B$ and of La from $EuPd_3$ to $LaPd_3$, the coherent potential approximation (CPA)[38] was used. For the ordered cases (x=0, a super-cell with x=0.5 and x=1) the CPA calculations were compared to usual ordered structure calculations using the Blackman-Esterling-Berk (BEB)[186] approach to check the accuracy.

Furthermore, for $EuPd_3$ the virtual crystal approximation (VCA) at the Pd site was used to model an electron doping of the system independent from structural changes.

Polycrystalline samples were prepared by arc melting of the elements under Ar atmosphere and carefully characterized (R. Gumeniuk, A. Leithe-Jasper, G. Auffermann, W. Carrillo-Cabrera, MPI CPFS, Dresden). The influence of B substitution on the $EuPd_3B_x$ and the Gd-reference system was studied by the combination of XRD, metallography, energy and wave-length dispersive X-ray spectroscopy as well as chemical analysis and a good statistics (for details see Ref. [189]). A combination of magnetic susceptibility (W. Schnelle, MPI CPFS, Dresden) and XAS (M. Schmidt and U. Burkhardt, performed at the German synchrotron light source DESY Hamburg) experiments were used to evaluate the valence state of the systems.

To study the influence of pressure, x-ray diffraction measurements (XRD) up to $30\,\mathrm{GPa}$ were performed at the high-pressure beam-line ID09 of the ESRF at room temperature for two different $\mathrm{EuPd_3B_x}$ samples ($x = 0.32, 0.48$) above the valence transition and two $\mathrm{GdPd_3B_x}$ compounds with corresponding B content as reference system ($x = 0.35, 0.44$). For best possible hydrostatic conditions we used a membrane diamond anvil cell (DAC) with helium as transmitting pressure medium. The pressure was determined using the ruby fluorescence method.[55] The collected pattern were integrated using the program FIT2D.[56] After a background correction the data were refined with the FULL-PROF package.[57]

Eu L_{III}-edge (6977 eV) x-ray absorption spectroscopy (XAS) measurements were collected at the energy dispersive XAS beam-line ID24 of the ESRF, on two $\mathrm{EuPd_3B_x}$ samples ($x = 0.32, 0.48$). The powder samples were pressurized up to $25\,\mathrm{GPa}$ within a non magnetic Cu-Be DAC using silicon oil as pressure transmitting medium. As in the high-pressure XRD experiment, a ruby chip was used for the pressure determination. The obtained XAS spectra were analyzed by a least squares fitting procedure to determine the average Eu valence ν by the relative intensities of $\mathrm{Eu^{2+}}$ and $\mathrm{Eu^{3+}}$ components, as described in Ref. [200]. See also Refs. [189] and [192].

B. Crystal Structures

The crystal structure data within this section are mostly not given in the representation of the original references, but are transformed according to the standard representation of the international tables of crystallography, which is needed as input for the FPLO scheme. The quantization axis in this DFT scheme runs along the z-axis. In several cases data sets were further transformed to allow an easier comparison between closely related compounds or to rotate the plane of the magnetic active orbitals perpendicular to the quantization axis. This way the analysis of orbital resolved DOS or the description of orbital characters by e.g. Wannier functions can be simplified. Thus, the following data should be understood as structure input data sets for the calculations.

Table B.1.: Left: The compound $AgCuVO_4$ crystallizes in the space group $Pnma$ (62) with $a = 9.255$Å, $b = 6.778$Å and $c = 5.401$Å (see Ref. [86]).

Site	x/a	y/b	z/c
Cu	0.5	0	0.5
Ag	0.13803	1/4	0.51485
V	0.3098	1/4	0.0576
O(1)	0.1142	1/4	0.0728
O(2)	0.1269	3/4	0.2654
O(3)	0.3741	0.4502	0.2165

Table B.2.: The γ-phase of Li_2ZrCuO_4 crystallizes in the space group $Cccm$ (66) with the lattice parameter $a = 9.385$Å, $b = 5.895$Å, and $c = 5.863$Å. (according Ref. [93] and ICSD(59618)) For the calculation Li(1) = (0.210, 0.742, 0) is shifted to (0.21, 0.75, 0). The small mixed occupancy of Cu and Li(2) are neglected in good approximation.

Site	x/a	y/b	z/c	exp. occupation
Cu	0	0	.5	0.95 Cu + 0.05 Li
Li(1)	.21	.75	0	0.5
Li(2)	0	.5	.25	0.97 Li + 0.03 Cu
Zr	.25	.25	0	1
O(1)	-.0246	.228	.5	1
O(2)	.2662	0	.25	1

Table B.3.: Left: Experimental structure S1 for $PbCuSO_4(OH)_2$ from the ICSD based on XRD by Effenberger *et al.* [102] with optimized H positions according to Ref. [100]. The S position from the ICSD (0.3319, 0.75, 0.8845) and the original paper (0.2219, 0.75, 0.8845) do not coincide. Our theoretical relaxed S position is closer to the S position published in Ref. [102] compared to the ICSD data. Space group $P2_1/m$ (11) with $a = 4.69$Å, $b = 5.65$Å, $c = 9.701$Å, $\beta = 102.65°$. Origin shifted. Right: Computational relaxed structure S1.

Site	x/a	y/b	z/c	Site	x/a	y/b	z/c
Cu	0	0	1/2	Cu	0	0	-1/2
Pb	.32838	1/4	.8420	Pb	0.49396	1/4	-0.13960
S	.1155	1/4	.1681	S	0.21718	1/4	0.15537
O	.2667	1/4	.5952	O	0.161673	1/4	-0.36338
O	.4307	1/4	.16530	O	-0.46197	1/4	0.142712
O	.7136	1/4	.4658	O	-0.24146	1/4	0.424504
O	.9344	1/4	.0246	O	0.04370	1/4	0.00860
O	.0574	.0355	.2469	O	0.17111	0.03276	0.23382
H	.06956	1/4	.62349	H	-0.00519	1/4	-0.31571
H	.60753	1/4	.36413	H	-0.29108	1/4	0.31920

Table B.4.: Left: Experimental crystal structure S2 for $PbCuSO_4(OH)_2$ from neutron scattering (NS) by Schofield *et al.* [101]. Space group $P2_1/m$ (11) with $a = 4.683$Å, $b = 5.646$Å, $c = 9.682$Å, $\beta = 102.66°$. Right: Computational relaxed structure S2.

Site	x/a	y/b	z/c	Site	x/a	y/b	z/c
Cu	1/2	0	1/2	Cu	1/2	0	-1/2
Pb	.5123	1/4	.8420	Pb	-0.49567	1/4	-0.15722
S	.0560	1/4	.1687	S	0.05199	1/4	0.16575
O	.0900	1/4	.0254	O	0.09217	1/4	0.01827
O	.3265	1/4	.5959	O	0.31688	1/4	-0.41061
O	.7340	1/4	.1624	O	-0.27031	1/4	0.16580
O	.7526	1/4	.4662	O	-0.24638	1/4	0.46448
O	.1893	.0372	.2473	O	0.18441	0.03329	0.24495
H	.105	1/4	.5555	H	0.09256	1/4	-0.45032
H	.756	1/4	.3682	H	-0.25056	1/4	0.36046

Table B.5.: Fictitious structure of $PbCuSO_4(OH)_2$ with planar chains constructed from the relaxed S2 (Ref. [101]). The H sites have been relaxed. Space group $P2_1/m$ (11) with $a = 4.683$Å, $b = 5.646$Å, $c = 9.682$Å, $\beta = 102.66°$

Site	x/a	y/b	z/c
Cu	1/2	0	-1/2
Pb	-0.49567	1/4	-0.15722
S	0.05199	1/4	0.16575
O	0.09217	1/4	0.01827
O	0.2817	1/4	-0.4376
O	-0.27031	1/4	0.16580
O	-0.2817	1/4	0.4376
O	0.18441	0.03329	0.24495
H	0.058813	1/4	-0.48157
H	-0.29577	1/4	0.33286

Table B.6.: The family of $EuPd_3B_x$ and $GdPd_3B_x$ compounds crystallizes in the space group $Pm\bar{3}m$ (221). The lattice parameters where optimized with respect to the B content. The calculations result in lattice parameters in the range of $a = 3.80 - 4.3$Å.

Site	x/a	y/b	z/c
Eu	0	0	0
Pd	1/2	1/2	0
B	1/2	1/2	1/2

Table B.7.: $Sr(Fe/Ru)_2As_2$ crystallize in the space group $I4/mmm$ (139). We optimized the structure on different levels. The full relaxation of the unit cell involves optimizing the ratio c/a and the As-z position. For the partially relaxed structure the As-z position was fixed to (0, 0, 0.36).

Site	x/a	y/b	z/c
Sr	0	0	0
Fe/Ru	0	1/2	1/4
As	0	0	0.36

Table B.8.: Left: Experimental crystal structure of $CuCl_2$ from Ref. [201]. Space group $C2/m$ (12) $a = 6.9038\,\text{Å}$, $b = 3.2995\,\text{Å}$, $c = 6.824\,\text{Å}$, $\beta = 122.197°$. Right: The crystal structure of $CuBr_2$ (according to Ref. [202]) was transformed in a way that the magnetic active orbitals lie in the x, y-plane (to facilitate the comparison to $CuCl_2$). Space group $C2/m$ (12) $a = 7.2096\,\text{Å}$, $b = 3.4742\,\text{Å}$, $c = 7.1719\,\text{Å}$, $\beta = 121.314°$.

Site	x/a	y/b	z/c	Site	x/a	y/b	z/c
Cu	0	0	0	Cu	0	0	0
Cl	0.5048	0	0.2294	Br	.4899	0	.7611

Table B.9.: Fictitious, relaxed crystal of CuF_2 in analogy to the crystal structures of $CuCl_2$ and $CuBr_2$. Space group $C2/m$ (12) with $a = 5.6883\,\text{Å}$, $b = 2.9427\,\text{Å}$, $c = 5.2609\,\text{Å}$, $\beta = 127°$.

Site	x/a	y/b	z/c
Cu	0	0	0
F	-0.5079	0	0.2252

Table B.10.: Crystal structure of $CuCl_2 \cdot 2H_2O$ according to Ref. [203]. Space group $Pmna$ (53) with $a = 8.104\,\text{Å}$, $b = 3.757\,\text{Å}$, $c = 7.433\,\text{Å}$. Calculations based on the crystal structure data according to Ref. [204] with small differences in the atomic positions give essentially the same results.

Site	x/a	y/b	z/c
Cu	0	0	0
Cl	0	0.3803	0.24020
H	0.3065	0.1295	0.0822
O	0.2402	0	0

Table B.11.: Crystal structure of fictitious $CuBr_2 \cdot 2H_2O$ after one iteration cycle of volume optimization and relaxation of atomic sites. Space group $P2_1/c$ (14) with $a = 4.0536\,\text{Å}$, $b = 7.005\,\text{Å}$, $c = 11.630\,\text{Å}$, $\beta = 104.6$.

Site	x/a	y/b	z/c
Cu	0	0	0
Br	0.4991	0.1377	0.1354
O	-0.0143	-0.1927	0.1208
H	-0.1727	-0.1235	0.1607
H	0.2045	-0.2062	0.1832

Table B.12.: YCo_5 crystallizes in the space group $P6/mmm$ (191). All atoms occupy special Wyckoff positions. [149] The lattice parameter where varied between $a = 4.54$Å and $a = 5.02$Å and $c = 3.69$Å and $c = 3.99$Å., respectively.

Site	x/a	y/b	z/c
Y	0	0	0
Co(1)	1/3	2/3	0
Co(2)	1/2	0	1/2

Table B.13.: Crystal structure data for A_2CuEO_6 (A =Ba, Sr and E =W,Te) according Ref. [141]. Space group $I4/m$ (87), with the following special positions: Ba/Sr(0, 1/2, 1/4), Cu(0, 0, 0), W/Te(0, 0, 1/2), O(1)(0, 0, z) and O(2)(x, y, 0).

	Ba_2CuWO_6	Sr_2CuWO_6	Sr_2TeO_6	Ba_2CuTeO_6
a [Å]	5.5642	5.429	5.4038	5.5903
c [Å]	8.6363	8.4155	8.4664	8.6426
O(1)(z)	0.280	0.276	0.280	0.281
O(2)(x)	0.272	0.289	0.297	0.263
O(2)(y)	0.238	0.213	0.206	0.244

Table B.14.: Left: Experimental crystal structure of $Na_2Cu_2TeO_6$ Ref. [123]. Space group $C2/m$ (12) with $a = 5.7059$ Å, $b = 8.6751$ Å, $c = 5.9380$ Å, $\beta = 113.74°$. Right: Relaxed crystal structure of $Na_2Cu_2TeO_6$.

Site	x/a	y/b	z/c	Site	x/a	y/b	z/c
Cu	0	0.66475	0	Cu	0	-0.3353	0
Te	0	0	0	Te	0	0	0
O(1)	0.1936	0.1632	0.2121	O(1)	0.19058	0.1682	0.2156
O(2)	0.7574	0	0.1640	O(2)	-0.2520	0	0.1648
Na	0.	0.1839	0.5	Na	0.	0.1849	0.5

Table B.15.: Relaxed crystal structure of $CuBr_2 \cdot 4H_2O$ based on the crystal structure data according to Ref. [205]. Space group $P2_1/c$ (14) with $a = 4.116$ Å, $b = 7.33$ Å, $c = 12.013$ Å, $\beta = 105.44$.

Site	x/a	y/b	z/c
Cu	0	0	0
Br	0.4338	0.2246	0.0366
O	0.1576	-0.0927	0.1647
O	-0.2466	0.0223	0.2920
H	-0.0038	-0.0488	0.2108
H	0.3826	-0.0321	0.2043
H	-0.2505	-0.0594	0.3591
H	-0.2093	0.1515	0.3208

Table B.16.: Experimental crystal structure of $Na_3Cu_2SbO_6$ Ref. [120]. Space group $C2/m$ (12) with $a = 5.6759$ Å, $b = 8.8659$ Å, $c = 5.8379$ Å, $\beta = 113.289$. For planar structure O(2) is changed to (.2069,0.5,-.225).

Site	x/a	y/b	z/c
Cu	0	0.6667	0
Sb	0	0	0
O(1)	0.2931	0.334	0.775
O(2)	0.2404	0.5	0.1774
Na	0	0.5	0.5
Na	0.5	0.328	0.5

Table B.17.: Cu_2PO_4OH experimental structure reported by Belik *et al.* [129]. Space group *Pnnm* (58) with $a = 8.0513$ Å, $b = 8.3775$ Å, $c = 5.8799$ Å.

Site	x/a	y/b	z/c
Cu	0	1/2	.2491
Cu	-.36181	.37495	1/2
P	-.23297	.25163	0
O	-.1331	.412	0
O	-.1029	.1159	0
O	-.3413	.2389	.2106
O	-.1236	.3974	1/2
H	-.095	.289	1/2

Table B.18.: Crystal structure of $Cu_2(PO_3)_2CH_2$ (privat comm. Wei Liu email 18.8.05). Space group *Pnma* (62) with $a = 13.696$ Å, $b = 8.0103$ Å, $c = 4.9034$ Å.

Site	x/a	y/b	z/c
Cu	0.3928	0.0609	0.1118
P(1)	0.5134	0.2500	0.5990
P(2)	0.2746	-0.2500	0.2864
O(1)	0.4383	0.2500	0.3688
O(2)	0.2841	-0.0913	0.1193
O(3)	0.4957	-0.0925	0.2233
O(4)	0.3240	0.2500	-0.0562
C	0.3672	-0.2500	0.5448
H	0.360	-0.156	0.665

C. Supporting Material

file	p_v [GPa]	p_n [GPa]	p [GPa]	a [Å]	b [Å]	c [Å]
46	2.52	2.52	2.52	9.159	6.715	5.356
47	2.52	2.52	2.52	9.159	6.715	5.357
48	5.32	5.33	5.33	9.094	6.660	5.322
49	6.46	6.58	6.52	9.065	6.647	5.308
50	6.58	6.59	6.59	9.064	6.648	5.307
51	7.05	7.20	7.13	9.057	6.636	5.303
52	7.49	7.45	7.47	9.052	6.637	5.299
53	7.37	7.30	7.34	9.054	6.640	5.301
54	6.66	6.59	6.63	9.066	6.643	5.311
55	6.14	6.09	6.12	9.079	6.649	5.311
56	5.38	5.36	5.37	9.079	6.654	5.315
57	4.67	4.61	4.64	9.096	6.666	5.324
58	4.07	4.01	4.04	9.118	6.681	5.333
59	3.33	3.24	3.29	9.137	6.707	5.350
60	1.99	1.89	1.94	9.175	6.728	5.375
61	0.87	0.61	0.74	9.214	6.747	5.387
62	0.61	0.63	0.62	9.212	6.750	5.386
63	0.29	0.22	0.26	9.227	6.752	5.394

Table C.1.: Refined lattice parameter for $AgCuVO_4$ from high pressure experiments at ID09 using a screw type of DAC with ethanol/methanol as pressure transmitting medium. Since the errors caused by the uncertainty of pressure and temperature are significantly larger than the estimated standard deviation from the refinement $(0.3 - 0.6 \cdot 10^{-3}$ for a, b and c, respectively) the individual e.s.d. are not given explicitly for each value.
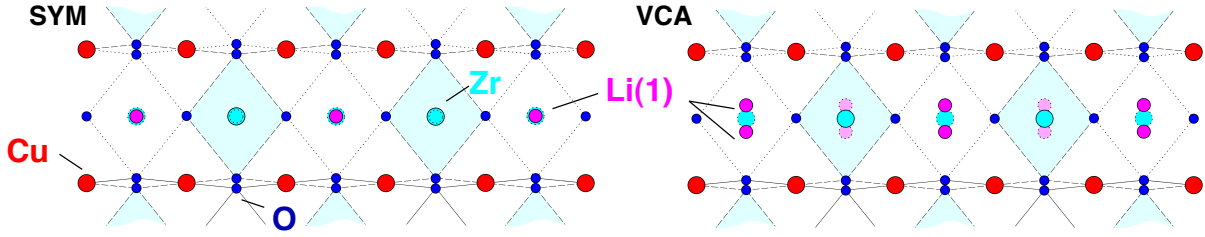
Figure C.1.: The SYM and VCA structural model to treat the Li(1) split position in Li$_2$ZrCuO$_4$: SYM - high symmetry position of Li(1); VCA - both sites of the split position occupied by partial Li(1) atoms.

file	p_v [GPa]	p_n [GPa]	p [GPa]	a [Å]	b [Å]	c [Å]
21	0.88	0.88	0.88	9.393	5.886	5.858
22	2.43	2.29	2.36	9.303	5.876	5.849
23	2.59	2.50	2.55	9.287	5.877	5.848
24	2.94	3.07	3.01	9.255	5.872	5.845
25	3.53	3.67	3.60	9.213	5.865	5.843
26	3.73	3.82	3.78	9.205	5.865	5.841
27	5.56	5.61	5.59	9.109	5.854	5.831
28	6.64	6.82	6.73	9.027	5.852	5.828
29	6.83	6.89	6.86	9.021	5.852	5.827
30	7.48	7.76	7.62	8.985	5.846	5.821
31	7.76	7.79	7.78	8.984	5.844	5.822
32	8.49	8.56	8.53	8.949	5.842	5.820
33	9.37	9.37	9.37	8.922	5.835	5.814
34	9.73	9.80	9.77	8.902	5.831	5.812
35	10.80	10.68	10.74	8.859	5.831	5.803
36	11.01	11.05	11.03	8.847	5.817	5.814
37	11.40	11.33	11.37	8.821	5.827	5.795
38	11.98	11.95	11.97	8.778	5.816	5.794
39	12.80	12.71	12.76	8.735	5.826	5.776
40	13.85	13.71	13.78	8.707	5.819	5.773

Table C.2.: Refined lattice parameter for Li$_2$ZrCuO$_4$ from high pressure experiment at ID09 using a screw type of DAC with ethanol/methanol as pressure transmitting medium. Since the errors caused by the uncertainty of pressure and temperature are significantly larger than the estimated standard deviation from the refinement ($0.3 - 0.6 \cdot 10^{-3}$ for a, b and c, respectively) the individual e.s.d. are not given explicitly for each value.
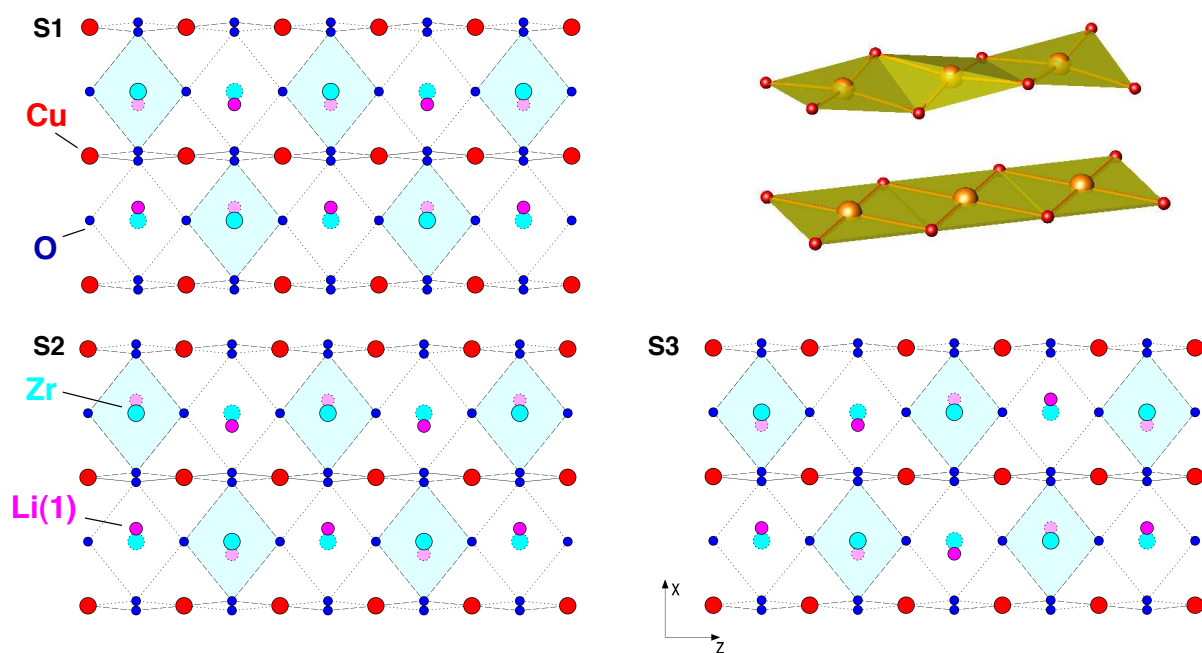
Figure C.2.: Different structural models (S1-S3) to simulate the Li split position in Li_2ZrCuO_4 using magnetic super cells. In S1 and S2 the Li(1) atoms along the chain are shifted parallel, while in S3 the Li(1) atoms alter along the chain direction. S1 and S2 differ in the Li(1) inter chain arrangement. In addition a small chain segment of the experimental observed, distorted chain geometry in comparison to a short chain segment with ideal, planar chain geometry is depicted (top, right panel).
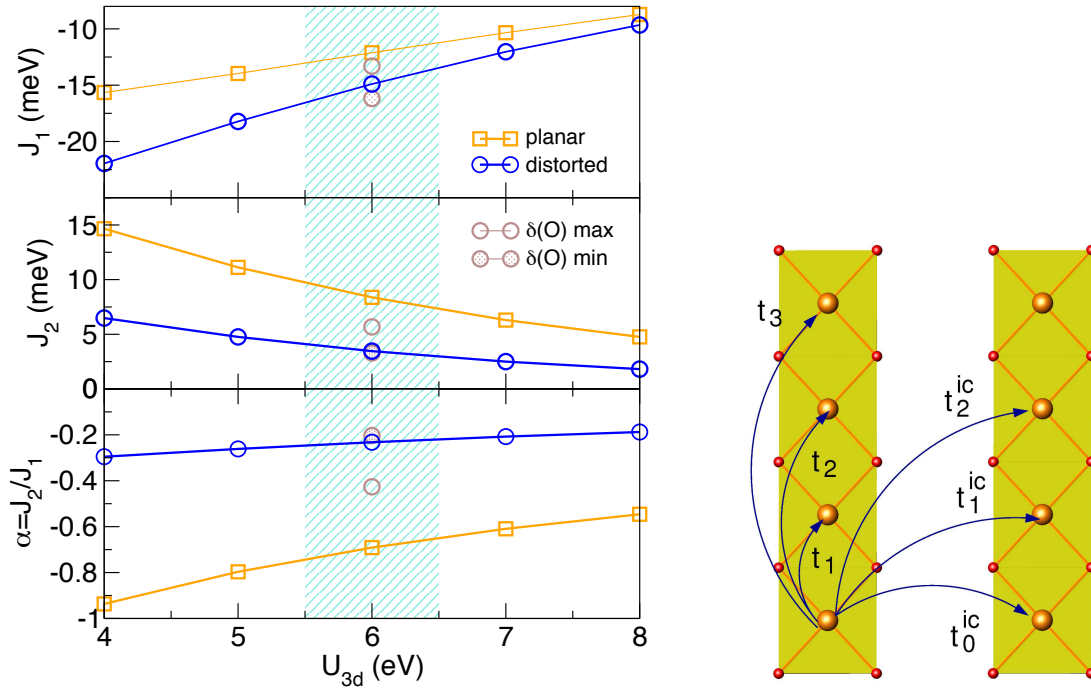
Figure C.3.: Left: Dependance of the leading exchange integrals and frustration ratio α of Li_2ZrCuO_4 from the applied Coulomb repulsion U_{3d}. Results for the distorted, experimental crystal structure and an ideal planar chain geometry. In addition, we give a first estimate of the influence of a full relaxation of the crystal structure, which influences the chain distortion. For $U_{3d} = 6\,eV$ the leading exchange integrals for the maximal and minimal O displacement (from the ideal planar chain geometry, derived from a full relaxation of the crystal structure) are given. Right: Sketch of the main transfer paths derived from our TB model.
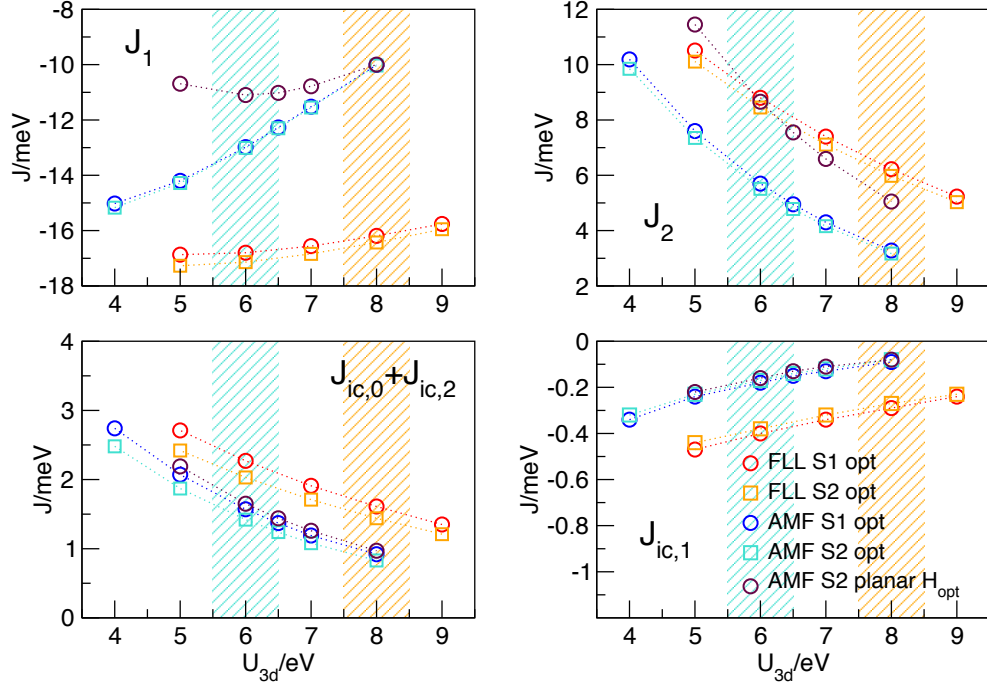
Figure C.4.: Dependance of the leading exchange integrals J_i from U_{3d} for $PbCuSO_4(OH)_2$ applying the AMF and FLL DCC.

compound	EE/cell [Ha/f.u.]
H_2O	-75.95780
$CuCl_2$	-2572.93311
$CuCl_2 \cdot 2H_2O$	-2724.88521
$CuBr_2$	-6859.24994
$CuBr_2 \cdot 4H_2O$	- 7163.16063
$CuBr_2 \cdot 2H_2O$ (optV)	-7011.15296
$CuBr_2 \cdot 2H_2O$ (relaxed)	-7011.18148

Table C.3.: Comparison of total energies for $CuCl_2$ and $CuBr_2$ and their hydrated variants. The total energy for H_2O is derived by calculating the crystal water as molecule.
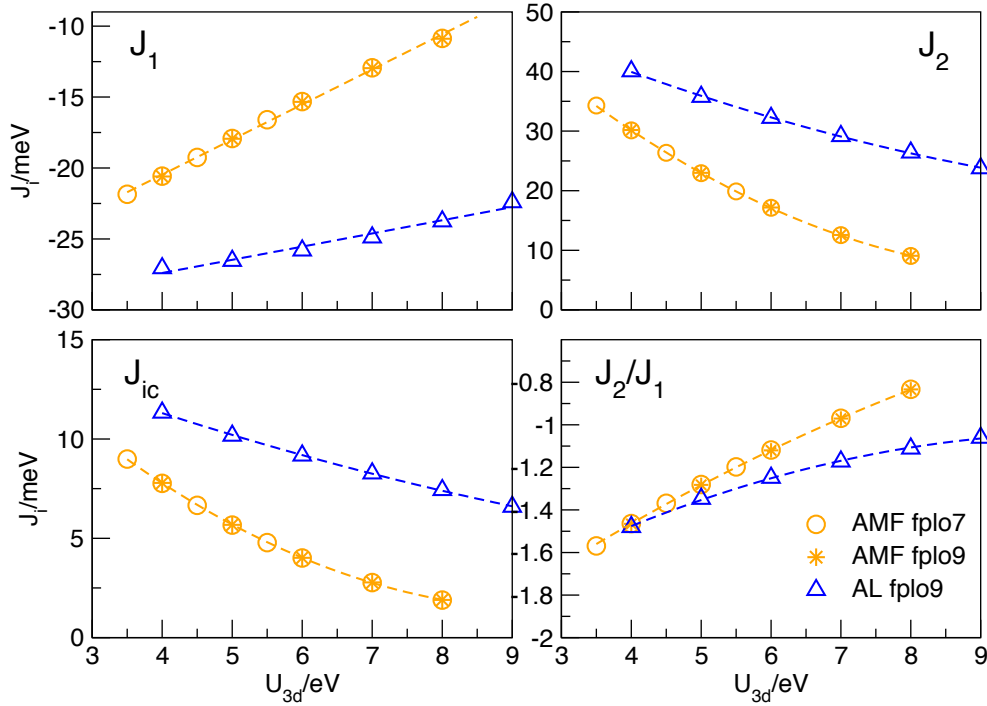
Figure C.5.: Influence of U_{3d} on the leading exchange integrals and the frustration ratio for CuCl$_2$.
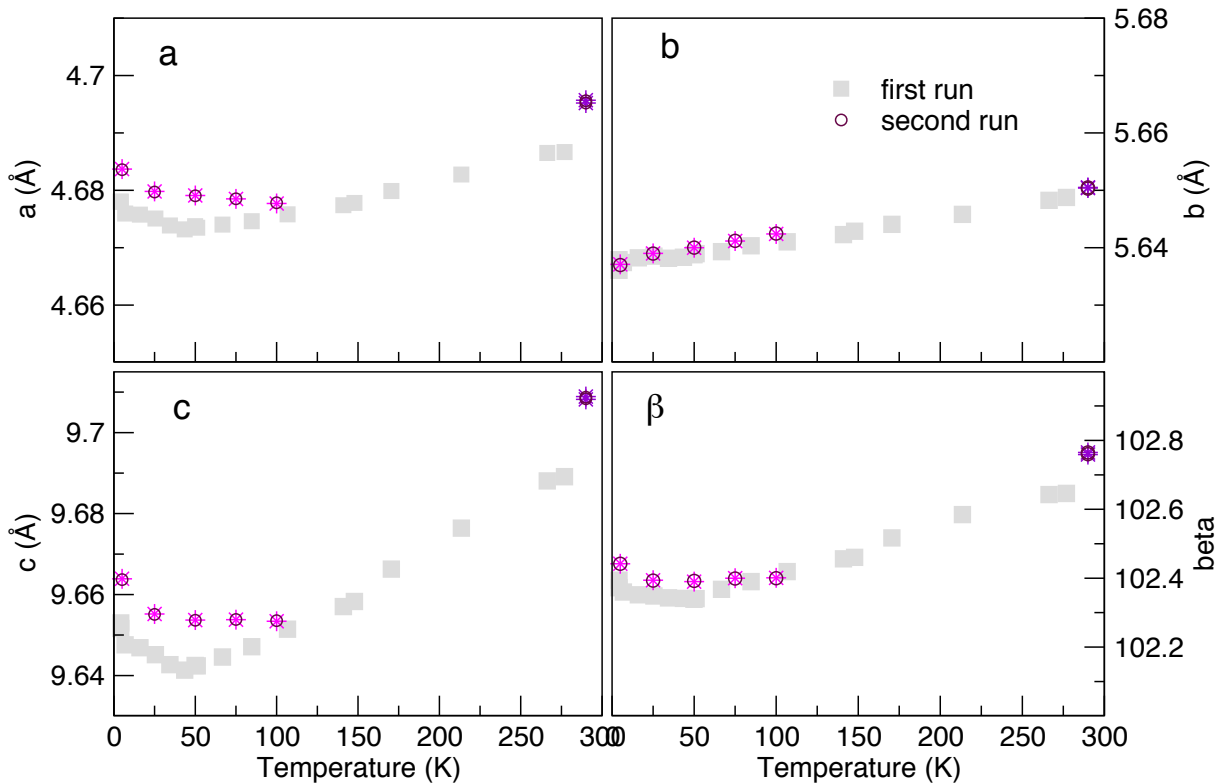
Figure C.6.: Refined lattice parameter for PbCuSO$_4$(OH)$_2$ from low temperature measurement performed at the high resolution beam line ID31 at the ESRF, Grenoble.
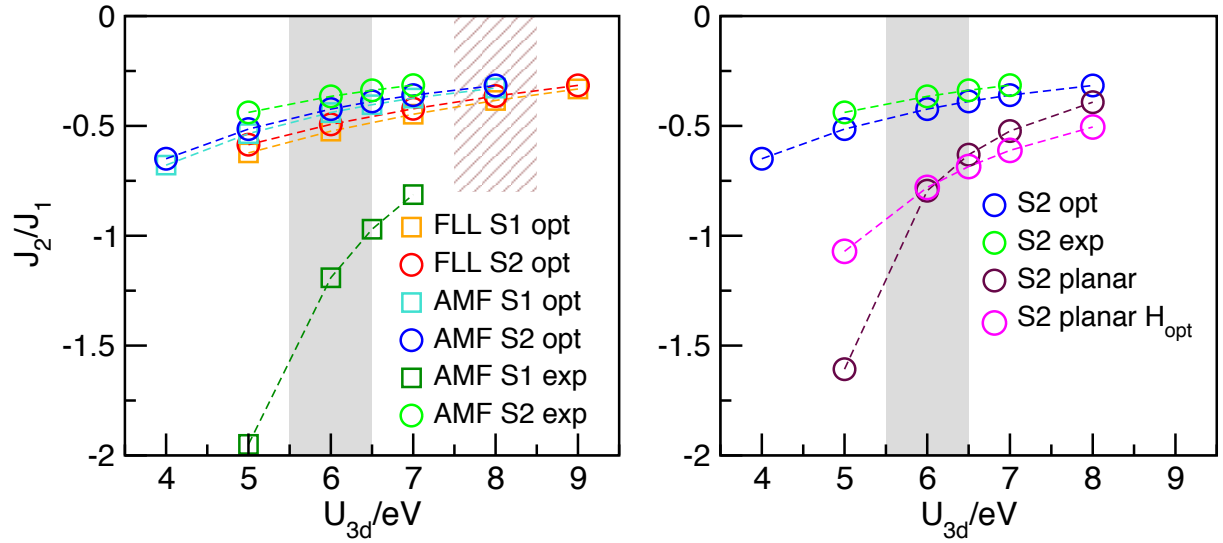
Figure C.7.: Left: Dependance of the calculated frustration ratio $\alpha = J_2/J_1$ from the Coulomb term U_{3d} for $PbCuSO_4(OH)_2$ based on the experimental (exp) and relaxed crystal structures (opt). The different H position in "S1 exp" has a dramatic influence. Right: Influence of the chain folding (changed chain geometry) and H position on the frustration ratio α for S2 exemplarily.
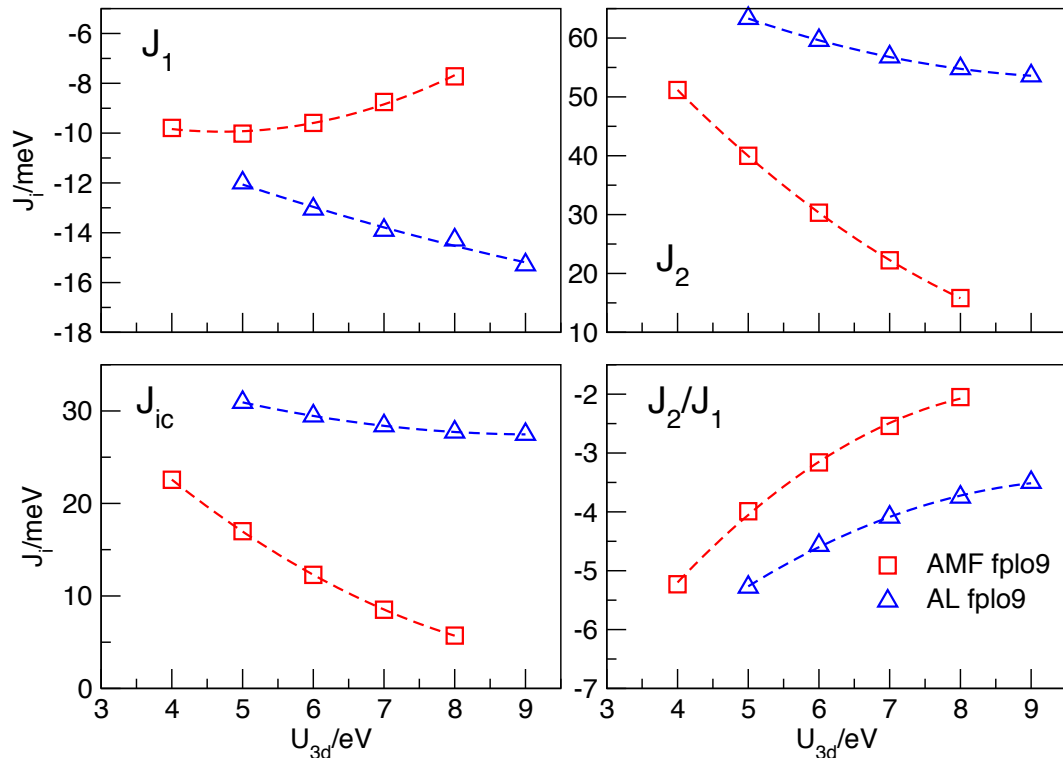
Figure C.8.: Dependance of the leading exchange integrals and frustration ratio from U_{3d} and the DCC for $CuBr_2$.
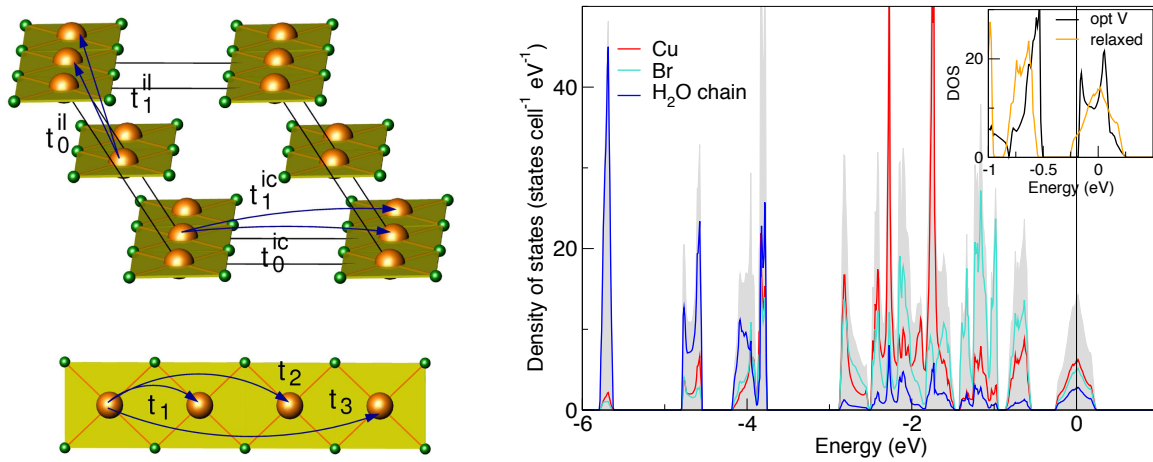
Figure C.9.: Left: Sketch of the leading hopping paths in the halides relevant for our TB model. Right: Atom resolved LDA density of states for the fictitious compound $CuBr_2 \cdot 2H_2O$. A direct comparison of the anti bonding dpσ states for two structural models (with and without rotated CuO_2Br_2 plaquettes) is depicted in the inset.
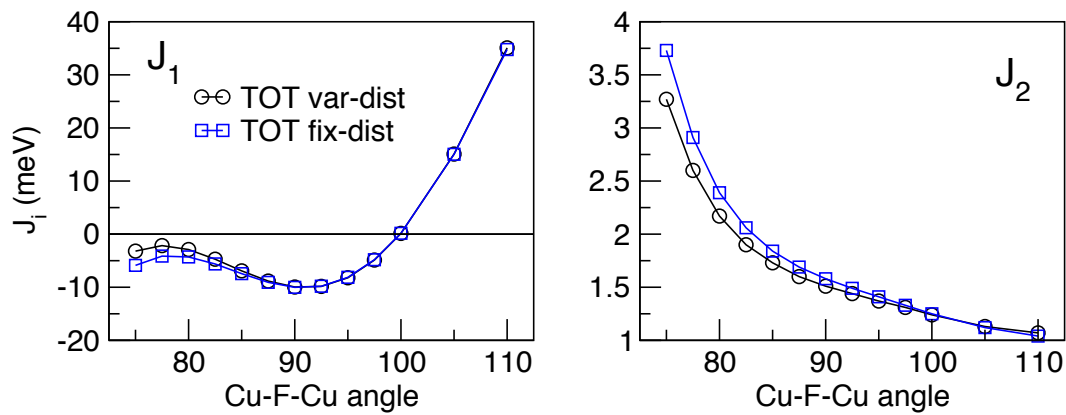
Figure C.10.: Dependance of the leading exchange integrals in the artificial compound CuF_2 from the Cu-F-Cu bridging angle along the edge shared chains. Comparing the relation for the angle variation with (var-dist) and without (fix-dist) a change of the inter atomic distances, reveal only a small influence on J_1 and J_2.
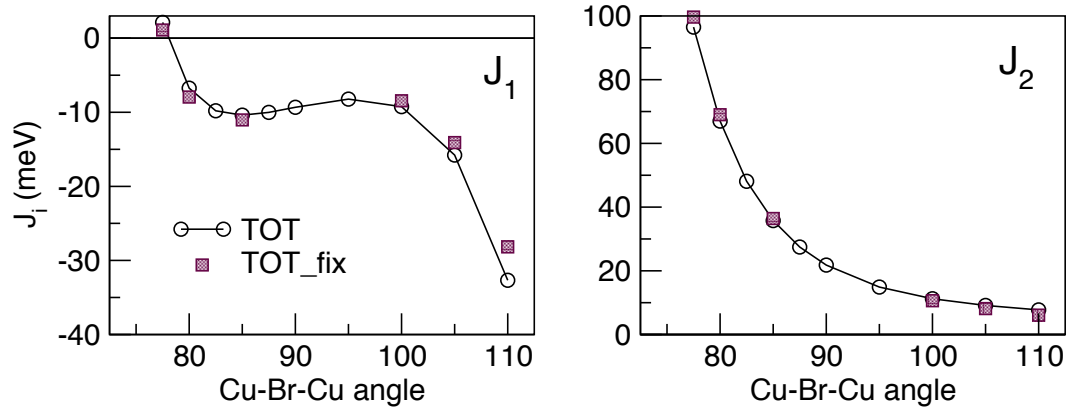
Figure C.11.: Leading exchange integrals for $CuBr_2$ as function of the Cu-Br-Cu bonding angle. During the variation of the chain geometry, the inter chain distance is modified. We probed the influence of inter chain distance on the NN and NNN exchange for selected angles. No sizable influence is observed compared to the all over behavior.
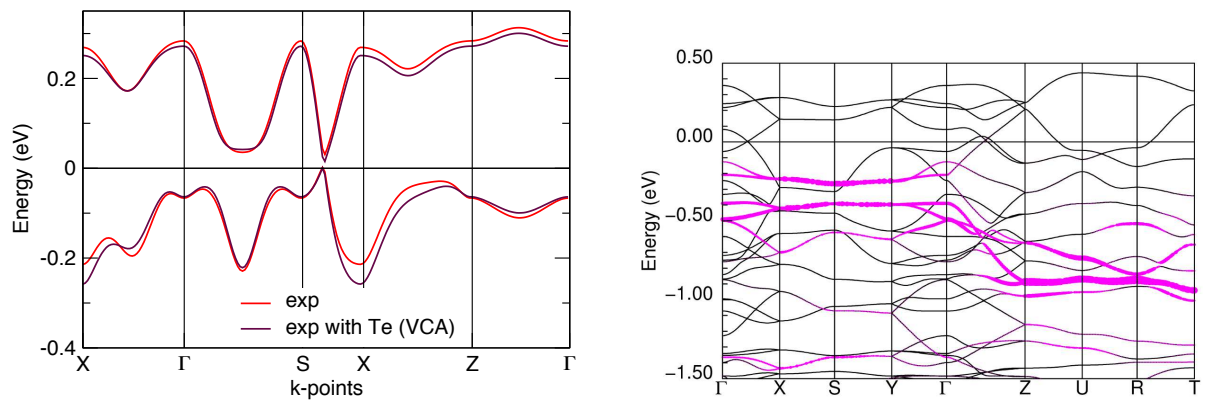
Figure C.12.: Left: Comparison of the anti bonding $dp\sigma$ band for $Na_3Cu_2SbO_6$ based on the experimental crystal structure and the structural variant exchanging Sb by Te within the same geometry using the VCA. Right: Valence band together with the band character of Cu $3d_{xy}$ states of Cu_2PO_4OH.

file	p_v[GPa]	p_n[GPa]	p [GPa]	a [Å]	b [Å]	c [Å]
41	0.72	0.72	0.72	13.686	8.002	4.920
42	0.72	0.72	0.72	13.678	8.008	4.921
43	1.25	1.25	1.25	13.660	7.995	4.924
44	1.67	1.61	1.64	13.653	7.995	4.920
45	2.54	2.44	2.49	13.617	7.988	4.915
46	2.88	2.76	2.82	13.579	8.000	4.908
47	3.82	3.88	3.85	13.544	7.987	4.893
58	3.74	3.74	3.74	13.551	7.984	4.895
59	4.87	4.83	4.85	13.534	7.954	4.881
60	5.49	5.52	5.51	13.518	7.949	4.871
62	6.19	6.17	6.18	13.482	7.953	4.856
64	6.61	6.61	6.61	13.463	7.929	4.852
66	7.09	7.12	7.11	13.439	7.927	4.845
67	8.01	8.01	8.01	13.417	7.919	4.830
68	9.23	9.40	9.32	13.392	7.900	4.817
69	10.45	10.65	10.55	13.360	7.886	4.804

Table C.4.: Refined lattice parameter for $Cu_2(PO_3)_2CH_2$ from high pressure XRD measurements using a screw type of DAC with methanol/ethanol as pressure transmitting medium performed at ID09. Since the errors caused by the uncertainty of pressure and temperature are significantly larger than the estimated standard deviation from the refinement ($0.3 - 0.6 \cdot 10^{-3}$ for a, b and c, respectively) the individual e.s.d. are not given explicitly for each value.
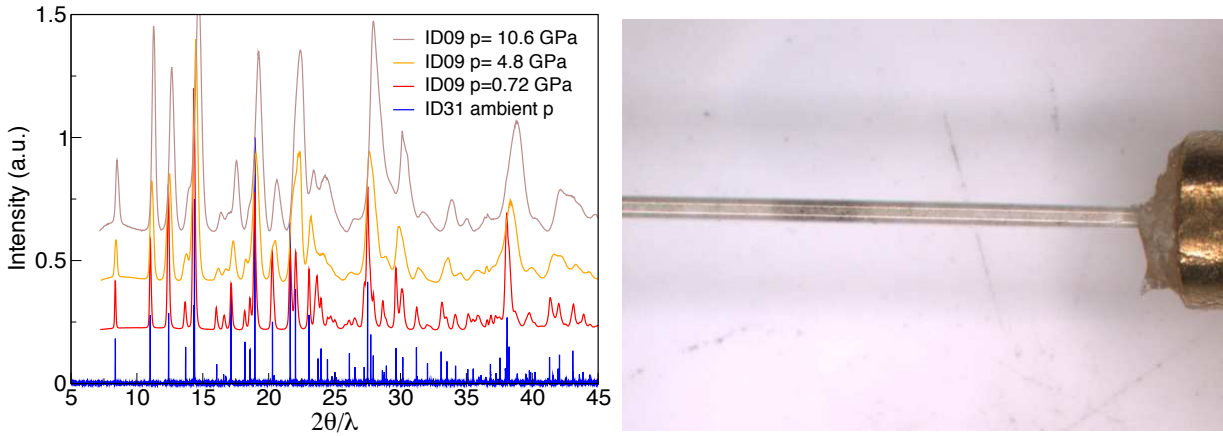
Figure C.13.: Left: Comparison of integrated powder pattern from XRD measurements performed at ID09 and ID31 for $Cu_2(PO_3)_2CH_2$. Right: Capillary filled with $Cu_2(PO_3)_2CH_2$ powder sample during the ID31 experiment. The color change of powder most likely raises from the beam intensity, which damaged the sample.
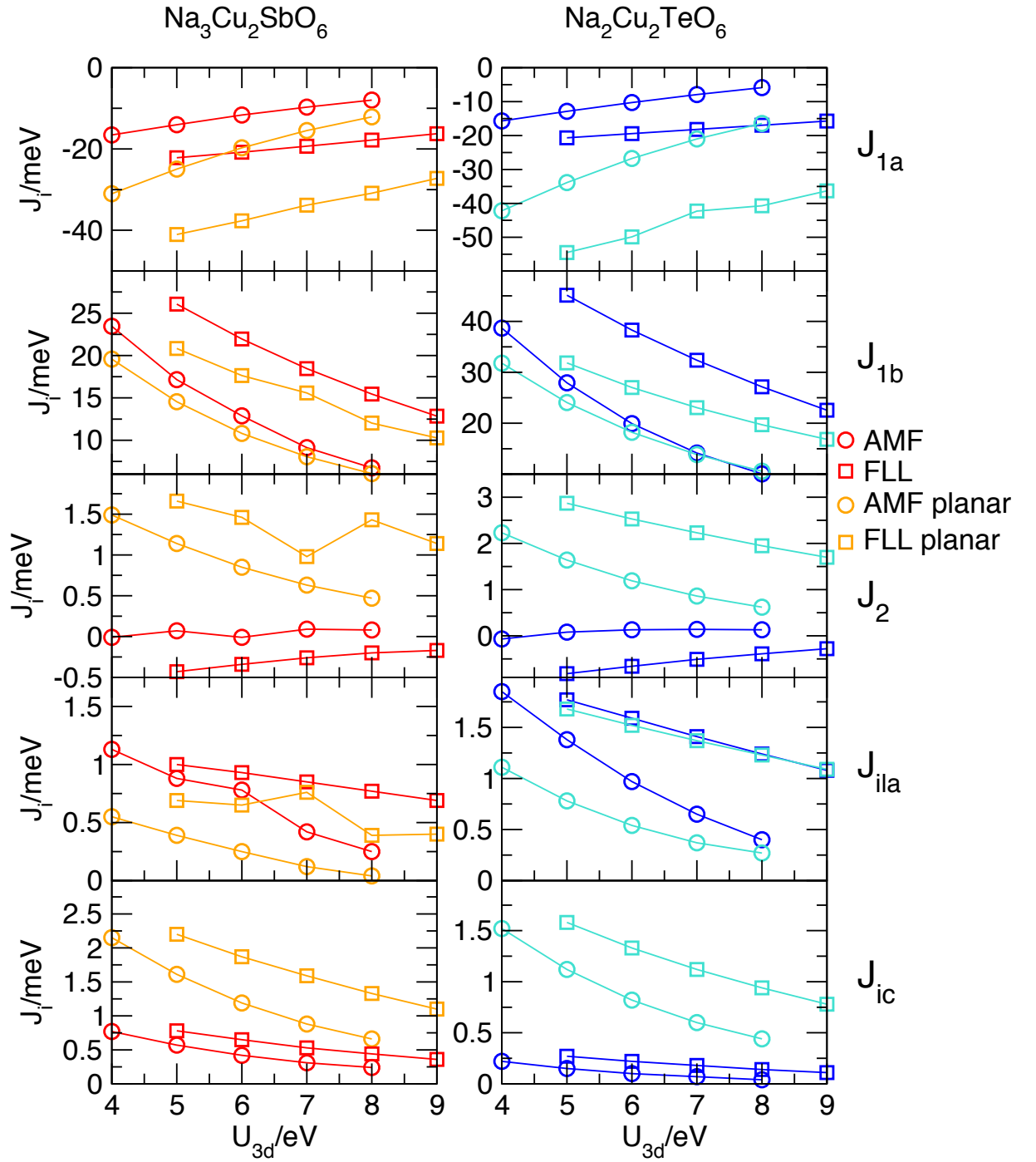
Figure C.14.: Influence of U_{3d} on the leading interaction in $Na_3Cu_2SbO_6$ (left) and $Na_2Cu_2TeO_6$ (right) using different DCC. For comparison the dependency of the fictitious systems containing ideal, planar chains are shown.
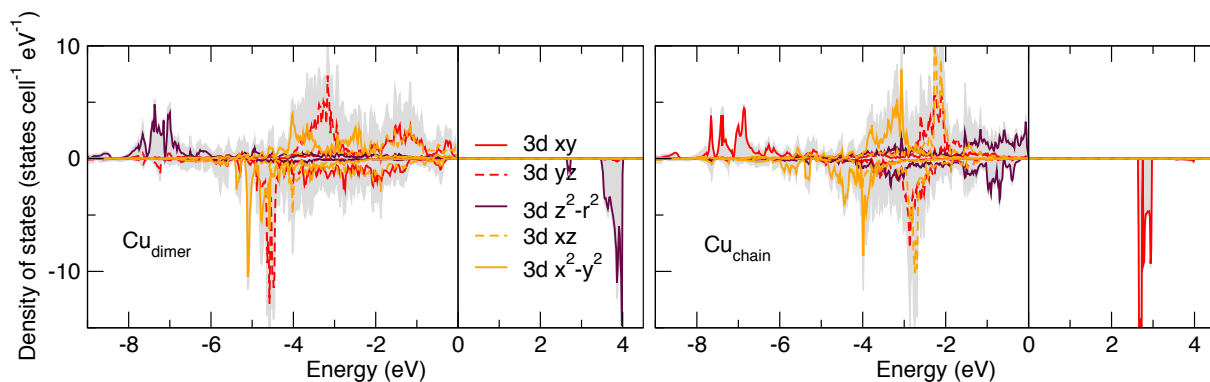
Figure C.15.: Orbital resolved LSDA+U density of states for the two inequivalent Cu sites in Cu_2PO_4OH. Considering the correlation effects shift the half filled bands from the Fermi energy. Due to the orbital order of the system the character of the half filled band for Cu(1) and Cu(2) is different.
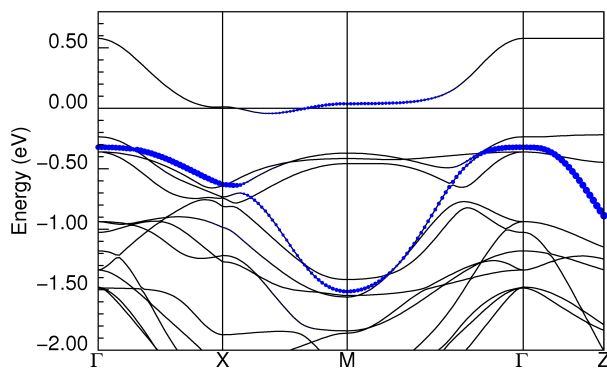
Figure C.16.: Band structure with band characters of the Cu $3z^2-r^2$ states of Ba_2CuTeO_6. The compound shows a sizable hybridization of the anti bonding dpσ states at M and X point.
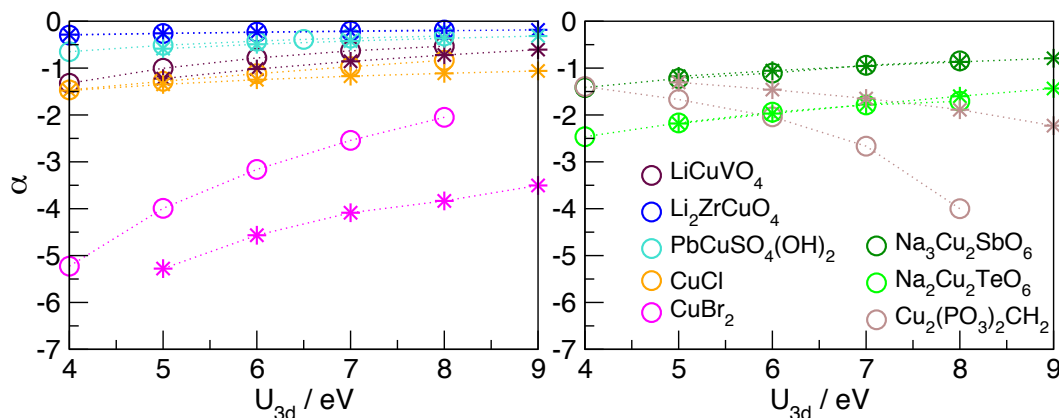
Figure C.17.: Influence of the correlation term U_{3d} and DCC on the frustration ratio for different Cu^{2+} chain compounds. (AMF=circle; FLL=stars)
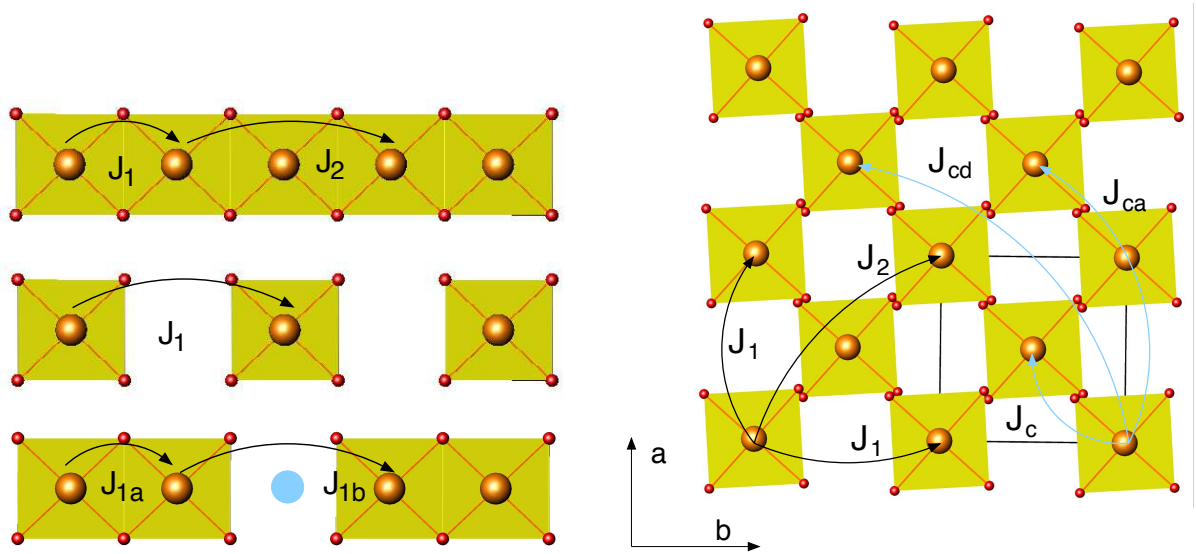
Figure C.18.: Left: Different variants of the edge shared Cu-O chain. From top to bottom: Edge shared $[CuO_2]$ chain, chain from isolated $[CuO_4]$ plaquettes and $[CuO_6]$ dimer chain. The main exchange paths (NN and NNN) are depicted. Right: Sketch of the main transfer paths J_1 and J_2 together with the interlayer transfer paths (blue) for the square lattice compound A_2CuEO_6.
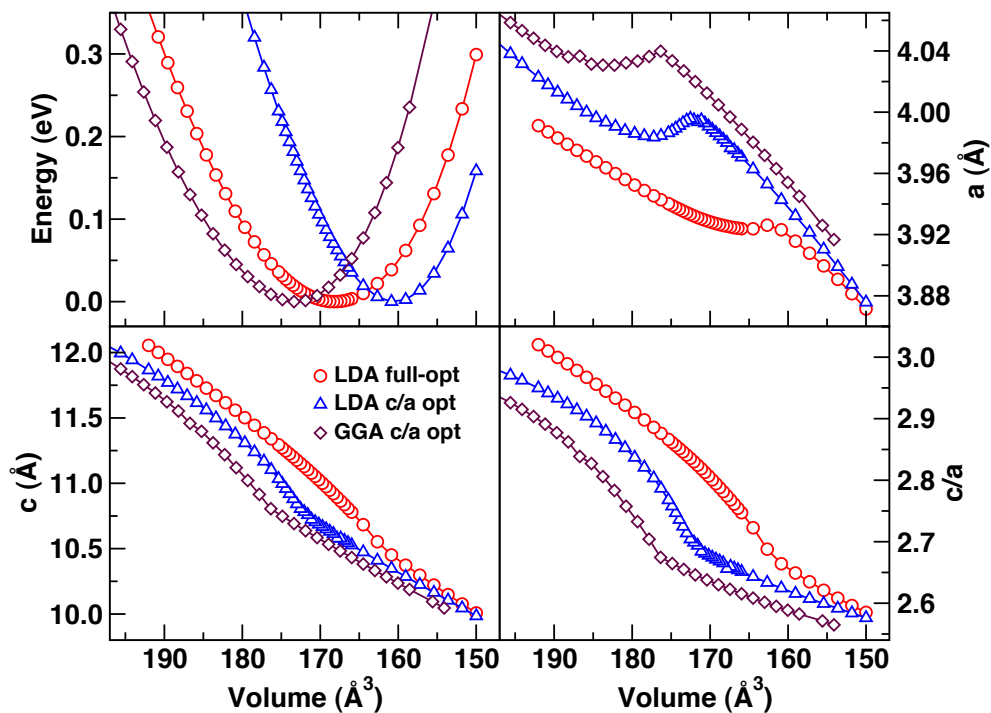
Figure C.19.: Calculated influence of the volume on the lattice parameter of $SrFe_2As_2$ using different functionals and steps of optimization. The full optimization of the crystal structure including the As z position weakens the signature of the phase transition.
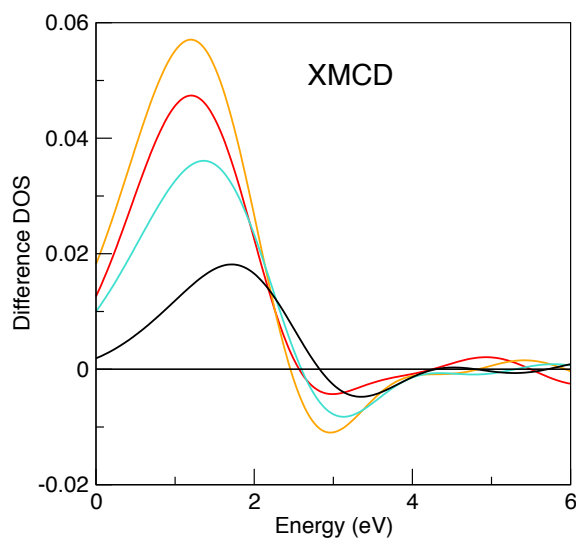
Figure C.20.: Full relativistic calculated pre-peak region of the XMCD signal broadened by the experimental resolution.
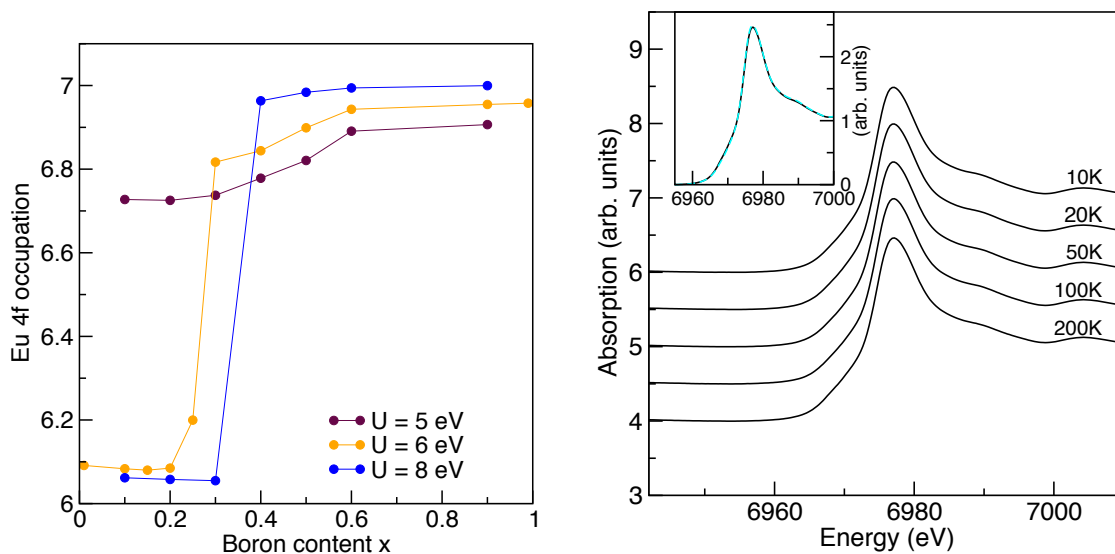
Figure C.21.: Left: Calculated occupation of Eu 4f sates as function of the B content in EuPd$_3$B$_x$. The strength of U_{4f} influences the onset of the transition, which appears for U_{4f} larger than 5 eV usually fulfilled for $4f$ systems. Right: Measured temperature dependence of XAS at the Eu L-edge. The inset shows a direct comparison of the maximal temperature difference. The stability of XAS for various temperatures points supports a mixed valence state rather than an intermediat valence scenario for EuPd$_3$B$_x$.
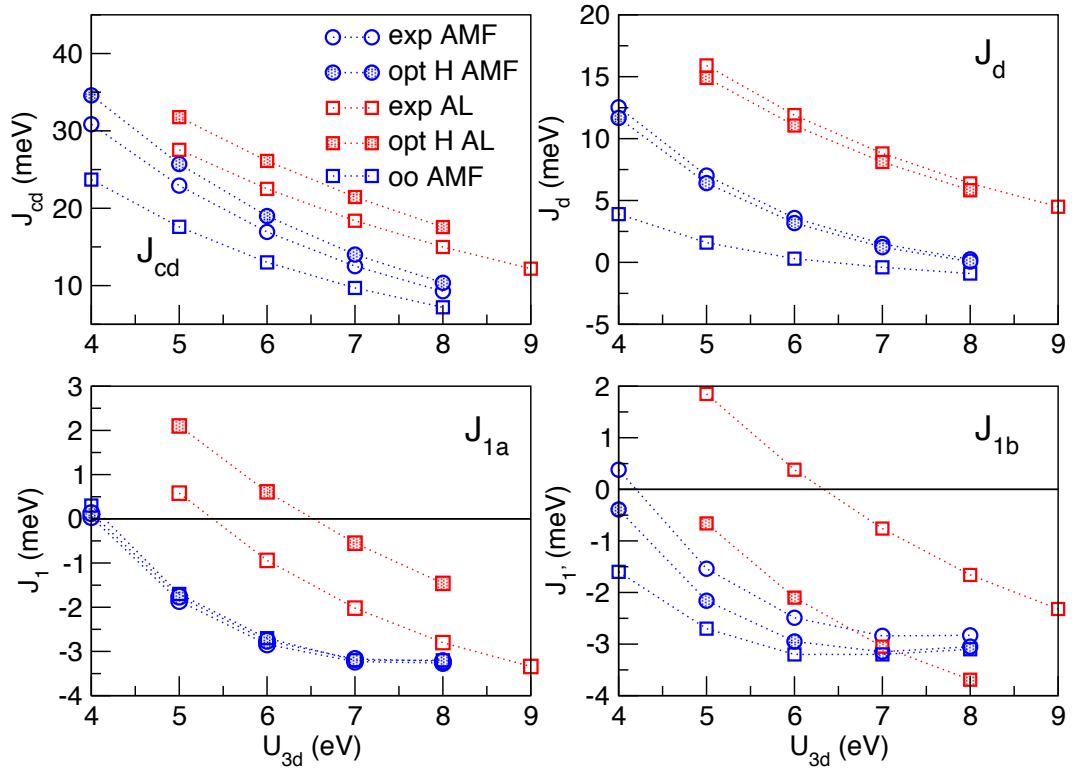
Figure C.22.: Derived exchange integrals for Cu_2PO_4OH as function of U_{3d} and different DCC. The relaxation of H sites has only minor influence to the dominant exchange integrals J_{cd} and J_d. (oo=orbital order, different character of orbitals considered by different strength of correlation. $U_{3d}(Cu1)=U_{3d}(Cu2)+2eV$)

p [GPa]	a [Å]	c [Å]	As z
0.00	3.9262	12.379	0.362
0.85	3.9155	12.261	0.360
0.96	3.9138	12.247	0.361
1.40	3.9087	12.198	0.362
1.84	3.9042	12.150	0.362
2.38	3.8997	12.093	0.362
2.87	3.8965	12.042	0.362
3.38	3.8921	11.985	0.364
3.55	3.8911	11.964	0.364
4.30	3.8864	11.876	0.364
4.61	3.8846	11.836	0.364
5.69	3.8807	11.682	0.364
6.50	3.8807	11.559	0.364
7.54	3.8826	11.411	0.363
8.67	3.8913	11.191	0.367
9.14	3.8973	11.073	0.369
9.64	3.9115	10.882	0.369
9.90	3.9181	10.783	0.368
11.07	3.9278	10.543	0.369
11.71	3.9276	10.474	0.370
12.81	3.9235	10.402	0.371
13.44	3.9205	10.356	0.371
14.62	3.9139	10.281	0.371
15.62	3.9087	10.233	0.371
16.66	3.9033	10.189	0.371
17.58	3.8980	10.148	0.371
18.04	3.8946	10.127	0.371
18.22	3.8939	10.124	0.371
18.60	3.8914	10.108	0.371
19.55	3.8870	10.071	0.371

Table C.5.: Refined lattice parameter and As-z position for $SrFe_2As_2$ from XRD measurements at the high pressure beam line ID09 using a membrane type of DAC with helium as pressure transmitting medium. Since the errors caused by the uncertainty of pressure and temperature are significantly larger than the estimated standard deviation from the refinement ($0.4 - 0.7 \cdot 10^{-4}$ for a and $0.4 - 0.6 \cdot 10^{-3}$ for c and As-z, respectively) the individual e.s.d. are not given explicitly for each value.

Bibliography

[1] M. D. Johannes, J. Richter, S.-L. Drechsler, and H. Rosner. *$Sr_2Cu(PO_4)_2$: A real material realization of the one-dimensional nearest neighbor Heisenberg chain*. Phys. Rev. B **74**, 174435 (2006).

[2] S. S. Salunke, M. A. H. Ahsan, R. Nath, A. V. Mahajan, and I. Dasgupta. *Electronic structure of spin- 1/2 Heisenberg antiferromagnetic systems: $Ba_2Cu(PO_4)_2$ and $Sr_2Cu(PO_4)_2$*. Phys. Rev. B **76**, 085104 (2007).

[3] H. Rosner, M. Schmitt, D. Kasinathan, A. Ormeci, J. Richter, S.-L. Drechsler, and M. D. Johannes. *Comment on: Electronic structure of spin- 1/2 Heisenberg antiferromagnetic systems: $Ba_2Cu(PO_4)_2$ and $Sr_2Cu(PO_4)_2$*. Phys. Rev. B **79**, 127101 (2009).

[4] S. Derakhshan, H. L. Cuthbert, J. E. Greedan, B. Rahaman, and T. Saha-Dasgupta. *Electronic structures and low-dimensional magnetic properties of the ordered rocksalt oxides $Na_3Cu_2SbO_6$ and $Na_2Cu_2TeO_6$*. Phys. Rev. B **76**, 104403 (2007).

[5] H.-J. Koo and M.-H. Whangbo. *Analysis of the spin lattice model for the spin-gapped layered compounds $Na_3Cu_2SbO_6$ and $Na_2Cu_2TeO_6$ on the basis of electronic structure calculations*. Inorg. Chem. **47**, 128 (2008).

[6] X. Liu, R. Dronskowski, R. K. Kremer, M. Ahrens, C. Lee, and M.-H. Whangbo. *Characterization of the magnetic and structural properties of copper carbodiimide, CuNCN, by neutron diffraction and first-principles evaluations of its spin exchange interactions*. J. Phys. Chem. **112**, 11013 (2008).

[7] A. A. Tsirlin and H. Rosner. *Uniform spin-chain physics arising from N-C-N bridges in CuNCN, the nitride analog of the copper oxides*. Phys. Rev. B **81**, 024424 (2010).

[8] F. Bert, D. Bono, P. Mendels, F. Ladieu, F. Duc, J. C. Trombe, and P. Millet. *Ground state of the kagome-like S=1/2 antiferromagnet volborthite $Cu_3V_2O_7(OH)_2 \cdot 2H_2O$*. Phys. Rev. Lett. **95**, 087203 (2005).

[9] T. Masuda, A. Zheludev, A. Bush, M. Markina, and A. Vasiliev. *Competition between Helimagnetism and Commensurate Quantum Spin Correlations in $LiCu_2O_2$*. Phys. Rev. Lett. **92**, 177201 (2004).

[10] C. Gros, P. Lemmens, K.-Y. Choi, G. Güntherodt, M. Baenitz, and H. H. Otto. *Quantum phase transition in the dioptase magnetic lattice*. Europhys. Lett. **60**, 276 (2002).

[11] M. Born and R. Oppenheimer. *Quantum theory of molecules*. Annalen der Physik (N.Y.) **84**, 457 (1927).

Bibliography

[12] P. Hohenberg and W. Kohn. *Self-Consistent Equations Including Exchange and Correlation Effects.* Phys. Rev. **140**, A1133 (1965).

[13] M. Levy. *Electron densities in search of Hamiltonians.* Phys. Rev. A **26**, 1200 (1982).

[14] E. H. Lieb. *Density functionals for Coulomb-systems.* Int. J. Quant. Chem. **24**, 243 (1983).

[15] W. Kohn and L. J. Sham. *Self-Consistent Equations Including Exchange and Correlation Effects.* Phys. Rev. **140**, A1133 (1965).

[16] D. M. Ceperly and B. J. Alder. *Ground State of the Electron Gas by a Stochastic Method.* Phys. Rev. Lett. **45**, 566 (1980).

[17] S. Kenny, G. Rajagopal, R. Needs, W.-K. Leung, M. Godfrey, A. Williamson, and W. Foulkes. *Quantum Monte Carlo Calculations of the Energy of the Relativistic Homogeneous Electron Gas.* Phys. Rev. Lett. **77**, 1099 (1996).

[18] U. von Barth and L. Hedin. *Local exchange correlation potential for spin polarized case.* J. Phys. C **5**, 1629 (1972).

[19] J. P. Perdew and A. Zunger. *Self-interaction correction to density-functional approximations for many-electron systems.* Phys. Rev. B **23**, 5048 (1981).

[20] J. P. Perdew and Y. Wang. *Accurate and simple analytic representation of the electron-gas correlation energy.* Phys. Rev. B **45**, 13244 (1992).

[21] J. P. Perdew, K. Burke, and M. Ernzerhof. *Generalized Gradient Approximation Made Simple.* Phys. Rev. Lett. **77**, 3865 (1996).

[22] A. D. Becke. *A new mixing of Hartree-Fock and local denisty-functional theories.* J. Chem. Phys. **98**, 1372 (1993).

[23] A. D. Becke. *Density-functional exchange-energy approximation with correct asymptotic behavior.* Phys. Rev. A **38**, 3098 (1988).

[24] C. Lee, W. Yang, and R. G. Parr. *Development of the Colle-Salvetti correlation-energy formula into a functional of the electron density.* Phys. Rev. B **37**, 785 (1988).

[25] J. Heyd and G. Scuseria. *Efficient hybrid density functional calculations in solids: Assessment of the Heyd-Scuseria-Ernzerhof screened Coulomb hybrid functional.* J. Chem. Phys. **121**, 1187 (2004).

[26] F. A. Hamprecht, A. Cohen, D. J. Tozer, and N. C. Handy. *Development and assessment of new exchange-correlation functionals.* J. Chem. Phys. **109**, 6264 (1998).

[27] M. T. Czyzyk and G. A. Sawatzky. *Local-density functional and on-site correlations: The electronic structure of La_2CuO_4 and $LaCuO_3$.* Phys. Rev. B **49**, 14211 (1994).

[28] G. Madsen and P. Novak. *Notes about constraint LDA calculations to determine U* (2007).

[29] M. S. Hybertsen, E. B. Stechel, M. Schluter, and D. R. Jennison. *Renormalization from density-functional theory to strong-coupling models for electronic states in Cu-O materials.* Phys. Rev. B **41**, 11068 (1990).

[30] K. Koch. *Crystal structure, electronic density and chemical bonding in inorganic compounds studied by the Electric Field Gradient.* Ph.D. thesis, TU Dresden (2009).

[31] A. B. Shick, W. E. Pickett, and A. I. Liechtenstein. *Ground and metastable states in gamma-Ce from correlated band theory.* J. Electron. Spectrosc. Relat. Phenom. **114-116**, 753 (2001).

[32] A. Georges, G. Kotliar, W. Krauth, and M. J. Rozenberg. *Dynamical mean-field theory of strongly correlated fermion systems and the limit of infinite dimensions.* Rev. Mod. Phys. **68**, 13 (1996).

[33] G. Kotliar, S. Y. Savrasov, K. Haule, V. S. Oudovenko, O. Parcollet, and C. A. Marianetti. *Electronic structure calculations with dynamical mean-field theory.* Rev. Mod. Phys. **78**, 865 (2006).

[34] P. Blaha, K. Schwarz, G. K. H. Madsen, D. Kvasnicka, and J. Luitz. K. Schwarz, Technische Universitaet Wien, Austria (2001).

[35] K. Koepernik and H. Eschrig. *Full-potential nonorthogonal local-orbital minimum-basis band-structure scheme.* Phys. Rev. B **59**, 1743 (1999).

[36] J. M. Wills and B. R. Cooper. *First-principles calculations for a model Hamiltonian treatment of hybridizing light actinide compounds.* Phys. Rev. B **42**, 4682 (1990).

[37] H. Eschrig, K. Koepernik, and I. Chaplygin. *Density functional application to strongly correlated electron systems.* Journal of Solid State Chemistry **176**, 482 (2003).

[38] K. Koepernik, B. Velicky, R. Hayn, and H. Eschrig. *Self-consistent LCAO-CPA method for disordered alloys.* Phys. Rev. B **55**, 5717 (1999).

[39] W. Schnelle, A. Leithe-Jasper, R. Gumeniuk, U. Burkhardt, D. Kasinathan, and H. Rosner. *Substitution-induced superconductivity in $SrFe_{2-x}Ru_xAs_2$ ($0 \leq x \leq 2$).* Phys. Rev. B **79**, 214516 (2009).

[40] Private communication, H. Rosner, K. Kopenerik and Yu. Grin (to be published).

[41] S. S. Salunke, A. V. Mahajan, and I. Dasgupta. *Magnetic properties and electronic structure of S=1/2 spin gap compound $BaCu_2V_2O_8$.* Phys. Rev. B **77**, 012410 (2008).

[42] O. Mentre, H. Koo, and M.-H. Whangbo. *Investigation of the Vanadyl Bond Ordering and Analysis of the Spin Exchange Interactions in $Pb_2V_3O_9$ and $Pb_2As_2VO_9$.* Chem. Mater. **20**, 6929 (2008).

[43] D. Kasinathan, K. Koepernik, and H. Rosner. *Quasi-One-Dimensional Magnetism Driven by Unusual Orbital Ordering in $CuSb_2O_6$.* Phys. Rev. Lett. **100**, 237202 (2008).

[44] K. Koepernik. *Wannier functions with FPLO.* www.fplo.de/download/wan_user.pdf (2010).

[45] J. Hubbard. *Electron correlation in narrow energy bands.* Proc. Roy. Soc. A **276**, 238 (1963).

[46] A. B. Harris and R. V. Lange. *Single-particle excitation in narrow energy bands.* Phys. Rev. B **157**, 295 (1967).

[47] M. D. Johannes, J. Richter, S.-L. Drechsler, and H. Rosner. *$Sr_2Cu(PO_4)_2$: A real material realization of the one-dimensional nearest neighbor Heisenberg chain.* Phys. Rev. B **74**, 174435 (2006).

[48] H. Rosner, S.-L. Drechsler, K. Koepernik, R. Hayn, and H. Eschrig. *Possibility of a spin-Peierls state in $CuSiO_3$ from electronic structure theory.* Phys. Rev. B **63**, 073104 (2001).

[49] H. Rosner, D. Koudela, U. Schwarz, A. Handstein, M. Hanfland, I. Opahle, K. Koepernik, M. D. Kuz'min, K.-H. Müller, J. A. Mydosh, and M. Richter. *Magneto-elastic lattice collapse in YCo_5.* Nature Physics **2**, 469 (2006).

[50] D. Häusermann and M. Hanfland. *Optics and beamlines for high-pressure research at the European Synchrotron Radiation Facility.* High Pressure Research. **14**, 223 (1996).

[51] G. Fiquet and D. Andrault. *Powder x-ray diffraction under extreme conditions of pressure and temperature.* J. Synchrotron Rad. **6**, 81 (1999).

[52] http://www.esrf.eu/.

[53] A. Jayaraman. *Diamond anvil cell and high-pressure physical investigations.* Rev. Mod. Phys. **55**, 65 (1983).

[54] S. Klotz, J.-C. Chervin, P. Munsch, and G. L. Marchand. *Hydrostatic limits of 11 pressure transmitting media.* J. Phys. D: Appl. Phys. **42**, 075413 (2009).

[55] R. A. Forman, G. J. Piermarini, J. D. Barnett, and S. Block. *Pressure measurements made by utilization of ruby sharp-line luminescence.* Science **176**, 284 (1972).

[56] A. P. Hammersley, S. O. Svensson, M. Hanfland, A. Fitch, and D. Hauesermann. *Two-dimensional detector software: From real detector to idealised image or two-theta scan.* High Press. Res. **14**, 235 (1996).

[57] J. Rodriguez-Carvajal. *Recent advances in magnetic-strcture determination by neutron powder diffraction.* Physica B **192**, 55 (1993).

[58] F. D. Murnaghan. *The compressibility of media under extreme pressure.* Proc. Natl. Acad. Sci. U.S.A. **30**, 244 (1944).

[59] U. Schwarz. *Untersuchung von druckinduzierten Phasenumwandlungen bei Valenzverbindungen und intermetallische Phasen mit Bindungen zwischen metallischen Elementen.* Ph.D. thesis, TU Darmstadt (1998).

[60] M. Hagelstein, A. S. Miguel, A. Fontaine, and J. Goulon. *The beamline ID24 at ESRF for energy dispersive X-ray absorption spectroscopy.* J. Phys. IV **7**, C2 (1997).

[61] S. Pascarelli, O. Mathon, and G. Aquilanti. *New opportunities for high pressure X-ray absorption spectroscopy using dispersive optics.* Journal of Alloys and Compounds **362**, 33 (2003).

[62] O. Mathon, P. van der Linden, T. Neisius, M. Sikora, J. M. Michalik, C. Ponchut, J. M. D. Teresa, and S. Pascarelli. *XAS and XMCD under high magnetic field and low temperature on the energy-dispersive beamline of the ESRF.* Journal of Synchrotron Radiation **14**, 409 (2007).

[63] S. Pascarelli and E. Plouviez. *Effect of horizontal fast electron beam position feedback on the performance of ESRF beamlines.* Nuc. Instrum. Meth. Phys. Res. A **467-468**, 226 (2000).

[64] J. Stoehr. *Exploring the microscopic origin of magnetic anisotropies with X-ray magnetic circular dichroism (XMCD) spectroscopy.* Journal of Magnetism and Magnetic Materials **200**, 470 (1999).

[65] F. de Groot. *High-Resolution X-ray Emission and X-ray Absorption Spectroscopy.* Chem. Rev. **101**, 1779 (2001).

[66] M. Mizumaki, S.Tsutsui, H. Tanida, T. Uruga, D. Kikuchi, H.Sugawara, and H. Sato. *The Mixed Valence States in the Unconventional Heavy Fermion Compound SmOs4Sb12.* J. Phys. Soc. Jpn. **76**, 053706 (2007).

[67] B. T. Thole, P. Carra, F. Sette, and G. van der Laan. *X-ray circular dichroism as a probe of orbital magnetization.* Phys. Rev. Lett. **68**, 1943 (1992).

[68] F. de Groot and G. van der Laan. *Collected works of Theo Thole: the spectroscopy papers.* J. Electron Spectrosc. Relat. Phenom **86**, 25 (1997).

[69] J. T. Chalker, P. C. W. Holdsworth, and E. F. Shender. *Hidden order in a frustrated system: Properties of the Heisenberg Kagom antiferromagnet.* Phys. Rev. Lett. **68**, 855 (1992).

[70] O. Janson, J. Richter, and H. Rosner. *Modified Kagome Physics in the Natural Spin-1/2 Kagome Lattice Systems: Kapellasite $Cu_3Zn(OH)_6Cl_2$ and Haydeeite $Cu_3Mg(OH)_6Cl_2$.* Phys. Rev. Lett. **101**, 106403 (2008).

[71] A. Chubukov. *Order from disorder in a kagome antiferromagnet.* Phys. Rev. Lett. **69**, 832 (1992).

[72] Y. Ran, M. Hermele, P. A. Lee, and X.-G. Wen. *Projected-Wave-Function Study of the Spin-1/2 Heisenberg Model on the Kagome Lattice.* Phys. Rev. Lett. **98**, 117205 (2007).

[73] Private communication U. Nitzsche,S.-L. Drechsler and H. Rosner (to be published).

[74] A. A. Gippius, E. N. Morozova, A. S. Moskvin, A. V. Zalessky, A. A. Bush, M. Baenitz, H. Rosner, and S.-L. Drechsler. *NMR and local-density-approximation evidence for spiral magnetic order in the chain cuprate LiCu$_2$O$_2$*. Phys. Rev. B **70**, 020406(R) (2004).

[75] S.-L. Drechsler, J. Malek, J. Richter, A. S. Moskvin, A. A. Gippius, and H. Rosner. *Comment on: Competition between Helimagnetism and Commensurate Quantum Spin Correlations in LiCu$_2$O$_2$*. Phys. Rev. Lett. **94**, 039705 (2005).

[76] M. Enderle, C. Mukherjee, B. Fak, R. Kremer, J. A. Broto, H. Rosner, S.-L. Drechsler, J. Richter, J. Malek, A. Prokofiev, W. Assmus, S. Pujol, J.-L. Raggazzoni, H. Rokoto, M. Rheinstaedter, and H. M. Ronnow. *Quantum helimagnetism of the frustrated spin-1/2 chain LiCuVO$_4$*. Europhys. Lett. **70**, 237 (2005).

[77] L. Capogna, M. Mayr, P. Horsch, M. Raichle, R. K. Kremer, M. Sofin, A. Maljuk, M. Jansen, and B. Keimer. *Helicoidal magnetic order in the spin-chain compound NaCu$_2$O$_2$*. Phys. Rev. B **71**, 140402(R) (2005).

[78] S.-L. Drechsler, J. Richter, A. Gippius, A. Vasiliev, A. Bush, A. Moskvin, Y. Prots, W. Schnelle, and H. Rosner. *Helical ground state and weak ferromagnetism in the edge-shared chain cuprate NaCu$_2$O$_2$*. Europhys. Lett. **73**, 83 (2006).

[79] S.-L. Drechsler, O. Volkova, A. N. Vasiliev, N. Tristan, J. Richter, M. Schmitt, H. Rosner, J. Malek, R. Klinger, A. A. Zvyagin, and B. Büchner. *Frustrated Cuprate Route from Antiferromagnetic to Ferromagnetic Spin-1/2 Heisenberg Chains: Li$_2$ZrCuO$_4$ as a Missing Link near the Quantum Critical Point*. Phys. Rev. Lett. **98**, 077202 (2007).

[80] M. Hase, I. Terasaki, and K. Uchinokura. *Observation of the spin-Peierls transition in linear Cu^{2+} (spin-1/2) chains in an inorganic compound CuGeO$_3$*. Phys. Rev. Lett. **70**, 3651 (1993).

[81] R. Melzi, P. Carretta, A. Lascialfari, M. Mambrini, M. Troyer, P. Millet, and F. Mila. *Li$_2$VO(Si,Ge)O$_4$, a Prototype of a Two-Dimensional Frustrated Quantum Heisenberg Antiferromagnet*. Phys. Rev. Lett. **85**, 1318 (2000).

[82] R. Shpanchenko, V. Chernaya, A. A. Tsirlin, P. Chizhov, D. Sklovsky, E. Antipov, E. Khlybov, V. Pomjakushin, A. Balagurov, J. Medvedeva, E. E. Kaul, and C. Geibel. *Synthesis, structure, and properties of new perovskite PbVO$_3$*. Chem. Mater. **16**, 3267 (2004).

[83] K. Oka, I. Yamada, S. Takeshita, K. H. Satoh, A. Koda, R. Kadono, M. Takano, and Y. Shimakawa. *Magnetic ground-state of perovskite PbVO$_3$ with large tetragonal distortion*. Inorg. Chem. **47**, 7355 (2008).

[84] H. Müller-Buschbaum. *Oxometallate mit ebener Koordination*. Angew. Chem. **89**, 704 (1977).

[85] J. Kanamori. *Theory of the magnetic properties of ferrous and cobaltous oxides*. Prog. Theor. Phys. **17**, 177 (1957).

[86] A. Möller and J. Jainski. *Synthesis and crystal structure of AgCuVO$_4$*. Z. Anorg. Allg. Chem. **634**, 1669 (2008).

[87] A. Möller, M. Schmitt, T. Förster, and H. Rosner. *AgCuVO$_4$: A quasi-one-dimensional S=1/2 chain compound*. Phys. Rev. B **80**, 125106 (2009).

[88] D. C. Johnston, R. K. Kremer, M. Troyer, X. Wang, A. Klümper, S. L. Budko, A. F. Panchula, and P. C. Canfield. *Thermodynamics of spin S=1/2 antiferromagnetic uniform and alternating-exchange Heisenberg chains*. Phys. Rev. B **61**, 9558 (2000).

[89] H. J. Schulz. *Dynamics of Coupled Quantum Spin Chains*. Phys. Rev. Lett. **77**, 2790 (1996).

[90] H. Rosner, S.-L. Drechsler, K. Koepernik, R. Hayn, and H. Eschrig. *Possibility of a spin-Peierls state in CuSiO$_3$ from electronic structure theory*. Phys. Rev. B **63**, 073104 (2001).

[91] H. Rosner, H. Eschrig, R. Hayn, S.-L. Drechsler, and J. Malek. *Electronic structure and magnetic properties of the linear chain cuprates Sr$_2$CuO$_3$ and Ca$_2$CuO$_3$*. Phys. Rev. B **56**, 3402 (1997).

[92] R. Konta, H. Kato, H. Kobayashi, and A. Kudo. *Photophysical properties and photocatalytic activities under visible light irradiation of silver vanadates*. Phys. Chem. Chem. Phys. **5**, 3061 (2003).

[93] C. Dussarrat, G. C. Maher, V. Caignaert, B. Domenges, J. G. Fletcher, and A. R. West. *Synthesis and crystal structures of Li$_2$CuZrO$_4$ polymorphs*. J. Solid State Chem. **166**, 311 (2002).

[94] M. Schmitt, J. Malek, S.-L. Drechsler, and H. Rosner. *Electronic structure and magnetic properties of Li$_2$ZrCuO$_4$: A spin-1/2 Heisenberg system close to a quantum critical point*. Phys. Rev. B **80**, 205111 (2009).

[95] F. Parmigiani, L. Sangaletti, A. Goldoni, U. del Pennino, C. Kim, Z.-X. Shen, A. Revcolevschi, and G. Dhalenne. *Electron-spectroscopy study of correlation mechanisms in CuGeO$_3$ single crystals*. Phys. Rev. B **55**, 1459 (1997).

[96] Y. Tarui, Y. Kobayashi, and M. Sato. *On the magnetic structure of quasi one dimensional spin 1/2 system of Li$_2$ZrCuO$_4$*. J. Phys. Soc. Jpn. **77**, 043703 (2008).

[97] R. Zinke, S. L. Drechsler, and J. Richter. *Influence of interchain coupling on spiral ground-state correlations in frustrated spin-1/2 $J_1 - J_2$ Heisenberg chains*. Phys. Rev. B **79**, 094425 (2009).

[98] E. Vavilova, A. Moskvin, Y. Arango, A. Sotnikov, V. Kataev, S.-L. Drechsler, O. Volkova, A. Vasiliev, and B. Büchner. *Quantum electric dipole glass and frustrated magnetism near a critical point in Li$_2$ZrCuO$_4$*. EPL **88**, 27001 (2009).

[99] Private communication A. A. Tsirlin within an ongoing common project.

[100] M. Baran, A. Jedrzejczak, H. Szymczak, V. Maltsev, G. Kamieniarz, G. Szukowski, C. Loison, A. Ormeci, S.-L. Drechsler, and H. Rosner. *Quasi-one-dimensional S = 1/2 magnet Pb[Cu(SO₄)(OH)₂]: frustration due to competing in-chain exchange.* Phys. Stat. Sol. **3**, 220 (2006).

[101] P. F. Schofield, C. C. Wilson, K. S. Knight, and C. A. Kirk. *Proton location and hydrogen bonding in the hydrous lead copper sulfates linarite, PbCu(SO₄)(OH)₂, and caledonite, Pb₅Cu₂(SO₄)₃CO₃(OH)₆.* The Canadian Mineralogist **47**, 649 (2009).

[102] H. Effenberger. *Crystal structure and chemical formula of Schmiederite, Pb₂Cu₂(OH)₄(SeO₃)(SeO₄), with a comparison to linarite, PbCu(OH)₂(SO₄).* Mineralogy and Petrology **36**, 3 (1987).

[103] H. J. Xiang and M.-H. Whangbo. *Density-Functional Characterization of the Multiferroicity in Spin Spiral Chain Cuprates.* Phys. Rev. Lett. **99**, 257203 (2007).

[104] A. Rusydi, I. Mahns, S. Müller, M. Rübhausen, S. Park, Y. Choi, C. Zhang, S.-W. Cheong, S. Smadici, P. Abbamonte, M. v. Zimmermann, and G. A. Sawatzky. *Multiferroicity in the spin-1/2 quantum matter of LiCu₂O₂.* Appl. Phys. Lett. **92**, 262506 (2008).

[105] S. Seki, T. Kurumaji, S. Ishiwata, H. Matsui, H. Murakawa, Y. Tokunaga, Y. Kaneko, T. Hasegawa, and Y. Tokura. *Cupric chloride CuCl₂ as an S=1/2 chain multiferroic.* Phys. Rev. B **82**, 064424 (2010).

[106] Unpublished, W. Schnelle private communication.

[107] A. U. B. Wolter, F. Lipps, M. Schäpers, S.-L. Drechsler, S. Nishimoto, R. Vogel, V. Kataev, B. Büchner, H. Rosner, M. Schmitt, M. Uhlarz, Y. Skourski, J. Wosnitza, K. C. Rule, S. Süllow, and G. Heide. *Magnetic properties and revisited assignment of the main exchange integrals of the frustrated spin s = 1/2 chain cuprate PbCuSO₄(OH)₂ - linarite.* Phys. Rev. B **85**, 014407 (2012).

[108] T. Masuda, A. Zheludev, A. Bush, M. Markina, and A. Vasiliev. *Masuda et al. Reply:.* Phys. Rev. Lett. **94**, 039706 (2005).

[109] H. G. Heide and K. Bolldornberger. *Die Struktur des Dioptas, Cu₆(Si₆O₁₈)·6H₂O.* Acta Cryst. **8**, 425 (1955).

[110] H. H. Otto and M. Meibohm. *Crystal structure of copper polysilicate, Cu[SiO₃].* Z. Kristallogr. **214**, 558 (1999).

[111] O. Janson, J. Richter, and H. Rosner. *Modified Kagome Physics in the Natural Spin-1/2 Kagome Lattice Systems: Kapellasite Cu₃Zn(OH)₆Cl₂ and Haydeeite Cu₃Mg(OH)₆Cl₂.* Phys. Rev. Lett. **101**, 106403 (2008).

[112] J. W. Stout and R. C. Chisholm. *Heat capacity and entropy of CuCl₂ and CrCl₂ from 11 degrees to 300 degrees K - magnetic ordering in linear chain crystals.* J. Chem. Phys. **36**, 979 (1962).

[113] L. J. DeJongh and A. R. Miedema. *Experiments on simple magnetic model systems.* Adv. Phys. **23**, 1 (1974).

[114] M. Schmitt, O. Janson, M. Schmidt, S. Hoffmann, W. Schnelle, S.-L. Drechsler, and H. Rosner. *Crystal-water-induced switching of magnetically active orbitals in CuCl$_2$*. Phys. Rev. B **79**, 245119 (2009).

[115] W. Marshall. *The antiferromagneticism of CuCl$_2$ ·2H$_2$O*. J. Phys. Chem. Solids **7**, 159 (1958).

[116] J. van den Handel, H. M. Gijsman, and N. J. Poulis. *The magnetic susceptibilities of an antiferromagnetic single crystal of CuCl$_{12}$·2H$_2$O*. Physica **18**, 862 (1952).

[117] M. G. Banks, R. K. Kremer, C. Hoch, A. Simon, B. Ouladdiaf, J.-M. Broto, H. Rakoto, C. Lee, and M.-H. Whangbo. *Magnetic ordering in the frustrated Heisenberg chain system cupric chloride CuCl$_2$*. Phys. Rev. B **80**, 024404 (2009).

[118] M. Taniguchi, M. Furusawa, and Y. Kiba. *Enthalpies of Dehydrations of Oxalate, Sulfate and Chloride Hydrates by Transpiration Method and DSC*. J. Therm. Anal. Cal. **64**, 177 (2001).

[119] J. A. Lumpkin and D. D. Perlmutter. *Thermal and water-vapor effects in the rate of the dehydration reaction of barium-chloride*. Thermochimica Acta **249**, 335 (1995).

[120] O. A. Smirnova, V. B. Nalbandyan, A. A. Petrenko, and M. Avdeev. *Subsolidus phase relations in Na$_2$O-CuO-Sb$_2$On system and crystal structure of new sodium copper antimonate Na$_3$Cu$_2$SbO$_6$*. Journal of Solid State Chemistry **178**, 1165 (2005).

[121] Y. Miura, R. Hirai, Y. Kobayashi, and M. Sato. *Spin-gap behavior of Na$_3$Cu$_2$SbO$_6$ with distorted honeycomb structure*. J. Phys. Soc. Jpn. **75**, 084707 (2006).

[122] Y. Miura, Y. Yasui, T. Moyoshi, M. Sato, and K. Kakurai. *Magnetic excitations of spin-gap system Na$_3$Cu$_2$SbO$_6$ with distorted honeycomb structure*. J. Phys. Soc. Jpn. **77**, 104709 (2008).

[123] J. Xu, A. Assoud, N. Soheilnia, S. Derakhshan, H. L. Cuthbert, J. E. Greedan, M. H. Whangbo, and H. Kleinke. *Synthesis, structure, and magnetic properties of the layered copper(II) oxide Na$_2$Cu$_2$TeO$_6$*. Inorg. Chem. **44**, 5042 (2005).

[124] K. Morimoto, Y. Itoh, K. Yoshimura, M. Kato, and K. Hirota. *Hole doping effects on spin-gapped Na$_2$Cu$_2$TeO$_6$ via topochemical Na deficiency*. J. Phys. Soc. Jpn. **75**, 083709 (2006).

[125] M. Schmitt, A. A. Gippius, K. S. Okhotnikov, W. Schnelle, K. Koch, O. Janson, W. Liu, Y.-H. Huang, Y. Skourski, F. Weickert, M. Baenitz, and H. Rosner. *Electronic structure and magnetic properties of the spin-gap compound Cu$_2$(PO$_3$)$_2$CH$_2$: Magnetic versus structural dimers*. Phys. Rev. B **81**, 104416 (2010).

[126] D. A. Tennant, S. E. Nagler, A. W. Garrett, T. Barnes, and C. C. Torardi. *Excitation Spectrum and Superexchange Pathways in the Spin Dimer VODPO$_4$·1/2D$_2$O*. Phys. Rev. Lett. **78**, 4998 (1997).

[127] K. Barthelet, M. Nogues, D. Riou, and G. Ferey. *Hydrothermal synthesis, structure determination, and magnetic properties of three new copper(II) methylenediphosphonates with hybrid frameworks (MIL-54, 55, 56), and of the Cu homologue of $Na_2Co(O_3P\text{-}CH_2\text{-}PO_3)\cdot(H_2O)$.* Chem. Mater. **14**, 4910 (2002).

[128] O. Janson, R. Kuzian, S.-L. Drechsler, and H. Rosner. *Electronic structure and magnetic properties of the spin- 1/2 Heisenberg magnet Bi_2CuO_4.* Phys. Rev. B **76**, 115119 (2007).

[129] A. A. Belik, H.-J. Koo, M.-H. Whangbo, N. Tsujii, P. Naumov, and E. Takayama-Muromachi. *Magnetic properties of synthetic libethenite Cu_2PO_4OH: a new spin-gap system.* Inorg. Chem. **46**, 8684 (2007).

[130] C. N. Kuo and C. S. Lue. *NMR evidence for the spin gap behavior in Cu_2PO_4OH.* Phys. Rev. B **78**, 212407 (2008).

[131] J.-W. Bos, C. V. Colin, and T. T. M. Palstra. *Magnetoelectric coupling in the cubic ferrimagnet Cu_2OSeO_3.* Phys. Rev. B **78**, 094416 (2008).

[132] G. Tams and H. Müller-Buschbaum. *Synthese und Kristallstruktur eines gemischt-valenten Natrium-Oxycuprats (I, II): $NaCu_2O_2$.* Journal of Alloys Compd. **189**, 241 (1992).

[133] O. Janson, A. A. Tsirlin, M. Schmitt, and H. Rosner. *Large quantum fluctuations in the strongly coupled spin-1/2 chains of green dioptase $Cu_6Si_6O_{18}\cdot6H_2O$.* Phys. Rev. B **82**, 014424 (2010).

[134] D. Kasinathan, K. Koepernik, and W. E. Pickett. *Pressure-driven magnetic moment collapse in the ground state of MnO.* New J. Phys. **9**, 235 (2007).

[135] D. Kasinathan, K. Koepernik, U. Nitzsche, and H. Rosner. *Ferromagnetism induced by orbital order in the charge-transfer insulator Cs_2AgF_4: An electronic structure study.* Phys. Rev. Lett. **99**, 247210 (2007).

[136] O. Janson, J. Richter, P. Sindzingre, and H. Rosner. *Coupled frustrated quantum spin-1/2 chains with orbital order in volborthite $Cu_3V_2O_7(OH)_2 \cdot 2H_2O$.* Phys. Rev. B **82**, 104434 (2010).

[137] N. Shannon, B. Schmidt, K. Penc, and P. Thalmeier. *Finite temperature properties and frustrated ferromagnetism in a square lattice Heisenberg model.* Eur. Phys. J. B **38**, 599 (2004).

[138] B. Schmidt, P. Thalmeier, and N. Shannon. *Magneto-caloric effect in the frustrated square lattice $J_1 - J_2$ model.* Phys. Rev. B **76**, 125113 (2007).

[139] J. Richter, R. Darradi, J. Schulenburg, D. J. J. Farnell, and H. Rosner. *Frustrated spin 1/2 $J_1 - J_2$ Heisenberg ferromagnet on the square lattice studied via exact diagonalization and coupled cluster methods.* Phys. Rev. B **81**, 174429 (2010).

[140] A. A. Tsirlin and H. Rosner. *Extension of the spin- 1/2 frustrated square lattice model: The case of layered vanadium phosphates.* Phys. Rev. B **79**, 214417 (2009).

[141] D. Iwanaga, Y. Inaguma, and M. Itoh. *Crystal structure and magnetic properties of B-site ordered perovskite-type oxides $A_2CuB'O_6$ (A = Ba, Sr; B' = W, Te)*. Journal of Solid State Chemistry **147**, 291 (1999).

[142] A. A. Tsirlin private communication.

[143] M. W. Lufaso, W. R. Gemmill, S. J. Mugavero, S.-J. Kim, Y. Lee, T. Vogt, and H.-C. zur Loye. *Synthesis, structure, magnetic properties and structural distortion under high pressure of a new osmate, Sr_2CuOsO_6*. Journal of Solid State Chemistry **181**, 623 (2008).

[144] Q. Zhou and B. J. Kennedy. *A variable temperature structural study of the Jahn-Teller distortion in Ba_2CuUO_6*. Journal of Physics and Chemistry of Solids **68**, 1643 (2007).

[145] A. A. Tsirlin, O. Janson, and H. Rosner. *Unconventional ferromagnetic superexchange in $CdVO_3$: The role of Cd* (2011). ArXiv:1104.2495.

[146] H. Jeschke, I. Opahle, H. Kandpal, R. Valent, H. Das, T. Saha-Dasgupta, O. Janson, H. Rosner, A. Brhl, B. Wolf, M. Lang, J. Richter, S. Hu, X. Wang, R. Peters, T. Pruschke, and A. Honecker. *Multistep Approach to Microscopic Models for Frustrated Quantum Magnets: The Case of the Natural Mineral Azurite*. Phys. Rev. Lett. **106**, 217201 (2011).

[147] M. Braden, G. Willkendorf, J. Lorenzana, M. Ain, G. J. McIntyre, M. Behruzi, G. Heger, G. Dhalenne, and A. Revcolevschi. *Structural analysis of $CuGeO_3$: Relation between nuclear structure and magnetic interaction*. Phys. Rev. B **54**, 1105 (1996).

[148] S. Lebernegg, M. Schmitt, O. Janson, G. Amthauer, and H. Rosner. *Magnetic exchange interactions of quasi 1D Cu^{2+} halogenides from DFT cluster calculation*. (to be published).

[149] D. Koudela, U. Schwarz, H. Rosner, U. Burkhardt, A. Handstein, M. Hanfland, M. D. Kuz'min, I. Opahle, K. Koepernik, K.-H. Müller, and M. Richter. *Magnetic and elastic properties of YCo_5 and $LaCo_5$ under pressure*. Phys. Rev. B. **77**, 024411 (2008).

[150] K. Haule, V. Oudovenko, S. Y. Savrasov, and G. Kotliar. *The alpha $\rightarrow$ gamma transition in Ce: A theoretical view from optical spectroscopy*. Phys. Rev. Lett. **94**, 036401 (2005).

[151] A. K. McMahan, K. Held, and R. T. Scalettar. *Thermodynamic and spectral properties of compressed Ce calculated using a combined local-density approximation and dynamical mean-field theory*. Phys. Rev. B **67**, 075108 (2003).

[152] A. Chatterjee, A. K. Singh, and A. Jayaraman. *Pressure-Induced Electronic Collapse and Structural Changes in Rare-Earth Monochalcogenides*. Phys. Rev. B **6**, 2285 (1972).

[153] O. Mathon, F. Baudelet, J. P. Itie, S. Pasternak, A. Polian, and S. Pascarelli. *XMCD under pressure at the FeK edge on the energy-dispersive beamline of the ESRF.* J. Synchrotron Radiat. **11**, 423 (2004).

[154] J. P. Rueff, R. M. Galera, C. Giorgetti, E. Dartyge, C. Brouder, and M. Alouani. *Rare-earth contributions to the x-ray magnetic circular dichroism at the Co K edge in rare-earthcobalt compounds investigated by multiple-scattering calculations.* Phys. Rev. B **58**, 12271 (1998).

[155] H. Rosner, M. Schmitt, U. Schwarz, A. Trapananti, G. Aquilanti, A. V. Adreev, M. D. Kuzmin, O. Mathon, and M. Richter. *Experimental evidence of a magneto-elastic electronic topological transition in YCo_5 using high-pressure X-ray magnetic circular dichroism.* Submitted to Phys. Rev. B.

[156] D. C. Johnston. *The Puzzle of High Temperature Superconductivity in Layered Iron Pnictides and Chalcogenides.* Advances in Physics **59**, 803 (2010). ArXiv:1005.4392v2.

[157] C. Krellner, N. Caroca-Canales, A. Jesche, H. Rosner, A. Ormeci, and C. Geibel. *Magnetic and structural transitions in layered iron arsenide systems: AFe_2As_2 versus $RFeAsO$.* Phys. Rev. B **78**, 100504 (2008).

[158] D. Kasinathan, A. Ormeci, K. Koch, U. Burkhardt, W. Schnelle, A. Leithe-Jasper, and H. Rosner. *AFe_2As_2 (A = Ca, Sr, Ba, Eu) and $SrFe_{2-x}TM_xAs_2$ (TM = Mn, Co, Ni): crystal structure, charge doping, magnetism and superconductivity.* New Journal of Physics **11**, 025023 (2009).

[159] M. Kumar, M. Nicklas, A. Jesche, N. Caroca-Canales, M. Schmitt, M. Hanfland, D. Kasinathan, U. Schwarz, H. Rosner, and C. Geibel. *Effect of pressure on the magnetostructural transition in $SrFe_2As_2$.* Phys. Rev. B **78**, 184516 (2008).

[160] A. Kreyssig, M. A. Green, Y. Lee, G. D. Samolyuk, P. Zajdel, J. W. Lynn, S. L. Budko, M. S. Torikachvili, N. Ni, S. Nandi, J. B. Leao, S. J. Poulton, D. N. Argyriou, B. N. harmon, R. J. McQueeney, P. C. Canfield, and A. I. Goldman. *Pressure-induced volume-collapsed tetragonal phase of $CaFe_2As_2$ as seen via neutron scattering.* Phys. Rev. B **78**, 184517 (2008).

[161] W. Uhoya, A. Stemshorn, G. Tsoi, Y. K. Vohra, A. S. Sefat, B. C. Sales, K. M. Hope, and S. T. Weir. *Collapsed tetragonal phase and superconductivity of $BaFe_2As_2$ under high pressure.* Phys. Rev. B **82**, 144118 (2010).

[162] M. Bishop, W. Uhoya, G. Tsoi, Y. K. Vohra, A. S. Sefat, and B. C. Sales. *Formation of collapsed tetragonal phase in $EuCo_2As_2$ under high pressure.* J. Phys.: Condens. Matter **22**, 425701 (2010).

[163] T. Yildirim. *Strong Coupling of the Fe-Spin State and the As-As Hybridization in Iron-Pnictide Superconductors from First-Principle Calculations.* Phys. Rev. Lett. **102**, 037003 (2009).

[164] Y. Zhang, H. C. Kandpal, I. Opahle, H. O. Jeschke, and R. Valenti. *Microscopic origin of pressure-induced phase transitions in the iron pnictide superconductors AFe_2As_2: An abinitio molecular dynamics study.* Phys. Rev. B **80**, 094530 (2009).

[165] R. Hoffmann and C. Zheng. *Making and breaking bonds in the solid-state - the $ThCr_2Si_2$ structure.* J. Phys. Chem. **89**, 4175 (1985).

[166] I. I. Mazin, M. D. Johannes, L. Boeri, K. Koepernik, and D. J. Singh. *Problems with reconciling density functional theory calculations with experiment in ferropnictides.* Phys. Rev. B **78**, 085104 (2008).

[167] M. D. Johannes, I. I. Mazin, and D. S. Parker. *Effect of doping and pressure on magnetism and lattice structure of iron-based superconductors.* Phys. Rev. B **82**, 024527 (2010).

[168] I. I. Mazin and M. D. Johannes. *A key role for unusual spin dynamics in ferropnictides.* Nature Phys. **5**, 141 (2009).

[169] D. Kasinathan, M. Schmitt, K. Koepernik, A. Omerci, K. Meier, U. Schwarz, M. Hanfland, A. Leithe-Jasper, W. Schnelle, Y. Grin, and H. Rosner. *Symmetry-preserving lattice collapse in tetragonal $SrFe_{2?x}Ru_xAs_2$ (x= 0,0.2): A combined experimental and theoretical study.* Phys. Rev. B **83**, 054511 (2011).

[170] J. Donohue. *The Structure of the Elements.* (Wiley, NewYork) (1974).

[171] M. Kohout. Int. J. Quantum Chem. **97**, 651 (2004).

[172] A. Ormeci, H. Rosner, F. R. Wagner, M. Kohout, and Y. Grin. J. Phys. Chem. A **110**, 1100 (2006).

[173] M. Kohout, basin, version 4.7, 2008.

[174] D. Johrendt, C. Felser, O. Jepsen, O. K. Andersen, A. Mewis, and J. Rouxel. *LMTO band structure calculations of $ThCr_2Si_2$-type transition metal compounds.* J. Solid State Chem. **130**, 254 (1997).

[175] C. Huhnt, G. Michels, M. Roepke, W. Schlabitz, A. Wurth, D. Johrendt, and A. Mewis. *First-order phase transitions in the $ThCr_2Si_2$-type phosphides ARh_2P_2 (A = Sr, Eu).* Physica B **240**, 26 (1997).

[176] A. R. Miedema. *On the valence state of europium in alloys.* J. Less Com. Met. **46**, 167 (1976).

[177] F. R. de Boer, W. H. Dijkman, W. C. M. Mattens, and A. R. Miedema. *Valence state of Yb and Ce in transition-metal intermetallic compounds.* J. Less Com. Met. **64**, 241 (1979).

[178] W. C. M. Mattens, F. R. de Boer, A. K. Nissen, and A. R. Miedema. *On the valence state of Yb, Eu and Ce in non-transition metal-compounds.* J. Magn. Magn. Mater. **31-34**, 451 (1983).

Bibliography

[179] J. M. Lawrence, P. S. Riseborough, and R. D. Parks. *Valence fluctuation phenomena.* Rep. Prog. Physica **44**, 1 (1981).

[180] S. K. Dhar, S. K. Malik, and R. Vijayaghavan. *Boron addition to RPd_3 compounds (R= rare-earth).* Mat. Res. Bull. **16**, 1557 (1981).

[181] S. K. Dhar, S. K. Malik, D. Rambabu, and R. Vijayaghavan. *Valence state of Europium in $EuPd_3B_x$ alloys - lattice-constant and susceptibility studies.* J. Appl. Phys. **53**, 8077 (1982).

[182] S. K. Dhar, R. Nagarajan, S. K. Malik, R. Vijayaghavan, M. M. Abd-Elmeguid, and H. Micklitz. *Valence behavior of europium in $EuPd_3B_x$ ($0 \leq x \leq 1$) alloys: Possible charge ordering in $EuPd_3B$.* Phys. Rev. B **29**, 5953 (1984).

[183] S. K. Malik, S. K. Dhar, and R. Vijayaghavan. *Structural and magnetic investigations of some new boron containing rare earth intermetallic compound.* Bull. Mater. Sci. **6**, 263 (1984).

[184] S. K. Malik, S. K. Dhar, and R. Vijayaghavan. *Studies on the valence state of Ce and Eu in some new boron and silicon containing rare-earthintermetallic compounds.* Pramana **22**, 329 (1984).

[185] C. Loison, A. Leithe-Jasper, and H. Rosner. *Electronic structures of intermetallic borides RPd3Bx (R=rare-earth metals).* Phys. Rev. B **75**, 205135 (2007).

[186] J. A. Blackman, D. M. Esterling, and N. F. Berk. *Generalized LocatorCoherent-Potential Approach to Binary Alloys.* Phys. Rev. B **4**, 2412 (1971).

[187] A. Paney, C. Mazumdar, and R. Ranghanatan. *Magnetism and transport studies in off-stoichiometric metallic perovskite compounds $GdPd_3B_x$ (x =0.25, 0.50 and 0.75).* J. Magn. Magn. Mater. **322**, 3765 (2010).

[188] O. Sologub and P. Rogl. *Phase equilibria and crystal structures in the system Eu-Pd-B.* Intermetallics **18**, 1642 (2010).

[189] R. Gumeniuk, M. Schmitt, C. Loison, W. Carrillo-Cabrera, U. Burkhardt, G. Auffermann, M. Schmidt, W. Schnelle, C. Geibel, A. Leithe-Jasper, and H. Rosner. *Boron induced change of the Eu valence state in $EuPd_3B_x$ ($0 \leq x \leq 0.53$): A theoretical and experimental study.* Phys. Rev. B **82**, 235113 (2010).

[190] L. Cianchi, S. de Gennaro, F. Gulisano, M. Mancini, and G. Spina. *The influence of boron distribution on the valence of Eu in $EuPd_3B$.* J. Phys.: Condens. Matter **3**, 781 (1991).

[191] A. Paney, C. Mazumdar, and R. Ranghanatan. *Negative pressure driven valence instability of Eu in cubic $Eu_{0.4}La_{0.6}Pd_3$.* J. Phys. Condens. Matter. **21**, 216002 (2009).

[192] M. Schmitt, R. Gumeniuk, A. Trapananti, G. Aquilanti, C. Strom, K. Meier, U. Schwarz, M. Hanfland, W. Schnelle, A. Leithe-Jasper, and H. Rosner. *Tuning the Eu valence in $EuPd_3B_x$ by pressure - a combined experimental and computational study.* Submitted to Phys. Rev. B.

[193] A. F. Albuquerque, F. Alet, P. Corboz, P. Dayal, A. Feiguin, S. Fuchs, L. Gamper, E. Gull, S. Gürtler, A. Honecker, R. Igarashi, M. Körner, A. Kozhevnikov, A. Läuchli, S. Manmana, M. Matsumoto, I. McCulloch, F. Michel, R. Noack, G. Pawlowski, and *et al. The ALPS project release 1.3: Open-source software for strongly correlated systems.* J. Mag. Magn. Mater. **310**, 1187 (2007).

[194] X. Wang and T. Xiang. *Transfer-matrix density-matrix renormalization-group theory for thermodynamics of one-dimensional quantum systems.* Phys. Rev. B **56**, 5061 (1997).

[195] R. Kanno, Y. Kawamoto, Y. Takeda, M. Hasegawa, O. Yamamoto, and N. Kinomura. *Structure and phase transition in the spinel system $Li_{1-x}CuVO_4$ (0$\leq$ x $\leq$0.2), with one-dimensional cooperative Jahn-Teller ordering.* Journal of Solid State Chemistry **96**, 397 (1992).

[196] R. Hoffmann and R. Hoppe. ZAAC **578**, 18 (1989).

[197] H. Voellenkle, A. Wittmann, and H. N. Nowotny. *Zur Kristallstruktur von $CuGeO_3$.* Monatshefte fuer Chemie **98**, 1352 (1967).

[198] G. Tunell, E. Posnjak, and C. J. Ksanda. *Geometrical and optical properties, and crystal structure of tenorite.* Zeitschrift fuer Kristallographie **90**, 120 (1935).

[199] T. Ami, M. K. Crawford, R. L. Harlow, Z. R. Wang, D. C. Johnston, Q. Huang, and R. W. Erwin. *Magnetic susceptibility of low-temperature structure of the linear chain cuprate Sr_2CuO_3.* Phys. Rev. B **51**, 5994 (1995).

[200] M. Mizumaki, S. Tsutsui, H. Tanida, T. Uruga, D. Kikuchi, H. Sugawara, and H. Sato. *The mixed valence states in the unconventional heavy fermion compound $SmOs_4Sb_{12}$.* J. Phys. Soc. Jpn. **76**, 053706 (2007).

[201] P. C. Burns and F. C. Hawthorne. *Tolbachite, $CuCl_2$, the first example of Cu^{2+} octahedrally coordinated by Cl^-.* American Mineralogist **78**, 187 (1993).

[202] O. Oeckler and A. Simon. *Redetermination of the cystal structure of copper dibromide, $CuBr_2$.* Zeitschrift fuer Kristallographie - New Crystal Structures **215**, 13 (2000).

[203] A. Engberg. *An X-Ray refinement of the crystal structure of copper(II) chloride dihydrate.* Acta Chemica Scandinavica **24**, 3510 (1970).

[204] S. Brownstein, N. F. Han, E. J. Gabe, and Z. le Page. *A redetermination of the crystal structure of cupric chloride dihydrate.* Zeitschrift fuer Kristallographie **189**, 13 (1989).

[205] K. Waizumi, H. Masuda, and H. Ohtaki. *X-ray structural studies of $FeBr_2 \cdot 4H_2O$, $CoBr_2 \cdot 4H_2O$, $NiCl_2 \cdot 4H_2O$ and $CuBr_2 \cdot 4H_2O$. cis/trans Selectivity in transition metal(II) dihalide tetrahydrate.* Inorganica Chimica Acta **192**, 173 (1992).

List of publications

Publications discussed in this thesis:

1. **Section 3.1.1:** A. Möller, **M. Schmitt**, W. Schnelle, T. Förster, and H. Rosner. *AgCuVO$_4$: a quasi one-dimensional S=1/2 chain compound*, Phys. Rev. B **80**, 125106 (2009).

2. **Section 3.1.2: M. Schmitt**, J. Malek, S.-L. Drechsler, and H. Rosner. *Electronic and magnetic properties of Li$_2$ZrCuO$_4$ - a spin 1/2 Heisenberg system in vicinity to a quantum critical point*, Phys. Rev. B **80**, 205111 (2009).

3. **Section 3.1.2:** A. A. Tsirlin, **M. Schmitt**, and H. Rosner. *Li$_2$ZrCuO$_4$ - new theoretical results about the Li(1) split position*, (in preparation).

4. **Section 3.1.3: M. Schmitt**, H. Borrmann, W. Schnelle, A. A. Tsirlin, A. Wolter, S.-L. Drechsler, and H. Rosner. *Magnetic properties ruled by H position in the natural mineral linarite PbCuSO$_4$OH - a joint theoretical and experimental study*, (in preparation).

5. **Section 3.1.3:** A. U. B. Wolter, F. Lipps, M. Schäpers, S.-L. Drechsler, S. Nishimoto, R. Vogel, V. Kataev, B. Büchner, H. Rosner, **M. Schmitt**, M. Uhlarz, Y. Skourski, J. Wosnitza, K. C. Rule, S. Süllow, and G. Heide, *Magnetic properties and revisited assignment of the main exchange integrals of the frustrated spin s = 1/2 chain cuprate PbCuSO$_4$(OH)$_2$ - linarite*, Phys. Rev. B **85**, 014407 (2012).

6. **Section 3.1.4: M. Schmitt**, O. Janson, M. Schmidt, S. Hoffmann, W. Schnelle, S.-L. Drechsler, and H. Rosner. *Crystal-water-induced switching of magnetically active orbitals in CuCl$_2$*, Phys. Rev. B **79**, 245119 (2009).

7. **Section 3.1.4: M. Schmitt**, M. Schmidt, W. Schnelle, S.-L. Drechsler, and H. Rosner. *Crystal water induced alteration of magnetic exchange interactions*, Z. Anorg. Allg. Chem. **634**, 2076 (2008).

8. **Section 3.1.5: M. Schmitt**, O. Janson, S. Golbs, M. Schmidt, W. Schnelle, J. Richter, and H. Rosner. *Alternating chain compounds Na$_3$Cu$_2$SbO$_6$ and Na$_2$Cu$_2$TeO$_6$*, (in preparation).

9. **Section 3.1.6: M. Schmitt**, A. A. Gippius, K. S. Okhotnikov, W. Schnelle, K. Koch, O. Janson, W. Liu, Y.-H. Huang, Y. Skourski, F. Weickert, M. Baenitz, and H. Rosner. *Electronic structure and magnetic properties of the spin-gap compound Cu$_2$(PO$_3$)$_2$CH$_2$: Magnetic versus structural dimers*, Phys. Rev. B **79**, 127101 (2009).

10. **Section 3.1.8: M. Schmitt**, O. Janson, A. A.Tsirlin, D. Kasinathan, M. Schmidt, W. Schnelle, and H. Rosner. *A$_2$CuEO$_6$ - a new family of spin 1/2 square lattice compounds*, (in preparation).

11. **Section 4.1.1:** H. Rosner, **M. Schmitt**, U. Schwarz, A. Trapananti, G. Aquilanti, A. V. Adreev, M. D. Kuzmin, O. Mathon, and M. Richter. *Experimental evidence of a magneto-elastic electronic topological transition in YCo_5 using high-pressure X-ray magnetic circular dichroism*, (submitted to Phys. Rev. B).

12. **Section 4.1.2:** D. Kasinathan, **M. Schmitt**, K. Koepernik, A. Omerci, K. Meier, U. Schwarz, M. Hanfland, A. Leithe-Jasper, W. Schnelle, Y. Grin, and H. Rosner. *Tetragonal lattice collapse in $SrFe_2As_2$ - a combined experimental and theoretical study*, Phys. Rev. B **83**, 054511 (2011).

13. **Section 4.2.1:** R. Gumeniuk, **M. Schmitt**, C. Loison, W. Carillo-Cabrera, U. Burkhardt, G. Auffermann, M. Schmidt, W. Schnelle, C. Geibel, A. Leither-Jasper, and H. Rosner. *Boron induced change of the Eu valence state in $EuPd_3B_x$ (0 < x < 0.53): a joint theoretical and experimental study*, Phys. Rev. B **82**, 235113 (2010).

14. **Chapter 4.2.1: M. Schmitt**, R. Gumeniuk, A. Trapananti, G. Aquilanti, C. Strom, K. Meier, U. Schwarz, M. Hanfland, W. Schnelle, A. Leithe-Jasper, and H. Rosner. *Tuning the Eu valence in $EuPd_3B_x$ by pressure - a combined experimental and computational study*, (submitted to Phys. Rev. B).

Other publications:

15. S.-L. Drechsler, N. Tristan, R. Klingeler, B. Büchner, J. Richter, J. Malek, O. Volkova, A. Vasiliev, **M. Schmitt**, A. Ormeci, C. Loison, W. Schnelle, and H. Rosner. *Helimagnetism and weak ferromagnetism in $NaCu_2O_2$ and related frustrated chain cuprates*, J. Phys.: Condens. Matter **19**, 145230 (2007).

16. H. Rosner, M. D. Johannes, S.-L. Drechsler, **M. Schmitt**, O. Janson, W. Schnelle, W. Liu, Y.-X. Huang, and R. Kniep. *Cu^{II} materialsFrom crystal chemistry to magnetic model compounds*, Sci. Tech. Adv. Mater. **8**, 352 (2007).

17. M. Kumar, M. Nicklas, A. Jesche, N. Craco-Canales, **M. Schmitt**, M. Hanfland, D. Kasinathan, U. Schwarz, H. Rosner, and C. Geibel. *Effect of pressure on the magnetostructural transition in $SrFe_2As_2$*, Phys. Rev. B **78**, 184516 (2008).

18. O. Janson, A. A. Tsirlin, **M. Schmitt**, and H. Rosner. *Large quantum fluctuations in the strongly coupled spin-1/2 chains of green dioptase $Cu_6Si_6O_{18}\cdot6H_2O$*, Phys. Rev. B **82**, 014424 (2010).

19. H. Rosner, **M. Schmitt**, D. Kasinathan, A. Ormeci, J. Richter, S. -L. Drechsler, and M. D. Johannes. *Comment on Electronic structure of spin-1/2 Heisenberg anti-ferromagnetic systems: $Ba_2Cu(PO_4)_2$ and $Sr_2Cu(PO_4)_2$*, Phys. Rev. B **79**, 127101 (2009).

20. S.-L. Drechsler, S. Nishimoto, R. Kuzian, J. Malek, J. Richter, J. v. d. Brink, **M. Schmitt**, and H. Rosner. *Comment on Two-spinon and four-spinon continuum in a frustrated ferromagnetic spin 1/2 chain*, Phys. Rev. Lett. **106**, 219701 (2011).

21. S. Nishimoto, S.-L. Drechsler, R. Kuzian, J. Richter, J. Malek, **M. Schmitt**, J. van den Brink, and H. Rosner. *The strength of frustration and quantum fluctuations in $LiCuVO_4$*, Eur. Phys. Lett. **98**, 37007(2012) and arXiv: 1105.2810v1.

22. R. Gumeniuk, **M. Schmitt**, W. Schnelle, U. Burkhardt, H. Rosner, and A. Leithe-Jasper. *SrPd$_4$B and BaPd$_4$B: New type of crystal structure and physical properties*, Z. Anorg. Allg. Chem. **636**, 954-961 (2010).

23. S. Lebernegg, **M. Schmitt**, O. Janson, G. Amthauer, and H. Rosner. *Magnetic exchange interactions of quasi 1D Cu^{2+} halogenides from DFT cluster calculation*, (in preparation).

24. K. Koch, **M. Schmitt**, K. Koepernik, Y. Grin, and H. Rosner. *Comparative study of different cuprates: interplay of crystal structure and electronic structure probed by the EFG*, (in preparation).

Acknowledgements

Versicherung

Hiermit versichere ich, dass ich die vorliegende Arbeit ohne unzulässige Hilfe Dritter und ohne Benutzung anderer als der angegebenen Hilfsmittel angefertigt habe; die aus fremden Quellen direkt oder indirekt übernommenen Gedanken sind als solche kenntlich gemacht. Die Arbeit wurde bisher weder im Inland noch im Ausland in gleicher oder ähnlicher Form einer anderen Prüfungsbehörde vorgelegt.

Die vorliegende Dissertation wurde unter der Betreuung von Prof. Dr. Helmut Eschrig und Dr. Helge Rosner in der Kompetenzgruppe Theoretische Physik im Max-Planck-Institut für chemische Physik fester Stoffe angefertigt.

Dresden, den 08.07.2011

(Miriam Schmitt)